



ICQNM 2011

The Fifth International Conference on Quantum, Nano and Micro Technologies

ISBN: 978-1-61208-151-9

August 21-27, 2011

Nice/Saint Laurent du Var, France

ICQNM 2011 Editors

Vladimir Privman, Clarkson University - Potsdam, USA

Victor Ovchinnikov, Aalto University, Finland

ICQNM 2011

Foreword

The Fifth International Conference on Quantum, Nano and Micro Technologies (ICQNM 2011), held between August 21-27, 2011 in Nice/Saint Laurent du Var, France, continued a series of events covering particularly promising theories and technologies. The conference covered fundamentals on designing, implementing, testing, validating and maintaining various kinds of materials, systems, techniques and mechanisms related to quantum-, nano- and microtechnologies.

Quantum technologies and nano technologies have a great potential to transform communications telecommunications infrastructure and communication protocols, and computers and networking devices. Nanotechnologies and micro-technologies already made their mark on smart materials, nano-medicine, nano-devices, molecular manufacturing, biotechnology, metrology, airspace.

The advancements in material science and computer science have allowed the building, launching and deploying of space exploration systems that continually do more and more as they become smaller and lighter. As an example, carbon nano-tubes have been created that are 250 times stronger than steel, 10 times lighter, and transparent. Similar advances are occurring in glass, plastics and concrete. Spacecraft are being launched, with hulls that are composed of carbon fibers, a light weight high strength material. Swarms is another concept of nano-robotics; swarms act in unison like bees. They theoretically will act as a flexible cloth like material, as strong as diamond. Interplanetary exploration can be foreseen as being carried on by nano-robots as well.

Electronic devices, medicine, environment, metrology, aerospace programs, clothes and materials, telecommunications, cryptography, semiconductors, manufacturing, and other domains are impacted by the progress on the areas mentioned above. Particularly, micro imaging, nano-medicine: (drug delivery; nano-particles i.e. viruses; proteins.), bio-nanostructures: (nano-tubes, nano-particles), microsystems, micro fluidics: (including nano-fluidics, modeling; fabrication and application), micro instrumentation / implantable microdevices (miniaturized bio-electronic systems etc.) and micro sensors benefits from the progress on quantum, nano and micro technologies.

We take here the opportunity to warmly thank all the members of the ICQNM 2011 technical program committee as well as the numerous reviewers. The creation of such a broad and high quality conference program would not have been possible without their involvement. We also kindly thank all the authors that dedicated much of their time and efforts to contribute to the ICQNM 2011. We truly believe that thanks to all these efforts, the final conference program consists of top quality contributions.

This event could also not have been a reality without the support of many individuals, organizations and sponsors. We also gratefully thank the members of the ICQNM 2011 organizing committee for their help in handling the logistics and for their work that is making this professional meeting a success.

We hope the ICQNM 2011 was a successful international forum for the exchange of ideas and results between academia and industry and to promote further progress in the area of quantum-, nano- and micro-technologies.

We hope Côte d'Azur provided a pleasant environment during the conference and everyone saved some time for exploring the Mediterranean Coast.

ICQNM 2011 Chairs

Advisory Chairs

Vladimir Privman, Clarkson University - Potsdam, USA

Christian Kollmitzer, AIT Austrian Institute of Technology GmbH, Austria

Wen-Ran Zhang, Georgia Southern University, USA

Victor Ovchinnikov, Aalto University, Finland

Research/Industry Chairs

Marco Genovese, Italian Metrological Institute (INRIM) -Torino, Italy

Keiji Matsumoto, National Institute of Informatics, Japan

Special Area Chairs

QSEC

Masahito Hayashi, Tohoku University, Japan

Fluidics

Alireza Azarbadegan, University College London (UCL), UK

Quantum algorithms and quantum complexity

Francois Le Gall, The University of Tokyo, Japan

Quantum control

Daoyi Dong, University of New South Wales, Australia

ICQNM 2011

Committee

ICQNM Advisory Chairs

Vladimir Privman, Clarkson University - Potsdam, USA
Christian Kollmitzer, AIT Austrian Institute of Technology GmbH, Austria
Wen-Ran Zhang, Georgia Southern University, USA
Victor Ovchinnikov, Aalto University, Finland

ICQNM 2011 Research/Industry Chairs

Marco Genovese, Italian Metrological Institute (INRIM) -Torino, Italy
Keiji Matsumoto, National Institute of Informatics, Japan

ICQNM 2011 Special Area Chairs

QSEC

Masahito Hayashi, Tohoku University, Japan

Fluidics

Alireza Azarbadegan, University College London (UCL), UK

Quantum algorithms and quantum complexity

Francois Le Gall, The University of Tokyo, Japan

Quantum control

Daoyi Dong, University of New South Wales, Australia

ICQNM 2011 Technical Program Committee

Gerardo Adesso, University of Nottingham, UK
Diederik Aerts, Brussels Free University, Belgium
Alireza Azarbadegan, University College London (UCL), UK
Irina Buyanova, Linköping University, Sweden
Weimin M. Chen, Linköping University, Sweden
Taksu Cheon, Kochi University of Technology - Tosa Yamada, Japan
Sorin Cotofana, Delft University of Technology, The Netherlands
Petre Dini, Cisco Systems, Inc., USA / Concordia University, Canada
Daoyi Dong, University of New South Wales, Australia
Sao-Ming Fei, Capital Normal University - Beijing, China
Akihiko Fujiwara, Japan Synchrotron Radiation Research Institute - Hyogo, Japan
Juan Carlos García-Escartín, Universidad de Valladolid, Spain
Liane Gabora, University of British Columbia - Kelowna, Canada
Yuval Gefen, The Weizmann Institute of Science, Israel
Marco Genovese, Italian Metrological Institute (INRIM) -Torino, Italy

Masahito Hayashi, Tohoku University, Japan
Travis Humble, Oak Ridge National Laboratory, USA
Elzbieta Jankowska, National Research Institute - Warsaw, Poland
Tzyh Jong Tarn, Washington University - St. Louis, USA
Andrei Khrennikov, Linnaeus University, Växjö-Kalmar, Sweden
Andreas Klappenecker, Texas A&M University, USA
Christian Kollmitzer, AIT Austrian Institute of Technology GmbH, Austria
David Kribs, University of Guelph, Canada
Francois Le Gall, The University of Tokyo, Japan
Gui Lu Long, Tsinghua University, China
Alex Lvovsky, University of Calgary, Canada
Stefano Mancini, University of Camerino, Italy
Louis Marchildon, Université du Québec à Trois-Rivières, Canada
Sylvain Martel, École Polytechnique de Montréal, Canada
Keiji Matsumoto, National Institute of Informatics, Japan
Constantinos Mavroidis, Northeastern University - Boston, USA
Rajagopal Nagarajan, University of Warwick, UK
Masaki Nakanishi, Nara Institute of Science and Technology, Japan
Munehiro Nishida, Hiroshima University, Japan
Luis Roa Oppliger, Universidad de Concepción, Chile
Victor Ovchinnikov, TKK Micronova/ Helsinki University of Technology, Finland
Telhat Özdoğan, Rize Üniversitesi, Turkey
Matteo G. A. Paris, Università degli studi di Milano, Italy
Martin B. Plenio, Imperial College London, UK
Vladimir Privman, Clarkson University - Potsdam, USA
Stefan Rass, Universität Klagenfurt, Austria
Norman Hugh Redington, MIT, USA
Philippe Renaud, Ecole Polytechnique Federale de Lausanne, Switzerland
Gerasimos G. Rigatos, Industrial Systems Institute - Rion Patras, Greece
Andrew Sachrajda, National Research Council of Canada, Canada
Barry Sanders, iCORE/University of Calgary, Canada
Peter Schartner, University of Klagenfurt, Austria
Sanjiv Sharma, Imperial College London, UK
Bijan Shirinzadeh, Monash University - Clayton, Australia
Ingo Sieber, Karlsruher Institut für Technologie (KIT), Germany
Don Sofge, Naval Research Laboratory - Washington D.C., USA
Igor Sokolov, Clarkson University - Potsdam, USA
Dian-Min Tong, Shandong University - Jinan, China
Sergey Vakulenko, Saint Petersburg State University of Technology and Design / Academy of Sciences - Saint Petersburg, Russia
Manuel Vázquez, Instituto de Ciencia de Materiales - CSIC, Madrid, Spain
Salvador E. Venegas-Andraca, Tecnológico de Monterrey, Mexico
Xudong Wang, University of Wisconsin-Madison - Madison, USA
Alexander Weddemann, Bielefeld University, Germany
Frank Wittbracht, University of Bielefeld in Germany, Germany
Shigeru Yamashita, Ritsumeikan University - Shiga, Japan
Jian-Qiang You, Fudan University - Shanghai 200433, China
Alexandre Zagoskin, Loughborough University, UK

Qi-Ren Zhang, Peking University - Beijing, China

Wen-Ran Zhang, Georgia Southern University, USA

J. X. Zheng-Johansson, Institute of Fundamental Physics Research - Nyköping, Sweden

Copyright Information

For your reference, this is the text governing the copyright release for material published by IARIA.

The copyright release is a transfer of publication rights, which allows IARIA and its partners to drive the dissemination of the published material. This allows IARIA to give articles increased visibility via distribution, inclusion in libraries, and arrangements for submission to indexes.

I, the undersigned, declare that the article is original, and that I represent the authors of this article in the copyright release matters. If this work has been done as work-for-hire, I have obtained all necessary clearances to execute a copyright release. I hereby irrevocably transfer exclusive copyright for this material to IARIA. I give IARIA permission to reproduce the work in any media format such as, but not limited to, print, digital, or electronic. I give IARIA permission to distribute the materials without restriction to any institutions or individuals. I give IARIA permission to submit the work for inclusion in article repositories as IARIA sees fit.

I, the undersigned, declare that to the best of my knowledge, the article does not contain libelous or otherwise unlawful contents or invading the right of privacy or infringing on a proprietary right.

Following the copyright release, any circulated version of the article must bear the copyright notice and any header and footer information that IARIA applies to the published article.

IARIA grants royalty-free permission to the authors to disseminate the work, under the above provisions, for any academic, commercial, or industrial use. IARIA grants royalty-free permission to any individuals or institutions to make the article available electronically, online, or in print.

IARIA acknowledges that rights to any algorithm, process, procedure, apparatus, or articles of manufacture remain with the authors and their employers.

I, the undersigned, understand that IARIA will not be liable, in contract, tort (including, without limitation, negligence), pre-contract or other representations (other than fraudulent misrepresentations) or otherwise in connection with the publication of my work.

Exception to the above is made for work-for-hire performed while employed by the government. In that case, copyright to the material remains with the said government. The rightful owners (authors and government entity) grant unlimited and unrestricted permission to IARIA, IARIA's contractors, and IARIA's partners to further distribute the work.

Table of Contents

| | |
|--|----|
| Introducing Interconnection Crossing in Ternary Quantum-dot Cellular Automata <i>Primoz Pecar</i> | 1 |
| Effect of Adhesion Layer on Morphology and Optical Properties of Self-Organized Metal Nanostructures <i>Victor Ovchinnikov</i> | 6 |
| A gradient-based approach to feedback control of quantum systems <i>Gerasimos Rigatos</i> | 12 |
| Reflectionless and Equiscattering Quantum Graphs <i>Taksu Cheon</i> | 18 |
| Combinatorial structures of quantum entangled states <i>Hoshang Heydari</i> | 23 |
| Reduced Hamiltonian Technique for Gate Design in Strongly Coupled Quantum Systems <i>Preethika Kumar, Steven Skinner, and Sahar Daraeizadeh</i> | 28 |
| Quantum Interaction Approach in Cognition, Artificial Intelligence and Robotics <i>Diederik Aerts, Marek Czachor, and Sandro Sozzo</i> | 35 |
| Quantum Computing with Charge States in Silicon : Towards a Leadless Approach <i>Thierry Ferrus, Rossi Alessandro, Aleksey Andreev, Paul Chapman, and David Arfon Williams</i> | 41 |
| Quantum Dynamics and Coherence of Qubits <i>Vladimir Privman</i> | 46 |
| New Method for Representation of Multi-qbit Systems Using Fractals <i>Mate Galambos and Sandor Imre</i> | 52 |
| Quantum Structure in Cognition: Fundamentals and Applications <i>Diederik Aerts, Liane Gabora, Sandro Sozzo, and Tomas Veloz</i> | 57 |
| DNA Lattice Nanostructures as Biointerface Materials for Electrochemical Biosensor Studies <i>Murugan Veerapandian, Chang-Hyun Jang, Guie-Sam Lim, Sung Ha Park, Min-Ho Lee, and Kyusik Yun</i> | 63 |
| Improved Linearity CMOS Active Resistor Structure Using Computational Circuits <i>Cosmin Popa</i> | 67 |
| Dry Film Resist Microfluidic Channels on Printed Circuit Board and its Application as Fluidic Interconnection for | 71 |

| | |
|---|-----|
| Nanofluidic Chips: Fabrication Challenges <i>Nuria Berenice Palacios Aguilera, Venkata R. S. S. Mokkalapati, Jeroen Bastemeijer, Jeff R. Mollinger, and Andre Bossche</i> | |
| The Radiobiological Effect of the TiO ₂ – Cyclodextrin Suspension <i>Mihaela Corneanu, Gabriel Corneanu, Aurel Ardelean, Carmen Lazau, Ioan Grozescu, Nicoleta G. Hadaruga, Daniel I. Hadaruga, and Lucian Barbu-Tudoran</i> | 77 |
| Indirect Eavesdropping in Quantum Networks <i>Stefan Rass and Sandra Konig</i> | 83 |
| Geometry Induced Microparticle Separation in Passive Contraction Expansion Straight Channels <i>Mustafa Yilmaz, Meral Cengiz, Huseyin Kizil, Arzu Ozbey, and Levent Trabzon</i> | 89 |
| Microfluidic gate - Utilization of Self-Assembling, Free-Flowing Superstructures of Superparamagnetic Beads for Enhanced Mixing and Colloidal Separation <i>Bernhard Eickenberg, Frank Wittbracht, Andreas Hutten, and Alexander Weddemann</i> | 94 |
| Rotating magnetic field assisted formation of highly ordered two-dimensional magnetic bead arrays <i>Frank Wittbracht, Bernhard Eickenberg, Alexander Weddemann, and Andreas Hutten</i> | 99 |
| Microfluidics Blood Separations through Optical Sorting and Deterministic Lateral Displacement <i>Alexander Zhanov and Sung Yang</i> | 103 |
| PVC Inorganic Hybrids Based on Kaolinite/Urea Intercalates <i>Alena Kalendova, Jitka Zykova, Vlastimil Matejka, Michal Machovsky, and Jiri Malac</i> | 109 |

Introducing Interconnection Crossing in Ternary Quantum-dot Cellular Automata

Primoz Pecar

University of Ljubljana, Faculty of Computer and Information Science, Ljubljana, Slovenia
primoz.pecar@fri.uni-lj.si

Abstract—The ternary Quantum-dot Cellular Automaton (tQCA), a processing platform based on interacting quantum dots, was demonstrated to be a promising paradigm for multi-valued processing. With the development of the ternary functionally complete set of elementary logic primitives and the ternary memorizing cell the design of complex processing structures is becoming feasible. Hence, the research focus is moving from the bottom-up design approach to the logic design approach. With the increase of processing functionality there comes also the increase in design complexity. Due to the specific tQCA cell geometry one of the most problematic area tends to be the interconnection crossing. This paper introduces a solution using a multi-layer approach.

Keywords—ternary Quantum-dot Cellular Automaton, tQCA interconnection, tQCA wire, tQCA interconnection crossing, multi-layer design

I. INTRODUCTION

The Quantum-dot Cellular Automaton (QCA) is perceived as one of the promising computing paradigms, which could be a solution to the technological limitations of the CMOS platform [1]. Its novel concept of operation where information is encoded in charge orientation lets information transmission and processing to be carried out by the same entities, named QCA cells [2].

The promising results in the binary domain have encouraged the research of possible implementations in the realm of multi-valued logic [3]. The redesign of the binary QCA (bQCA) cell, called ternary QCA (tQCA) cell, allowed the representation of three logic values [4]–[6] and the adaptation of adiabatic pipelining was used to solve the issues of the tQCA logic primitives [7], [8]. Hence, the adjustments were made to preserve the operation mechanics and design rules that were extensively researched in the binary domain [9]–[12].

Ternary logic is defined as a generalization of binary logic so one cannot simply use the binary functionally complete set [13]. Therefore chain-based Post logic [14] was used as the foundation of the tQCA implementation of a ternary functionally complete set. The set comprises the ternary majority gate, used to obtain conjunction and disjunction, and the ternary characteristic functions. While the majority gate was implemented using proven approaches from bQCA design [8], this was not the case for the characteristic functions. They were developed following the bottom-up approach, i.e., by observing the behavior of simple tQCA segments and their subsequent composition according to

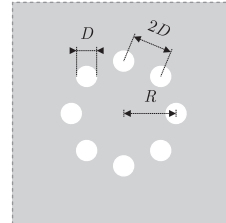


Figure 1. The geometry of the ternary quantum-dot cell.

physical design rules [15]. The existence of a functionally complete set made the design of the basic ternary memorizing cell possible [16].

The described ternary building blocks promote composition of complex ternary processing structures following a logic design approach. However, the research results from the bQCA domain show that efficient design highly depends on effective solutions of building block interconnection [17]. The currently developed basic tQCAs are constrained to remain on a coplanar surface, hence the increase of processing functionality brings also the increase in interconnection complexity. A great deal of it is contributed by crossover problems. Due to specific tQCA cell geometry one of the unique bQCA paradigm features, a coplanar wire crossing, cannot be efficiently implemented in the tQCA domain. This paper presents a study of a possible noncoplanar (multi-layer) approach, which promises an efficient solution of the previously described issue.

Section II starts with a brief overview of the tQCA platform. Section III continues with the presentation of the tQCA wire, the interconnection crossing problem and proposes the multi-layer solution. The conclusion follows in Section IV.

II. tQCA PLATFORM

In general, a QCA is a planar array of quantum-dot (QCA) cells [1]. The fundamental unit of a ternary QCA is a tQCA cell [4]. It comprises eight quantum dots and two mobile electrons. The quantum dots with diameter $D = 10$ nm are arranged in a circular pattern with radius $R = D/\sin(\pi/8)$, so that the distance between neighboring quantum dots equals $2D$ (see Fig. 1). The electrons can only reside at quantum dots or tunnel between adjacent quantum dots, but cannot tunnel outside the cell. The Coulomb interaction

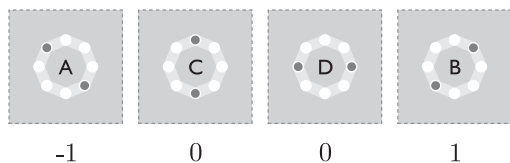


Figure 2. The four possible arrangements of the electrons contained in a tQCA cell that are mapped to balanced ternary values -1, 0 and 1.

between the electrons causes them to localize in quantum dots that ensure their maximal separation (energetic minimal state). The four arrangements, which correspond to the energetic minimal states (ground states), are marked as A, B, C and D (see Fig. 2). The four states can be interpreted as balanced ternary logic values, so A is interpreted as logic value -1 , B as logic value 1 and C and D as 0 . The arrangement D is typically not allowed (desired) for input or output cells [5]–[7]. The charge distribution in one or more cells in the observed cell’s neighborhood, causes one of the four arrangements to become the favored ground state. The cell to cell interaction is strictly Coulombic and involves only rearrangements of electrons within individual cells, thus it enables computation. With specific planar arrangements of cells it is possible to construct logic gates as well as interconnects among them [18].

The reliability of the behavior of a QCA device depends foremost on the reliability of the switching process, i.e., the transition of a cell’s state that corresponds to one logic value to a state that corresponds to another and vice versa. It is achieved by means of the adiabatic switching concept, where a cyclic signal, namely adiabatic clock, is used to control the cells’ switching dynamic [7], [9]. The signal comprises four phases. The switch phase serves the cells’ gradual update of the state with respect to their neighbors. The hold phase is intended for the stabilization of the cells’ states when they are to be passed on to the neighbors that are in the switch phase. The release and the relax phase support the cells’ gradual preparation for a new switch.

The correct behavior of tQCA logic gates requires a synchronized data transfer, achievable through a pipelined architecture based on the adiabatic clock [8]. The four phased nature of the clock signal allows any tQCA to be decomposed to smaller stages, or subsystems, controlled by phase shifted signals, each defining its own clocking zone (see Fig. 3). Subsystems that are in the hold phase act as inputs for subsystems that are in the switch phase. A subsystem, after performing its computation locks its state and acts as the input for the following subsystem. As the transaction and processing in the second subsystem is finished it can lock its state while the first prepares for accepting new inputs. With the correct assignment of cells to clocking zones, the direction of data flow can be controlled. Large regions of nearby cells are usually assigned to the same clocking zone in order to eliminate the challenges that

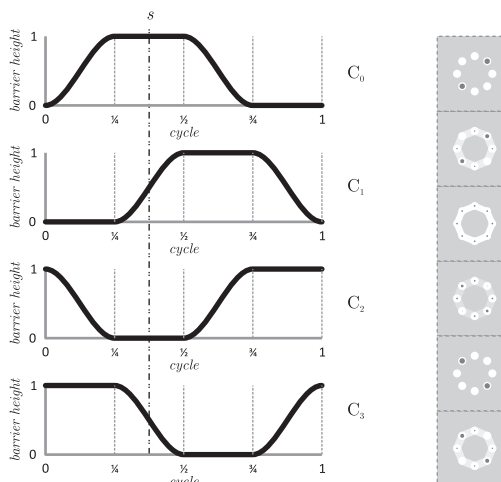


Figure 3. The four phase shifted adiabatic clock signals and an example of the adiabatic pipeline architecture applied to the QCA wire. Let C_0 denote the base signal and C_i , $i = \{0, 1, 2, 3\}$ the base signal phase shifted by i phases.

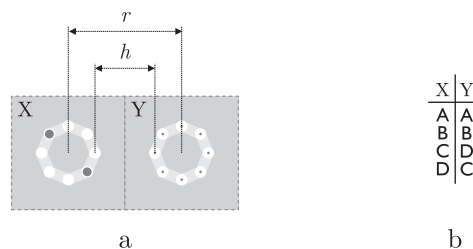


Figure 4. The coplanar layout of tQCA cells (a) and the result of cell to cell interaction (b).

would be caused by attempting to deliver a separate clock signal to every cell.

The latency of a QCA circuit is determined by the number of clocking zones along its critical path. A sequence of four clocking zones causes the delay of one clock cycle. Consequently minimizing the number of clocking zones leads to better designs [19].

III. INTERCONNECTION CROSSING

The basic cell to cell interaction shown in Fig. 4a comprises two coplanar tQCA cells, where cell X acts as the input and cell Y as the observed output. Current simulations, based on the Intercellular Hartree Approximation (ICHA) method that uses a tight-binding Hubbard-type Hamiltonian, show that a suitable coplanar intercellular distance for correct state transfer equals $r = 110$ nm, hence the minimum spacing between quantum-dots of neighboring cells is approximately $h = r - 2R = 58$ nm [8]. The interaction result showed in Fig. 4b reveals that the output cell assumes the same state when the input cell’s state is A (logic value -1) or B (logic value 1). However, when the input cell’s state is C (logic value 0) the state propagates

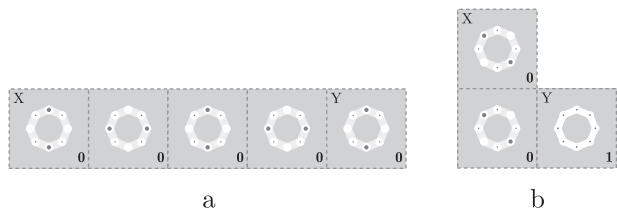


Figure 5. The pipeline architecture for a robust tQCA wire: straight wire (a), corner wire (b).



Figure 6. The noncoplanar layout of tQCA cells (a) and the result of cell to cell interaction (b).

in an alternating fashion. This empowered the construction of the basic tQCA logic primitive called tQCA wire. The alternating propagation of state C effectively means that wires have to be of odd lengths [6].

While the straight wire can be constructed as a single stage pipeline (see Fig. 5a), the correct behavior of the corner wire is ensured by means of a pipeline of two stages, as can be seen on Fig. 5b. The first stage ensures the propagation of the input value to the corner, and the second stage ensures its propagation to the output cell.

One of the unique features of bQCA is coplanar rectangular wire crossover [18]. Unfortunately, in case of tQCA this is not possible as there is no equivalent to the rotated bQCA cell [2]. The only possible solution is the noncoplanar approach (using multiple layers of tQCA cells), at least until an alternative approach is found.

The vertical transmission of a cell's state can be achieved with the rearrangement of cells in a manner that one cell is placed above the other so that the minimum spacing h between quantum-dots remains unchanged (see Fig. 6a). Thus, both layouts, i.e., coplanar and noncoplanar, obey the same spacing rules, only the intercellular position is changed. With the described vertical tQCA cell placement one can construct a vertical tQCA wire that is used for the propagation of data between layers. The analysis of the behavior of the vertical wire (see Fig. 6b) during the transmission of states from input cell X to output cell Y shows that states propagate in alternating fashion, regardless of the input state. Comparing the behavior results in Fig. 4b and Fig. 6b indicates that the cell-cell Coulomb interaction and minimum energy condition differ between co-axial and co-planar arrangements in case of input states A and B, while remain the same in case of states C and D.

The promotion of states from a coplanar wire to a vertical

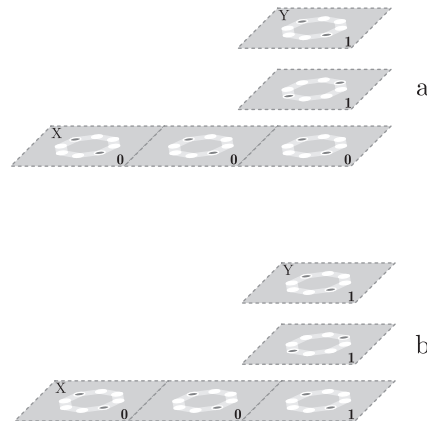


Figure 7. The two possible pipeline solutions of vertical corner wire.

wire, and vice versa, requires the presence of a tQCA that acts as a vertical corner wire, as presented in Fig. 7. Robust behavior can be achieved using the pipeline concept, i.e., splitting the corner wire to two stages, controlled by two phase shifted clock signals C_0 and C_1 . The implementation itself is not so rigid as in the case of its coplanar counterpart (see Fig. 3b) and offers two possible approaches. The one demonstrated in Fig. 7a is directly derived from the coplanar solution, while the one showed in Fig. 7b uses clock signal C_0 for the control of the coplanar wire and signal C_1 for the control of the vertical wire.

The presented tQCAs facilitate the construction of a noncoplanar tQCA wire crossover. The two implementations of the vertical corner wire result in four possible solutions for the crossover, where two of them are shown in Fig. 8 and the other two are their combinations. For example, the crossover approach in Fig. 8a uses the pipeline solution based on corner wire shown in Fig. 7a for input and for output part. In order to avoid interference between the crossing wires two additional layers are needed, i.e., besides the main (bottom) layer. The middle layer is used only as a via layer, while the top one acts as the crossing wire. Hence, the crossing wires are separated by a distance of $2h$. The distance between the vertical wire and the wire that is crossed has to be at least $2r$.

Simulations show that the correct behavior of the crossover requires four pipeline stages controlled by four phase shifted clock signals C_0, C_1, C_2 and C_3 , which determine a delay of one clock cycle. This means that the behavior of the crossover wire is independent of the clock phase applied to the crossed wire. It can be easily seen that the crossover wire can span across multiple wires on the bottom layer. The span depends only on the length of the crossing wire on the top layer.

IV. CONCLUSION

The interconnection crossover represents one of the most challenging design problems in the tQCA domain. This

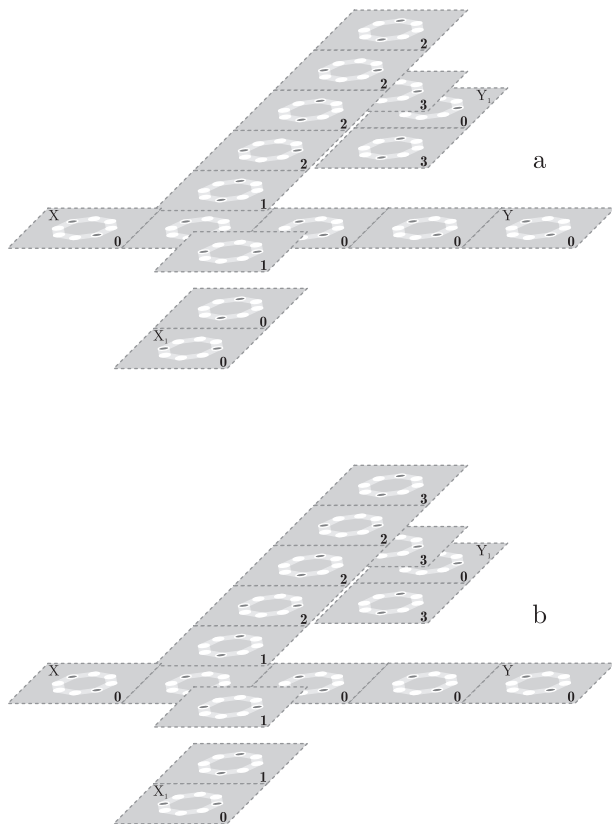


Figure 8. Two multilayer tQCA wire crossovers.

paper gives a solution that exploits a noncoplanar, i.e., multi-layer, arrangement of tQCA cells with adiabatic pipeline control. The crossover constructed in this manner exhibits robustness and flexibility of data propagation. The latter goes on the account of using four pipeline stages, which on the other hand may introduce a synchronization problem, specially in the case of multiple crossovers of the same wire. Therefore, our research is focused on developing a crossover that would need less stages, thus diminishing data transfer delay. One of the most promising is a two-layer approach, which would also substantially simplify the fabrication challenges [20].

ACKNOWLEDGMENT

This work was done at the Computer Structures and Systems Laboratory, Faculty of Computer and Information Science, University of Ljubljana, Slovenia and is part of a PhD thesis that is being prepared by P. Pecar. It was funded in part by the Slovenian Research Agency (ARRS) through the Pervasive Computing research programme (P2-0395).

REFERENCES

[1] C. Lent, P. Tougaw, W. Porod, and G. Bernstein, "Quantum cellular automata," *Nanotechnology*, vol. 4, pp. 49–57, 1993.

[2] C. Lent and P. Tougaw, "Lines of interacting quantum-dot cells: A binary wire," *Journal of Applied Physics*, vol. 74, no. 10, pp. 6227–6233, 1993.

[3] K. Walus and G. Jullien, "Design Tools for an Emerging SoC Technology: Quantum-Dot Cellular Automata," *Proceedings of the IEEE*, vol. 94, no. 6, pp. 1225–1244, Jun. 2006.

[4] I. Lebar Bajec and M. Mraz, "Towards multi-state based computing using quantum-dot cellular automata," in *Unconventional Computing 2005: From Cellular Automata to Wetware*, C. Teucher and A. Adamatzky, Eds. Beckington: Luniver Press, 2005, pp. 105–116.

[5] I. Lebar Bajec, N. Zimic, and M. Mraz, "The ternary quantum-dot cell and ternary logic," *Nanotechnology*, vol. 17, no. 8, pp. 1937–1942, 2006.

[6] —, "Towards the bottom-up concept: extended quantum-dot cellular automata," *Microelectronic Engineering*, vol. 83, no. 4-9, pp. 1826–1829, 2006.

[7] P. Pecar, M. Mraz, N. Zimic, M. Janez, and I. L. Bajec, "Solving the ternary QCA logic gate problem by means of adiabatic switching," *Japanese Journal of Applied Physics*, vol. 47, no. 6, pp. 5000–5006, 2008.

[8] P. Pecar, A. Ramsak, N. Zimic, M. Mraz, and I. Lebar Bajec, "Adiabatic pipelining: A key to ternary computing with quantum dots," *Nanotechnology*, vol. 19, no. 49, p. 495401, 2008.

[9] P. Tougaw and C. Lent, "Dynamic behaviour of quantum cellular automata," *Journal of Applied Physics*, vol. 80, no. 8, pp. 4722–4736, 1996.

[10] C. Lent and P. Tougaw, "A device architecture for computing with quantum dots," *Proceedings of the IEEE*, vol. 85, no. 4, pp. 541–557, 1997.

[11] G. H. Bernstein, I. Amlani, A. O. Orlov, C. S. Lent, and G. L. Snider, "Observation of switching in a quantum-dot cellular automata cell," *Nanotechnology*, vol. 10, no. 2, pp. 166–173, Jun. 1999.

[12] K. Walus, G. Schulhof, G. Jullien, R. Zhang, and W. Wang, "Circuit design based on majority gates for applications with quantum-dot cellular automata," in *Signals, Systems and Computers, 2004. Conference Record of the Thirty-Eighth Asilomar Conference on*, vol. 2, 2004, pp. 1354 – 1357 Vol.2.

[13] E. Dubrova, Y. Jamal, and J. Mathew, "Non-silicon non-binary computing: Why not?" in *1st Workshop on Non-Silicon Computation*, Boston, Massachusetts, 2002, pp. 23–29.

[14] E. L. Post, "Introduction to a general theory of elementary propositions," *American Journal of Mathematics*, vol. 43, no. 3, pp. 163–185, 1921.

[15] M. Janez, I. Lebar Bajec, P. Pecar, A. Jazbec, N. Zimic, and M. Mraz, "Automatic design of optimal logic circuits based on ternary quantum-dot cellular automata," *WSEAS Trans. Cir. and Sys.*, vol. 7, pp. 919–928, 2008.

- [16] P. Pecar, M. Janez, N. Zimic, M. Mraz, and I. Bajec, "The ternary quantum-dot cellular automata memorizing cell," in *VLSI, 2009. ISVLSI '09. IEEE Computer Society Annual Symposium on*, May 2009, pp. 223–228.
- [17] A. Chaudhary, D. Z. Chen, X. S. Hu, M. T. Niemier, R. Ravichandran, and K. Whitton, "Fabricatable Interconnect and Molecular QCA Circuits," *IEEE Transactions on Computer-Aided Design of Integrated Circuits and Systems*, vol. 26, no. 11, pp. 1978–1991, Nov. 2007.
- [18] P. D. Tougaw and C. S. Lent, "Logical devices implemented using quantum cellular automata," *Journal of Applied Physics*, vol. 75, no. 3, pp. 1818–1825, 1994.
- [19] M. T. Niemier and P. M. Kogge, "Problems in designing with QCAs: Layout = timing," *International Journal of Circuit Theory and Applications*, vol. 29, pp. 49–62, 2001.
- [20] A. Gin, P. D. Tougaw, and S. Williams, "An alternative geometry for quantum-dot cellular automata," *Journal of Applied Physics*, vol. 85, no. 12, pp. 8281–8286, Jun. 1999.

Effect of Adhesion Layer on Morphology and Optical Properties of Self-Organized Metal Nanostructures

Victor Ovchinnikov

MICRONOVA Nanofab

School of Electrical Engineering, Aalto University

Espoo, Finland

e-mail: Victor.Ovchinnikov@aalto.fi

Abstract The inexpensive fabrication method of self-organized metal nanostructures with adhesion layer over large area is proposed. The method combines dry etching using a self-organized mask to prepare a template and directional metal deposition on the elevated part of the obtained template. The technique peculiarities were studied during fabrication of metal lace-like nanostructures prepared with Ti layer and without it. The results demonstrate the overall difference in transmittance and reflectance spectra of the samples due to presence of Ti layer. Surface enhanced Raman spectroscopy (SERS) experiments were performed with methylene blue and confirmed decreasing of SERS intensity of the gold nanostructures with adhesion layer. The obtained results can be used in fabrication of self-organized metal nanostructures with controllable adhesion.

Keywords-self-organized; fabrication method; metal nanostructure; random array; plasmonics; SERS substrate

I. INTRODUCTION

Metal nanostructures have greatly broadening applications in many areas of chemical and biological sensing [1], subwavelength imaging[2], metamaterials[3] and etc. The best studied and attractive from the theoretical point of view are periodic arrays of metal nanoparticles, but their mass production is a challenging task, which waits for the decision. Traditional semiconductor technology provides reliable and reproducible process flows, but its acceptance as a general fabrication tool of metal nanostructures has been hindered by two obstacles: (1) limited resolution of optical lithography and (2) lack of dry etching processes for most metals. That is why, the dominant fabrication method of regular metal nanostructures is electron beam lithography (EBL) together with lift-off removing of useless metal. However, by this process is highly difficult to obtain features smaller than 50 nm. Additionally, the extensive processing time needed in EBL for fabrication of arrays of nanostructures over large areas makes it expensive and time-consuming.

As alternative to serial EBL, several non-lithography or self-organizing methods exist to produce nanostructures in parallel way. These techniques create structures with a random nature, i.e. arrays of metal nanostructures with randomly distributed size and space of elements. Active areas beyond $1 \times 1 \text{ cm}^2$ and low price are inherent to the techniques, but functional properties of nanostructures

deteriorate, narrowing application area of random arrays. In spite of this, the random nanostructures are used as a catalyst in carbon nanotube growth [4], as a light trapping layer in thin film solar cells [5], as magnetic nanodot arrays [6], as surface enhanced Raman scattering (SERS) substrates [7] and sensors [8]. As examples of non-lithography techniques can be mentioned nanosphere lithography [9], using of porous alumina template [10], oblique angle deposition [11] and etc. They have own application areas, but the most attractive method is generation of metal nanostructures by self-assembling on the surface with poor adhesion, e.g., Au-Ag nanoislands on glass [12]. The method possesses nanometer range resolution, cheapness and compatibility with semiconductor technology.

Unfortunately, broad application of this self-organizing technique is restrained by poor adhesion of produced metal structures to a dielectric substrate and limited set of structure configurations (mainly round-shaped islands and holes). By the nature of phenomenon, self-organization occurs in a thin layer of noble metal on dielectric substrate at non-equilibrium thermodynamic conditions without firm contact between metal and substrate. The fabricated random arrays can be easily damaged during rinsing in de-ionized water and are not suitable for incorporation in more complicated devices. It is therefore desirable to improve the adhesion properties of self-organized structures, e.g., by introducing of intermediate adhesion layer.

Lift-off based methods, including EBL, inherently include an adhesion layer to preserve functional metal elements during mask removing. Therefore, nanostructures without adhesion layer cannot be produced by these methods and direct estimation of influence of intermediate layer on the functional properties is impossible. As a consequence, there are only experimental results for different (non-zero) thicknesses of adhesion layer in nanostructures or comparison of flat (non-patterned) metal films with and without adhesion layer [13, 14].

In this paper, a fabrication method of self-organized metal nanostructures with adhesion layer over large area is considered. The method was used to create lace-like Au and Ag nanostructures with and without Ti layer on glass and silicon substrates. This gave an opportunity to study the influence of adhesion layer on morphology and optical properties of fabricated nanostructures by direct comparison.

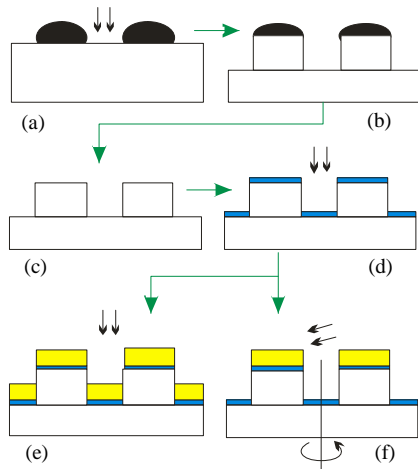


Figure 1. Fabrication process of metal nanostructures with intermediate layer.

Despite of vast transformation of optical response due to presence of Ti layer, it was demonstrated that gold lace-like nanostructures with gap width below 10 nm can be used as effective SERS substrates.

In the subsequent sections, the description of the fabrication method is presented, followed by detailed sample preparation and measurement procedures. After presenting of SEM images of the obtained nanostructures, the reflectance and SERS spectra are discussed.

II. FABRICATION METHOD

The idea of the method consists in fabrication of a nanostructure template from a substrate and directional deposition of metal layers on the template. For template preparation any patterning method, providing vertical sidewalls can be used: lithography and etching, self-organizing structures and etching, direct writing by laser or focused ion beam [15, 16]. In this work, self-organized gold nanostructures are used as a mask for anisotropic dry etching of the substrate (Fig. 1a,b). To create the mask a thin gold layer is evaporated on the substrate at low deposition rate. The film has lace-like structure, if the gold thickness does not exceed 15 nm and the adhesion between metal and the substrate is poor. Other metals or additional annealing after deposition can be used to modify the mask morphology. For example, silver provides round-shaped nanoislands with size and separation controlled by annealing [17]. The poor adhesion of gold to a substrate limits the etching methods for patterning of the nanostructures, e.g., wet etching must be eliminated. On the other hand, dry etching still can be used, because surface tension forces and interlayer diffusion of liquid have no place. Additionally, dry etching, e.g., reactive ion etching (RIE), provides vertical (Fig. 1b) sidewalls of the nanostructures.

In the next step the residues of the mask metal are removed by selective wet etching to obtain a nanotemplate made of the substrate material (Fig. 1c). The template elements replicate the shape and size of the mask (e.g., lace-

like structure) and, in general, can have any lateral geometry (e.g., disks for silver self-organizing mask). The template is then covered by a thin adhesion layer of easily oxidized metal (e.g., Ti or Cr). At atmospheric ambient the adhesion layer, which is not protected by upper metal is readily oxidized and does not affect on functional properties of nanostructures. It is important to deposit the adhesion layer only on horizontal surfaces of the template and leave the sidewalls uncovered (Fig. 1d) to avoid firm contact of the second metal with vertical surfaces. This requirement is fulfilled by using a physical vapour deposition (e.g., evaporation) at normal incidence. Due to poor adhesion of the metal to sidewalls, it can be easily removed by rinsing in ultrasound bath.

The final step is coating of the template with a functional metal layer, for example gold or silver. It is done immediately after deposition of the adhesion layer to prevent possible oxidation of the latter. This time metal coating of the template can be made in two ways. In the first one, the metal is evaporated in a direction normal to the wafer surface, which simultaneously deposits metal on the elevated nanostructure planes and the backplane (Fig. 1e). In the second way, the metal is deposited at the angle (Fig. 1f) on the rotating or unmovable template. The rotation provides uniform covering of structure tops, while static deposition leads to 3D nanostructures, in which sidewalls and tops are covered simultaneously. The deposition angle is chosen to be large enough to minimize metal coating of backplane. In this case, the height h of the sidewall metallization (measured from structure top) can be roughly estimated as [18]

$$h_m = \frac{l}{\tan \alpha}, \quad (1)$$

where l is the average space between structures. In practice, deviations from (1) are happened, especially for small l , when sidewalls are not become covered by metal at all.

III. EXPERIMENTAL

The samples were fabricated on precleaned squares of borosilicate glass and oxidized Si (100) with size $22 \times 22 \times 0.5$ mm³. The cleaning procedure begins with sonicating in acetone and 2-propanol. After that the samples were RCA-1 cleaned for 10 minutes and processed in oxygen plasma during 1 minute. The pretreatment is needed to equalize the surface conditions through the whole substrate. The Si pieces with a 60 nm thick layer of SiO₂ were used to optimize the whole process, because it makes possible to observe the fabricated nanostructures with SEM. At the same time all process steps lead to identical results on glass and on oxide.

The metal films were deposited in e-beam evaporation system IM-9912 (Instrumentti Mattila Oy) with adjustable substrate inclination and rotation speed at base pressure of 4×10^{-7} Torr and at room temperature of the substrate. The deposition rates for each film were measured using quartz crystal microbalance. The RIE of template was done in a 13.56 MHz driven parallel electrode reactor Plasmalab 80

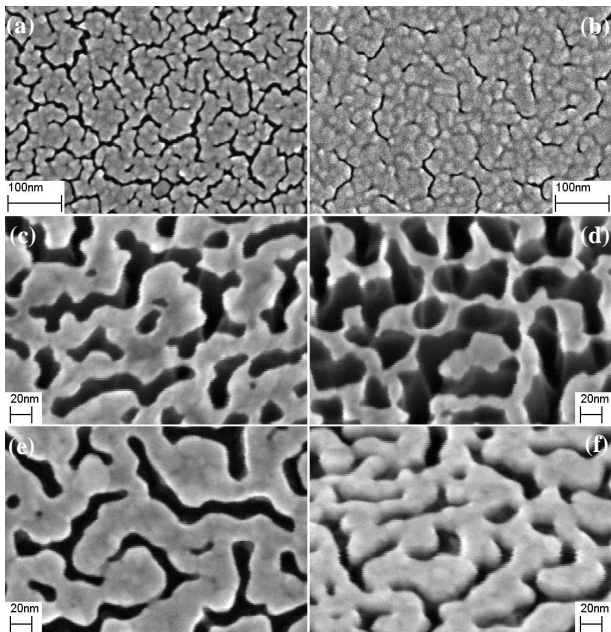


Figure 2. SEM images of lace-like nanostructures after main process steps: (a,b) 10 and 15 nm thick gold films; (c,d) RIE for 20 and 25 minutes, respectively; plain (e) and tilted (f) views of 16 nm thick gold nanostructures.

Plus (Oxford Instruments Plasma Technology). An anisotropic etching process based on fluorine chemistry (gas mixture $\text{CF}_4:\text{CHF}_3=1:3$) was used for glass and SiO_2 etching. The etching experiments were performed at a total gas flow of 80 sccm, pressure 30 mTorr and rf power 40 W. The remaining gold was removed in aqua regia (1:3 volume mixture of 69% HNO_3 and 37% HCl , respectively) during 20 s at room temperature, leaving a lace-like structures from SiO_2 or glass.

Plane-view and tilted at 30° SEM images of the samples were observed with Zeiss Supra 40 field emission scanning electron microscope. Transmittance and reflectance measurements at normal incidence were carried out using PerkinElmer Lambda 950 UV-VIS spectrometer in the spectral range from 300 to 850 nm. All reflectance spectra were collected with integrating sphere as a detector. Raman scattering was studied in WITec Alpha 300 Raman microscope equipped with a Nd:YAG (532 nm) laser as an excitation source. Methylene blue (MB) at the concentration of 3×10^{-4} M was used as a test molecule with water as a solvent. MB solution was dropped on SERS samples using a pipette and then dried in air to obtain a uniform molecule deposition.

IV. RESULTS

To check the method lace-like nanostructures from gold and silver with Ti adhesion layer were fabricated. Both metals have poor adhesion to glass, but are very attractive for plasmonic applications. Fig. 2 illustrates most important steps in the nanofabrication. As a self-organized mask was used a 10 nm thick gold layer deposited at 0.5 \AA/s . In

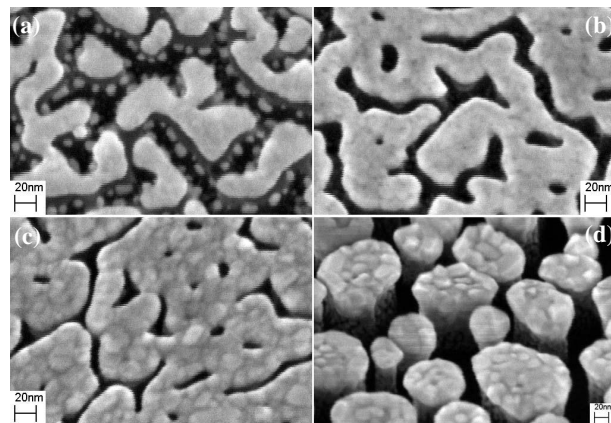


Figure 3. SEM images of nanostructures: (a,b) 8 nm thick gold nanostructures without Ti and with Ti, respectively; (c,d) 8 nm thick silver and 16 nm thick gold nanostructures with Ti deposited at 70° with rotation.

contrast to well known self-organizing masks from Au and Ag [19], annealing is not required; the film is used as-deposited to preserve feature sizes as small as possible. Such a procedure results in lace-like structure, consisting of channels (depressions) and protrusions (projections) (Fig. 2a). Average width of the first ones is about 7 nm, the second ones ≈ 30 nm. Protrusion and channel sizes can be tuned by gold thickness, substrate temperature and deposition rate. As an example, in Fig. 2b is shown the 15 nm thick gold film deposited at the same conditions, which has smaller width and density of the channels. Unfortunately, mask thickness is only a little larger than the thickness of the deposited metal and limits the depth of RIE (Fig. 2c,d). Till the certain moment during etching the mask pattern is unchanged (Fig. 2c) and channel widths in SiO_2 and gold are equal. Further etching increases channel width and destroys flatness of protrusion tops (Fig. 2d), what is connected with gold mask erosion during ion bombardment. Additionally, it leads to deviation of sidewall profile from vertical. The maximum etching depth of 75 nm reached after 25 minutes of RIE (Fig. 2d), resulted in increasing of channel width to 25 nm. Deposition of 1 nm thick Ti and 16 nm thick gold layers on the structure shown in Fig. 2d was done in static mode (Fig. 1e,f) and led to shrinking of the channel width back to 7 nm.

To further clarify the mechanism of nanostructure metallization, the gold film was also deposited on the template without Ti adhesion layer (Fig. 3a). Metal nanostructures do not exactly follow the template pattern, like in case of Ti layer (Fig. 3b); instead of this, they are broken in shorter segments and surrounded by small nanoclusters. It looks that on the tops of protrusions there are favorable thermodynamic conditions for gold migration to the centre of isolated areas. This facilitates formation of large islands in the middle of protrusions due to non-wetting property of Au on SiO_2 surface. At the same time, protrusion edge is a favorable place for cluster nucleation, but due to limited amount of gold, these clusters are small in size. In

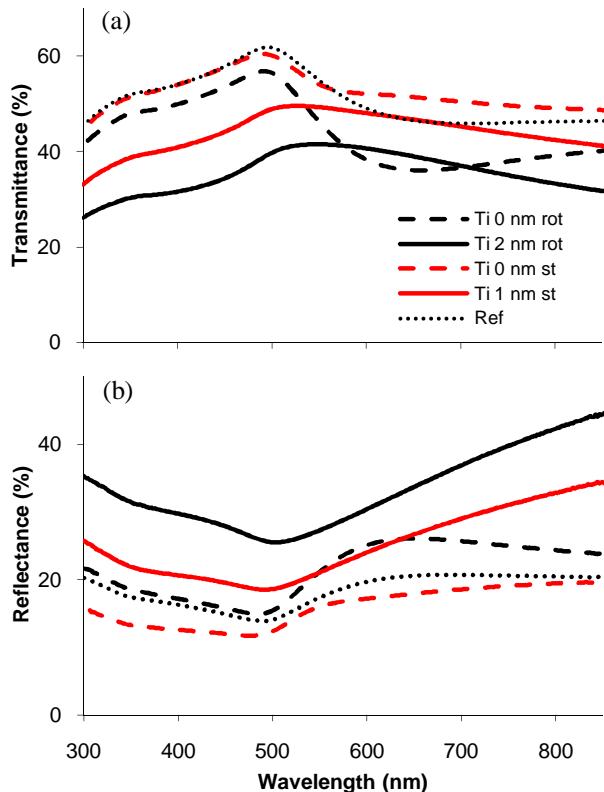


Figure 4. Transmittance (a) and reflectance (b) spectra of 8 nm thick gold nanostructures with Ti and without Ti on glass deposited at normal angle (st) or at 70° with rotation (rot). Ref ó 8 nm gold on glass without Ti.

case of Ti/Au layer (Fig. 3b), surface diffusion of gold atoms is limited and the film grows uniformly above protrusion tops. Growth rate of the metal film is higher on the protrusion edge, what leads to formation of rim around nanostructure (Fig. 2f). The rim shadows sidewalls from metal deposition, decreases channel width and diminishes amount of metal on the backplane. The lateral growth rate of the rim can be controlled by tilting and rotating the substrate during deposition. Fig. 3c, d display lace-like Ag structures similar ones shown Fig. 3b and SiO₂ pillars covered by gold, respectively. In both cases deposition was done on rotating substrate at the angle 70°. As a result of rotation, the channel width is smaller in comparison with static deposition (Fig. 3b) and diameter of metal disks on the pillar tops is 40 nm larger than pillar diameter.

Whatever the deposition result, samples appear extremely attractive for plasmonic and especially SERS applications. This supposition is confirmed by transmittance and reflectance of gold nanostructures on glass substrate shown in Fig. 4. To make the template, glass was etched during 16 minutes, what was resulted in channel depth about 65 nm. The reference sample is 8 nm thick gold film deposited on plain surface of glass substrate. Optical properties for wavelength shorter 500 nm reflect interband transitions of *d*-electrons in gold and are not connected with surface plasmon resonance (SPR). All samples consist of strongly interacting structures with size deviation, what leads to broadening and

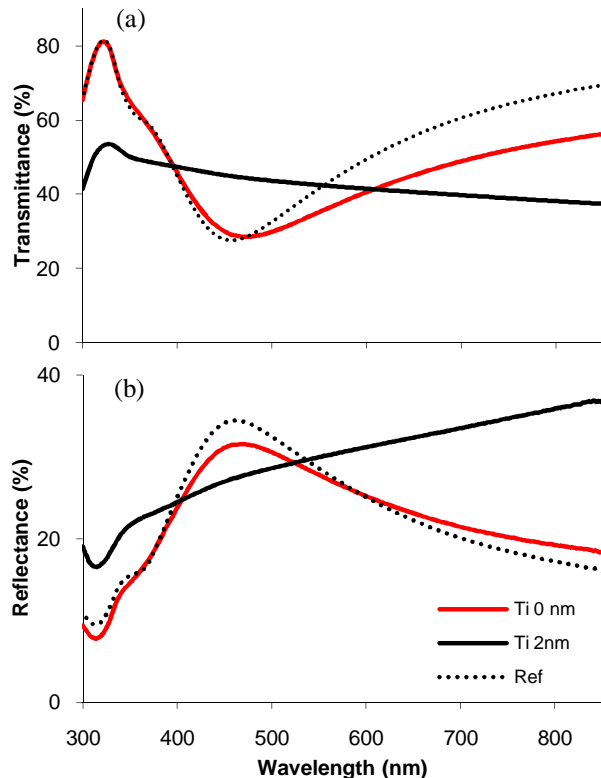


Figure 5. Transmittance (a) and reflectance (b) spectra of 8 nm thick silver nanostructures with Ti and without Ti on glass deposited at 70° with rotation. Ref ó 8 nm silver on glass without Ti.

shifting of resonance peaks inherent to gold nanoparticles [20].

Samples without Ti layer demonstrate SPR near 650 nm, which is stronger for sample deposited at angle and weaker for sample deposited at normal direction. But spectra of structures with Ti layer are totally different. Low transmittance in the blue half of spectra is caused by high reflectance and justifies narrowing of the channels (increasing metal covered area). Redshift and broadening of maximum transmittance band near 500 nm is attributed to influence of Ti layer absorbance, which monotonically decreases for visible range of wavelength. Modification of red half of spectra is connected with flattening of metal nanostructures (Fig. 3) and increased interaction between oscillators due to shrinking of channels. The result is strong and non-uniform splitting of SPR, observed as featureless spectrum.

Transmittance and reflectance of silver nanostructures, prepared on the same template as gold ones are shown in Fig. 5. As well as in case of gold nanostructures, reference sample and lace-like nanostructures without Ti demonstrate similar spectra. There are longitudinal SPR at 460 nm and transverse SPR at 360 nm. However, after introducing of Ti layer only weak sings on these SPRs can be visible on practically flat spectra due to nanostructure shape variation and dampening caused by Ti layer. It cost to note, that for wavelength longer than 600 nm the appearance of Ti/Au and

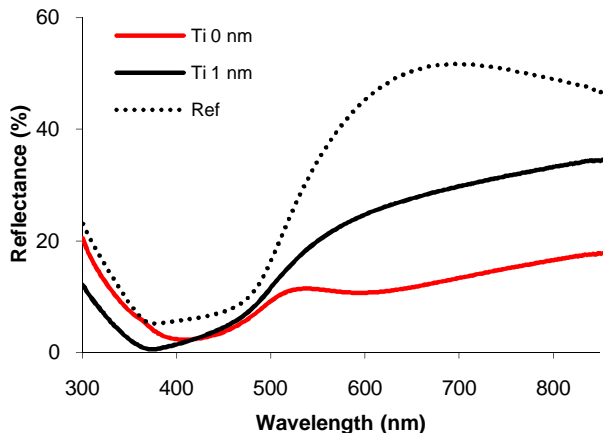


Figure 6. Reflectance spectra of 8 nm thick gold nanostructures with and without Ti on Si/SiO₂ deposited at normal angle. Ref is 11 nm gold on the same substrate.

Ti/Ag spectra is practically the same (Fig. 4, 5), in contrast to the behavior of Au and Ag reference samples. It can be considered as evidence of template (not metal) effect on optical properties of nanostructures.

Reflectance of gold nanostructures, prepared in the same process as glass samples, but on silicon substrate, is shown in Fig.6. Spectra demonstrate interference picture in the system Si/SiO₂ modified by absorption in nanostructure layer. Due to this, SPRs manifest themselves as minimums of reflectance and can be visible in pure Au sample (600 nm) and extrapolated in reference sample (beyond of 900 nm). SPRs are redshifted in comparison with glass samples (Fig. 4b), due to high effective dielectric constant of environment, modified by Si substrate. At the same time redshift in pure Au sample (no Ti layer) is much less than in reference sample, because the etched channels partly compensate effect of Si substrate on permittivity of environment. Low reflectance in the left part of spectra (shorter 500 nm) is attributed to absorption in gold together with destructive

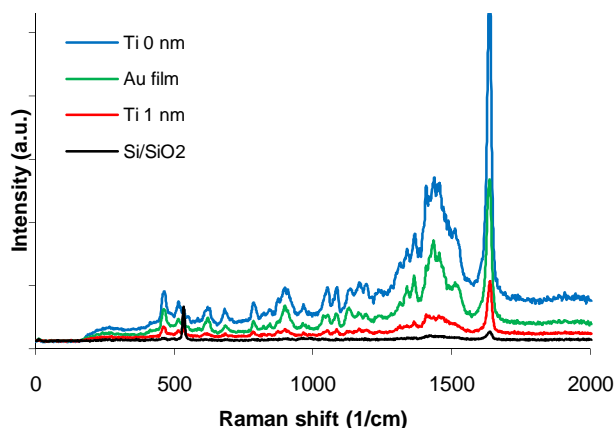


Figure 7. SERS spectra of methylene blue for the gold nanostructures described in Fig. 6.

interference in SiO₂ layer. The special point at 375 nm is connected with peak of reflectance in crystalline Si. As in case of glass substrate, sample with adhesion layer is featureless.

The raw Raman spectra of MB on Si/SiO₂ samples, represented by reflectance spectra in Fig. 6 are shown in Fig. 7 (blue and red lines). The peak at 530 cm⁻¹ corresponds to the Raman scattering of the crystalline Si substrate. Black and green spectra present the Raman scattering of the bare Si/SiO₂ and 11 nm thick gold layer on Si/SiO₂. It is not surprise, that the maximum enhancement effect on Raman scattering demonstrates sample without Ti layer. Indeed, this sample possesses SPR (600 nm) close to SERS excitation wavelength (532 nm). Relatively strong SERS activity is also attributed to plain substrate with Au film. But SERS intensity of the sample fabricated with Ti layer exceeds only the intensity of bare oxide layer. This difference clearly indicates that plasmonic properties drastically deteriorate by adhesion layer. However, intensity of observed SERS signal for the Ti/Au nanostructures is still enough to distinguish the characteristic peaks of MB at around 1638 and 466 cm⁻¹ [21]. This fact and high mechanical stability of the Ti/Au nanostructures make them attractive for embedding in complex devices.

V. CONCLUSIONS

In summary, it has been proposed and demonstrated a new nanofabrication method of self-organized nanostructures both with adhesion layer and without it. With the help of proposed method it has been experimentally studied the influence of Ti adhesion layer on morphology and optical properties of lace-like nanostructures from gold and silver by direct comparison of the samples. The pure gold and silver nanostructures repeat template shape only roughly, concentrating in the middle part of the protrusion tops. The presence of a very thin adhesion layer (e.g., 1 nm thick Ti) leads to uniform covering of top planes of the template and drastically changes nanostructure morphology. As a consequence, SPR features in absorbance and reflectance spectra of the samples with Ti layer are transformed and weakened. Despite of this Ti/Au lace-like nanostructures demonstrate relatively high SERS activity measured with MB as the reference analyte. The obtained results suggest that developed nanofabrication method is promising in preparation of noble metal nanostructures with adhesive layer to withstand further process treatments. The method is also valuable in fabrication of self-organized nanostructures from any evaporatable metal, e.g., Fe or Al. For future work, it is expected to optimize the template structure and gold thickness for obtaining of maximum SERS enhancement.

REFERENCES

- [1] J. N. Anker et al., "Biosensing with plasmonic nanosensors", *Nature Materials*, vol. 7, 2008, pp. 442-453.
- [2] X. Zhang and Z. Liu, "Superlenses to overcome the diffraction limit", *Nature Materials*, vol. 7, 2008, pp. 435-441.

- [3] E. Cortes, L. Mochán, B. S. Mendoza, G. P. Ortiz, "Optical properties of nanostructured metamaterials", *Phys. Status Solidi B*, vol. 247, 2010, pp. 2102 ó 2107.
- [4] Y. F. Guan, A. V. Melechko, A. J. Pedraza, M. L. Simpson and P. D. Rack, "Non-lithographic organization of nickel catalyst for carbon nanofiber synthesis on laser-induced periodic surface structures", *Nanotechnology*, vol. 18, 2007, pp. 335306 ó 335312.
- [5] X. Sheng et al., "Design and Non-Lithographic Fabrication of Light Trapping Structures for Thin Film Silicon Solar Cells", *Adv. Mater.* vol. 23, 2011, pp. 843 ó 847.
- [6] R. M. Tofizur, N. N. Shams, C.-H. Lai, "Nonlithographic fabrication of 25 nm magnetic nanodot arrays with perpendicular anisotropy over a large area", *J of App. Phys.* vol. 105, 2009, pp. 07C112 ó 07C112-3.
- [7] M. Fan, G. F.S. Andrade and A. G. Brolo, "A Review on the fabrication of substrates for surface enhanced Raman spectroscopy and their applications in analytical chemistry", *Analytica Chimica Acta*, (in press).
- [8] E. Galopin et al., "Short- and Long-Range Sensing Using Plasmonic Nanostructures: Experimental and Theoretical Studies", *J. Phys. Chem. C*, vol. 113, 2009, pp. 15921 ó 15927.
- [9] X. Zhang, L. Zhang, M. Gao, W. Zhou, S. Xie, "High-Resolution Nanosphere Lithography (NSL) to Fabricate Highly-Ordered ZnO Nanorod Arrays", *J. Nanosci. Nanotechnol.*, , *J. Nanosci. Nanotechnol.*, vol. 10, 2010, pp. 7432 ó 7435.
- [10] Y. Piao, H. Kim, "Fabrication of nanostructured materials using porous alumina template and their applications for sensing and electrocatalysis", *J. Nanosci. Nanotechnol.*, vol. 9, 2009, pp. 2215 ó 2233.
- [11] S. Jayawardhana, G. Kostovski, A. P. Mazzolini, and P. R. Stoddart, "Optical fiber sensor based on oblique angle deposition", *Appl. Opt.*, Vol. 50, 2011, pp. 155 ó 162.
- [12] J. Sancho-Parramon et al., "Optical and structural properties of Au-Ag islands films for plasmonic applications", *Appl. Phys. A*, vol. 103, 6 January 2011, Online First, doi: 10.1007/s00339-010-6231-x.
- [13] B. Lahiri, R. Dylewicz, R. M. De La Rue, and N. P. Johnson, "Impact of titanium adhesion layers on the response of arrays of metallic split-ring resonators (SRRs)", *Optics Express*, vol. 18, pp. 11202 ó 11208.
- [14] K.W. Vogt, P.A. Kohl, W.B. Carter, R.A. Bell and L.A. Bottomley, "Characterization of thin titanium oxide adhesion layers on gold: resistivity, morphology, and composition", *Surf. Sci.*, 1993, vol. 301, 1994, pp. 203 ó 213.
- [15] K.C. Vishnubhatla et al., "Femtosecond laser direct writing of gratings and waveguides in high quantum efficiency erbium-doped Baccarat glass", *J. Phys. D*, vol. 42, 2009, p. 205106 ó 201112.
- [16] R.M. Langford, "Focused ion beam nanofabrication: a comparison with conventional processing techniques", *J. Nanosci. Nanotechnol.*, vol. 6, 2006, pp. 661 ó 668.
- [17] C. Eminian, F.-J. Haug, O. Cubero, X. Niquille, C. Ballif, "Photocurrent enhancement in thin film amorphous silicon solar cells with silver nanoparticles", *Progress in Photovoltaics: Research and Applications*, vol. 19, 2011, pp. 260 ó 265.
- [18] V. Ovchinnikov and A. Shevchenko, "Large-Area Arrays of Pillar-Based Metal Nanostructures", *Proc. Third International Conference on Quantum, Nano and Micro Technologies (ICQNM 2009)*, The IEEE Computer Society, Feb. 2009, pp. 125-129, doi bookmark: <http://doi.ieeecomputersociety.org/10.1109/ICQNM.2009.31>.
- [19] G. Gupta et al., "Cross-sectional Transmission Electron Microscopy and Optical Characterization of Gold Nanoislands", *Jpn. J. Appl. Phys.*, vol. 48, 2009, pp. 080207 ó 080208.
- [20] J. Fu and Y. Zhao, "Au nanoparticle based localized surface plasmon resonance substrates fabricated by dynamic shadowing growth", *Nanotechnology*, vol. 21, 2010, pp. 175303 ó 175311.
- [21] R. R. Naujok, R. V. Duevel, R. M. Corn, "Fluorescence and Fourier Transform surface-enhanced Raman scattering measurements of methylene blue adsorbed onto a sulfur-modified gold electrode", *Langmuir*, vol. 9, 1993, pp. 1771 ó 1774.

A gradient-based approach to feedback control of quantum systems

Gerasimos G. Rigatos
 Unit of Industrial Automation
 Industrial Systems Institute
 26504, Rion Patras, Greece
 Email: grigat@isi.gr

Abstract—The paper proposes a gradient-based feedback control approach to the stabilization of quantum systems. The spin model is used to define the eigenstates of the quantum system. Using Lindblad's differential equation an estimate of the state of the quantum system is obtained. Moreover, by applying Lyapunov's stability theory and LaSalle's invariance principle a gradient control law is derived which assures that the quantum system's state will track the desirable state within acceptable accuracy levels. The performance of the control loop is studied through simulation experiments for the case of a two-qubit quantum system.

Keywords—gradient-based feedback control, quantum systems, Schrödinger's equation, Lindblad's equation, Lyapunov stability, LaSalle's invariance principle.

I. INTRODUCTION

The main approaches to the control of quantum systems are: (i) open-loop control and (ii) measurement-based feedback control [1]. In open-loop control, the control signal is obtained using prior knowledge about the quantum system dynamics and assuming a model that describes its evolution in time. Some open-loop control schemes for quantum systems have been studied in [2-3]. Previous work on quantum open-loop control includes flatness-based control on a single qubit gate [4]. On the other hand measurement-based quantum feedback control provides more robustness to noise and model uncertainty [5]. In measurement-based quantum feedback control, the overall system dynamics are described by the estimation equation called stochastic master equation or Belavkin's equation [6]. An equivalent approach can be obtained using Lindblad's differential equation [1]. Several researchers have presented results on measurement-based feedback control of quantum systems using the stochastic master equation or the Lindblad differential equation, while theoretical analysis of the stability for the associated control loop has been also attempted in several cases [7-8].

In this paper, a gradient-based approach to the control of quantum systems will be examined. Previous results on control laws which are derived through the calculation of the gradient of an energy function of the quantum system can be found in [9-12]. Convergence properties of gradient algorithms have been associated to Lyapunov stability theory in [13]. The paper considers a quantum system confined in a cavity that is weakly coupled to a probe laser. The spin

model is used to define the eigenstates of the quantum system. The dynamics of the quantum model are described by Lindblad's differential equation and thus an estimate of the system's state can be obtained. Using Lyapunov's stability theory a gradient-based control law is derived. Furthermore, by applying LaSalle's invariance principle it can be assured that under the proposed gradient-based control the quantum system's state will track the desirable state within acceptable accuracy levels. The performance of the control loop is studied through simulation experiments for the case of a two-qubit quantum system.

The structure of the paper is as follows: In Section II the spin eigenstates are used to define a two-level quantum system. In Section III the Lindblad and Belavkin description of the quantum system dynamics are introduced as an analogous to Schrödinger's equation. In Section IV the feedback control approach to quantum system stabilization is explained. A gradient-based feedback control law is derived using Lyapunov stability analysis and LaSalle's invariance principle, both for the case that Schrödinger's equation and Lindblad's equation are used to describe the evolution of the quantum system in time. In Section V simulation tests are given on the performance of the proposed measurement-based feedback control scheme for the case of a two-qubit (four level) quantum system. Finally, in Section VI concluding remarks are stated.

II. THE SPIN AS A TWO-LEVEL QUANTUM SYSTEM

A. Description of a particle in spin coordinates

The basic equation of quantum mechanics is *Schrödinger's equation*, i.e.

$$i \frac{\partial \psi}{\partial t} = H \psi(x, t) \quad (1)$$

where $|\psi(x, t)|^2$ is the probability density function of finding the particle at position x at time instant t , and H is the system's Hamiltonian, i.e. the sum of its kinetic and potential energy, which is given by $H = p^2/2m + V$, with p being the momentum of the particle, m the mass and V an external potential. The solution of Eq. (1) is given by $\psi(x, t) = e^{-iHt} \psi(x, 0)$ [14].

However, cartesian coordinates are not sufficient to describe the particle's behavior in a magnetic field and thus the

spin variable taking values in SU(2) has been introduced. In that case the solution ψ of Schrödinger's equation can be represented in the basis $|r, \epsilon\rangle$ where r is the position vector and ϵ is the spin's value which belongs in $\{-\frac{1}{2}, \frac{1}{2}\}$ (fermion). Thus vector ψ which appears in Schrödinger's equation can be decomposed in the vector space $|r, \epsilon\rangle$ according to $|\psi\rangle = \sum_{\epsilon} \int d^3r |r, \epsilon\rangle \langle r, \epsilon | \psi \rangle$. The projection of $|\psi\rangle$ in the coordinates system r, ϵ is denoted as $\langle r, \epsilon | \psi \rangle = \psi_{\epsilon}(r)$. Equivalently one has $\psi_{+}(r) = \langle r, + | \psi \rangle$ and $\psi_{-}(r) = \langle r, - | \psi \rangle$. Thus one can write $\psi(r) = [\psi_{+}(r), \psi_{-}(r)]^T$.

B. Measurement operators in the spin state-space

It has been proven that the eigenvalues of the particle's magnetic moment are $\pm\frac{1}{2}$ or $\pm\hbar\frac{1}{2}$. The corresponding eigenvectors are denoted as $|+\rangle$ and $|-\rangle$. Then the relation between eigenvectors and eigenvalues is given by $\sigma_z|+\rangle = +(\hbar/2)|+\rangle$, $\sigma_z|-\rangle = -(\hbar/2)|-\rangle$, which shows the two possible eigenvalues of the magnetic moment [14]. In general the particle's state, with reference to the spin eigenvectors, is described by

$$|\psi\rangle = \alpha|+\rangle + \beta|-\rangle \quad (2)$$

with $|\alpha|^2 + |\beta|^2 = 1$ while matrix σ_z has the eigenvectors $|+\rangle = [1, 0]$ and $|-\rangle = [0, 1]$ and is given by

$$\sigma_z = \frac{\hbar}{2} \begin{pmatrix} 1 & 0 \\ 0 & -1 \end{pmatrix} \quad (3)$$

Similarly, if one assumes components of magnetic moment along axes x and z , one obtains the other two measurement (Pauli) operators

$$\sigma_x = \frac{\hbar}{2} \begin{pmatrix} 0 & 1 \\ 1 & 0 \end{pmatrix}, \quad \sigma_y = \frac{\hbar}{2} \begin{pmatrix} 0 & -i \\ i & 0 \end{pmatrix} \quad (4)$$

C. The spin eigenstates define a two-level quantum system

The spin eigenstates correspond to two different energy levels. A neutral particle is considered in a magnetic field of intensity B_z . The particle's magnetic moment M and the associated kinetic moment Γ are collinear and are related to each-other through the relation $M = \gamma\Gamma$. The potential energy of the particle is $W = -M_z B_z = -\gamma B_z \Gamma_z$. Variable $\omega_0 = -\gamma B_z$ is introduced, while parameter Γ_z is substituted by the spin's measurement operator S_z .

Thus the Hamiltonian H which describes the evolution of the spin of the particle due to field B_z becomes $H_0 = \omega_0 S_z$, and the following relations between eigenvectors and eigenvalues are introduced:

$$H|+\rangle = +\frac{\hbar\omega_0}{2}|+\rangle, \quad H|-\rangle = -\frac{\hbar\omega_0}{2}|-\rangle \quad (5)$$

Therefore, one can distinguish 2 different energy levels (states of the quantum system) $E_+ = +\frac{\hbar\omega_0}{2}$, $E_- = -\frac{\hbar\omega_0}{2}$. By applying an external magnetic field the probability of

finding the particle's magnetic moment at one of the two eigenstates (spin up or down) can be changed. This can be observed for instance in the Nuclear Magnetic Resonance (NMR) model and is the objective of quantum control [14].

III. THE LINDBLAD AND BELAVKIN DESCRIPTION OF QUANTUM SYSTEMS

A. The Lindblad description of quantum systems

It will be shown that the Lindblad and the Belavkin equation can be used in place of Schrödinger's equation to describe the dynamics of a quantum system. These equation use as state variable the probability density matrix $\rho = |\psi\rangle\langle\psi|$, associated to the probability of locating the particle at a certain eigenstate. The Lindblad and Belavkin equations are actually the quantum analogous of the Kushner-Stratonovich stochastic differential equation which denotes that the change of the probability of the state vector x to take a particular value depends on the difference (innovation) between the measurement $y(x)$ and the mean value of the estimation of the measurement $E[y(x)]$. It is also known that the Kushner-Stratonovich SDE can be written in the form of a Langevin SDE [11]

$$dx = \alpha(x)dt + b(x)dv \quad (6)$$

which finally means that the Lindblad and Belavkin description of a quantum system are a generalization of Langevin's SDE for quantum systems [1]. For a quantum system with state vector x and eigenvalues $\lambda(x) \in \mathcal{R}$, the Lindblad equation is written as [1], [15]

$$\hbar\dot{\rho} = -i[\hat{H}, \rho] + D[\hat{c}]\rho \quad (7)$$

where ρ is the associated probability density matrix for state x , i.e. it defines the probability to locate the particle at a certain eigenstate of the quantum system and the probabilities of transition to other eigenstates. The variable \hat{H} is the system's Hamiltonian, operator $[A, B]$ is a Lie bracket defined as $[A, B] = AB - BA$, the vector $\hat{c} = (\hat{c}_1, \dots, \hat{c}_L)^T$ is also a vector of operators, variable D is defined as $D[\hat{c}] = \sum_{l=1}^L D[\hat{c}_l]$, and finally \hbar is Planck's constant.

B. The Belavkin description of quantum systems

The Lindblad equation (also known as stochastic master equation), given in Eq. (7), is actually a differential equation which can be also written in the form of a stochastic differential equation that is known as *Belavkin equation*. The most general form of the Belavkin equation is:

$$\hbar d\rho_c = dt D[\hat{c}]\rho_c + H[-i\hat{H}dt + dz^+(t)\hat{c}]\rho_c \quad (8)$$

Variable H is an operator which is defined as follows

$$H[\hat{r}]\rho = \hat{r}\rho + \rho\hat{r}^+ - Tr[\hat{r}\rho + \rho\hat{r}^+]\rho \quad (9)$$

Variable \hat{H} stands for the Hamiltonian of the quantum system. Variable \hat{c} is an arbitrary operator obeying $\hat{c}^+\hat{c} = \hat{R}$, where \hat{R} is an hermitian operator. The infinite dimensional complex variables vector dz is defined as $dz = (dz_1, \dots, dz_L)^T$, and in analogy to the innovation dv of the Langevin equation (see Eq. (6)), variable dz expresses innovation for the quantum case. Variable dz^+ denotes the conjugate-transpose $(dz^*)^T$. The statistical characteristics of dz are $dzdz^+ = \hbar H_c dt$, $dzdz^T = \hbar Y dt$. In the above equations matrix Y is a symmetric complex-valued matrix. Variable H_c is defined as $m_1 = \{H_c = \text{diag}(n_1, \dots, n_L) : \forall l, n_l \in [0, 1]\}$, where n_l can be interpreted as the possibility of monitoring the l -th output channel. There is also a requirement for matrix U to be positive semi-definite. As far as the *measured output* of the Belavkin equation is concerned one has an equation of complex currents $J^T dt = \langle \hat{c}H_c + \hat{c}^+Y \rangle_c + dz^T$, where $\langle \rangle$ stands for the mean value of the variable contained in it [1]. Thus, in the description of the quantum system according to Belavkin's formulation, the state equation and the output equation are given by Eq. (10).

$$\begin{aligned} \hbar d\rho_c &= dtD[\hat{c}]\rho_c + H[-i\hat{H}dt + dz^+(t)\hat{c}]\rho_c \\ J^T dt &= \langle \hat{c}^T H_c + \hat{c}^+ Y_c \rangle dt + dz^T \end{aligned} \quad (10)$$

where ρ_c is the probability density matrix (state variable) for remaining at one of the quantum system eigenstates, and J is the measured output (current).

C. Formulation of the control problem

The control loop consists of a cavity where the multi-particle quantum system is confined and of a laser probe which excites the quantum system. Measurements about the condition of the quantum system are collected through photodetectors and thus the projections of the probability density matrix ρ of the quantum system are turned into weak current. By processing this current measurement and the estimate of the quantum system's state which is provided by Lindblad's or Belavkin's equation, a control law is generated which modifies a magnetic field applied to the cavity. In that manner, the state of the quantum system is driven from the initial value $\rho(0)$ to the final desirable value $\rho_d(t)$ (see Fig. 1).

When Schrödinger's equation is used to describe the dynamics of the quantum system the objective is to move the quantum system from a state ψ , that is associated to a certain energy level, to a different eigenstate associated with the desirable energy level. When Lindblad's or Belavkin's equation is used to describe the dynamics of the quantum system, the control objective is to stabilize the probability density matrix $\rho(t)$ on some desirable quantum state $\rho_d(t) \in C^n$, by controlling the intensity of the magnetic field. The value of the control signal is determined by processing

the measured output which in turn depends on the projection of $\rho(t)$ defined by $Tr\{P\rho(t)\}$.

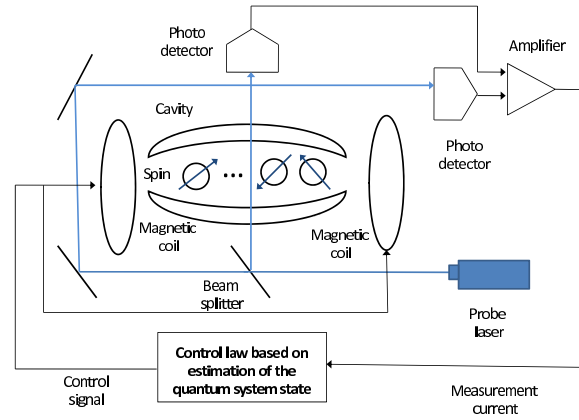


Figure 1. Feedback control loop for quantum systems

IV. A FEEDBACK CONTROL APPROACH FOR QUANTUM SYSTEM STABILIZATION

A. Control law calculation using Schrödinger's equation

It is assumed that the dynamics of the controlled quantum system is described by a Schrödinger equation of the form

$$i\hbar\dot{\psi}(t) = [H_0 + f(t)H_1]\psi(t) \quad \psi(t) \in C^n \quad (11)$$

where H_0 is the system's Hamiltonian, H_1 is the control Hamiltonian and $f(t)$ is the external control input. The following Lyapunov function is then introduced [9]

$$V(\psi) = (\psi^+ Z \psi - Z_d)^2 \quad (12)$$

where $+$ stands for the transposition and complex conjugation, Z is the quantum system's observable and is associated to the energy of the system. The term $\psi^+ Z \psi$ denotes the observed mean energy of the system at time instant t and Z_d is the desirable energy value. The first derivative of the Lyapunov function of Eq. (12) is

$$\dot{V}(\psi) = 2[\psi^+ Z \psi - Z_d][\dot{\psi}^+ Z \psi + \psi^+ Z \dot{\psi}] \quad (13)$$

while from Eq. (11) it also holds $\dot{\psi}(t) = -\frac{i}{\hbar}[H_0 + f(t)H_1]\psi(t)$, which results into

$$\dot{V}(\psi) = \frac{2i}{\hbar}(\psi^+ Z \psi - Z_d) \cdot \psi^+ \{H_0 Z - Z H_0 + f(H_1 Z - Z H_1)\} \psi \quad (14)$$

Choosing the control signal $f(t)$ to be proportional to the gradient with respect to f of the first derivative of the Lyapunov function with respect to time (velocity gradient) i.e. $f(t) = k \nabla_f \{\dot{V}(\psi)\}$, and for Z such that $\psi^+ H_0 Z \psi = \psi^+ Z H_0 \psi$ (e.g. $Z = H_0$) one obtains

$$f(t) = \frac{2i}{\hbar}(\psi^+ Z \psi - Z_d) \psi^+ (H_1 Z - Z H_1) \psi \quad (15)$$

Substituting Eq. (15) into Eq. (14) provides $\dot{V}(\psi) = k \frac{2i}{\hbar}(\psi^+ Z \psi - Z_d) \psi^+ [\frac{2i}{\hbar}(\psi^+ Z \psi - Z_d) \psi^+ (H_1 Z - Z H_1) \psi (H_1 Z - Z H_1)] \psi$, and finally results in the following form of the first derivative of the Lyapunov function

$$\dot{V}(\psi) = -k \frac{4}{\hbar^2} (\psi^* Z \psi - Z_d)^2 \psi^{+2} (H_1 Z - Z H_1)^2 \psi^2 \leq 0 \quad (16)$$

which is non-positive along the system trajectories. This implies stability for the quantum system and in such a case La Salle's principle shows convergence not to an equilibrium but to an area round this equilibrium, which is known as *invariant set*. La Salle's theorem is expressed as follows [16]:

Theorem 1: Assume the autonomous system $\dot{x} = f(x)$ where $f : D \rightarrow R^n$. Assume $C \subset D$ a compact set which is positively invariant with respect to $\dot{x} = f(x)$, i.e. if $x(0) \in C \Rightarrow x(t) \in C \forall t$. Assume that $V(x) : D \rightarrow R$ is a continuous and differentiable Lyapunov function such that $\dot{V}(x) \leq 0$ for $x \in C$, i.e. $V(x)$ is negative semi-definite in C . Denote by E the set of all points in C such that $\dot{V}(x) = 0$. Denote by M the largest invariant set in E and its boundary by L^+ , i.e. for $x(t) \in E : \lim_{t \rightarrow \infty} x(t) = L^+$, or in other words L^+ is the positive limit set of E . Then every solution $x(t) \in C$ will converge to M as $t \rightarrow \infty$.

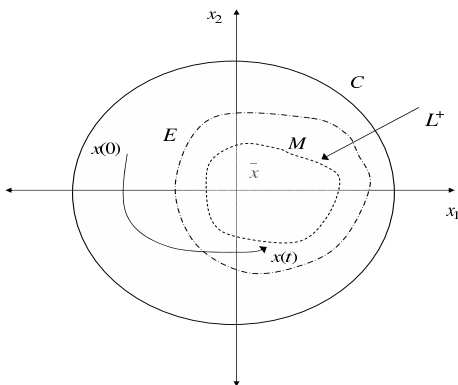


Figure 2. LaSalle's theorem: C : invariant set, $E \subset C$: invariant set which satisfies $\dot{V}(x) = 0$, $M \subset E$: invariant set, which satisfies $\dot{V}(x) = 0$, and which contains the limit points of $x(t) \in E$, L^+ the set of limit points of $x(t) \in E$

Consequently, from Eq. (16) and LaSalle's theorem, any solution of the system $\psi(t)$ remains in the invariant set $M = \{\psi : \dot{V}(\psi) = 0\}$.

B. Control law calculation using Lindblad's equation

Next, it will be shown how a gradient-based control law can be formulated using the description of the quantum system

according to Lindblad's equation. The following bilinear Hamiltonian system is considered (Lidblad equation)

$$\dot{\rho}(t) = -i[H_0 + f(t)H_1, \rho(t)] \quad (17)$$

where H_0 is the interaction Hamiltonian of the quantum system, H_1 is the control Hamiltonian of the quantum system and $f(t)$ is the real-valued control field for the quantum system. The control problem consists of calculating the control function $f(t)$ such that the system's state (probability transition matrix $\rho(t)$) with initial conditions $\rho(0) = \rho_0$ converges to the desirable final state ρ_d for $t \rightarrow \infty$. It is considered that the initial state ρ_0 and the final state ρ_d have the same spectrum and this is a condition needed for reachability of the final state through unitary evolutions. Because of the existence of the interaction Hamiltonian H_0 it is also considered that the desirable target state also evolves in time according to the Lindblad equation, i.e.

$$\dot{\rho}_d(t) = -i[H_0, \rho_d(t)] \quad (18)$$

The target state is considered to be stationary if it holds $[H_0, \rho_d(t)] = 0$, therefore in such a case it also holds $\dot{\rho}_d(t) = 0$. When $[H_0, \rho_d(t)] \neq 0$ then one has $\dot{\rho}_d \neq 0$ and the control problem of the quantum system is a tracking problem. The requirement $\rho(t) \rightarrow \rho_d(t)$ for $t \rightarrow \infty$ implies a trajectory tracking problem, while the requirement $\rho(t) \rightarrow O(\rho_d)(t)$ for $t \rightarrow \infty$ is an orbit tracking problem.

It will be shown that the calculation of the control function $f(t)$ which assures that $\rho(t)$ converges to $\rho_d(t)$ can be performed with the use of the Lyapunov method. To this end, a suitable Lyapunov function $V(\rho, \rho_d)$ will be chosen and it will be shown that there exists a gradient-based control law $f(t)$ such that $\dot{V}(\rho, \rho_d) \leq 0$.

The dynamics of the state of the quantum system, as well as the dynamics of the target state are jointly described by $\dot{\rho}(t) = -i[H_0 + f(t)H_1, \rho(t)]$, $\dot{\rho}_d(t) = -i[H_0, \rho_d(t)]$. A potential Lyapunov function for the considered quantum system is taken to be

$$V = 1 - Tr(\rho_d \rho) \quad (19)$$

It holds that $V > 0$ if $\rho \neq \rho_d$. The Lyapunov function given in Eq. (19) can be also considered as equivalent to the Lyapunov function $V(\psi, \psi_d) = 1 - | \langle \psi_d(t) | \psi(t) \rangle |^2$, which results from the description of the quantum system with the use of Schrödinger's equation given in Eq. (1). The term $\langle \psi_d(t) | \psi(t) \rangle$ expresses an internal product which takes value 1 if $\psi_d(t)$ and $\psi(t)$ are aligned. The first derivative of the Lyapunov function defined in Eq. (19) is

$$\dot{V} = -Tr(\dot{\rho}_d \rho) - Tr(\rho_d \dot{\rho}) \quad (20)$$

One can continue on the calculation of the first derivative of the Lyapunov function $\dot{V} = -Tr(\dot{\rho}_d \rho) - Tr(\rho_d \dot{\rho}) \Rightarrow \dot{V} = -Tr([-iH_0, \rho_d] \rho) -$

$$\begin{aligned} \text{Tr}(\rho_d[-iH_0, \rho]) - f(t)\text{Tr}(\rho_d[-iH_1, \rho]) &\Rightarrow \dot{V} = \\ -\text{Tr}([-iH_0\rho_d + \rho_d iH_0]\rho) - \text{Tr}(\rho_d[-iH_0\rho + \rho iH_0]) - & \\ f(t)\text{Tr}(\rho_d[-iH_1, \rho]) &\Rightarrow \dot{V} = -\text{Tr}(-iH_0\rho_d\rho + \rho_d iH_0\rho - \\ \rho_d iH_0\rho + \rho_d \rho iH_0) - f(t)\text{Tr}(\rho_d[-iH_1, \rho]) \end{aligned}$$

Using that $\text{Tr}(iH_0\rho_d\rho) = \text{Tr}(\rho_d\rho iH_0)$ one obtains

$$\dot{V} = -f(t)\text{Tr}(\rho_d[-iH_1, \rho]) \quad (21)$$

The control signal $f(t)$ is taken to be the gradient with respect to f of the first derivative of the Lyapunov function i.e. $f(t) = -k\nabla_f \dot{V}(t)$, which gives

$$f(t) = k\text{Tr}(\rho_d[-iH_1, \rho]) \quad k > 0 \quad (22)$$

and which results in a negative semi-definite Lyapunov function $\dot{V} \leq 0$. Choosing the control signal $f(t)$ according to Eq. (22) assures that for the Lyapunov function of the quantum system given by Eq. (19) it holds

$$\begin{aligned} V > 0 \quad \forall (\rho, \rho_d) \neq 0 \\ \dot{V} \leq 0 \end{aligned} \quad (23)$$

and since a negative semi-definite Lyapunov function is examined, LaSalle's theorem is again applicable [16].

According to LaSalle's theorem, explained in subsection IV-A, the state $(\rho(t), \rho_d(t))$ of the quantum system converges to the invariant set $M = \{(\rho, \rho_d) | \dot{V}(\rho(t), \rho_d(t)) = 0\}$. Attempts to define more precisely the convergence area for the trajectories of $\rho(t)$ when applying La Salle's theorem can be found in [8], [17].

V. SIMULATION TESTS

Simulation tests about the performance of the gradient-based quantum control loop are given for the case of a two-qubit (four-level) quantum system. Indicative results from two different simulation experiments are presented, each one associated to different initial conditions of the target trajectory and different desirable final state.

The Hamiltonian of the quantum system was considered to be ideal, i.e. $H_0 \in C^4$ was taken to be strongly regular and $H_1 \in C^4$ contained non-zero non-diagonal elements. The two-qubit quantum system has four eigenstates which are denoted as $\psi_1 = (1000), \psi_2 = (0100), \psi_3 = (0010)$ and $\psi_4 = (0001)$. For the first case, the desirable values of elements $\rho_{ii}^d, i = 1, \dots, 4$ corresponding to quantum states ψ_1 to ψ_4 are depicted in Fig. 3(a), while the convergence of the actual values $\rho_{ii}, i = 1, \dots, 4$ towards the associated desirable values is shown in Fig. 3(b). Similarly, for the second case, the desirable values of elements $\rho_{ii}^d, i = 1, \dots, 4$ are shown in Fig. Fig. 4(a), while the associated actual values are depicted in Fig. 4(b). It can be observed that the gradient-based control calculated according to Eq. (22) enabled convergence of ρ_{ii} to ρ_{ii}^d , within acceptable accuracy levels. Fig. 5 presents the evolution in time of the Lyapunov

function of the two simulated quantum control systems. It can be noticed that the Lyapunov function decreases, in accordance to the negative semi-definiteness proven in Eq. (23). Finally, in Fig. 6, the control signals for the two aforementioned simulation experiments are presented. The simulation tests verify the theoretically proven effectiveness of the proposed gradient-based quantum control scheme. The results can be extended to the case of control loops with multiple control inputs f_i and associated Hamiltonians $H_i, i = 1, \dots, n$.

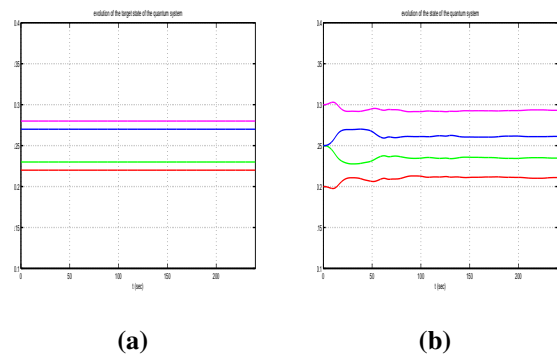


Figure 3. (a) Desirable quantum states in the first test case, (b) Actual quantum states in the first test case

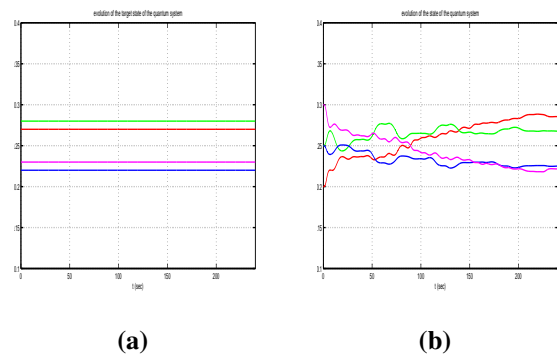


Figure 4. (a) Desirable quantum states in the second test case, (b) Actual quantum states in the second test case

VI. CONCLUSIONS

The paper has presented a gradient-based approach to feedback control of quantum systems. Different descriptions of the quantum system dynamics were formulated using Schrödinger's and Lindblad's differential equations, as well as Belavkin's stochastic differential equation. When Schrödinger's equation is used to describe the dynamics of the quantum system the objective is to move the quantum system from an eigenstate associated to a certain energy level to a different eigenstate associated to the desirable

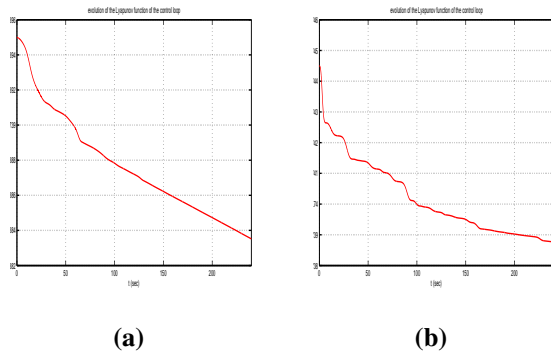


Figure 5. (a) Lyapunov function of the first test case, (b) Lyapunov function of the second test case

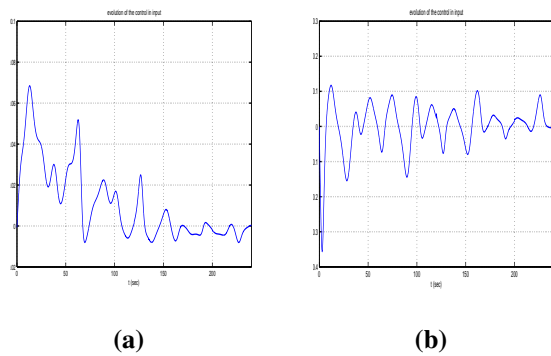


Figure 6. (a) Control input of the first test case, (b) Control input of the second test case

energy level. When Lindblad’s or Belavkin’s equations are used to describe the dynamics of the quantum system the control objective is to stabilize the probability density matrix ρ on some desirable quantum state $\rho_d \in C^n$ by controlling the intensity of the magnetic field. The control input is calculated by processing the measured output, which in turn depends on the projection of the probability density matrix ρ , as well as on processing of the estimate of ρ provided by Lindblad’s or Belavkin’s equation. It was shown that using either the Schrödinger or the Lindblad description of the quantum system a gradient-based control law can be formulated which assures tracking of the desirable quantum state within acceptable accuracy levels. The convergence properties of the gradient-based control scheme were proven using Lyapunov stability theory and LaSalle’s invariance principle. Finally, simulation experiments for the case of a two-qubit (four-level) quantum system verified the theoretically established efficiency of the proposed gradient-based control approach.

REFERENCES

[1] H.M. Wiseman and G.J. Milburn, Quantum measurement and control, Cambridge University Press, 2010.

[2] G.G. Rigatos. Spin-orbit interaction in particles’ motion as a model of quantum computation, PhysCon 2009, 4th Intl. Conference on Physics and Control, Catania, Italy, Sep.2009.

[3] G.G. Rigatos, Open-loop control of particle systems based on a model of coupled stochastic oscillators, ICQNM 2009 Intl. Conference on Quantum Micro and Nano Technologies, Mexico, 2009.

[4] P.S.P. da Silva and P. Rouchon, Flatness-based control of a single qubit-gate. *IEEE Transactions on Automatic Control*, vol. 53, no.3, pp. 775-779, 2008.

[5] C. Chen, G. Rigatos, D. Dong and J. Lam, Partial Feedback Control of Quantum Systems Using Probabilistic Fuzzy Estimator, IEEE CDC 2009, Joint 48th IEEE Conference on Decision and Control and 28th Chinese Control Conference, Sanghai, China, Dec. 2009.

[6] V.P. Belavkin, On the theory of controlling observable quantum systems. *Automation and Remote Control*, Springer, vol. 44, no.2, pp. 178-188, 1983.

[7] K. Beauchard, J.M. Coron, M. Mirrahimi and P. Rouchon, Implicit Lyapunov control of finite dimensional Schrödinger equations, *Systems and Control Letters*, Elsevier, vol. 56, pp. 388-395, 2007.

[8] X. Wang and S. Schirmer, Analysis of Lyapunov control for Hamiltonian quantum systems, ENOC 2008, St. Petersburg, Russia, July 2008.

[9] M.S. Ananievskii and A.L. Fradkov, Control of the observables in the finite-level quantum systems, *Automation and Remote Control*, Springer, vol. 66, no. 5, pp. 734-745, 2005.

[10] E. Aero, A. Fradkov, B. Andrievsky and S. Vakulenko, Dynamics and control of oscillations in a complex crystalline lattice, *Physics Letters A*, Elsevier, vol. 353, pp. 24-29, 2006.

[11] G.G. Rigatos, Cooperative behavior of nano-robots as an analogous of the quantum harmonic oscillator, *Annals of Mathematics and Artificial Intelligence*, Springer, vol. 55, no 3-4, pp. 277-294, 2009.

[12] G.G.Rigatos and S.G. Tzafestas Parallelization of a fuzzy control algorithm using quantum computation. *IEEE Transactions on Fuzzy Systems*, 10, pp. 451-460, 2002.

[13] A. Benvensite, M. Metivier and P. Priouret, Adaptive algorithms and stochastic approximations. Springer: Applications of Mathematics Series, 22, 1990.

[14] C. Cohen-Tannoudji, B. Diu and F. Laloë, *Mécanique Quantique I*. Hermann, 1998.

[15] H.P. Breuer and F. Petruccione, *The theory of open quantum systems*, Clarendon Press, Oxford, 2006.

[16] H. Khalil, *Nonlinear Systems*, Prentice Hall, 1996.

[17] W. Wang, L. C. Wang, and X. X. Yi, Lyapunov control on quantum open systems in decoherence-free subspaces, *Physical Review A*, vol. 82, 034308, 2010.

Reflectionless and Equiscattering Quantum Graphs

Taksu Cheon

Laboratory of Physics, Kochi University of Technology, Tosa Yamada, Kochi 782-8502, Japan

Email: taksu.cheon@kochi-tech.ac.jp

Abstract—The inverse scattering problem of a quantum star graph is shown to be solvable as a diagonalization problem of Hermitian unitary matrix when the connection condition is given by scale invariant Tsutsui-Fulop form. This enables the construction of quantum graphs with desired properties in tailor-made fashion. The quantum vertices with uniform and reflectionless scatterings are examined, and their finite graph approximations are constructed.

Index Terms—quantum graph; singular vertex; quantum wire; inverse scattering

I. INTRODUCTION

The inverse scattering is one of the most intriguing problems in quantum mechanics. The interest in the inverse scattering problem of quantum graph [1], [2], [3], in particular, is two-fold. Since the quantum graph is a prime example of nontrivial solvable system [4], it presents a challenge for extending the range of solvable inverse scattering problems. The inverse scattering problem of quantum graph is also important for its relevance as the design principle of nanowire-based single electron devices.

In this article, we consider the inverse scattering problem on a star graph with Fulop-Tsutsui vertices [5], the scale invariant subset of most general vertex couplings [6]. A star graph is the elementary building block of generic graph having many half-lines connected together at a single point, the singular vertex. The scattering matrix of star graph with Fulop-Tsutsui condition is energy independent. We exploit this simplicity to give the full answer to its inverse scattering problem in the form of eigenvalue problem of Hermitian unitary matrix. Two special examples of inverse scattering problems, that of reflectionless transmission, and of equal-scattering including the reflection, are examined. Intriguing designs emerge for the realization of quantum device with such properties. Since any singular vertex is effectively reduced to Fulop-Tsutsui vertex in both high and low energy limits [7], our study hopefully opens up a door for the full study of inverse scattering problems for general singular vertex.

This article is organized as follows: In the second section, we formulate the inverse scattering problem of scale invariant graph vertices in terms of matrix diagonalization. In the third section, a scheme to approximate the vertex with small structures made up of δ -vertices is developed. In the fourth section, the scheme is applied to obtain reflectionless and equitransmitting quantum graphs. The accuracy of the approximating procedure is examined in the fifth section, which is followed by the concluding sixth section.

II. INVERSE SCATTERING AS DIAGONALIZATION

Consider a singular quantum vertex of degree n , having n half-lines sticking out of a point-like node. The scale invariant subfamily of most general connection condition is characterized by a complex matrix T of size $(n - m) \times m$ where m can take the integer value $m = 1, 2, \dots, n - 1$, and is given by

$$\begin{pmatrix} I^{(m)} & T \\ 0 & 0 \end{pmatrix} \Psi' = \begin{pmatrix} 0 & 0 \\ -T^\dagger & I^{(n-m)} \end{pmatrix} \Psi, \quad (1)$$

where $I^{(l)}$ signifies the identity matrix of size $l \times l$, and the boundary vectors Ψ and Ψ' are defined by

$$\Psi = \begin{pmatrix} \psi_1(0) \\ \vdots \\ \psi_n(0) \end{pmatrix}, \quad \Psi' = \begin{pmatrix} \psi'_1(0) \\ \vdots \\ \psi'_n(0) \end{pmatrix}, \quad (2)$$

in which $\psi_i(x_i)$ and $\psi'_i(x_i)$ are the wave function and its derivative on i -th line [8]. The coordinates x_i on the i -th line are labeled outwardly from the singular vertex, which is assigned $x_i = 0$ for all i . To achieve the form (1), we may have to suitably renumber lines, in general. The quantum particle coming in from the j -th line and scattered off the singular vertex is described by the scattering wave function on the i -th line, $\psi_i^{(j)}(x)$ which is given in the form

$$\psi_i^{(j)}(x) = \delta_{i,j} e^{-ikx} + \mathcal{S}_{i,j} e^{ikx}. \quad (3)$$

From (1) and (3), we obtain the equation

$$ik \begin{pmatrix} I^{(m)} & T \\ 0 & 0 \end{pmatrix} (\mathcal{S} - I^{(n)}) = \begin{pmatrix} 0 & 0 \\ -T^\dagger & I^{(n-m)} \end{pmatrix} (\mathcal{S} + I^{(n)}). \quad (4)$$

We easily obtain the explicit solution of the scattering matrix $\mathcal{S} = \{\mathcal{S}_{i,j}\}$ in the form

$$\mathcal{S} = -I^{(n)} + 2 \begin{pmatrix} I^{(m)} \\ T^\dagger \end{pmatrix} \left(I^{(m)} + TT^\dagger \right)^{-1} \begin{pmatrix} I^{(m)} & T \end{pmatrix}. \quad (5)$$

We can rewrite this solution in the form of a products of three Hermitian matrices as

$$\mathcal{S} = X_m^{-1} Z_m X_m, \quad (6)$$

where we define

$$X_m = \begin{pmatrix} I^{(m)} & T \\ T^\dagger & -I^{(n-m)} \end{pmatrix}, \quad Z_m = \begin{pmatrix} I^{(m)} & 0 \\ 0 & -I^{(n-m)} \end{pmatrix}. \quad (7)$$

Note the Hermitian unitarity of \mathcal{S} ;

$$\mathcal{S}^\dagger = \mathcal{S}, \quad \mathcal{S}^\dagger \mathcal{S} = I^{(n)}. \quad (8)$$

Interestingly, (6) can also be viewed as the diagonalization of Hermitian unitary matrix \mathcal{S} by a non-unitary Hermitian matrix X_m . We can show, in fact, that this form leads to the path to the inverse scattering problem for quantum graph vertex of Fulop-Tsutsui type: Let us suppose that the full set of scattering data is given in terms of an arbitrary Hermitian unitary matrix \mathcal{S} . Let us signify the rank of the matrix $\mathcal{S} + I^{(n)}$ by m . After proper renumbering of lines, we can write this matrix in the form

$$\mathcal{S} + I^{(n)} = \begin{pmatrix} I^{(m)} \\ T^\dagger \end{pmatrix} M \begin{pmatrix} I^{(m)} & T \end{pmatrix}, \quad (9)$$

where M is a Hermitian $m \times m$ matrix, and T , a complex $(n - m) \times m$ matrix. From the unitarity of \mathcal{S} , we find the relation $(\mathcal{S} + I^{(n)})^2 = 2(\mathcal{S} + I^{(n)})$, from which we obtain

$$M = 2(I^{(m)} + TT^\dagger)^{-1}, \quad (10)$$

and we therefore arrive at (5). It is notable that any Hermitian unitary matrix can be viewed as a solution \mathcal{S} of a Fulop-Tsutsui vertex, which is necessarily independent of the incoming momentum k . For a quantum star graph to break scale invariance and obtain k -dependence, its scattering matrix has to obtain non-Hermiticity. These observations, along with the very fact of the existence and uniqueness of inverse scattering solution of quantum star graph, can be reached easily and directly from the original ‘‘U-form’’ of connection condition using a unitary matrix [1], [6], but our procedure holds definite advantage of giving us T directly, which is known [8] to allow us the physical construction of a finite quantum graph whose small size limit reproduces the prescribed \mathcal{S} .

The procedure of diagonalization, in practice, can be cumbersome for large n . There are simpler alternative to obtain T from \mathcal{S} : Let us divide \mathcal{S} into four submatrices \mathcal{S}_{11} , \mathcal{S}_{12} , \mathcal{S}_{21} and \mathcal{S}_{22} of size $m \times m$, $m \times (n - m)$, $(n - m) \times m$ and $(n - m) \times (n - m)$, respectively as

$$\mathcal{S} = \begin{pmatrix} \mathcal{S}_{11} & \mathcal{S}_{12} \\ \mathcal{S}_{21} & \mathcal{S}_{22} \end{pmatrix}. \quad (11)$$

These submatrices have the properties

$$\mathcal{S}_{11}^\dagger = \mathcal{S}_{11}, \quad \mathcal{S}_{22}^\dagger = \mathcal{S}_{22}, \quad \mathcal{S}_{21}^\dagger = \mathcal{S}_{12}, \quad (12)$$

and also

$$\begin{aligned} \mathcal{S}_{11}^2 + \mathcal{S}_{12}^2 &= I^{(m)}, & \mathcal{S}_{22}^2 + \mathcal{S}_{21}^2 &= I^{(n-m)}, \\ \mathcal{S}_{11}\mathcal{S}_{12} + \mathcal{S}_{12}\mathcal{S}_{22} &= 0. \end{aligned} \quad (13)$$

We have the explicit expressions of T in terms of \mathcal{S}_{ij} :

$$T = \left(I^{(m)} + \mathcal{S}_{11} \right)^{-1} \mathcal{S}_{12} = \mathcal{S}_{21}^\dagger \left(I^{(n-m)} - \mathcal{S}_{22} \right)^{-1}. \quad (14)$$

It is easy to check that the forms (5) and (6) can be kept under the index renumbering $\alpha \leftrightarrow \beta$ both for $\alpha, \beta \leq m$ and for $\alpha, \beta > m$ with the proper transformation for the elements of T ; It is given by $t_{\alpha j} \leftrightarrow t_{\beta j}$ for the former and $t_{i\alpha} \leftrightarrow t_{i\beta}$ for the latter. For the case of $\alpha \leq m$ and $\beta > m$, it is given by $t_{ij} \rightarrow t'_{ij}$ with

$$t'_{ij} = \frac{t_{ij}t_{\alpha\beta} - t_{\alpha j}t_{i\beta}}{t_{\alpha\beta}} \bar{\delta}_{i\alpha} \bar{\delta}_{j\beta} - \frac{t_{\alpha j}\delta_{i\alpha} - \delta_{\alpha j}t_{i\alpha} + \delta_{i\alpha}\delta_{j\beta}}{t_{\alpha\beta}}, \quad (15)$$

where we define $\bar{\delta}_{ij} = 1 - \delta_{ij}$. This implies that it is not possible to exchange the indices α and β whose $t_{\alpha\beta}$ is zero. This corresponds to the index ordering for which both $(I^{(m)} + \mathcal{S}_{11})$ and $(I^{(n-m)} - \mathcal{S}_{22})$ are singular and the T is undefined, thus the boundary condition at the singular vertex does not take the form (1).

III. FINITE APPROXIMATION

Finite tubes connected at a node tend, in their small diameter limit, to a vertex with delta-like connections, and very often to its strength zero limit, a free vertex [9]. We might also consider applying localized magnetic field to achieve phase change. It is natural, therefore, to devise a design principle to construct arbitrary connection condition out of this elementary vertex. Once all elements of $T = \{t_{ij}\}$, $i = 1, \dots, m$ and $j = m + 1, \dots, n$, are obtained, a finite graph with internal lines and the δ -coupling vertices can be constructed systematically, whose small-size limit reproduces the boundary condition of Fulop-Tsutsui vertex, (1). The scheme [10] works as follows.

(i) Assemble the edges of n half lines which we assign the numbers $j = 1, 2, \dots, n$, and connect them in pairs (i, j) by internal lines of length d/r_{ij} except when $r_{ij} = 0$, for which case, the pairs are left unconnected. Apply vector potential A_{ij} on the line (i, j) to produce extra phase shift χ_{ij} between the edges when its value is nonzero. Place δ potential of strength v_i at each edge i .

(ii) The length ratio r_{ij} and the phase shift χ_{ij} are determined from the non-diagonal elements of the matrix Q defined by

$$Q = \begin{pmatrix} T \\ I^{(n-m)} \end{pmatrix} \begin{pmatrix} -T^\dagger & I^{(m)} \end{pmatrix} = \begin{pmatrix} -TT^\dagger & T \\ -T^\dagger & I^{(m)} \end{pmatrix}, \quad (16)$$

by the relation $r_{ij}e^{i\chi_{ij}} = Q_{ij}$ ($i \neq j$). This means that we have $r_{ij}e^{i\chi_{ij}} = t_{ij}$ for $i \leq m, j > m$, and $r_{ij}e^{i\chi_{ij}} = \sum_{l>m} t_{il}t_{jl}^*$ for $i, j \leq m$. For $i, j > m$, we have $r_{ij} = 0$ and naturally also $\chi_{ij} = 0$.

(iii) The strength v_i is given by the diagonal elements of the matrix V defined by

$$V = \frac{1}{d}(2I^{(n)} - J^{(n)})R, \quad (17)$$

where R is the matrix whose elements are made from absolute values of matrix elements of Q , i.e. $R = \{r_{ij}\} = \{|Q_{ij}|\}$. The matrix $J^{(n)}$ is of size $n \times n$ with all elements given by 1. This means that we have $v_i = \frac{1}{d}(1 - \sum_{l \leq m} r_{li})$ for $i > m$, and $v_i = \frac{1}{d}(\sum_{l>m} [r_{il}^2 - r_{il}] - \sum_{l(\neq i) \leq m} r_{il})$ for $i \leq m$. These fine tunings of length and strength are necessary to counter the generic opaqueness brought in with every addition of vertices and lines into a graph.

The wave function $\phi(x) = \phi_{i,j}(x)$ on any internal line (i, j) , we have the relation

$$\begin{pmatrix} \phi'(0) \\ e^{i\chi} \phi'(\frac{d}{r}) \end{pmatrix} = -\frac{r}{d} \begin{pmatrix} F(\frac{d}{r}) & -G(\frac{d}{r}) \\ G(\frac{d}{r}) & -F(\frac{d}{r}) \end{pmatrix} \begin{pmatrix} \phi(0) \\ e^{i\chi} \phi(\frac{d}{r}) \end{pmatrix}, \quad (18)$$

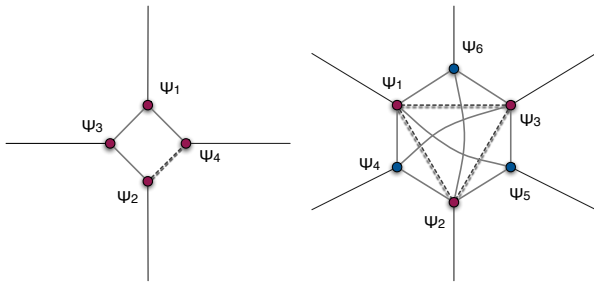


Fig. 1. Finite approximation to the reflectionless Fulop-Tsutsui vertices corresponding to (22) (left) and (28) (right) constructed according to (16)-(17). Dotted line indicates the existence of non-zero phase shift χ_{ij} .

with $F(x) = x \cot x$ and $G(x) = x \operatorname{cosec} x$. Combining (18) with the condition at the i -th endpoint,

$$\psi'_i(0) + \sum_{j \neq i} \phi'_{ij}(0) = v_i \psi_i(0) \quad (19)$$

where we have the δ -potential of strength v_i , we obtain the relations between the boundary values $\psi_i = \psi_i(0)$ and $\psi'_i = \psi'_i(0)$ in the form

$$d\psi'_i = \left(v_i d + \sum_{l \neq i} r_{il} F_{il} \right) \psi_i - \sum_{l \neq i} e^{i\chi_{ij}} r_{il} G_{il} \psi_l, \quad (20)$$

where the obvious notations $F_{ij} = \frac{d}{r_{ij}} \cot \frac{d}{r_{ij}}$ and $G_{ij} = \frac{d}{r_{ij}} \operatorname{cosec} \frac{d}{r_{ij}}$ are adopted. Note that the equation (20) is exact and does not involve any approximation. In the short range limit $d \rightarrow 0$, we have $F_{ij} = 1 + O(d^2)$ and $G_{ij} = 1 + O(d^2)$. We can then show, with a straightforward calculation in the manner of [8], that the limit $d \rightarrow 0$ gives the desired connection condition for Fulop-Tsutsui vertex (1).

IV. EXAMPLES

With the solution of the inverse scattering fully formulated, it is now possible to find a Fulop-Tsutsui vertex from a given scattering matrix with specific requirement. Our previous results detailed in [10] showing the reconstruction of ‘‘Free-like’’ scattering is one such example, and could have been achieved easier with current method. We now ask whether there is fully reflectionless graph whose scattering matrix has only zeros for its diagonal elements, $S_{ii} = 0$. Vertices yielding such scattering matrix is known to be useful in developing semiclassical theory of quantum spectra [11]. If we limit ourselves to real S , it becomes symmetric matrix with $S_{ij} = S_{ji}$.

We note a useful relation concerning the trace of the scattering matrix. Taking the trace of (6) and utilizing $\operatorname{tr}(AB) = \operatorname{tr}(BA)$, we have

$$\operatorname{tr} S = \operatorname{tr} Z_m = 2m - n. \quad (21)$$

Since S for reflectionless scattering is traceless, we can have such scattering only for $n = 2m$.

Our first example is with $n = 4$ whose S is given by

$$S = \begin{pmatrix} 0 & 0 & a & \sqrt{1-a^2} \\ 0 & 0 & \sqrt{1-a^2} & -a \\ a & \sqrt{1-a^2} & 0 & 0 \\ \sqrt{1-a^2} & -a & 0 & 0 \end{pmatrix}, \quad (22)$$

and the corresponding T , by

$$T = \begin{pmatrix} a & \sqrt{1-a^2} \\ \sqrt{1-a^2} & -a \end{pmatrix}. \quad (23)$$

The finite approximation is characterized by

$$r_{12} = r_{34} = 0, \quad r_{13} = r_{24} = a, \quad r_{23} = r_{14} = \sqrt{1-a^2},$$

$$e^{i\chi_{24}} = -1, \quad e^{i\chi_{ij}} = 1 \text{ all others,}$$

$$v_1 = v_2 = v_3 = v_4 = \frac{1-a-\sqrt{1-a^2}}{d}, \quad (24)$$

The finite graph approximation is schematically illustrated in the left side of Figure 1.

We next turn to reflectionless scattering with uniform transmission to all other lines. The smallest non-trivial example of such matrix exists for $n = 4$, and given by

$$S = \frac{1}{\sqrt{5}} \begin{pmatrix} 0 & 1 & 1 & 1 \\ 1 & 0 & -i & i \\ 1 & i & 0 & -i \\ 1 & -i & i & 0 \end{pmatrix}. \quad (25)$$

The corresponding T is given by

$$T = \begin{pmatrix} \omega & \omega^{-1} \\ \omega^{-4} & \omega^4 \end{pmatrix}. \quad (26)$$

with $\omega = e^{i\frac{\pi}{6}}$. Our finite approximation is specified by following numbers.

$$r_{13} = r_{14} = r_{23} = r_{24} = 1, \quad r_{12} = r_{34} = 0, \\ e^{i\chi_{13}} = e^{i\frac{\pi}{6}}, \quad e^{i\chi_{14}} = e^{-i\frac{\pi}{6}}, \quad e^{i\chi_{23}} = e^{-4i\frac{\pi}{6}}, \quad e^{i\chi_{24}} = e^{4i\frac{\pi}{6}}, \\ v_1 = v_2 = v_3 = v_4 = -\frac{1}{d}, \quad (27)$$

The finite graph approximation is schematically illustrated in the right side of Figure 1.

If we limit ourselves to real scattering matrix, such matrix, called *symmetric conference matrix*, is known to exist for $n = 6, 10, 14, 18, 26, 30, 38, \dots$. We look at the example of $n = 6$ whose S is given by

$$S = \frac{1}{\sqrt{5}} \begin{pmatrix} 0 & -1 & -1 & -1 & 1 & 1 \\ -1 & 0 & -1 & 1 & -1 & 1 \\ -1 & -1 & 0 & 1 & 1 & -1 \\ -1 & 1 & 1 & 0 & 1 & 1 \\ 1 & -1 & 1 & 1 & 0 & 1 \\ 1 & 1 & -1 & 1 & 1 & 0 \end{pmatrix}. \quad (28)$$

The corresponding T is given by

$$T = \begin{pmatrix} 1 & 1+\gamma & 1+\gamma \\ 1+\gamma & 1 & 1+\gamma \\ 1+\gamma & 1+\gamma & 1 \end{pmatrix}. \quad (29)$$

where $\gamma = (\sqrt{5} - 1)/2$ is the golden mean. Our finite approximation is specified by following numbers.

$$\begin{aligned}
 r_{12} = r_{23} = r_{13} &= 4 + 3\gamma, \quad r_{14} = r_{25} = r_{36} = 1, \\
 r_{15} = r_{16} = r_{26} = r_{24} = r_{31} = r_{32} &= 1 + \gamma, \\
 r_{45} = r_{46} = r_{56} &= 0, \\
 e^{i\chi_{12}} = e^{i\chi_{23}} = e^{i\chi_{13}} &= -1, \quad e^{i\chi_{ij}} = 1 \text{ all others,} \\
 v_1 = v_2 = v_3 &= -6 \frac{\gamma + 1}{d}, \quad v_4 = v_5 = v_6 = -2 \frac{\gamma + 1}{d}. \quad (30)
 \end{aligned}$$

The finite graph approximation is schematically illustrated in the right side of Figure 1.

Our next example is the reflectionless equitransmitting graph with $n = 10$, that corresponds to the \mathcal{S} matrix given by $n = 10$ conference matrix

$$\mathcal{S} = \frac{1}{3} \begin{pmatrix} 0 & -1 & 1 & 1 & -1 & -1 & 1 & 1 & 1 & 1 \\ -1 & 0 & -1 & 1 & 1 & 1 & -1 & 1 & 1 & 1 \\ 1 & -1 & 0 & -1 & 1 & 1 & 1 & -1 & 1 & 1 \\ 1 & 1 & -1 & 0 & -1 & 1 & 1 & 1 & -1 & 1 \\ -1 & 1 & 1 & -1 & 0 & 1 & 1 & 1 & 1 & -1 \\ -1 & 1 & 1 & 1 & 1 & 0 & 1 & -1 & -1 & 1 \\ 1 & -1 & 1 & 1 & 1 & 1 & 0 & 1 & -1 & -1 \\ 1 & 1 & -1 & 1 & 1 & -1 & 1 & 0 & 1 & -1 \\ 1 & 1 & 1 & -1 & 1 & -1 & -1 & 1 & 0 & 1 \\ 1 & 1 & 1 & 1 & -1 & 1 & -1 & -1 & 1 & 0 \end{pmatrix} \quad (31)$$

The trace of \mathcal{S} is zero again, and we have $m = \frac{n}{2} = 5$. The matrix T specifying the vertex is given by

$$T = \begin{pmatrix} -1 & 0 & 1 & 1 & 0 \\ 0 & -1 & 0 & 1 & 1 \\ 1 & 0 & -1 & 0 & 1 \\ 1 & 1 & 0 & -1 & 0 \\ 0 & 1 & 1 & 0 & -1 \end{pmatrix}, \quad (32)$$

where $\sigma = \sqrt{2} - 1$ is the silver mean. Our finite approximation is specified by following numbers for verteces;

$$\begin{aligned}
 r_{12} = r_{23} = r_{34} = r_{45} = r_{15} &= 1, \\
 r_{16} = r_{27} = r_{38} = r_{49} = r_{5a} &= 1, \\
 r_{18} = r_{29} = r_{3a} = r_{46} = r_{57} &= 1, \\
 r_{19} = r_{2a} = r_{36} = r_{47} = r_{58} &= 1, \\
 r_{13} = r_{14} = r_{24} = r_{25} = r_{35} &= 2, \\
 r_{17} = r_{28} = r_{39} = r_{4a} = r_{56} &= 0, \\
 r_{1a} = r_{26} = r_{37} = r_{48} = r_{59} &= 0, \\
 r_{67} = r_{78} = r_{89} = r_{9a} = r_{6a} &= 0, \\
 r_{68} = r_{79} = r_{8a} = r_{69} = r_{7a} &= 0, \\
 e^{i\chi_{12}} = e^{i\chi_{23}} = e^{i\chi_{34}} = e^{i\chi_{45}} = e^{i\chi_{15}} &= -1 \\
 e^{i\chi_{16}} = e^{i\chi_{27}} = e^{i\chi_{38}} = e^{i\chi_{49}} = e^{i\chi_{5a}} &= -1 \\
 e^{i\chi_{ij}} &= 1 \text{ all others,} \\
 v_1 = v_2 = v_3 = v_4 = v_5 &= -\frac{6}{d}, \\
 v_6 = v_7 = v_8 = v_9 = v_a &= -\frac{2}{d}. \quad (33)
 \end{aligned}$$

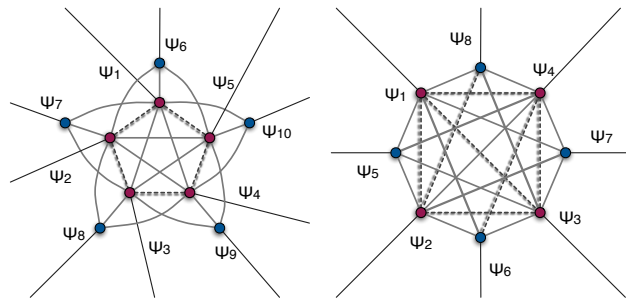


Fig. 2. Finite approximation to the equal-scattering Fulop-Tsutsui vertex corresponding to $n = 10$ conference matrix, (31) (left) and $n = 8$ Hadamard matrix, (34) (right) constructed according to (16)-(17).

Here, a in subscript stands for the index for 10th edge. The finite graph approximation for this case is schematically illustrated in the left side of Figure 2.

The last example is the equal-scattering graph, in which the line of incoming is uniform in all lines including the line of incoming particle. Such matrix, called *symmetric Hadamard matrix*, is known to exist for $n = 2^k$, $k = 0, 1, \dots$. An example of such \mathcal{S} for $n = 8$ is given by

$$\mathcal{S} = \frac{1}{\sqrt{8}} \begin{pmatrix} 1 & -1 & -1 & -1 & -1 & 1 & 1 & 1 \\ -1 & 1 & -1 & -1 & 1 & -1 & 1 & 1 \\ -1 & -1 & 1 & -1 & 1 & 1 & -1 & 1 \\ -1 & -1 & -1 & 1 & 1 & 1 & 1 & -1 \\ -1 & 1 & 1 & 1 & -1 & 1 & 1 & 1 \\ 1 & -1 & 1 & 1 & 1 & -1 & 1 & 1 \\ 1 & 1 & -1 & 1 & 1 & 1 & -1 & 1 \\ 1 & 1 & 1 & -1 & 1 & 1 & 1 & -1 \end{pmatrix}. \quad (34)$$

The trace of \mathcal{S} is again zero, and we have $m = \frac{n}{2} = 4$. The matrix T specifying the Fulop-Tsutsui the vertex is given by

$$T = \frac{1}{\sigma + 1} \begin{pmatrix} \sigma & 1 & 1 & 1 \\ 1 & \sigma & 1 & 1 \\ 1 & 1 & \sigma & 1 \\ 1 & 1 & 1 & \sigma \end{pmatrix}. \quad (35)$$

where $\sigma = \sqrt{2} - 1$ is the silver mean. Our finite approximation is specified by following numbers for verteces;

$$\begin{aligned}
 r_{12} = r_{13} = r_{14} = r_{23} = r_{24} = r_{34} &= 1 + \sigma, \\
 r_{15} = r_{26} = r_{37} = r_{48} &= \frac{\sigma}{1 + \sigma}, \\
 r_{16} = r_{17} = r_{18} = r_{27} = r_{28} = r_{38} &= \frac{1}{1 + \sigma}, \\
 r_{25} = r_{35} = r_{36} = r_{45} = r_{46} = r_{47} &= \frac{1}{1 + \sigma}, \\
 r_{56} = r_{57} = r_{58} = r_{67} = r_{68} = r_{78} &= 0, \\
 e^{i\chi_{12}} = e^{i\chi_{13}} = e^{i\chi_{14}} = e^{i\chi_{23}} &= e^{i\phi_{24}} = e^{i\chi_{34}} = -1, \quad e^{i\chi_{ij}} = 1 \text{ all others,} \\
 v_1 = v_2 = v_3 = v_4 &= -\frac{5\sigma - 3}{d}, \\
 v_5 = v_6 = v_7 = v_8 &= -\frac{\sigma + 1}{d}. \quad (36)
 \end{aligned}$$

The finite graph approximation is schematically illustrated in the right side of Figure 2.

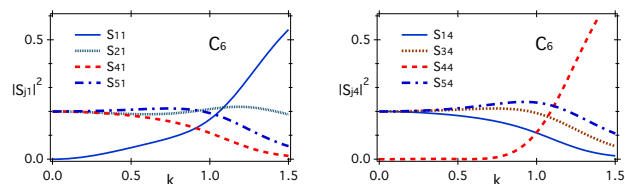


Fig. 3. Scattering probabilities as functions of incoming momentum k (in the unit of $1/d$) of finite quantum graph approximating the equal-transmitting reflectionless vertex with $n = 6$ edges represented in Figure 1, right.

V. CONVERGENCE OF FINITE APPROXIMATIONS

Finally, we take a look at the convergence of the finite size graph approximation by numerical calculations. In Figure 3, we display the scattering matrix of the finite graph that is constructed to approximate equal-scattering reflectionless matrix, (28). These are calculated directly from (20). The value of the wave length k is in the unit of $1/d$. The convergence can be seen as quite good below $kd \lesssim 0.2$. Numerical analysis of other examples of different graphs give essentially the same conclusion that the construction does represent physical realization of singular Fulop-Tsutsui vertex.

VI. CONCLUSION AND PROSPECTS

Now that the problem of finding desired property of Fulop-Tsutsui graph is turned into mathematical one on Hermitian unitary matrix, the search of system with \mathcal{S} having other interesting specifications should follow. various questions would arise along the line, such as whether it is always $\text{tr}S = 0$ for systems with “exchange symmetric” $|S_{ij}|$. Generalization to complex \mathcal{S} is also an interesting problem [11]. Other open questions include the generalization to non-Fulop-Tsutsui connection which yields general unitary \mathcal{S} not limited to Hermitian ones. The study of the bound state spectra is one thing we have completely neglected in this work. Application to non-quantum waves, including electro-magnetic wave and water wave should be another interesting subject.

In this work, through the finite construction of star graph with no internal lines, we have actually studied the low energy properties of graphs with internal lines all of whose edges are connected to external lines, which we might term *depth-one* graphs. The examination of *depth-two* graphs and beyond seems to be the natural future direction. Our result showing the full solution to the inverse scattering problem is, in a sense, a partial fulfillment of the hope that quantum graph somehow could be a solvable model and useful design tool at the same time.

ACKNOWLEDGMENT

This research was supported by the Japanese Ministry of Education, Culture, Sports, Science and Technology under the Grant number 21540402.

REFERENCES

- [1] M. Harmer, J. Phys. A: Math. Theor. **38**, 4875–4885 (2005).
- [2] J. Boman and P. Kurasov, Adv. Appl. Math. **35**, 58–70 (2005).

- [3] B. Gutkin and U. Smilansky, J. Phys. A: Math. Gen. **34** 6061-6068 (2005).
- [4] P. Exner, J.P. Keating, P. Kuchment, T. Sunada, A. Teplyaev, eds., *Analysis on Graphs and Applications*, AMS “Proceedings of Symposia in Pure Mathematics” Series, vol. 77, Providence, R.I., 2008, and references therein.
- [5] T. Fülöp, I. Tsutsui, Phys. Lett. **A264**, 366–374 (2000).
- [6] V. Kostrykin, R. Schrader, J. Phys. A: Math. Gen. **32**, 595–630 (1999).
- [7] T. Cheon, P. Exner and O. Turek, Phys. Lett. A **375**, 113–118 (2010).
- [8] T. Cheon, P. Exner and O. Turek, Ann. Phys. (NY) **325**, 548–578 (2010).
- [9] P. Exner, O. Post, J. Phys. A: Math. Theor. **42**, 415305 (2009).
- [10] T. Cheon and O. Turek, Phys. Lett. A **374**, 4212–4221 (2010).
- [11] J.M. Harrison, U. Smilansky and B. Winn, J. Phys. A: Math. Theor. **40**, 14181 (2007).

Combinatorial Structures of Quantum Entangled States

Hoshang Heydari
 Physics Department
 Stockholm University
 Stockholm, Sweden
 Email: hoshang@fysik.su.se

Abstract—We investigate the combinatorial structures of multipartite quantum systems based on algebraic varieties. In particular, we study the relations between resolution of conifold, toric varieties, separable states, and quantum entangled states. We show that the resolved or deformed conifold is equivalent with the space of a pure entangled two-qubit state. We also generalize this result into multi-qubit states. The results give new insight about multipartite systems and also a new way of representing quantum entangled multipartite systems and quantum operations with potential applications in quantum computing.

Keywords—Quantum entanglement, multipartite quantum systems, quantum information.

I. INTRODUCTION

Pure quantum states are usually defined on complex Hilbert spaces which are very complicated to visualize. The simplest case, namely, the space of a single qubit state can be visualized with Bloch or Riemann sphere. Beyond that there have been little progresses to visualize quantum state. Recently, we have established a relation between quantum states and toric varieties. Based on such a construction or mapping it is possible to visualize the complex Hilbert space by lattice polytop.

In algebraic geometry [1], a conifold is a generalization of the notion of a manifold. But, a conifold can contain conical singularities, e.g., points whose neighborhood look like a cone with a certain base. The base is usually a five-dimensional manifold. However, the base of a complex conifold is a product of one dimensional complex projective space. Conifold are interesting space in string theory, e.g., in the process of compactification of Calabi-Yau manifolds. A Calabi-Yau manifold is a compact Kähler manifold with a vanishing first Chern class. A Calabi-Yau manifold can also be defined as a compact Ricci-flat Kähler manifold.

During recent decade toric varieties have been constructed in different contexts in mathematics [2], [3], [4]. A toric variety \mathbf{X} is a complex variety that contains an algebraic torus $T = (\mathbf{C}^*)^n$ as a dense open set and with action of T on \mathbf{X} whose restriction to $T \subset \mathbf{X}$ is the usual multiplication on T .

In this paper, we establish relations between toric varieties and space of entangled states of bipartite and multipartite quantum systems. In particular, we discuss resolving the

singularity and deformation of conifold and toric variety of the conifold. We show that by removing the singularity of conifold we get a space which is not anymore toric variety but it is the space of an entangled two-qubit state. We also investigate the combinatorial structure of multi-qubit systems based on deformation of each faces of cube (hypercube) which is equivalent to deformation of conifold. In particular, in section II we give a short introduction to conifold. In section III we review the construction of toric variety. In section IV and V we investigate conifold and resolution of toric singularity for two-qubits and three qubits states. Finally, in section VI we generalize our results to multi-qubits states. Through this paper we will use the following notation

$$|\Psi\rangle = \sum_{x_m=0}^1 \sum_{x_{m-1}=0}^1 \cdots \sum_{x_1=0}^1 \alpha_{x_m x_{m-1} \cdots x_1} |x_m x_{m-1} \cdots x_1\rangle, \quad (1)$$

with $|x_m x_{m-1} \cdots x_1\rangle = |x_m\rangle \otimes |x_{m-1}\rangle \otimes \cdots \otimes |x_1\rangle \in \mathcal{H}_{\mathcal{Q}} = \mathcal{H}_{\mathcal{Q}_1} \otimes \mathcal{H}_{\mathcal{Q}_2} \otimes \cdots \otimes \mathcal{H}_{\mathcal{Q}_m}$ for a pure multi-qubit state, where $\mathcal{H}_{\mathcal{Q}_j}$ is the Hilbert space of j th subsystem. Our reviewer also has pointed out that there are other ways of visualization of entangled states, especially, recently proposed visualization with the aid of classical random fields [5], [6].

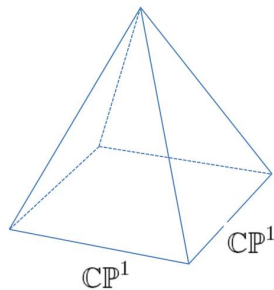
II. CONIFOLD

In this section we will give a short review of conifold. Let \mathbf{C} be a complex algebraic field. Then, an affine n -space over \mathbf{C} denoted \mathbf{C}^n is the set of all n -tuples of elements of \mathbf{C} . An element $P \in \mathbf{C}^n$ is called a point of \mathbf{C}^n and if $P = (a_1, a_2, \dots, a_n)$ with $a_j \in \mathbf{C}$, then a_j is called the coordinates of P . A complex projective space $\mathbf{P}_{\mathbf{C}}^n$ is defined to be the set of lines through the origin in \mathbf{C}^{n+1} , that is,

$$\mathbf{P}_{\mathbf{C}}^n = \frac{\mathbf{C}^{n+1} - \{0\}}{(x_0, \dots, x_n) \sim (y_0, \dots, y_n)}, \quad \lambda \in \mathbf{C} - 0, \quad y_i = \lambda x_i \quad (2)$$

for all $0 \leq i \leq n$. An example of real (complex) affine variety is conifold which is defined by

$$\mathcal{V}_{\mathbf{C}}(z) = \{(z_1, z_2, z_3, z_4) \in \mathbf{C}^4 : \sum_{i=1}^4 z_i^2 = 0\}. \quad (3)$$


 Figure 1. Complex cone over $\mathbf{CP}^1 \times \mathbf{CP}^1$.

Conifold as a real affine variety is define by

$$\begin{aligned} \mathcal{V}_{\mathbf{R}}(f_1, f_2) &= \{(x_1, \dots, x_4, y_1, \dots, y_4) \in \mathbf{R}^8 : \sum_{i=1}^4 x_i^2 = \\ &= \sum_{j=1}^4 y_j^2, \sum_{i=1}^4 x_i y_i = 0\}. \end{aligned} \quad (4)$$

where $f_1 = \sum_{i=1}^4 (x_i^2 - y_i^2)$ and $f_2 = \sum_{i=1}^4 x_i y_i$. This can be seen by defining $z = x + iy$ and identifying imaginary and real part of equation $\sum_{i=1}^4 z_i^2 = 0$. As a real space, the conifold is cone in \mathbf{R}^8 with top the origin and base space the compact manifold $\mathbf{S}^2 \times \mathbf{S}^3$. One can reformulate this relation in term of a theorem. The conifold $\mathcal{V}_{\mathbf{C}}(\sum_{i=1}^4 z_i^2)$ is the complex cone over the Segre variety $\mathbf{CP}^1 \times \mathbf{CP}^1 \rightarrow \mathbf{CP}^3$. To see this let us make a complex linear change of coordinate

$$\begin{pmatrix} \alpha'_{00} & \alpha'_{01} \\ \alpha'_{10} & \alpha'_{11} \end{pmatrix} \rightarrow \begin{pmatrix} z_1 + iz_2 & -z_4 + iz_3 \\ z_4 + iz_3 & z_1 - iz_2 \end{pmatrix}. \quad (5)$$

Thus after this linear coordinate transformation we have

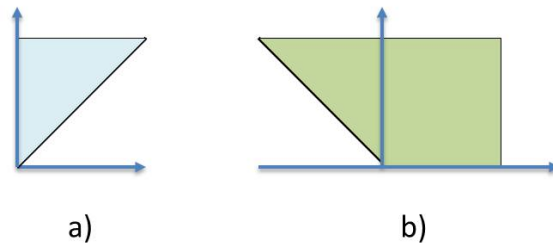
$$\mathcal{V}_{\mathbf{C}}(\alpha'_{00}\alpha'_{11} - \alpha'_{01}\alpha'_{10}) = \mathcal{V}_{\mathbf{C}}(\sum_{i=1}^4 z_i^2) \subset \mathbf{C}^4. \quad (6)$$

Thus we can think of conifold as a complex cone over $\mathbf{CP}^1 \times \mathbf{CP}^1$ see Figure 1. We will comeback to this result in section IV where we establish a relation between these varieties, two-qubit state, resolution of singulary, and deformation theory.

III. TORIC VARIETIES

The construction of toric varieties usually are based on two different branches of mathematics, namely, combinatorial geometry and algebraic geometry. Here, we will review the basic notations and structures of toric varieties [2], [3], [4].

A general toric variety is an irreducible variety \mathbf{X} that satisfies the following conditions. First of all $(\mathbf{C}^*)^n$ is a Zariski open subset of \mathbf{X} and the action of $(\mathbf{C}^*)^n$ on itself can extend to an action of $(\mathbf{C}^*)^n$ on the variety \mathbf{X} . As an example we will show that the complex projective space \mathbf{P}^n is a toric variety. If z_0, z_1, \dots, z_n are homogeneous


 Figure 2. Example of a cone σ a) and its dual σ^\wedge b).

coordinate of \mathbf{P}^n . Then, the map $(\mathbf{C}^*)^n \rightarrow \mathbf{P}^n$ is defined by $(t_1, t_2, \dots, t_n) \mapsto (1, t_1, \dots, t_n)$ and we have

$$(t_1, t_2, \dots, t_n) \cdot (a_0, a_1, \dots, a_n) = (a_0, t_1 a_1, \dots, t_n a_n) \quad (7)$$

which proof our claim that \mathbf{P}^n is a toric variety. We can also define toric varieties with combinatorial information such as polytope and fan (which we will define next). But first we will give a short introduction to the basic of combinatorial geometry which is important in definition of toric varieties. Let $S \subset \mathbf{R}^n$ be finite subset, then a convex polyhedral cone is defined by

$$\sigma = \text{Cone}(S) = \left\{ \sum_{v \in S} \lambda_v v \mid \lambda_v \geq 0 \right\}. \quad (8)$$

In this case σ is generated by S . In a similar way we define a polytope by

$$P = \text{Conv}(S) = \left\{ \sum_{v \in S} \lambda_v v \mid \lambda_v \geq 0, \sum_{v \in S} \lambda_v = 1 \right\}. \quad (9)$$

We also could say that P is convex hull of S . A convex polyhedral cone is called simplicial if it is generated by linearly independent set. Now, let $\sigma \subset \mathbf{R}^n$ be a convex polyhedral cone and $\langle u, v \rangle$ be a natural pairing between $u \in \mathbf{R}^n$ and $v \in \mathbf{R}^n$. Then, the dual cone of the σ is define by

$$\sigma^\wedge = \{u \in \mathbf{R}^{n*} \mid \langle u, v \rangle \geq 0 \forall v \in \sigma\}, \quad (10)$$

where \mathbf{R}^{n*} is dual of \mathbf{R}^n . We also define the polar of σ as

$$\sigma^\circ = \{u \in \mathbf{R}^{n*} \mid \langle u, v \rangle \geq -1 \forall v \in \sigma\}. \quad (11)$$

As an example we consider the cone $\sigma = \text{Cone}(e_1 + e_2, e_2) \subset \mathbf{R}^2$. In this case the cone σ and its dual are illustrated in Figure 1. We call a convex polyhedral cone strongly convex if $\sigma \cap (-\sigma) = \{0\}$.

Next we will define rational polyhedral cones. A free Abelian group of finite rank is called a lattice, e.g., $N \simeq \mathbf{Z}^n$. The dual of a lattice N is defined by $M = \text{Hom}_{\mathbf{Z}}(N, \mathbf{Z})$ which has rank n . We also define a vector space and its dual by $N_{\mathbf{R}} = N \otimes_{\mathbf{Z}} \mathbf{R} \simeq \mathbf{R}^n$ and $M_{\mathbf{R}} = M \otimes_{\mathbf{Z}} \mathbf{R} \simeq \mathbf{R}^{n*}$ respectively. Moreover, if $\sigma = \text{Cone}(S)$ for some finite

set $S \subset N$, then $\sigma \subset N_{\mathbf{R}}$ is a rational polyhedral cone. Furthermore, if $\sigma \subset N_{\mathbf{R}}$ is a rational polyhedral cone, then $S_{\sigma} = \sigma^{\wedge} \cap M$ is a semigroup under addition with $0 \in S_{\sigma}$ as additive identity which is finitely generated by Gordan's lemma [2].

Here we will define a fan which is important in the construction of toric varieties. Let $\Sigma \subset N_{\mathbf{R}}$ be a finite non-empty set of strongly convex rational polyhedral cones. Then Σ is called a fan if each face of a cone in Σ belongs to Σ and the intersection of any two cones in Σ is a face of each.

Now, we can obtain the coordinate ring of a variety by associating to the semigroup S a finitely generated commutative \mathbf{C} -algebra without nilpotent as follows. We associate to an arbitrary additive semigroup its semigroup algebra $\mathbf{C}[S]$ which as a vector space has the set S as basis. The elements of $\mathbf{C}[S]$ are linear combinations $\sum_{u \in S} a_u \chi^u$ and the product in $\mathbf{C}[S]$ is determined by the addition in S using $\chi^u \chi^{u'} = \chi^{u+u'}$ which is called the exponential rule. Moreover, a set of semigroup generators $\{u_i : i \in I\}$ for S gives algebra generators $\{\chi^{u_i} : i \in I\}$ for $\mathbf{C}[S]$.

Now, let $\sigma \subset N_{\mathbf{R}}$ be a strongly convex rational polyhedral cone and $A_{\sigma} = \mathbf{C}[S_{\sigma}]$ be an algebra which is a normal domain. Then,

$$\mathbf{X}_{\sigma} = \text{Spec}(\mathbf{C}[S_{\sigma}]) = \text{Spec}(A_{\sigma}) \quad (12)$$

is called a affine toric variety. Next we need to define Laurent polynomials and monomial algebras. But first we observe that the dual cone σ^{\vee} of the zero cone $\{0\} \subset N_{\mathbf{R}}$ is all of $M_{\mathbf{R}}$ and the associated semigroup S_{σ} is the group $M \simeq \mathbf{Z}^n$. Moreover, let (e_1, e_2, \dots, e_n) be a basis of N and $(e_1^*, e_2^*, \dots, e_n^*)$ be its dual basis for M . Then, the elements $\pm e_1^*, \pm e_2^*, \dots, \pm e_n^*$ generate M as semigroup. The algebra of Laurent polynomials is defined by

$$\mathbf{C}[z, z^{-1}] = \mathbf{C}[z_1, z_1^{-1}, \dots, z_n, z_n^{-1}], \quad (13)$$

where $z_i = \chi^{e_i^*}$. The terms of the form $\lambda \cdot z^{\beta} = \lambda z_1^{\beta_1} z_2^{\beta_2} \dots z_n^{\beta_n}$ for $\beta = (\beta_1, \beta_2, \dots, \beta_n) \in \mathbf{Z}$ and $\lambda \in \mathbf{C}^*$ are called Laurent monomials. A ring R of Laurent polynomials is called a monomial algebra if it is a \mathbf{C} -algebra generated by Laurent monomials. Moreover, for a lattice cone σ , the ring $R_{\sigma} = \{f \in \mathbf{C}[z, z^{-1}] : \text{supp}(f) \subset \sigma\}$ is a finitely generated monomial algebra, where the support of a Laurent polynomial $f = \sum \lambda_i z^i$ is defined by $\text{supp}(f) = \{i \in \mathbf{Z}^n : \lambda_i \neq 0\}$. Now, for a lattice cone σ we can define an affine toric variety to be the maximal spectrum $\mathbf{X}_{\sigma} = \text{Spec} R_{\sigma}$. A toric variety \mathbf{X}_{Σ} associated to a fan Σ is the result of gluing affine varieties $\mathbf{X}_{\sigma} = \text{Spec} R_{\sigma}$ for all $\sigma \in \Sigma$ by identifying \mathbf{X}_{σ} with the corresponding Zariski open subset in $\mathbf{X}_{\sigma'}$ if σ is a face of σ' . That is, first we take the disjoint union of all affine toric varieties \mathbf{X}_{σ} corresponding to the cones of Σ . Then by gluing all these affine toric varieties together we get \mathbf{X}_{Σ} . A affine toric variety \mathbf{X}_{σ} is non-singular if and only if the normal polytope has a unit volume.

IV. CONIFOLD AND RESOLUTION OF TORIC SINGULARITY FOR TWO-QUBITS

In this section we study the simplicial decomposition of affine toric variety. For two qubits this simplicial decomposition coincides with desingularizing a conifold [8]. We also show that resolved conifold is space of an entangled two-qubit state. For a pairs of qubits $|\Psi\rangle = \sum_{x_2=0}^1 \sum_{x_1=0}^1 \alpha_{x_2 x_1} |x_2 x_1\rangle$ we can also construct following simplex. For this two qubit state the separable state is given by the Segre embedding of $\mathbf{CP}^1 \times \mathbf{CP}^1 = \{((\alpha_0^1, \alpha_1^1), (\alpha_0^2, \alpha_1^2)) : (\alpha_0^1, \alpha_1^1) \neq 0, (\alpha_0^2, \alpha_1^2) \neq 0\}$. Let $z_1 = \alpha_1^1 (\alpha_0^1)^{-1}$ and $z_2 = \alpha_1^2 (\alpha_0^2)^{-1}$. Then we can cover $\mathbf{CP}^1 \times \mathbf{CP}^1$ by four charts

$$\mathbf{X}_{\Delta_1} = \{(z_1, z_2)\}, \quad \mathbf{X}_{\Delta_2} = \{(z_1^{-1}, z_2)\}, \quad (14)$$

$$\mathbf{X}_{\Delta_3} = \{(z_1, z_2^{-1})\}, \quad \mathbf{X}_{\Delta_4} = \{(z_1^{-1}, z_2^{-1})\}, \quad (15)$$

The fan Σ for $\mathbf{CP}^1 \times \mathbf{CP}^1$ has edges spanned by $(1, 0), (0, 1), (-1, 0), (0, -1)$. Next we observe that the space $\mathbf{CP}^1 \times \mathbf{CP}^1$ and the conifold have the same toric variety. If we split the conifold into a fan which has two cones as shown in Figure 3. Then this process converts the conifold into a resolved conifold. The cones are three dimensional and the dual cones are two copies of \mathbf{C}^3 . The procedure of replacing an isolated singularity by a holomorphic cycle is called a resolution of the singularity. We can also remove the singularity by deformation. The process of deformation modifies the complex structure manifolds or algebraic varieties. Based on our discussion of conifold we know that this space is defined by $\alpha_{00}\alpha_{11} - \alpha_{01}\alpha_{10}$. Now, if we rewrite this equation in the following form

$$\alpha_{00}\alpha_{11} - \Gamma\alpha_{01}\alpha_{10} + \Lambda\alpha_{10} = 0, \quad (16)$$

then the constant Γ and Λ can be absorbed in new definition of α_{10} such as $\alpha'_{10} = \Gamma\alpha_{10} - \Lambda$. Next let T_n be the group of translations. Then an affine variety over complex field of dimension n can be transformed using the following action $GL(n, \mathbf{C}) \times T_n$. For a generic polynomial of degree two we have 15 possible parameters, but most of them can be removed with the action of $GL(4, \mathbf{C}) \times T_4$. However, we cannot remove the constant term with such transformation and we end up with the following variety

$$\alpha_{00}\alpha_{11} - \alpha_{01}\alpha_{10} = \Omega. \quad (17)$$

which is called deformed conifold. This space is now non-singular, but it is not a toric variety since the deformation break one action of torus. Thus we also could proposed that the deformed conifold is the space of an entangled pure two-qubit state. Moreover, if we take the absolute value of this equation that is $|\Omega|$, then this value is proportional to concurrence which is a measure of entanglement for a pure two-qubit state, that is

$$|\alpha_{00}\alpha_{11} - \alpha_{01}\alpha_{10}| = |\Omega| = C(\Psi)/2. \quad (18)$$

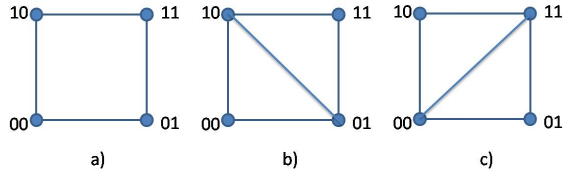


Figure 3. Two-qubit system. a) toric polytope of a two-qubit systems. b) and c) two ways of removing the singularity of conifold.

In general let X be an algebraic variety, then the space of all complex deformations of X is called the complex moduli space of X .

V. THREE-QUBIT STATES

Next, we will discuss a three-qubit state $|\Psi\rangle = \sum_{x_3, x_2, x_1=0}^1 \alpha_{x_3 x_2 x_1} |x_3 x_2 x_1\rangle$. For this state the separable state is given by the Segre embedding of $\mathbf{CP}^1 \times \mathbf{CP}^1 \times \mathbf{CP}^1 = \{((\alpha_0^1, \alpha_1^1), (\alpha_0^2, \alpha_1^2), (\alpha_0^3, \alpha_1^3)) : (\alpha_0^1, \alpha_1^1) \neq 0, (\alpha_0^2, \alpha_1^2) \neq 0, (\alpha_0^3, \alpha_1^3) \neq 0\}$. Now, for example, let $z_1 = \alpha_1^1/\alpha_0^1$, $z_2 = \alpha_1^2/\alpha_0^2$, and $z_3 = \alpha_1^3/\alpha_0^3$. Then we can cover $\mathbf{CP}^1 \times \mathbf{CP}^1 \times \mathbf{CP}^1$ by eight charts

$$\begin{aligned} \mathbf{X}_{\Delta_1} &= \{(z_1, z_2, z_3)\}, & \mathbf{X}_{\Delta_2} &= \{(z_1^{-1}, z_2, z_3)\}, \\ \mathbf{X}_{\Delta_3} &= \{(z_1, z_2^{-1}, z_3)\}, & \mathbf{X}_{\Delta_4} &= \{(z_1, z_2, z_3^{-1})\}, \\ \mathbf{X}_{\Delta_5} &= \{(z_1^{-1}, z_2^{-1}, z_3)\}, & \mathbf{X}_{\Delta_6} &= \{(z_1^{-1}, z_2, z_3^{-1})\}, \\ \mathbf{X}_{\Delta_7} &= \{(z_1, z_2^{-1}, z_3^{-1})\}, & \mathbf{X}_{\Delta_8} &= \{(z_1^{-1}, z_2^{-1}, z_3^{-1})\}, \end{aligned}$$

The fan Σ for $\mathbf{CP}^1 \times \mathbf{CP}^1 \times \mathbf{CP}^1$ has edges spanned by $(\pm 1, \pm 1, \pm 1)$. Now, let $S = \mathbf{Z}^3$ and consider the polytope Δ centered at the origin with vertices $(\pm 1, \pm 1, \pm 1)$. This gives the toric variety $\mathbf{X}_\Delta = \text{SpecC}[S_\Delta]$. To describe the fan of \mathbf{X}_Δ , we observe that the polar Δ° is the octahedron with vertices $\pm e_1, \pm e_2, \pm e_3$. Thus the normal fan is formed from the faces of the octahedron which gives a fan Σ whose 3-dimensional cones are octants of \mathbf{R}^3 . Thus this shows that the toric variety $\mathbf{X}_\Sigma = \mathbf{CP}^1 \times \mathbf{CP}^1 \times \mathbf{CP}^1$.

In this case we split the faces of 3-cube $E_{2,3} = 2^{3-2} \frac{3(3-1)}{2} = 6$ into two cones see Figure 4. Then, this process converts the 3-cube into a nonsingular space which is not anymore toric variety. Following the same procedure, we can also remove all singularities of toric variety of three-qubits by deformation. Based on our discussion of conifold we can write six equations describing the faces of 3-cube. Here we will analyze one face of this 3-cube, namely

$$\alpha_{000}\alpha_{011} - \alpha_{001}\alpha_{010} = \alpha_0 \otimes (\alpha_{00}\alpha_{11} - \alpha_{01}\alpha_{10})$$

Now, if we rewrite these equations e.g., in the following form

$$\alpha_0(\alpha_{00}\alpha_{11} - \Gamma\alpha_{01}\alpha_{10} + \Lambda\alpha_{10}) = 0, \quad (19)$$

then the constant Γ and Λ can be absorbed in new definition of α_{10} such as $\alpha'_{10} = \Gamma\alpha_{10} - \Lambda$. At the end e.g., we have the following variety

$$\alpha_{000}\alpha_{011} - \alpha_{001}\alpha_{010} = \Omega \quad (20)$$

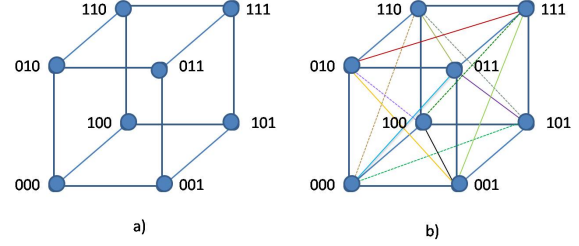


Figure 4. Three-qubit systems. a) toric polytope of a separable three-qubit systems. b) resolved space of entangled state, where each diagonal line is equivalent to the resolution of singularity of a conifold.

which is equivalent to the deformed conifold. If we do this procedure for all faces of the 3-cube, then the whole space becomes non-singular, but it is not a toric variety anymore. Thus we also could proposed that the deformed conifold is the space of an entangled pure three-qubit state. There are other relations between toric variety and measures of quantum entanglement that can be seen from the toric structures of multipartite systems. For example three-angle or 3-hyperdeterminant can be constructed from the toric variety.

VI. MULTI-QUBIT STATES

Next, we will discuss a multi-qubit state $|\Psi\rangle$ defined by equation (1). For this state the separable state is given by the Segre embedding of $\mathbf{CP}^1 \times \mathbf{CP}^1 \times \dots \times \mathbf{CP}^1 = \{((\alpha_0^1, \alpha_1^1), (\alpha_0^2, \alpha_1^2), \dots, (\alpha_0^m, \alpha_1^m)) : (\alpha_0^1, \alpha_1^1) \neq 0, (\alpha_0^2, \alpha_1^2) \neq 0, \dots, (\alpha_0^m, \alpha_1^m) \neq 0\}$. Now, for example, let $z_1 = \alpha_1^1/\alpha_0^1, z_2 = \alpha_1^2/\alpha_0^2, \dots, z_m = \alpha_1^m/\alpha_0^m$. Then we can cover $\mathbf{CP}^1 \times \mathbf{CP}^1 \times \dots \times \mathbf{CP}^1$ by 2^m charts

$$\begin{aligned} \mathbf{X}_{\Delta_1} &= \{(z_1, z_2, \dots, z_m)\}, \\ \mathbf{X}_{\Delta_2} &= \{(z_1^{-1}, z_2, \dots, z_m)\}, \\ &\vdots \\ \mathbf{X}_{\Delta_{2^{m-1}}} &= \{(z_1, z_2^{-1}, \dots, z_m^{-1})\}, \\ \mathbf{X}_{\Delta_{2^m}} &= \{(z_1^{-1}, z_2^{-1}, \dots, z_m^{-1})\} \end{aligned}$$

The fan Σ for $\mathbf{CP}^1 \times \mathbf{CP}^1 \times \dots \times \mathbf{CP}^1$ has edges spanned by $(\pm 1, \pm 1, \dots, \pm 1)$. Now, let $S = \mathbf{Z}^m$ and consider the polytope Δ centered at the origin with vertices $(\pm 1, \pm 1, \dots, \pm 1)$. This gives the toric variety $\mathbf{X}_\Delta = \text{SpecC}[S_\Delta]$. To describe the fan of \mathbf{X}_Δ , we observe that the polar Δ° is the octahedron with vertices $\pm e_1, \pm e_2, \dots, \pm e_m$. Thus this shows that the toric variety $\mathbf{X}_\Sigma = \mathbf{CP}^1 \times \mathbf{CP}^1 \times \dots \times \mathbf{CP}^1$. In this case we split the faces of m -cube

$$E_{2,m} = 2^{m-2} \frac{m(m-1)}{2} \quad (21)$$

into two cones. Then this process converts the m -cube into a nonsingular space which is not anymore toric variety.

Following the same procedure, we can also remove all singularities of toric variety of a multi-qubit state by deformation. Based on our discussion of conifold we can write six equations describing the faces of m -cube. For example for one face (2-cube) of this m -cube, we have

$$\alpha_{00\dots 0}\alpha_{0\dots 011} - \alpha_{0\dots 01}\alpha_{0\dots 010} = \Omega \quad (22)$$

which is equivalent to the deformed conifold, since e.g., we could have $|\Psi\rangle = \frac{1}{\sqrt{2}}(|00\dots 000\rangle + |00\dots 011\rangle) = \frac{1}{\sqrt{2}}|00\dots 0\rangle \otimes (|00\rangle + |11\rangle)$. If we do this procedure for all faces of the m -cube, then the whole space becomes non-singular, but it is not a toric variety anymore. Thus we also could propose that this space is the space of an entangled pure multi-qubit state.

VII. CONCLUSION

In this paper we have investigated the geometrical and combinatorial structures of entangled multipartite systems. We have shown that by removing singularity of conifold or by deforming the conifold we obtain the space of a pure entangled two-qubit state. We have also generalized our construction into multipartite entangled systems. The space of multipartite systems are difficult to visualize but the transformation from complex spaces to the combinatorial one makes this task much easier to realize. Hence our results give new insight about multipartite systems and also a new way of representing quantum entangled bipartite and multipartite systems with many possible applications in the field quantum computing. For example we could visualize action of holonomic quantum gates entangler on multi-qubit states based on these combinatorial structures. However, these issues need further investigations.

ACKNOWLEDGMENT

The work was supported by the Swedish Research Council (VR).

REFERENCES

- [1] P. Griffiths and J. Harris, *Principle of algebraic geometry*, Wiley and Sons, New York, 1978.
- [2] G. Ewald, *Combinatorial Convexity and Algebraic Geometry*, Springer, (1996).
- [3] I. M. Gelfand, M. M. Kapranov, and A.V. Zelevinsky, *Discriminants, resultants, and multidimensional determinants*, Birkhuser, Boston, (1994),
- [4] W. Fulton, *Introduction to Toric Varieties*, (1991).
- [5] A. Khrennikov, *Europhysics Lett.* **90**, 40004, 6pp (2010).
- [6] A. Khrennikov, *J. of Russian Laser Research*, **31**, (2), pp. 191-200 (2010).
- [7] H. Heydari and G. Björk, *J. Phys. A: Math. Gen.* **38**, pp. 3203-3211 (2005).

- [8] C. Closset, lectures given at the Modave Summer School in Mathematical Physics 2008, e-print 0901.3695v2.
- [9] I. R. Klebanov, and E. Witten, . I. R. Klebanov and E. Witten, *Nucl. Phys. B* 536, 199 (1998), e-print hep-th/9807080.
- [10] D. R. Morrison and M. R. Plesser , e-print hep-th/9810201.
- [11] H. Heydari, *Quantum Information and Computation* 6, pp. 400-409 (2006).
- [12] P. Candelas and X. C. de la Ossa, *Nucl. Phys. B* 342, 246. Volume 342, Issue 1, pp. 246-268 (1990).

Reduced Hamiltonian Technique for Gate Design in Strongly Coupled Quantum Systems

Preethika Kumar, Steven R. Skinner and, Sahar Daraeizadeh

Department of Electrical Engineering and Computer Science

Wichita State University

Wichita, USA

preethika.kumar@wichita.edu, steven.skinner@wichita.edu, sxdaraeizadeh@wichita.edu

Abstract—We introduce a new reduced-Hamiltonian scheme for realizing universal quantum computing in strongly coupled multi-qubit systems. This technique provides analytic solutions to the time evolution of the system, so that experimentalists can easily choose system parameters to realize desired quantum gates. We show how to implement arbitrary controlled-unitary operations in a one-dimensional nearest-neighbor architecture by deriving system parameters to achieve these operations. The key feature of the scheme is that all gate operations are realized by varying only a single control parameter, which greatly reduces the circuit complexity. Furthermore, we do not require the ability to tune couplings during a computation. We also show how the scheme can be extended to realize a controlled-unitary operation, involving N control qubits and one target qubit, in a single pulse.

Keywords—quantum; nearest-neighbor; gates; controlled-unitary; coupling; Hamiltonian

I. INTRODUCTION

A quantum computer comprises several qubits interacting with each other. Most schemes for implementing a quantum computer in different physical quantum systems are nearest-neighbor (NN), which comprise one- and two-dimensional arrays of qubits where each qubit interacts only with the qubits adjacent to it [1-26]. In these systems, when performing single- and multi-qubit gate operations, if the interactions are not turned off, the evolution of the qubit on which the gate operation is performed is affected by the other qubits it is coupled to. As a result, a number of methods for isolating a qubit from its neighbors, by shutting off the coupling, have been devised in various quantum systems [12-19, 27-34]. For instance, in phosphorus doped silicon systems, a method is employed of applying voltage biases to surface control electrodes, in order to vary the exchange coupling between neighboring donor atoms [27]. In GaAs/AlGaAs electron spin quantum dots, the strength of the exchange interaction, which depends on the overlap of the respective electron wavefunctions, is varied by changing the voltage applied to the gate controlling the tunnel barrier between the two dots [17]. In charge qubits, nearest neighbors are coupled via loop-shaped electrodes with Josephson junctions (JJs) at the loop intersections, where the bias currents through the coupling JJs serve as interaction control knobs [19]. In coupled quantum dot molecules, the coupling is switched off by grounding metal film electrodes between two qubits which turns off the Coulomb interaction between qubits [26]. While all these

methods of switching couplings facilitate multi-qubit operations, there are disadvantages in using tunable coupling. The ability to switch couplings usually involves performing fast changes in the qubit parameters or using additional circuit elements, both of which increase the complexity of the experimental set-up and open the system to noise.

A desirable alternative to the ability to switch couplings is to devise methods for performing computations with always-on interactions, wherein the ability to tune couplings is no longer required. To this end, a number of schemes have been proposed [33-41]. In [35], Zhou *et al.* devised a two-dimensional architectural scheme for universal and scalable quantum computation where the coupling between encoded qubits are effectively turned on and off by computing in and out of carefully designed interaction free subspaces analogous to decoherence free subspaces. In [36], Benjamin *et al.* showed how to perform computations along a one-dimensional array by tuning the Zeeman transition energies of individual qubits. Recently, schemes employing global control have been proposed [37, 38] and implemented in optical systems [39] and antiferromagnetic spin rings [40]. While each of these methods allows us to perform computations without having to switch couplings, each method has its own disadvantages. From a practical standpoint, the scheme in [35] is complex in terms of the two-dimensional physical arrangement of qubits, initialization, and the steps involved in generating gates. The scheme in [36] requires placing intervening qubits in definite classical states in order to negate the residual Ising interaction, thereby increasing the computational overhead. The scheme in [37], which uses translation-invariant operations to perform universal quantum computations, has a constant spatial and linear temporal overhead.

In this paper, we present a new reduced-Hamiltonian scheme for implementing universal quantum computing in strongly coupled systems. The technique works in both NN and non-NN architectures, and without having to shut off the coupling between qubits. In systems with switchable interactions, the couplings can be tuned to desired values at the start of a computation. These couplings, once set, will not be varied during the computation. The main advantage of our scheme is that it is simple and efficient, because only a single control parameter is pulsed high for all gate operations. The number of pulses for a gate operation varies depending on the number of qubits involved in the gate operation. For instance, in a one-dimensional Linear NN (LNN) array, a three-qubit Toffoli gate requires one pulse, a two-qubit CNOT gate

requires two pulses, and a single qubit gate requires four pulses. In this work, we first describe how to implement gate operations in a one-dimensional LNN architecture. We include the effects of finite rise and fall times due to non-ideal pulses on gate operations. Next, we extend the scheme to show how a controlled-unitary operation with multiple controls and a single target qubit can be realized in a single pulse. Unlike previous schemes [35, 36], our method does not require encoding physical qubits into logical qubits. Neither does it require separating qubit-bearing spins by passive “barrier” spins [37], thereby, significantly minimizing the computational overhead.

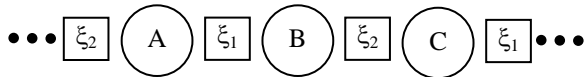


Figure 1. Linear nearest-neighbor array of qubits where each qubit is only coupled to the two qubits adjacent to it. Here, the circles represent individual qubits and the squares represent the couplings between qubits. There are two coupling constants, ξ_1 and ξ_2 , which alternate along the length of the chain.

The paper is organized as follows. In Section II, we describe how to implement gate operations in an LNN architecture. We show how to reduce the Hamiltonian of a three-qubit system, and then calculate parameters to implement gate operations. We assume a diagonal-type Ising interaction between qubits and then extend the scheme to Heisenberg interactions. In Section III, we present the conclusions.

II. GATE OPERATIONS IN LNN ARCHITECTURES

Figure 1 shows an LNN architecture, where each qubit is represented as a circle, and the couplings between qubits are represented by squares. Each qubit is coupled to every qubit through an Ising-type interaction, which is diagonal in the interaction basis. Such an Ising type coupling between qubits is commonly seen in proposals for superconducting Josephson junction qubits [34, 35], and also arises as one limit of dipole-dipole or J-coupling systems [34, 36]. In our design, we assume only two coupling constants, ξ_1 and ξ_2 , which alternate along the length of the architecture. The design can be implemented in systems with and without tunable couplings. For instance, in charge qubits with fixed couplings [42], the coupling capacitances between adjacent boxes can be fabricated to alternate along a line of qubits. If the coupling is tunable, as in [19] where nearest-neighbor charge qubits are coupled through loop-shaped electrodes with JJs at the loop intersections, the bias currents through alternate JJs can be fixed such that they alternate along the length of the chain. These currents, once set, will not be varied during the computation.

Consider only three adjacent qubits along the line – qubits A, B and C in Fig. 1. The Hamiltonian describing the evolution of this system is an 8×8 matrix:

$$\mathbf{H} = \sum_{i=A,B,C} \left(\Delta \sigma_{x_i} + k \sigma_{y_i} + \varepsilon_i \sigma_{z_i} \right) + \xi_1 \sigma_{z_A} \sigma_{z_B} + \xi_2 \sigma_{z_B} \sigma_{z_C} \quad (1)$$

Here, ε_i is the bias acting on individual qubits, which will be the control parameter in our system. We assume the qubits to be identical in design, in that the tunneling parameters (Δ and k) are identical. The bias parameter controls the tendency of the qubit to remain in its state. The tunneling parameter controls the tendency of the qubit to switch between the two basis states. We will also choose the magnitude of the coupling to be much larger than the tunneling, i.e., $\xi_1 \gg \Delta$ (or k) and $\xi_2 \gg \Delta$. Two different values of the coupling are required, so that qubit B can distinguish between qubits A and C.

Suppose that, initially, the bias equal zero for all qubits. Next, the bias on qubit, B, is raised to some value of ε_B . As a result, Eq. (1) becomes:

$$\mathbf{H} = \Delta \left(\sigma_{x_A} + \sigma_{x_B} + \sigma_{x_C} \right) + k \left(\sigma_{y_A} + \sigma_{y_B} + \sigma_{y_C} \right) + \varepsilon_B \sigma_{z_B} + \xi_1 \sigma_{z_A} \sigma_{z_B} + \xi_2 \sigma_{z_B} \sigma_{z_C} \quad (2)$$

Since $\xi_1 \gg \Delta$ and $\xi_2 \gg \Delta$, the expectation values of the σ_{z_A} and σ_{z_C} operators are either +1 or -1, depending on whether qubits A and C are in the $|0\rangle$ or $|1\rangle$ states, respectively. Therefore, we can write four 2×2 reduced Hamiltonians for qubit B in the subspaces where qubits A and C are in the $|00\rangle$, $|01\rangle$, $|10\rangle$ and $|11\rangle$ states, respectively:

$$\mathbf{H}_B^{(00)} = \Delta \sigma_X + k \sigma_Y + (\varepsilon_B + \xi_1 + \xi_2) \sigma_Z, \quad (3)$$

$$\mathbf{H}_B^{(01)} = \Delta \sigma_X + k \sigma_Y + (\varepsilon_B + \xi_1 - \xi_2) \sigma_Z, \quad (4)$$

$$\mathbf{H}_B^{(10)} = \Delta \sigma_X + k \sigma_Y + (\varepsilon_B - \xi_1 + \xi_2) \sigma_Z, \quad (5)$$

$$\mathbf{H}_B^{(11)} = \Delta \sigma_X + k \sigma_Y + (\varepsilon_B - \xi_1 - \xi_2) \sigma_Z. \quad (6)$$

Observe that if $\varepsilon_B \ll \xi_1$ (ξ_2), qubit B undergoes Z rotations in each subspace. However, since the couplings directly add to or subtract from the parameter ε_B in each subspace, ε_B can be so chosen as to cancel or minimize the effects of the large coupling. As a result, unitary gate operations other than Z rotations can be realized. We will use this principle to realize different controlled-unitary and single-qubit operations in the system of 3 qubits.

A controlled-unitary operation, $C^N(\mathbf{U})$, comprises N control qubits and one target qubit [43]. The desired unitary operation, \mathbf{U} , is performed on the target qubit when the control qubits are in a given state, usually when all the controls are in the $|1\rangle$ state. Suppose we want to perform a controlled-unitary operation, $C^2(\mathbf{U})$, on qubits A, B and C, with qubits A and C as controls and qubit B as the target. A general single-qubit unitary operation can be written as:

$$\mathbf{U} = \begin{pmatrix} \exp\left(-i\left(\frac{\beta+\delta}{2}\right)\right)\cos\left(\frac{\gamma}{2}\right) & -\exp\left(-i\left(\frac{\beta-\delta}{2}\right)\right)\sin\left(\frac{\gamma}{2}\right) \\ \exp\left(+i\left(\frac{\beta-\delta}{2}\right)\right)\sin\left(\frac{\gamma}{2}\right) & \exp\left(+i\left(\frac{\beta+\delta}{2}\right)\right)\cos\left(\frac{\gamma}{2}\right) \end{pmatrix}, \quad (7)$$

where \mathbf{U} is a 2×2 unitary matrix belonging to $\mathbf{SU}(2)$ [43], which is the set of 2×2 unitary matrices with unit determinant. The values of β , δ and γ can be chosen to realize the desired unitary transformation. Suppose we desire that only in the subspace where the control qubits are in the $|11\rangle$ state, the unitary operation given by Eq. (7) be performed on the target qubit B. This implies that the unitary matrices generated by each of the Hamiltonians given by Eqs. (3) through (5) be 2×2 identity matrices. Likewise, the unitary matrix generated by the Hamiltonian given by Eq. (6) must be \mathbf{U} . Since ξ_1 (ξ_2) $\gg \Delta$, we require that $(\varepsilon_B - \xi_1 - \xi_2)$ be of the order of Δ , i.e.,

$$\varepsilon_B - \xi_1 - \xi_2 = m\Delta, \quad (8)$$

where $0 \leq m \leq 1$. Note that $m \gg 1$ will correspond to the condition $\varepsilon_B \gg \Delta$, in which case, the target undergoes Z rotations. Using Eq. (8) in Eqs. (3) through (6), we have,

$$\begin{aligned} \mathbf{H}_B^{(00)} &= \Delta\sigma_x + k\sigma_y + (m\Delta + 2(\xi_1 + \xi_2))\sigma_z, \\ &\approx 2(\xi_1 + \xi_2)\sigma_z \end{aligned} \quad (9)$$

$$\mathbf{H}_B^{(01)} = \Delta\sigma_x + k\sigma_y + (m\Delta + 2\xi_1)\sigma_z \approx 2\xi_1\sigma_z, \quad (10)$$

$$\mathbf{H}_B^{(10)} = \Delta\sigma_x + k\sigma_y + (m\Delta + 2\xi_2)\sigma_z \approx 2\xi_2\sigma_z, \quad (11)$$

$$\mathbf{H}_B^{(11)} = \Delta\sigma_x + k\sigma_y + m\Delta\sigma_z. \quad (12)$$

We can see that under the first three Hamiltonians, Eqs. (9) through (11), target qubit B undergoes Z rotations. However, the values of ξ_1 and ξ_2 can be so chosen that within the time step of the gate operation, the Z rotations correspond to integer multiples of 2π , wherein the unitary matrices generated are identity operations. Integrating the Hamiltonian given by Eq. (12), we obtain the following unitary matrix:

$$\begin{pmatrix} \cos(2\pi ft) - i\frac{m\Delta}{f}\sin(2\pi ft) & \frac{k-i\Delta}{f}\sin(2\pi ft) \\ \frac{-k-i\Delta}{f}\sin(2\pi ft) & \cos(2\pi ft) + i\frac{m\Delta}{f}\sin(2\pi ft) \end{pmatrix}, \quad (13)$$

$$f = \sqrt{\Delta^2 + k^2 + m^2\Delta^2}. \quad (14)$$

Here, we have normalized Planck's constant to 1. Equating Eqs. (7) and (13), and simplifying terms, we obtain the following conditions to realize the unitary operation:

$$m = -\frac{\sin\left(\frac{\beta+\delta}{2}\right)\cos\left(\frac{\gamma}{2}\right)}{\sin\left(\frac{\gamma}{2}\right)\sin\left(\frac{\beta-\delta}{2}\right)}, \quad (15)$$

$$k \sin\left(\frac{\beta-\delta}{2}\right) = -\Delta \cos\left(\frac{\beta-\delta}{2}\right), \quad (16)$$

$$\sqrt{(\Delta^2 + k^2 + m^2\Delta^2)} = \frac{\cos^{-1}\left(\cos\left(\frac{\beta+\delta}{2}\right)\cos\left(\frac{\gamma}{2}\right)\right)}{2\pi T}. \quad (17)$$

Here, T is the time step within which the desired unitary operation is to be realized. Given the values of β , δ , and γ , Eqs. (15) through (17) can now be solved to find the parameters to realize different unitary gate operations. All parameters except ε_B , will be treated as fixed constants of the system, while implementing a gate operation. Figure 2 shows the bias that will be applied on the target qubit, B, for a time step T, during which the gate operation is realized. The magnitude of the bias will be " $\xi_1 + \xi_2 + m\Delta$ " as given by Eq. (8).

As an example, suppose we wish to realize a Toffoli gate, $C^2(\mathbf{X})$, in which case the \mathbf{U} matrix given by Eq. (7) is the **NOT** gate (denoted by \mathbf{X}), where

$$\mathbf{X} = \begin{bmatrix} 0 & 1 \\ 1 & 0 \end{bmatrix}. \quad (18)$$

One set of values for the angles β , δ , and γ are π , 0 and π , respectively. From Eqs. (15) and (16), we have $m = 0$ and $k = 0$ (which is typical for Josephson-junction qubits. Note that for $\beta = \delta = 0$, and $\gamma = \pi$, we have $m = 0$ and $\Delta = 0$.) If we choose the time step, T, of the gate operation to be 10ns, then from Eq. (17), we find Δ to be 25MHz, which is a typical value for the tunneling parameter of SQUIDs [44]. Since ξ_1 (ξ_2) $\gg \Delta$, we choose ξ_1 and ξ_2 to be 400MHz and 200MHz, respectively. These values are arbitrarily chosen such that under each of the Hamiltonians given by Eqs. (9) through (11), qubit B undergoes Z rotations that are integer multiples of 2π within the time step, T. Under the Toffoli gate operation, the bias on qubit B is pulsed from zero to 600MHz (Eq. (8) with $m=0$) for 10ns. That is, in Fig. 2, the magnitude of the bias pulse is 600MHz and the time step is 10ns. Observe that the biases on qubits A and C remain zero throughout the operation, and need not be varied, which is an advantage. Numerical simulations of the 8×8 Hamiltonian verify this technique, with a maximum error of 0.93% in the output probability amplitudes. It is important to point that, since the reduced-Hamiltonian technique uses the approximation ξ_1 (ξ_2) $\gg \Delta$ in finding an analytic solution for calculating the system parameters,

stronger the coupling, greater is the fidelity of the gate operation. For instance, if ξ_1 and ξ_2 are 2GHz and 1GHz, respectively, the maximum error in the output probability amplitudes is 0.04%. However, in this case, the bias on target B will have to be raised to 3GHz.

Likewise, suppose we want to implement a controlled-controlled-Hadamard gate, $C^2(\mathbf{Had})$, where the Hadamard gate, \mathbf{Had} , is defined by the following matrix operation:

$$\mathbf{Had} = \frac{1}{\sqrt{2}} \begin{bmatrix} 1 & 1 \\ 1 & -1 \end{bmatrix}. \quad (19)$$

Since the tunneling is a fixed parameter of our system, we will use the same value of Δ and k as we previously derived for the Toffoli gate, i.e., $\Delta = 25\text{MHz}$, $k=0$. One set of values for β , δ and γ to realize a \mathbf{Had} gate are 2π , π and $\pi/2$, respectively. Note from Eq. (16) that these values of the angles satisfy the condition $k = 0$. Also, from Eq. (15), we have $m = 1$. Using Eq. (17), we calculate T to be 7.1ns. Therefore, to implement a $C^2(\mathbf{Had})$ gate, the bias on qubit B is pulsed from zero to 625MHz (Eq. (8) with $m=1$) for 7.1ns. That is, in Fig. 2, the magnitude of the bias on qubit B is 625MHz, and T is 7.1ns. Observe that for both gate operations we used the same value of the couplings, i.e., the couplings are fixed. This has the advantage that even in a system with tunable couplings, the values of the couplings need to be adjusted only at the start of a computation, which can greatly reduce the circuit complexity, and the number of computational steps.

In most quantum systems, gate operations themselves are not realized perfectly, due to the structure of the internal Hamiltonian. For instance, observing Eq. (13), an \mathbf{X} gate or \mathbf{Had} gate is realized with an overall global phase of $\pm \pi/2$ for $k=0$. As a result, the $|101\rangle$ and $|111\rangle$ states pick up relative phases of $\pm \pi/2$ with respect to the other basis states when implementing a Toffoli (or $C^2(\mathbf{Had})$) gate. To overcome these phases we require an additional coupling parameter, ξ , between qubits A and C. However, this additional “next-to-nearest-neighbor” coupling, if present, affects the gate operation itself, unless accounted for when applying the bias pulses on the target qubit. Details of the effects of next-to-nearest-neighbor couplings on gate operations have been presented elsewhere.

We will next show how to use our scheme to implement two-qubit controlled-unitary operations and single-qubit unitary operations. Two-qubit controlled-unitary operations, $C^1(\mathbf{U})$, can be realized by applying two pulses as shown in Fig. 3(a). Suppose we want to perform a $C^1(\mathbf{U})$ gate with qubit A as the control qubit and qubit B as the target qubit. Qubit C behaves as the “dummy” qubit in this case. The first pulse on target qubit B is a bias value of “ $\xi_1 + \xi_2 + m\Delta$ ” (Eq. (8)). For the second pulse, the bias on target qubit B is raised to a value of “ $\xi_1 - \xi_2 + m\Delta$ ”. This is because, in this case, we want qubit B to undergo a unitary operation (Eq. (7)) under the reduced Hamiltonian given by Eq. (5). Similarly, to realize a single qubit unitary operation, four pulses are applied. The values of the bias pulses on qubit B will be “ $-\xi_1 - \xi_2 + m\Delta$ ”, “ $-\xi_1 + \xi_2 + m\Delta$ ”, “ $\xi_1 - \xi_2 + m\Delta$ ”, and “ $\xi_1 + \xi_2 + m\Delta$ ”, respectively, for the four gate operations shown in Fig. 3(b). Observe that unlike some previous methods that use “isolation” qubits (qubits fixed in $|0\rangle$ and $|1\rangle$ states) to separate the qubits used in the gate operations

from their nearest neighbors, our scheme has no such requirement. This is a great advantage for two reasons – the same gate operation can be realized without using additional qubits, and swap gate operations are not required to bring together qubits separated by “isolation” qubits.

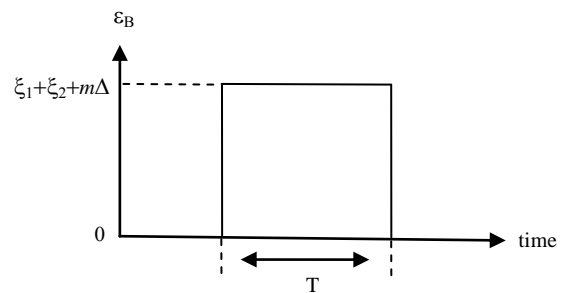


Figure 2. Bias pulse on the target qubit, B, during a $C^2(\mathbf{U})$ gate operation on a three-qubit system. The bias is raised from zero to a value “ $\xi_1 + \xi_2 + m\Delta$ ” as given by Eq. (8). The biases on control qubits, A and C, are kept zero throughout the gate operation.

As shown, the reduced-Hamiltonian technique presented here allows experimentalists the ability to choose system parameters to realize quantum gates, for ideal pulses. However, in real systems, pulses are not ideal. Given non-ideal characteristics, experimentalists can fine-tune control parameters through numerical simulation, as shown in [45] and [46]. For example, real pulses exhibit finite rise (T_R) and fall (T_F) times. Simulations carried out for the Toffoli gate under different values of T_R and T_F show that, under a non-ideal pulse, to increase the fidelity of a Toffoli gate, the pulse width has to be increased. For instance, when $\epsilon_B = 600\text{MHz}$, for $T_R = T_F = 1\text{ns}$, the pulse width becomes 10.4ns, instead of 10ns as originally calculated. In this case, the maximum error in the output probability amplitudes is 2.97%. If, however, $\epsilon_B = 3\text{GHz}$ (for $\xi_1=2\text{GHz}$; $\xi_2=1\text{GHz}$), for $T_R = T_F = 1\text{ns}$, the pulse width is 10.7ns, giving a maximum error of 0.54% in the output probability amplitudes. Even though the probability amplitudes can be improved by adjusting the pulse width, random relative phases occur between the basis states in the final state. These phases are hard to keep track of since they vary with the rise/fall times and the maximum amplitude of the bias pulse. However, in [47], we present an architectural layout of qubits that is immune to such relative phase errors.

While we have restricted our discussion to LNN architectures where the qubits are coupled via Ising interactions, the method presented here easily extends to systems coupled via Heisenberg interactions. Equation (20) shows a three-qubit system coupled via anisotropic interactions [48].

$$\mathbf{H} = \sum_{i=A,B,C} \left(\Delta \sigma_{x_i} + k \sigma_{y_i} + \epsilon_i \sigma_{z_i} \right) + \xi_1 \left(\sigma_{z_A} \sigma_{z_B} + \alpha \left(\sigma_{x_A} \sigma_{x_B} + \sigma_{y_A} \sigma_{y_B} \right) \right) + \xi_2 \left(\sigma_{z_B} \sigma_{z_C} + \alpha \left(\sigma_{x_B} \sigma_{x_C} + \sigma_{y_B} \sigma_{y_C} \right) \right) \quad (20)$$

If $\alpha \ll 1$, i.e., the off-diagonal $\sigma_X \sigma_X$ and $\sigma_Y \sigma_Y$ couplings are much smaller than the diagonal $\sigma_Z \sigma_Z$ couplings, the

interactions are pre-dominantly of the Ising type. Therefore, the same parameters that were used to realize a $C^2(\mathbf{U})$ operation in a system described by Eq. (5), can be used to realize the operation in a system described by Eq. (20). For instance, consider the Toffoli gate. The coupling parameters, ξ_1 and ξ_2 , are 400MHz and 200MHz, respectively. Simulation results showed that when α was 0.01, 0.05, and 0.1, the maximum error in the output probability amplitudes were 0.3%, 1.64%, and 11.36% respectively. The high error in the probability amplitude when α is 0.1 is because, the magnitudes of the $\sigma_X\sigma_X$ and $\sigma_Y\sigma_Y$ couplings are much larger than the tunneling parameter. As a result, the high off-diagonal couplings cause the control qubits to undergo unitary dynamics that are no longer simple Z rotations. In other words, the control qubits no longer remain in their states, but actually can change their state from $|0\rangle$ to $|1\rangle$, and vice versa, with a probability that depends on the value of α . Moreover, it was also found that by decreasing the pulse width of the gate operation, a higher accuracy can be obtained. For $\alpha = 0.1$, when T was reduced to 8.4ns, the maximum error in the output probability amplitudes was reduced to 4.9%. Next, for $\alpha = 0.05$, the off-diagonal couplings are almost equal to the tunneling, which results in a much lower error. Here again, by reducing T (9.2 ns), a much lower error in the output probability amplitudes can be obtained (0.6%). Finally, for $\alpha = 0.01$, the error is very low since the off-diagonal couplings are lower than the tunneling. Therefore, they have a negligible effect on the evolution of the system as a whole.

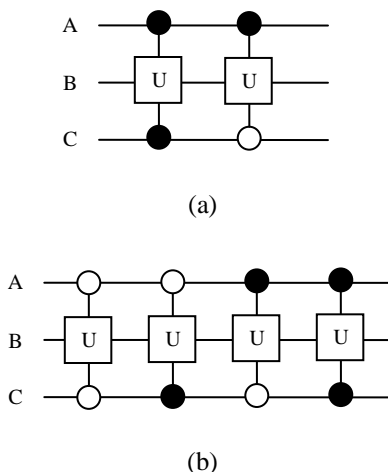


Figure 3. Methods for realizing a two-qubit controlled-unitary operation and a single-qubit unitary operation. (a) Qubit A is the control and qubit B is the target. Qubit C functions as a dummy qubit. The overall gate operation requires 2 pulses. (b) Qubit B is the qubit on which a unitary operation is to be performed. Qubits A and C are dummy qubits. The gate operation is realized in four pulses, each of which corresponds to a $C^2(\mathbf{U})$ gate operation.

In a previous reduced-Hamiltonian scheme for weakly coupled qubits [44], we showed how to implement two-qubit controlled-unitary operations, $C^1(\mathbf{U})$, without having to shut off coupling between qubits. This approach required that the bias on the control qubit be maintained at an arbitrarily large value throughout the gate operation, and the bias on the target qubit be pulsed low during the gate operation [44]. While the scheme

worked at achieving arbitrary $C^1(\mathbf{U})$ operations, it had two disadvantages. The first was that the high value of the bias on the control qubit during $C^1(\mathbf{U})$ operations caused the control qubit to precess at very fast rates. Therefore, slight mismatches in timing or in the bias parameter gave rise to large variations in the relative phases between the basis states. The second, and more important disadvantage, was that the scheme could not be generalized towards realizing controlled-unitary operations on a target qubit involving more than two control qubits, i.e., $C^N(\mathbf{U})$ with $N > 2$. In the scheme presented here, once the values of m , Δ , k and T are found by solving Eqs. (15) through (17), a $C^N(\mathbf{U})$ operation, for any value of $N \geq 1$, can be simply realized by raising the bias on the target qubit from zero to a value given by

$$\varepsilon = m\Delta + \sum_{i=1}^N \xi_i. \quad (21)$$

where ξ_i are the couplings between the target qubit and each of the N control qubits. No two couplings can have the same magnitude as the target qubit will not be able to distinguish between the different control qubits. Equation (21) shows that, as N varies, the values of m , Δ , k and T do not change for a desired unitary operation given by Eq. (11). Only the bias varies according to the number of coupling terms in Eq. (21). (Note that since $\xi_i \gg \Delta$, for $i = 1, \dots, N$, the values of ξ_i are chosen such that " $\xi_i T$ " is an integer multiple of 2π , so that an identity operation is realized on the target qubit when all the control qubits are not in the $|1\rangle$ state). Thus, the scheme can be easily extended to 2-dimensional layouts and to architectures where couplings are not restricted to nearest neighbors.

The scheme presented here has yet another advantage. Single qubit Z rotations can be easily realized by varying the biases on individual qubits. For instance, an $R_Z(\theta)$ gate, which is a Z rotation by angle θ , can be realized on qubit A (B or C), by raising the bias slightly on it to a value ε_A (ε_B or ε_C) such that $2\pi \varepsilon_A T = \theta$, where T is the time within which the rotation is realized. Since the scheme in [44] required high biases on all qubits during idle times, it was difficult to perform single qubit rotations, especially since qubits were precessing at very fast rates and relative phases were difficult to control. Moreover, the scheme presented here, where the couplings are larger and chosen so that within a 10ns interval no phases occur, the small magnitudes of the always-on couplings in [44] always generate additional phases, which are hard to keep track of through timing.

It is important to point out that while in this work we have assumed the qubits to be identical in design with no asymmetries in the architectural layout, relative phases can occur as a result of parameter mismatches, which might alter the results of a computation. The performance of gate operations in the presence of parameter mismatches and asymmetry in design is being considered as a future work.

III. CONCLUSIONS

In this paper, we have presented a new reduced-Hamiltonian scheme for implementing universal quantum computation in strongly coupled multi-qubit systems. The technique provides analytic solutions to the time evolution of

the system, so that system parameters can easily be solved for, to realize desired quantum gates. The scheme is general and can be extended towards any two-level system whose Hamiltonian can be reduced to that of a spin boson. We described how to implement gate operations in a one-dimensional NN architecture, where the effects of finite rise and fall times due to non-ideal pulses on gate operations were considered. The scheme was then extended to show how a controlled-unitary operation with N controls and a single target qubit can be realized in a single pulse. The main advantage of the scheme presented in this paper is that it is simple and efficient because only a single control parameter is required. Also, we do not require the ability to tune couplings during a computation. Moreover, unlike some other methods, neither does ours' require encoding physical qubits into logical qubits, nor does it require separating qubit-bearing spins by passive "barrier" spins, thereby, significantly minimizing the computational overhead.

ACKNOWLEDGMENT

This material is based upon work supported, in part, by the National Science Foundation under Award No. EPS-0903806 and matching support from the State of Kansas through Kansas Technology Enterprise Corporation.

REFERENCES

- [1] B. E. Kane, "A silicon-based nuclear spin quantum computer," *Nature London*, vol. 393, pp. 133-136, May 1998.
- [2] A. J. Skinner, M. E. Davenport and B. E. Kane, "Hydrogenic spin quantum computing in silicon: a digital approach," *Phys. Rev. Lett.*, vol. 90, pp. 087901-087904, February 2003.
- [3] L. C. L. Hollenberg, *et al.*, "Charge-based quantum computing using single donors in semiconductors," *Phys. Rev. B*, vol. 69, pp. 113301-113304, March 2004.
- [4] K. Yang, S. Zhu, and Z. Wang, "Universal quantum gates based on both geometric and dynamic phases on quantum dots," *Chinese Phys. Lett.*, vol. 20, pp. 991-994 (2003).
- [5] J. K. Pachos and P. L. Knight, "Quantum computation with a one-dimensional optical lattice," *Phys. Rev. Lett.*, vol. 91, pp. 107902-107905, September 2003.
- [6] M. Friesen, *et al.*, "Practical design and simulation of silicon-based quantum-dot qubits," *Phys. Rev. B*, vol. 67, pp. 121301-121304 (R), March 2003.
- [7] P. Solinas, P. Zanardi, N. Zanghi and F. Rossi, "Semiconductor-based geometric quantum gates," *Phys. Rev. B*, vol. 67, pp. 121307-121310 (R), March 2003.
- [8] J. H. Jefferson, M. Fearn and D. L. J. Tipton, "Two-electron quantum dots as scalable qubits," *Phys. Rev. A* 66, pp. 042328-042338, October 2002.
- [9] V. N. Golovach and D. Loss, "Electron spins in artificial atoms and molecules for quantum computing," *Semicond. Sci. Tech.*, vol. 17, pp. 355-366, March 2002.
- [10] T. D. Ladd, J. R. Goldman, F. Yamaguchi and Y. Yamamoto, "All-silicon quantum computer," *Phys. Rev. Lett.*, vol. 89, pp. 017901-017904, June 2002.
- [11] B. Golding and M. I. Dykman, "Acceptor-based silicon quantum computing," *cond-mat/0309147*, September 2003.
- [12] E. Novais and A. H. Castro Neto, "Nuclear spin qubits in a pseudospin quantum chain," *Phys. Rev. A*, vol. 69, pp. 062312-062317, June 2004.
- [13] R. Vrijen, *et al.*, "Electron-spin-resonance transistors for quantum computing in silicon-germanium heterostructures," *Phys. Rev. A*, vol. 62, pp. 012306-012315, June 2000.
- [14] L. Tian and P. Zoller, "Quantum computing with atomic Josephson-junction arrays," *Phys. Rev. A*, vol. 68, pp. 042321-042330, October 2003.
- [15] L. M. K. Vandersypen, *et al.* in *Quantum Computing and Quantum Bits in Mesoscopic Systems*, edited by A. J. Leggett, B. Ruggiero, and P. Silvestrini (Kluwer Academic/Plenum Publishers, New York, 2003).
- [16] V. V'yurkov and L. Y. Gorelik, "Charge based quantum computer without charge transfer," *Quant. Comput. and Comput.*, vol. 1, pp. 77-83, 2000.
- [17] N.-J. Wu, M. Kamada, A. Natori, and H. Yasunaga, "Quantum computer using coupled-quantum-dot molecules," *Jpn. J. Appl. Phys.* 39, pp. 4642-4646, 2000.
- [18] S. H. W. van der Ploeg *et al.*, "Controllable coupling of superconducting flux qubits," *Phys. Rev. Lett.*, vol. 98, pp. 057004-057007, February 2007.
- [19] J. Lantz, M. Wallquist, V. S. Shumeiko, and G. Wendin, "Josephson junction qubit network with current-controlled interaction," *Phys. Rev. B*, vol. 70, pp. 140507-140510 (R), October 2004.
- [20] R. Stock and D. F. V. James, "Scalable, high-speed measurement-based quantum computer using trapped ions," *Phys. Rev. Lett.*, vol. 102, pp. 170501-170504, April 2009.
- [21] D. Jaksch, "Optical lattices, ultracold atoms and quantum information processing," *Contemp. Phys.*, Vol 45, pp. 367-381, September 2004.
- [22] D. P. DiVincenzo, "Fault tolerant architectures for superconducting qubits," *Nobel Symposium on Qubits for Quantum Information*, arXiv:0905.4839 (2009).
- [23] R. Van Meter, T. D. Ladd, A. G. Fowler, and Y. Yamamoto, "Distributed quantum computation architecture using semiconductor nanophotonics," *Int. J. Quantum Inf.*, vol. 8, pp. 295-323, 2010.
- [24] N. C. Jones, *et al.*, "A layered architecture for quantum computing using quantum dots," arXiv:1010.5022, 2009.
- [25] A. G. Fowler, "Two-dimensional color-code quantum computing," *Phys. Rev. A*, vol. 83, pp. 042310-042317, April 2011.
- [26] D. M. Hugh, and J. Twamley, "Quantum computing using a trapped-ion spin molecule and microwave radiation," *Phys. Rev. A*, vol. 71, pp. 012315-012320, January 2005.
- [27] C. J. Wellard, L.C.L. Hollenberg, L.M. Kettle, and H-S Goan, "Voltage control of exchange coupling in phosphorus doped silicon," *J. Phys.: Condens. Matter* 16, No. 32, pp. 5697-5704, 2004.
- [28] E. A. Stinaff, *et al.*, "Optical signatures of coupled quantum dots," *Science*, vol. 311, pp. 636-639, January 2006.
- [29] S. Ashhab, and F. Neri, "Switchable coupling for superconducting qubits using double resonance in the presence of cross talk," *Phys. Rev. B*, vol. 76, pp. 132513-132516, October 2007.
- [30] A. O. Niskanen, *et al.*, "Quantum coherent tunable coupling of superconducting qubits," *Science*, vol. 316, pp. 723-726, March 2007.
- [31] D. P. DiVincenzo, G. Burkard, D. Loss, and E. V. Sukhorukov, in *Quantum Mesoscopic Phenomena and Mesoscopic Devices in Microelectronics*, edited by I.O. Kulik and R. Ellialtuglu (NATO ASI, Turkey, June 13-25, 1999); *cond-mat/99112445*.
- [32] D. P. DiVincenzo, D. Bacon, J. Kempe, G. Burkard, and K. B. Whaley, "Universal quantum computation with the exchange interaction," *Nature*, vol. 408, pp. 339-342, October 2000.
- [33] G. P. Berman, G. D. Doolen, and V. I. Tsifrinovich, "Solid-state quantum computation: a new direction for nanotechnology," *Superlattices and Microstructures*, vol. 27, pp. 89-104, February 2000.
- [34] G. P. Berman, G. D. Doolen, D. I. Kamenev, and V. I. Tsifrinovich, in: *Quantum Computation and Information*, *Complementary Mathematics* 305, 13, 2002.
- [35] X. Zhou, Z. Zhou, G. Guo and M. J. Feldman, "Quantum computation with untunable couplings," *Phys. Rev. Lett.*, vol. 89, pp. 197903-197906, October 2002.
- [36] S.C. Benjamin, and S. Bose, "Quantum computing with an always-on Heisenberg interaction," *Phys. Rev. Lett.*, vol. 90, pp. 247901-247904, June 2003.

- [37] R. Raussendorf, "Quantum computation via translation-invariant operations on a chain of qubits," *Phys. Rev. A*, vol. 72, pp. 052301-052306, November 2005.
- [38] J. Fitzsimons, and J. Twamley, "Globally controlled quantum wires for perfect qubit transport, mirroring, and computing," *Phys. Rev. Lett.*, vol. 97, pp. 090502-090505, September 2006.
- [39] B. W. Lovett, "Global optical control of a quantum spin chain," *New J. of Phys.*, vol. 8, p. 69, May 2006.
- [40] F. Troiani, M. Affronte, S. Carretta, P. Santini, and G. Amoretti, "Proposal for quantum gates in permanently coupled antiferromagnetic spin rings without need of local fields," *Phys. Rev. Lett.*, vol. 94, 190501-190504, May 2005.
- [41] G.F. Mkrtchian, "Universal quantum logic gates in a scalable Ising spin quantum computer," *Phys. Lett. A*, vol. 372, pp. 5270-5273, August 2008.
- [42] T. Yamamoto, Y.A. Pashkin, O. Astafiev, Y. Nakamura, and J.S. Tsai, "Demonstration of conditional gate operation using superconducting charge qubits," *Nature*, vol. 425, pp. 941-944, October 2003.
- [43] M. A. Nielsen and I. L. Chuang, *Quantum Computation and Quantum Information* (Cambridge University Press, Cambridge, England, 2001).
- [44] P. Kumar and S. R. Skinner, "Simplified approach to implementing controlled-unitary operations in a two-qubit system," *Phys. Rev A*, vol. 76, pp. 022335-022345, August 2007.
- [45] P. K. Gagnebin, *et al.*, "Quantum gates using a pulsed bias scheme," *Phys. Rev A*, vol. 72, pp. 042311-042319, October 2005.
- [46] P. Kumar and S. R. Skinner, "Universal quantum computing in linear nearest neighbor architectures," *Quant. Inf. and Comput.*, vol. 11, pp. 0300-0312, March 2011.
- [47] P. Kumar, S. R. Skinner, and S. Daeizadeh, "Nearest-neighbor architecture to overcome effects of qubit precessions in gate operations," *IEEE Congress on Evolutionary Computation*, June 2011, "in press".
- [48] J. Zhang and K. B. Whaley, "Generation of quantum logic operations from physical hamiltonians," *Phys. Rev. A*, vol. 71, pp. 052317-052329, May 2005.

Quantum Interaction Approach in Cognition, Artificial Intelligence and Robotics

Diederik Aerts, Sandro Sozzo
 Center Leo Apostel for Interdisciplinary Studies
 Vrije Universiteit Brussel
 Krijgskunderstraat 33, B-1160 Brussels, Belgium
 diraerts@vub.ac.be, ssozzo@vub.ac.be

Marek Czachor
 Department of Physics
 Politechnika Gdanska
 Narutowicza 11/12, 90-952 Gdansk, Poland
 mcachor@pg.gda.pl

Abstract—The mathematical formalism of quantum mechanics has been successfully employed in the last years to model situations in which the use of classical structures gives rise to problematical situations, and where typically quantum effects, such as *contextuality* and *entanglement*, have been recognized. This *Quantum Interaction Approach* is briefly reviewed in this paper focusing, in particular, on the quantum models that have been elaborated to describe how concepts combine in cognitive science, and on the ensuing identification of a quantum structure in human thought. We point out that these results provide interesting insights toward the development of a unified theory for meaning and knowledge formalization and representation. Then, we analyze the technological aspects and implications of our approach, and a particular attention is devoted to the connections with symbolic artificial intelligence, quantum computation and robotics.

Keywords-quantum mechanics; quantum cognition; artificial intelligence; robotics;

I. INTRODUCTION

The use of the mathematical formalism of quantum mechanics as a modeling instrument in disciplines different from physics is now a well established practice and has historically been motivated by different reasons. Firstly, this is due to the flexibility and richness of quantum structures (vector spaces, inner products, quantum probability, quantum logic connectives, etc.). Secondly, there are two aspects that are seemingly characteristic of quantum entities, i.e., *contextuality* and *entanglement*, and that appear instead independently of the microscopic nature of these entities. Thirdly, the fact that since the fifties and sixties several effects have been recognized in a variety of areas, such as, economics, biology, psychology ... in which the application of classical structures (set theory, classical logic, Kolmogorovian probability, etc.) is problematical and generates paradoxes. The Allais [1] and Ellsberg [2] paradoxes in economics, the conjunction fallacy [3] and disjunction effect [4] in decision theory, the representation of concepts and the formalization of meaning in cognitive science [5], are the most important examples of situations in which classical structures do not provide satisfactory results, but more general structures are needed. In particular, the impossibility of formalizing and structuring human and artificial knowledge slackened, notwithstanding the impressive technological success, in

the development of some applied research fields, such as artificial intelligence and robotics.

The above difficulties led scholars to look for alternative approaches. Quantum mechanics then provided a fresh conceptual framework to address these problems in a totally new light. Hence, a *Quantum Interaction Approach* was born as an interdisciplinary perspective in which the formalism of quantum mechanics was used to model specific situations in domains different from the microscopic world. In particular, the new emerging field of Quantum Interaction focusing on the application of quantum structures to cognition has been named *Quantum Cognition* [6]. It is interesting, in our opinion, to dwell upon the main results obtained by the scholars involved in this Quantum Interaction Approach. We stress, however, that the following presentation does not pretend to be either historically complete or exhaustive of the various subjects and approaches that have been put forward, but it just aims to provide an overall conceptual background for the approach on quantum cognition in which the authors of the present article and their collaborators are themselves intensively involved.

The first insights came from psychology. In 1994 one of the authors and his collaborators proved that classical probability cannot be used to study a class of psychological situations of decision processes, but a more general probabilistic framework is needed [7]. In 2002 a contextual formalism generalizing quantum mechanics was worked out to model concept combinations [8]. This *SCoP formalism* was successively improved and extended to provide a solution of the *Pet-Fish problem* [9], [10]. Since 2007 explicit quantum models in Hilbert and Fock spaces have been elaborated to describe experimental membership weights of concept disjunctions and conjunctions [11], [12], [13], [14], [15], [16]. These models were then applied to study the Ellsberg paradox, the conjunction fallacy and disjunction effect in decision theory [12], [14], [17], and a number of quantum effects, e.g., superposition, interference, entanglement, contextual emergence, have been recognized in these effects. This fact led the authors to put forward the hypothesis that human thought presents two intertwined modes, one modeled by classical logic and the other mostly modeled by quantum mechanics [14].

Concerning cognitive models of knowledge representation, it was shown that modern approaches to semantic analysis, if reformulated as Hilbert space problems, reveal quantum structures similar to those employed in concept representation. In 2004 two of the authors recognized quantum structures in latent semantic analysis and in distributed representations of cognitive structures developed for the purposes of neural networks [18].

Interesting ideas came from information retrieval. In 2003 Dominic Widdows proved that the use of quantum logic connective for negation, i.e., orthogonality, provided a more efficient algorithm than the corresponding Boolean ‘not’ of classical logic for exploring and analyzing word and meaning [19], [20], [21]. In 2004 Keith van Rijbergen claimed in his book that the Hilbert space formalism was more effective than an unstructured vector space to supply theoretical models in information retrieval [22]. Since then, several quantum effects have been recognized in information retrieval and natural language processing, e.g., superposition, uncertainty, entanglement [23].

In 2006, Peter Bruza and his collaborators applied quantum structures to model semantic spaces and cognitive structures. More specifically, they undertook studies on the formalization of context effects in relation to concepts [24], and investigated the role of quantum structures in language, i.e., the entanglement of words in human semantic space resulting from violations of Bell’s inequalities [25], [26].

In decision making important contributions were made by Jerome Busemeyer, Andrei Khrennikov and their collaborators. More specifically, in 2006 Busemeyer modeled the game theoretic variant of the disjunction effect on a quantum game theoretic model and used the Schrödinger equation to describe the dynamics of the decision process [27]. The proposed model is a part of a general operational approach of comparing classical stochastic models with quantum dynamic models, and deciding by comparison with experimental data which of them has most predictive power [28]. In 2008 Khrennikov presented a quantum model for decision making: he found an algorithm to represent probabilistic data by means of complex probability amplitudes, and used the algorithm to model the Prisoners Dilemma and the disjunction effect [29].

Quantum structures were hypothesized in the studies of holographic models of memory, which is an old research field in the psychology of memory. The metaphor which originally started this field is *holography*, that is, the observed fact that the human brain seems to have not really ‘places’ for different functions (*holonomic brain theory*) [30]. But, holography is a ‘wave effect related to electromagnetism’, as is well known from physics [31]. For this reason, some authors suggested that the results obtained in these holographic models of memory are due to an underlying quantum structure [32], [33], [34].

We will discuss the presence of quantum structures and

their role in cognition, knowledge representation and information retrieval in a forthcoming paper [35]. In the present paper we instead focus on the application of quantum structures to semantic analysis, artificial intelligence and robotics. More specifically, we summarize in Sec. II the main results that have been obtained by one of us in quantum cognition, including the hypothesis about the existence of a quantum layer in human mind. In Sec. III we instead explore how quantum structures can be successfully used to construct models in semantic analysis and symbolic artificial intelligence. Finally, in Sec. IV we investigate the links between our quantum cognition approach and quantum robotics, which is an emerging field that connects robot technology with quantum computation. We suggest, in particular, that macroscopic devices can be constructed which efficiently simulate quantum computers, thus avoiding the difficulties arising from the utilization of microscopic entities in quantum computation and robotics.

To conclude this section, we recall that the Quantum Interaction Group organizes each year an international conference on the Quantum Interaction Approach (see, e.g., [36], for the first three editions) in which physicists, mathematicians, philosophers, psychologists, computer scientists meet to present and discuss the new results obtained in applying quantum structures to social, cognitive, semantic processes. We finally stress that, by the locution ‘quantum structures’, we actually mean those structures which do not admit a classical representation, thus requiring either the entire quantum formalism or a generalization of it. A better locution would be ‘quantum-like structures’. We however prefer maintaining the former locution in this paper both because it is widespread in the literature and to emphasize the non-classical character of such structures.

II. QUANTUM STRUCTURE IN HUMAN THOUGHT

The proposal of using non-classical logical and probabilistic structures outside physics came primarily from an accurate analysis of the nature of the quantum mechanical probability model and of the difference between classical and quantum probabilities [37], [38], [39], [40], [41], [42]. This critical comparison led us to conclude that classical probabilistic structures formalize the subjective ignorance about what actually happens, hence they model only situations that admit an underlying deterministic process. However, it is well known that situations exist in quantum mechanics which are fundamentally indeterministic, in the sense that there is not necessarily an underlying deterministic process independent of the context. Whenever this reasoning is applied to decision processes, one can see that human decision models are quantum in essence, because opinions are not always determined. This result has been shown by one of us by working out a quantum model for the decision process in an opinion poll [7]. But, the domain where classical set-theoretical based structures most manifestly failed was

concept theory and, specifically, the study of ‘how concepts combine’. This failure was explicitly revealed by Hampton’s experiments [43], [44] which measured the deviation from classical set-theoretic membership weights of exemplars with respect to pairs of concepts and their conjunction or disjunction. Hampton’s investigation was motivated by the so-called *Guppy effect* in concept conjunction found by Osherson and Smith [5]. These authors considered the concepts *Pet* and *Fish* and their conjunction *Pet-Fish*, and observed that, while an exemplar such as *Guppy* was a very typical example of *Pet-Fish*, it was neither a very typical example of *Pet* nor of *Fish*. Therefore, the typicality of a specific exemplar with respect to the conjunction of concepts shows a classically unexpected behavior. Since the work of Osherson and Smith, the problem has been referred to as the *Pet-Fish problem* and the effect has been called the *Guppy effect*. It can be shown that fuzzy set based theories [45], [46], [47] cannot model this ‘typicality effect’. Hampton identified a Guppy-like effect for the membership weights of exemplars with respect to both the conjunction [43] and the disjunction [44] of pairs of concepts. Several experiments have been performed (see, e.g., [48]) and many approaches have been propounded to provide a satisfactory mathematical model of concept combinations, but none of them provides a satisfactory description or explanation of such effects. Trying to cope with these difficulties one of the authors has proposed, together with some co-workers, a *SCoP formalism* which is a generalization of the quantum formalism [8], [9], [10], [49]. In the SCoP formalism each concept is associated with well defined sets of states, contexts and properties. Concepts change continuously under the influence of a context and this change is described by a change of the state of the concept. For each exemplar of a concept, the typicality varies with respect to the context that influences it, which implies the presence of both a *contextual typicality* and an *applicability effect*. The *Pet-Fish problem* is solved in the SCoP formalism because in different combinations the concepts are in different states. In particular, in the combination *Pet-Fish* the concept *Pet* is in a state under the context *The Pet is a Fish*. The state of *Pet* under the context *The Pet is a Fish* has different typicalities, which explains the guppy effect. Inspired by the SCoP formalism, a mathematical model using the formalism of quantum mechanics, both the quantum probability and Hilbert space structures, has been worked out which allows one to reproduce the experimental results obtained by Hampton on conjunctions and disjunctions of concepts. This formulation identifies the presence of typically quantum effects in the mechanism of combination of concepts, e.g., contextual influence, superposition, interference and entanglement [11], [12], [13], [14], [15], [16], [50]. Quantum models have also been elaborated to describe the disjunction effect and the Ellsberg paradox, which accord with the experimental data collected in the literature [12], [14], [17].

The analysis above allowed the authors to put forward the hypothesis that two structured and superposed layers can be identified in human thought: a *classical logical layer*, that can be modeled by using a classical Kolmogorovian probability framework, and a *quantum conceptual layer*, that does not admit a Kolmogorovian probabilistic model. The latter mode can instead be modeled by using the probabilistic formalism of quantum mechanics. We stress, to conclude this section, that the thought process in the quantum conceptual layer is strongly influenced by the overall conceptual landscape, hence context effects become fundamental.

III. QUANTUM STRUCTURE IN ARTIFICIAL INTELLIGENCE

Cognitive models of knowledge representation are relevant also from a technological point of view, for the representation of objects, categories, relations between objects, etc., play a central role in the development of artificial intelligence. In the last years techniques coming from quantum information theory have been implemented in the studies on semantic analysis and neural networks. In 2004 two of the authors proved that modern approaches to quantitative linguistics and semantic analysis, when reformulated as Hilbert space problems, reveal formal structures that are similar to those known in quantum mechanics and quantum information theory, hence in the quantum models on concept representation [18]. Similar situations are recurring in distributed representation of cognitive structures developed for the purpose of neural networks. Let us discuss two interesting aspects of these quantum approaches.

Modern approaches to semantic analysis typically model words and their meanings by vectors from finite-dimensional vector spaces (see, e.g., latent semantic analysis [51]). Semantic analysis is mainly based on text co-occurrence matrices and data-analysis technique employing singular value decomposition. Various models of semantic analysis provide powerful methods of determining similarity of meaning of words and passages by analysis of large text corpora. The procedures are fully automatic and allow to analyze texts by computers without an involvement of any human understanding. The interesting thing is that there are strong similarities between latent semantic analysis and formal structures of quantum information theory. Latent semantic analysis is essentially a Hilbert space formalism. One represents words by vectors spanning a finite-dimensional space and text passages are represented by linear combinations of such words, with appropriate weights related to frequency of occurrence of the words in the text. Similarity of meaning is represented by scalar products between certain word-vectors (belonging to the so-called semantic space). In quantum information theory words, also treated as vectors, are being processed by quantum algorithms or encoded/decoded by means of quantum cryptographic protocols. Although one starts to think of quantum programming languages, the semantic

issues of quantum texts are difficult to formulate. Latent semantic analysis is in this context a natural candidate as a starting point for “quantum linguistics”. Still, latent semantic analysis has certain conceptual problems of its own. As stressed by many authors, the greatest difficulty of this theory is that it treats a text passage as a “bag of words”, a set where order is irrelevant. The difficulty is a serious one since it is intuitively clear that syntax is important for evaluation of text meaning. The sentences “Mary hit John” and “John hit Mary” cannot be distinguished by latent semantic analysis; “Mary did hit John” and “John did not hit Mary” have practically identical representations in this theory because ‘not’ is in latent semantic analysis a very short vector. What latent semantic analysis can capture is that the sentences are about violence. We think that experience from quantum information theory may prove useful here. A basic object in quantum information theory is not a word but a letter. Typically one works with the binary alphabet consisting of 0 and 1 and qubits. Ordering of qubits is obtained by means of the tensor product: we maintain that ordering of words can be obtained in the same way.

In 1990 Smolensky [52] proposed the introduction of tensor products of vectors to solve the so-called *binding problem*, i.e., how to keep track of which features belong to which objects in a formal connectionist model of coding. In the linguistic framework of semantic analysis the binding problem is equivalent to the problem of representing syntax. More specifically, one represents an *activity state* of a network by a vector (in a fixed basis), then a predicate $p(a, b)$, such as $eat(John, fish)$, is represented by the vector $r_1 \otimes a + r_2 \otimes b$, where the vectors r_k represent *roles* and a, b are *fillers*. A predicate is, accordingly, represented by an *entangled activity state*. It is important to note that tensor products are more ‘economic’ than Cartesian products, because of the identifications $(\alpha|\psi\rangle) \otimes |\phi\rangle = |\psi\rangle \otimes (\alpha|\phi\rangle) = \alpha(|\psi\rangle \otimes |\phi\rangle)$, thus Hilbert (or Fock) spaces automatically perform a kind of dimensional reduction, which is the main idea of both latent semantic analysis and distributed representation. Furthermore, if one is interested in binding, more than ordering, words, then further compression is possible by employing bosonic or fermionic Fock spaces.

The above proposals on the advantages of using the quantum formalism in theories as semantic analysis and symbolic artificial intelligence find a straightforward theoretical support in our approach in cognitive science followed in [9], [10] and summarized in Sec. II. Indeed, if the conceptual mode of human thought has a formal quantum structure, then it is natural to assume that the quantum formalism should be more successfully employed in cognitive disciplines. The same conclusion can be drawn if one assumes that the brain is a quantum device, as done in [53]. But we stress that such an assumption is not needed in our approach (a similar remark will be made in Sec. IV with respect to quantum robotics).

IV. QUANTUM STRUCTURE IN ROBOTICS

The idea of a quantum robot meant as a complex quantum system interacting with an external environment through quantum computers was introduced by Paul Benioff in 1998 [54]. Benioff undertook the study of quantum robots from a physical perspective. The first applications of Benioff’s proposal to robot technology are due to Daoyi Dong et al. [55]. The model of a quantum robot suggested by these authors is made up of multi-quantum computing units, a quantum controller/actuator and information acquisition units. A quantum robot has also several learning control algorithms, including quantum searching algorithms and quantum reinforcement learning algorithms. The standard problems afflicting classical robotics, i.e., robots’ intelligence, sensor performance, speed of learning and decision making, are solved by using quantum sensors, parallel computing, fast searching and efficient learning from quantum algorithms. In particular, the authors point out the advantages in using Grover’s search algorithm, which reduces the complexity of the search algorithm with respect to classical robots.

We observe that the above insights and ideas rest on the possibility of constructing real quantum computers, implementing quantum operations on microscopic entities, and thus exploiting the computational advantages that quantum computation should guarantee over classical computation. It is however well known that several technical difficulties, besides conceptual hindrances, occur whenever one accepts to consider seriously the possibility of constructing a concrete quantum computer. The control and manipulation of individual quantum systems, the necessity of robustly representing quantum information, the actual feasibility in performing quantum algorithms, are examples of such difficulties. Hence, also the realizability of an efficient quantum robot strongly depends on these technological obstacles.

Let us now come to our quantum cognition approach summarized in Sec. II. Here, the fact that the formalism of quantum mechanics can be successfully employed to model concept representation, decision making and cognitive processes suggests that, conversely, the processes working in human mind have structurally a quantum nature. And this fact does not necessarily entail the compelling requirement that microscopic quantum processes occur in human mind. Indeed, following the quantum cognition approach, the hypothesis is rather that macroscopic processes can entail quantum structure without the necessity of the presence of microscopic quantum processes giving rise to these macroscopic processes. As a consequence of this hypothesis, one could maintain that human mind itself works as a system which is closer to a quantum computer than it is to a classical computer. It does not necessarily have to be equivalent with a quantum computer – we believe it is not –, but entailing quantum structure gives it similar advantages in computing power than the ones that quantum computers

have over classical computers. This insight could explain, in particular, why artificial intelligence and robotics are still facing some fundamental problems, notwithstanding their impressive technological success: this is due to the fact that they use the paradigm of classical computation which is not powerful enough to perform the operations that the human mind is able to do. Let us finally recall that some of us have worked out macroscopic models (*connected vessels of water, quantum machine, ...*) which show a quantum behavior and exhibit typical features of quantum mechanical entities, i.e., contextuality, entanglement, violation of Bell's inequalities, etc. [39], [40], [41], [49]. This result is relevant in the perspective of quantum robotics because it opens up the possibility that the resources of quantum computation can be sought in other types of realizations than microscopic quantum entities and qubits. One could indeed envisage the possibility of elaborating (eventually complex) macroscopic devices which perform quantum algorithms, thus simulating quantum computers and exploiting the enormous extra power coming from quantum computation. In this way, the foregoing problems connected with the control of microscopic entities would be avoided and, better, the possibility of performing quantum computation by using only classical physics could potentially allow one to increase the resources of quantum computation itself.

ACKNOWLEDGMENT

This research was supported by Grants G.0405.08 and G.0234.08 of the Flemish Fund for Scientific Research.

REFERENCES

- [1] M. Allais, "Le comportement de l'homme rationnel devant le risque: Critique des postulats et axiomes de l'École Américaine," *Econometrica*, vol. 21, pp. 503–546, 1953.
- [2] D. Ellsberg, "Risk, ambiguity, and the Savage axioms," *Quart. J. Econ.*, vol. 75, no. 4, pp. 643–669, 1961.
- [3] A. Tversky and D. Kahneman, "Extension versus intuitive reasoning: The conjunction fallacy in probability judgment," *Psych. Rev.*, vol. 90, pp. 293–315, 1983.
- [4] A. Tversky and E. Shafir, "The disjunction effect in choice under uncertainty," *Psych. Sci.*, vol. 3, pp. 305–309, 1992.
- [5] D. N. Osherson and E. E. Smith, "On the adequacy of prototype theory as a theory of concepts," *Cognition*, vol. 9, pp. 35–58, 1981.
- [6] See the recent wikipedia page on Quantum Cognition: http://en.wikipedia.org/wiki/Quantum_cognition.
- [7] D. Aerts and S. Aerts, "Applications of quantum statistics in psychological studies of decision processes," *Found. Sci.*, vol. 1, pp. 85–97, 1994.
- [8] L. Gabora and D. Aerts, "Contextualizing concepts using a mathematical generalization of the quantum formalism," *J. Exp. Theor. Art. Int.*, vol. 14, pp. 327–358, 2002.
- [9] D. Aerts and L. Gabora, "A theory of concepts and their combinations I: The structure of the sets of contexts and properties," *Kybernetes*, vol. 34, pp. 167–191, 2005.
- [10] D. Aerts and L. Gabora, "A theory of concepts and their combinations II: A Hilbert space representation," *Kybernetes*, vol. 34, pp. 192–221, 2005.
- [11] D. Aerts, "Quantum particles as conceptual entities. A Possible Explanatory Framework for Quantum Theory," *Found. Sci.*, vol. 14, pp. 361–411, 2009.
- [12] D. Aerts, "Quantum structure in cognition," *J. Math. Psych.*, vol. 53, pp. 314–348, 2009.
- [13] D. Aerts, S. Aerts, and L. Gabora, "Experimental evidence for quantum structure in cognition," *Lecture Notes in Artificial Intelligence*, vol. 5494, pp. 59–70, 2009.
- [14] D. Aerts and B. D'Hooghe, "Classical logical versus quantum conceptual thought: Examples in economy, decision theory and concept theory," *Lecture Notes in Artificial Intelligence*, vol. 5494, pp. 128–142, 2009.
- [15] D. Aerts, "Quantum interference and superposition in cognition: Development of a theory for the disjunction of concepts," in *Worldviews, Science and Us: Bridging Knowledge and Its Implications for Our Perspectives of the World*, D. Aerts, B. D'Hooghe, and N. Note, Eds. Singapore: World Scientific, 2011, to be published.
- [16] D. Aerts, "General quantum modeling of combining concepts: A quantum field model in Fock space," archive reference and link: <http://uk.arxiv.org/abs/0705.1740>.
- [17] D. Aerts, B. D'Hooghe, and E. Haven, "Quantum experimental data in psychology and economics," *Int. J. Theor. Phys.*, vol. 49, pp. 2971–2990, 2010.
- [18] D. Aerts and M. Czachor, "Quantum aspects of semantic analysis and symbolic artificial intelligence," *J. Phys. A-Math. Gen.*, vol. 37, pp. L123–L132, 2004.
- [19] D. Widdows, "Orthogonal negation in vector spaces for modelling word-meanings and document retrieval," in *Proceedings of the 41st Annual Meeting of the Association for Computational Linguistics*, 2003, pp. 136–143.
- [20] D. Widdows, *Geometry and Meaning*, CSLI Publications, IL: University of Chicago Press, 2006.
- [21] D. Widdows and S. Peters, "Word vectors and quantum logic: Experiments with negation and disjunction," in *Mathematics of Language 8*, Indiana, IN: Bloomington, 2003, pp. 141–154.
- [22] K. van Rijsbergen, *The Geometry of Information Retrieval*, Cambridge, UK: Cambridge University Press, 2004.
- [23] Y. Li and H. Cunningham, "Geometric and quantum methods for information retrieval," *ACM Sigir Forum*, vol. 42, no. 2, pp. 22–32, 2003.
- [24] P. D. Bruza and R. J. Cole, "Quantum logic of semantic space: An explanatory investigation of context effects in practical reasoning," in *We Will Show Them: Essays in Honour of Dov Gabbay*, S. Artemov et al., Eds., College Publications, 2005.

- [25] P. D. Bruza, K. Kitto, D. McEvoy, and C. McEvoy, "Entangling words and meaning," in *Proceedings of the Second Quantum Interaction Symposium*, Oxford, UK, Oxford University Press, 2008, pp. 118–124.
- [26] P. D. Bruza, K. Kitto, D. Nelson, and C. McEvoy, "Extracting spooky-activation-at-a-distance from considerations of entanglement," in *Proceedings of QI 2009-Third International Symposium on Quantum Interaction*, P. D. Bruza, D. Sofge, W. Lawless, C. J. van Rijsbergen, and M. Klusch, Eds., LNCS vol. 5494, Berlin, Heidelberg: Springer, 2009, pp. 71–83.
- [27] J. R. Busemeyer, Z. Wang, and J. T. Townsend, "Quantum dynamics of human decision-making," *J. Math. Psych.*, vol. 50, pp. 220–241, 2006.
- [28] E. M. Pothos and J. R. Busemeyer, "A quantum probability explanation for violations of 'rational' decision theory," *Proceedings of the Royal Society B*, 2009.
- [29] A. Y. Khrennikov and E. Haven, "Quantum mechanics and violations of the Sure-Thing Principle: The use of probability interference and other concepts," *J. Math. Psych.*, vol. 53, pp. 378–388, 2009.
- [30] K. H. Pribram, *Languages of the Brain: Experimental Paradoxes and Principles in Neuropsychology*, New York, NY: Prentice Hall, 1971.
- [31] D. Gabor, "Holographic model for temporal recall," *Nature*, vol. 217, 1288–1289, 1968.
- [32] P. Kanerva, "Large patterns make great symbols: An example of learning from example," *Hybrid Neural Systems*, pp. 194–203, 1998.
- [33] T. Plate, *Holographic Reduced Representation: Distributed Representation for Cognitive Structures*, Stanford, CA: CSLI Publications, 2003.
- [34] D. Aerts, M. Czachor, and B. De Moor, "Geometric analogue of holographic reduced representation," *J. Math. Psych.*, Vol. 53, pp. 389–398, 2009.
- [35] D. Aerts, L. Gabora, S. Sozzo, and T. Veloz, "Quantum interaction approach in cognition, artificial intelligence and robotics," in *Proceedings of the Fifth International Conference on Quantum, Nano and Micro Technologies (ICQNM 2011)*, Nice, France, August 21–27, 2011, accepted for publication.
- [36] See the pages <http://ir.dcs.gla.ac.uk/qi2007/>, <http://ir.dcs.gla.ac.uk/qi2008/> and <http://www-ags.dfki.uni-sb.de/klusch/qi2009/>.
- [37] D. Aerts, "A Possible explanation for the probabilities of quantum mechanics," *J. Math. Phys.*, vol. 27, pp. 202–210, 1986.
- [38] D. Aerts, "Quantum structures, separated physical entities and probability," *Found. Phys.*, vol. 24, pp. 1227–1259, 1994.
- [39] D. Aerts, S. Aerts, B. Coecke, B. D'Hooghe, T. Durt, and F. Valckenborgh, "A model with varying fluctuations in the measurement context," in *New Developments on Fundamental Problems in Quantum Physics*, M. Ferrero and A. van der Merwe, Eds. Dordrecht, The Netherlands: Springer, 1997, pp. 7–9.
- [40] D. Aerts, "The hidden measurement formalism: What can be explained and where paradoxes remain," *Int. J. Theor. Phys.*, vol. 37, pp. 291–304, 1998.
- [41] D. Aerts, "Foundations of quantum physics: A general realistic and operational approach," *Int. J. Theor. Phys.*, vol. 38, pp. 289–358, 1999.
- [42] D. Aerts, "Reality and probability: Introducing a new type of probability calculus," in *Probing the Structure of Quantum Mechanics: Nonlinearity, Nonlocality, Probability and Axiomatics*, D. Aerts, M. Czachor, and T. Durt, Eds. Singapore: World Scientific, 2002, pp. 205–229.
- [43] J. A. Hampton, "Overextension of conjunctive concepts: Evidence for a unitary model for concept typicality and class inclusion," *J. Exp. Psych.: Lear. Mem. Cog.*, vol. 14, pp. 12–32, 1988.
- [44] J. A. Hampton, "Disjunction of natural concepts," *Memory & Cognition*, vol. 16, pp. 579–591, 1988.
- [45] L. Zadeh, "Fuzzy sets," *Information & Control*, vol. 8, pp. 338–353, 1965.
- [46] L. Zadeh, "A note on prototype theory and fuzzy sets," *Cognition*, vol. 12, pp. 291–297, 1982.
- [47] D. N. Osherson and E. E. Smith, "Gradedness and conceptual combination," *Cognition*, vol. 12, pp. 299–318, 1982.
- [48] J. A. Hampton, "Conceptual combination," in *Knowledge, Concepts, and Categories*, K. Lamberts and D. Shanks, Eds. Hove, UK: Psychology Press, 1997, pp. 133–159.
- [49] D. Aerts, M. Czachor, and B. D'Hooghe, "Towards a quantum evolutionary scheme: Violating Bell's inequalities in language," in *Evolutionary Epistemology, Language and Culture - A Non Adaptationist Systems Theoretical Approach*, N. Gontier, J. P. Van Bendegem, and D. Aerts, Eds. Dordrecht, The Netherlands: Springer, 2006.
- [50] D. Aerts, "Interpreting quantum particles as conceptual entities," *Int. J. Theor. Phys.*, vol. 49, pp. 2950–2970, 2010.
- [51] T. K. Landauer, P. W. Foltz, and D. Laham, "Introduction to latent semantic analysis," *Discourse Process*, vol. 25, 259, 1998.
- [52] P. Smolensky, "Tensor product variable binding and the representation of symbolic structures in connectionist systems," *Artif. Intell.*, vol. 46, pp. 159, 1990.
- [53] R. Penrose, *The Emperor's New Mind*, Oxford, UK: Oxford University Press, 1990.
- [54] P. Benioff, "Quantum robots and environments," *Phys. Rev. A*, vol. 58, no. 2, pp. 893–904, 1998.
- [55] D. Dong, C. Chen, C. Zhang, and Z. Chen, "Quantum robots: Structure, algorithms and applications," *Robotica*, vol. 24, pp. 513–521, 2006.

Quantum Computing with Charge States in Silicon : Towards a Leadless Approach

Thierry Ferrus, Alessandro Rossi, Aleksey Andreev, Paul Chapman and David Arfon Williams
Hitachi Cambridge Laboratory, J J Thomson avenue, CB3 0HE, Cambridge, United Kingdom
 Email: taf25@cam.ac.uk

Abstract—Coherence time and the ease of operability of a device are well-known requirements for the realization of individual qubits. However, the successful integration of many devices further restricts the choices for implementation. In this article, we describe a device in which manufacturing considerations have been taken into account for the device design and the choice for material, and where leadless control of the qubit is possible.

Keywords-Quantum computing, silicon, charge qubit, quantum dots

I. INTRODUCTION

Since the early development of integrated circuits in 1958, the continuous decrease in transistor size, as described by Moore's law [1], has been driven by the continued demand for increasing computing power. This has been mainly facilitated by technological advances, which allow the incorporation of a progressively large number of smaller transistors onto a single chip. Quantum mechanical effects have been found to be increasingly important in the behavior of conventional devices at the nanometer scale, and this has led to substantial research into the quantum properties of nanoscale objects. In addition, devices on this scale offer the possibility of making circuits for quantum information processing and quantum computing, a notion first suggested by Feynman [2].

In the past decades, many architectures have been proposed as platforms for quantum computation [3] most using an optical or a solid-state approach. All make use of quantum bits or qubits, an analogue of the classical bit, as an essential element of computation. Some of these realizations have been particularly successful, such as superconductor-based qubits with Josephson junctions, trapped ions or coherent photon states. This is primarily due to the choice of the material, the ability to perform fast measurements as well as the simplicity of the system. However, a practical implementation for circuit applications requires high fidelity results, a good scalability, and preferably a high compatibility with existing manufacturing techniques. This has driven several proposals attempting to use silicon as the basis for qubit realization, because of its compatibility with current fabrication methods. (An example is the well-known Kane proposal for quantum computation [4]) Silicon has intrinsic properties such as potentially the absence of intrinsic nuclear spins, which make it a desirable choice for qubit as well as conventional transistor fabrication. In

semiconductor approaches, we can broadly define two qubit types: Charge qubits, where the basis states are defined by two distinct electron distributions, and spin qubits where the representation is in the spin orientation of electron or nucleus.

In this article, we first review the technological and commercial constraints that led to our choice for employing charge qubits in an isolated silicon structure, with an emphasis on flexibility, reliability, cost and compatibility with conventional fabrication techniques. We then define the qubit states for that specific system and describe how basic quantum operations could be performed under DC voltages, in particular the initialization stage and swap operations. Supported by recent and ongoing experimental investigations, we finally show that specific device features could be used for future leadless operation of the system that would ultimately simplify scalability.

II. TECHNOLOGICAL CHOICES

Some materials that have been considered for the manufacture of qubits, such as III-V compounds, possess apparently significant advantages, in particular a direct band gap and the possibility to reduce interface scattering through layer design [5]. However, issues such as the finite nuclear spin, leading to spin qubit decoherence, and strong dipole scattering from polar phonons, decohering charge qubits, make silicon still appear a material of choice for manufacturing future qubit processors.

Another important consideration for future commercialization is the need for high reproducibility, both in the device fabrication and in quantum operation readouts. Devices must have a high fabrication yield and their electronic characteristics or behaviors must be consistently reproducible. There are several pathways to realize a solid state qubit. One of the more recent consists in using the spin state of a localized electron at a donor site in silicon [6], [7], as was suggested by Kane [4]. Although easily allowing both charge and spin qubit manipulation, this concept is difficult to scale because of the requirement for precise single ion positioning and the inherent donor diffusion during anneal stages. Another option in silicon is the use of quantum dots with dimensions of a few tens of nanometers. For such a structure, a singly charged quantum dot pair or double quantum dot is appropriate. Because the dimensions lie within the range of transistor sizes that are currently

manufactured, the industrial infrastructure is already well adapted to this future technology.

In order to realize any type of solid-state qubit, one has to minimize sources of noise to keep a coherence time sufficiently long and be able to perform a significant number of operations before re-initialization of the qubit becomes necessary. Unfortunately, and despite line filtering and careful contact designs, high frequency noise can reach the device via highly conducting paths such as gate or source and drain leads. In addition, it is desirable to minimize the number of leads to ease the process fabrication, especially for 3D integration purposes as well as minimizing possible interference effects. From this perspective, ungated devices seem preferable, and these will be described here.

These devices consist of a double-dot charge qubit, where the quantum states $|0\rangle$ and $|1\rangle$ are represented by two different electron distributions between the lobes of the device, coupled with a detector to measure the changes in charge distribution.

In many solid-state approaches to quantum computation, single electron transistors (SETs) have been the primary choice for detection of charge movement at the fractional charge level. Their design relies on the presence of two tunnel barriers of conductance $\ll e^2/h$ separated by a confined region made of a single dot. Their operation principle is based on Coulomb blockade (CB) resulting in electrons being blocked for transport if the electrostatic configuration is not energetically favourable for tunneling. Tunnel barriers can be controlled by forming metal gates on top of the structure or by patterning constrictions in the device and thus modifying the potential barrier height between the contact and the quantum dot. In both cases, the dot potential has to be controlled by an additional gate. The method described here provides the advantage of physically decoupling the detector from its control gate by allowing a side-gate to be patterned laterally and by etching the unnecessary material between the gate and the dot.

One potential difficulty to be overcome in using doped silicon results from the potential noise in the device itself due to tunneling or hopping events of electrons in the vicinity of the device. In particular, random telegraph signals are detrimental to the measured signal quality, most especially at low temperatures due to electron hops between donor sites. However, such electron dynamics may be controlled by adjusting the doping density, varying the electrostatic field inside the structure [8] or manipulating the trap population by microwave measurement [9]. Following the previous discussions, the use of a doped silicon SET with constrictions and a sidegate then seems a reasonable choice for a qubit state detector.

The noise reduction implementations in the structure can be carried out further by etching the material around the qubit structure, so that direct electron transfer between the qubit and the detector becomes prohibited. Although

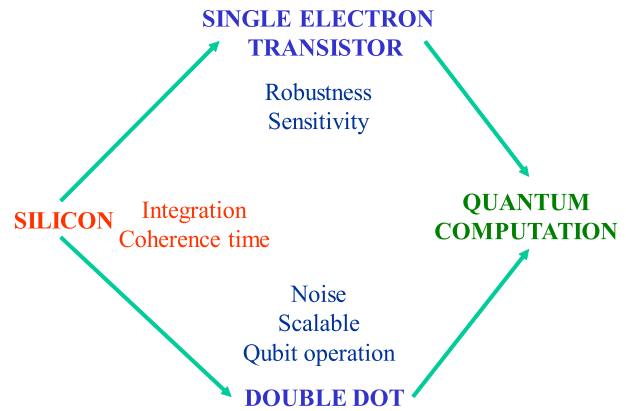


Figure 1. Industrial choices for qubit structures.

necessary in order to obtain longer coherence times, this choice makes measurement more challenging because it is not possible directly to probe the states of the qubit, for example, by using source and drain contacts.

In the next sections, we describe the operation of an isolated double quantum dot (IDQD) structure and present some specific electronic properties. In particular, we show that strong detection of the qubit states could be obtained using a SET (Figure 1) and that leadless qubit operation using microwaves is conceivable.

III. PRINCIPLES AND DC QUBIT OPERATION

A. Qubit definition and initialization

Owing to the doping concentration, the size, and the geometry of the dots, usual simulations based on capacitance calculations are insufficient fully to describe the transport characteristics of the device [8]. Indeed, the operation of the qubit is strongly influenced by the presence of localized states at the edge of the structure and electron-electron interaction within and between dots. As a consequence, electron tunneling between dopant states may induce a charge reorganization in the structure. The understanding of the electronic properties of an IDQD capacitively coupled to an SET then requires the use of multi-electron physics in simulations.

To this end, the qubit states have to be defined as an effective charge excess in one of the two IDQD dots. An effective charge is defined by the variation in the electrostatic potential that would be created by a single-electron tunneling event in a metallic structure. This takes into account the possibility for the electron to tunnel between donor sites in the same dot as well as charge rearrangement. The initial electron population in each dot, N_1 and N_2 , is initially defined by the range of gate voltages used to operate the device. We then have :

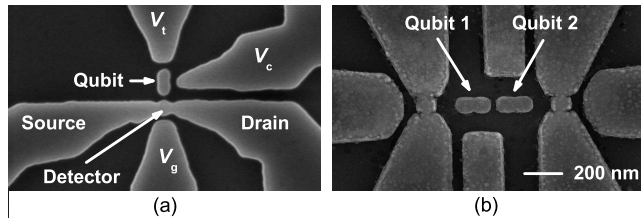


Figure 2. a) Single qubit device and its detector. Control gate are V_g for the SET and V_c and V_t for the IDQD. b) Fabricated two qubit devices with two SET detectors in the same configuration

$$|0\rangle = |N_1, N_2\rangle \quad (1a)$$

$$|1\rangle = |N_1 + \delta, N_2 - \delta\rangle \text{ with } N_1 + N_2 = N \quad (1b)$$

Here, N is the total number of electrons in the IDQD, excluding localized electrons at the Si-SiO₂ interface and δ the effective charge displaced. N is fixed at the etching stage in the process.

Within the proposed geometry, a single qubit structure required two gates to be patterned. One close to SET and one close to the IDQD. Due to capacitance coupling between the gates, the SET and the IDQD, compensation techniques [10] have to be implemented in order to maintain the detector in the most sensitive region during qubit operations. Such a structure design allows high scalability to ungated multi-qubits (Figure 2b). However, for a single qubit test structure, it is possible to use a third detuning gate in order to avoid compensating voltages [8] (Figure 2a).

The initial states $|0\rangle$ and $|1\rangle$ are defined by mapping the SET current with the SET gate and the IDQD gate V_c . The presence of a significant shift in the CB peak position defines the set of gate voltages (V_{g0}, V_{c0}) and (V_{g1}, V_{c1}) for which the two states could be accessed. The magnitude of the Coulomb peak displacement in gate voltage is dependent on the tunnel barrier between the two IDQD dots but also on the relative coupling strength between the SET and the two IDQD dots. The efficiency in the charge detection is then enhanced if the IDQD is oriented perpendicular to the source drain leads of the SET because of the produced difference of sensitivity and capacitance between the SET and the respective upper and lower IDQD dot. This configuration was chosen to this end.

In the case of uncompensated operations, the gate voltages are fixed at the degeneracy region where the two states are in superposition of states (V_g^*, V_c^*) and the third gate defines the $|0\rangle$ and $|1\rangle$ states (V_{t0}^*, V_{t1}^*) (Figure 3).

B. Quantum logic operations

Quantum logic operations are usually performed by a set of pulses sent via the side-gate leads and describing simple unitary operations. Such a technique has been successfully

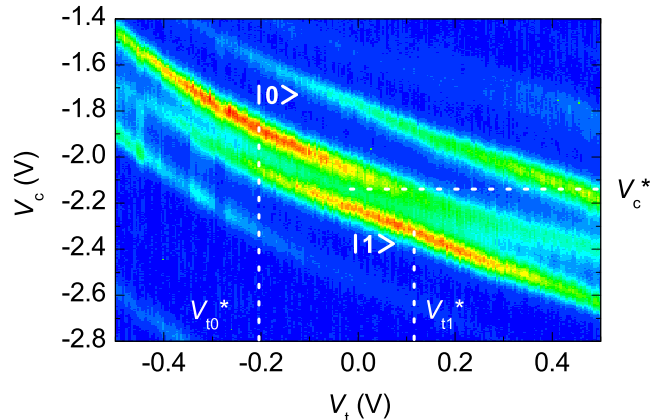


Figure 3. Operation points for the qubit with $|0\rangle$ and $|1\rangle$ states. Colors map the dependence of the SET current I_{SD} on gate voltages, with high (low) current values in red (blue).

applied in a SET coupled IDQD structure and Rabi oscillations have been demonstrated [11]. Due to capacitance coupling between the different elements of the nanostructure, including the qubit, the detector and the various gates, reliable operations require the use of gate compensation technique, synchronous triggering of the gate signals and well-controlled pulse transmission in high frequency lines.

As an alternative method to trigger and control the displacement of electrons between the two IDQD dots, in the next section we describe an experimental approach to control a qubit using centimeter-waves with leadless coupling.

IV. LEADLESS OPERATION AND SCALING

Radio and microwave signals can be coupled to the device either directly, via gates, or in a leadless approach by broadcasting them using an antenna (electrical coupling) or a coil (magnetic coupling) [12]. For the latter, the coupling is weaker but efficient matching can be obtained even at low temperature. In previous experiments, the control signal $h\nu$ was set to be in resonance with the energy difference between two neighboring phosphorous sites in the SET [9]. In most cases, the operating frequency was in the gigahertz (GHz) range and electrons were able to be displaced between the two sites. This was possible although $h\nu \ll kT$ because of the poor electron-phonon coupling in these structures [13]. Such a microwave-induced electron displacement can be coherent, and control of the Rabi rate can be achieved, as demonstrated in similar devices [14]. In these experiments, the resonant condition was determined by a sharp increase in the SET current due to a modification of the tunneling barrier profile. Because the SET and the IDQD are made of the same material, it is conceivable that specific frequencies may address localized electrons at the phosphorous sites in the IDQD. Although some electron hops in the IDQD will not be detected by the SET due to their location,

away from the detector, some can induce a sufficiently large effective charge displacement so that the SET could detect them. This possibility is supported by the observation of the effect of random telegraph signals (RTS) on the electron population in the IDQD dots in some devices. RTS result from random jumps of electrons between donor sites and are generally considered as a source of electronic noise at low temperature. If present in devices, they result in abrupt shifts in the CB peak positions in gate voltage in single electron transistors.

However, there is a difference depending on such events take place in the SET or in the IDQD. For the former, the charge occupancy in the dot is abruptly modified and leads to a shift in all CB peak positions in gate voltage by a same amount and independently of the IDQD configuration. However, RTS in the IDQD mostly affect the SET at the degeneracy region. Due the dot electrical insulation, RTS in the IDQD can only be probed indirectly by assessing their influence on the SET conductivity.

When the qubit is set in the superposition of state $|0\rangle\cos(\phi) + |1\rangle\sin(\phi)$, RTS induces a phase shift close to $\pi/2$, leading to a partial electron population inversion in the IDQD (Figures 4 and 5). Because RTS operate in the same way as previous microwave controlled electron tunneling, this observation enlighten the possibility to control the qubit for specific microwave frequencies. Such an experimental test was carried out by coupling microwave to the device in a leadless approach that resolves the problem of impedance matching, both in a region of qubit operability and outside for comparison. At a frequency of 7.5775 GHz, we observe that the normal SET operation is not affected by the microwave for any power whereas a partial population inversion was realized when the qubit is tuned in its operating point and the power of the microwave close to 0 dBm (Figure 6). For this configuration we did not observe any heating effect due to the microwave absorption nor increase in the electron temperature. These results thus demonstrate that a suitable frequency and power level could lead to a controlled population inversion in the qubit and so to a phase shift.

Because the value of the frequency operating the qubit is depending on both geometrical constraints and the quantum dot internal structure, it is possible to modify or adjust the frequency during the process of the device, so that different frequencies could be associated to different qubits. This is technologically advantageous for scalability purposes because the difficulty in addressing various qubits is reduced to the implementation of frequency multiplexing. This idea was partly demonstrated in previous experiments [15].

V. CONCLUSION

We have presented a possible implementation of a solid-state qubit that is compatible with current commercial fabrication techniques and with a potentially long decoher-

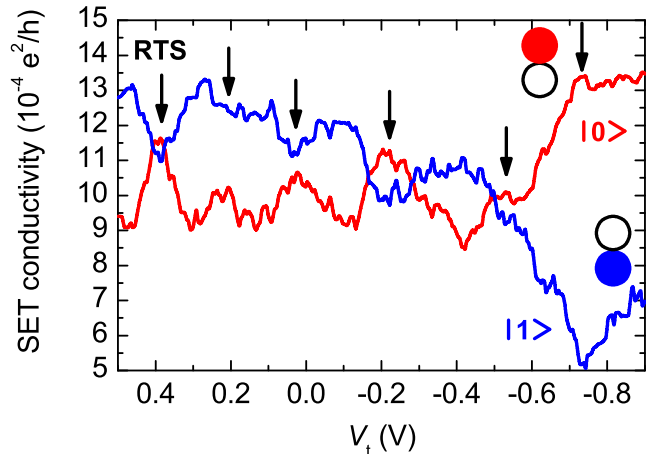


Figure 4. SET current profiles along V_t for the two qubit state configurations. RTS events are present and induce partial population inversions when the qubit is set in an entangled state with $\phi \sim \pi/4$. For $V_t < -0.6$ V, states are clearly projected on qubit basis states.

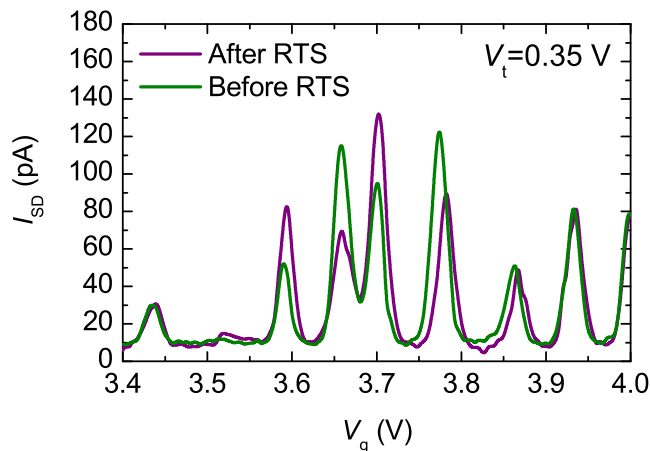


Figure 5. CB oscillations as a function of V_g at a fixed qubit gate voltage V_t . RTS events modify the SET current I_{SD} level around the degeneracy region ($V_g \sim 3.7 \pm 0.1$ V) whereas the other CB peaks remain unaffected.

ence time due to its isolated nature. Despite geometrical constraints, a successful and large detection signal was obtained and the qubit basis states were mapped in a gate dependency diagram. We have also shown that this specific implementation can offer the possibility for leadless operation, especially in the microwave range, leading to easier scalability. Finally, the choice for silicon as a base material to realize the qubit offers the advantage of using a similar structure in order to implement spin qubits.

ACKNOWLEDGMENT

This work was partly supported by Special Coordination Funds for Promoting Science and Technology in Japan.

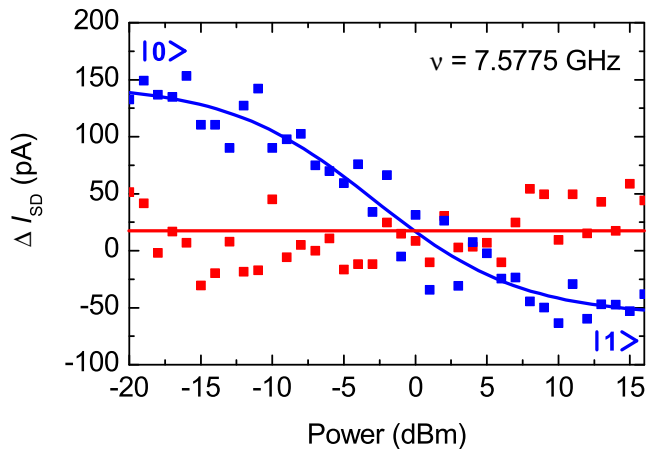


Figure 6. Microwave manipulation of the qubit. ΔI_{SD} is related to the change in the number of electrons in the upper IDQD dot ($|0\rangle$ state). The red trace shows the dependence of the SET current in a region outside the operating point of the qubit whereas the blue trace shows a transition from the $|0\rangle$ to the $|1\rangle$ state.

REFERENCES

- [1] G. Moore, *Cramming More Components onto Integrated Circuits*, Electronics Magazine, vol. 38, No. 8, 1965
- [2] R. P. Feynman, *Simulating physics with computers*, Int. J. Theor. Phys., vol. 21, pp. 467-488, 1982; *ibid Quantum Mechanical Computers*, Optics News, Vol. 11 Issue 2, pp.11-20, 1985
- [3] W. S. Warren, *The Usefulness of NMR Quantum Computing*, Science, vol 277, pp. 1688, 1997; A. Shnirman, G. Schön, and Z. Hermon, *Quantum Manipulations of Small Josephson Junctions*, Phys. Rev. Lett., vol 79, pp. 2371, 1997; A. Steane, *he Ion Trap Quantum Information Processor*, Appl. Phys. B., vol 64, pp. 623, 1997; S. Takeuchi, *Experimental demonstration of a three-qubit quantum computation algorithm using a single photon and linear optics*, Phys. Rev. A, vol 62, pp. 032301, 2000; D. Loss and D. P. DiVincenzo, *Quantum computation with quantum dots*, Phys. Rev. A, vol 57, pp. 120, 1998
- [4] B. E. Kane, *A silicon-based nuclear spin quantum computer*, Nature, vol 393, pp 133, 1998
- [5] C. C. Dean and M. Pepper, *The transition from two- to one-dimensional electronic transport in narrow silicon accumulation layers*, J. Phys. C: Solid State Phys., vol 15, pp. L1287, 1982
- [6] P. T. Greenland, S. A. Lynch, A. F. G. van der Meer, B. N. Murdin, C. R. Pidgeon, B. Redlich, N. Q. Vinh, and G. Aeppli, *Coherent Control of Rydberg States in Silicon*, Nature, vol 465, pp. 1057, 2010
- [7] A. Morello, J. J. Pla, F. A. Zwanenbourg, K. W. Chan, H. Huebl, M. Mottonen, C. D. Nugroho, C. Yang, J. A. van Donkelaar, A. D. C. Alves, D. N. Jamieson, C. C. Escott, L. C. L. Hollenberg, R. G. Clark, and A. S. Dzurak, *Single-shot readout of an electron spin in silicon*, Nature, vol 467, pp. 687, 2010
- [8] T. Ferrus, A. Rossi, M. Tanner, G. Podd, P. Chapman, and D. A. Williams, *Electron dynamics in a non-metallic silicon isolated double quantum dot capacitively coupled to a single electron transistor*, arXiv:0907.2635, 2011
- [9] T. Ferrus, D. G. Hasko, Q. R. Morrissey, S. R. Burge, E. J. Freeman, M. J. French, A. Lam, L. Creswell, R. J. Collier, D. A. Williams, and G. A. D. Briggs, *Cryogenic instrumentation for fast current measurement in a silicon single electron transistor*, J. Appl. Phys., vol 106, pp. 033705, 2009
- [10] A. Rossi, T. Ferrus, G. J. Podd, and D. A. Williams, *Charge Detection in Phosphorus-doped Silicon Double Quantum Dots*, Appl. Phys. Lett., vol 97, pp. 223506, 2010
- [11] J. Gorman, D. G. Hasko, and D. A. Williams, *Charge-Qubit Operation of an Isolated Double Quantum Dot*, Phys. Rev. Lett., vol 95, pp. 090502, 2005
- [12] D. G. Hasko, T. Ferrus, Q. R. Morrissey, S. R. Burge, E. J. Freeman, M. J. French, A. Lam, L. Creswell, R. J. Collier, D. A. Williams, and G. A. D. Briggs, *Single shot measurement of a silicon single electron transistor*, Appl. Phys. Lett., vol 93, no 19, pp. 192116, 2008
- [13] J. Ogi, T. Ferrus, T. Kodera, Y. Tsuchiya, K. Uchida, D. A. Williams, S. Oda, and H. Mizuta, *Experimental observation of enhanced electron-phonon interaction in suspended Si double quantum dots*, Jpn. J. Appl. Phys., vol 49, pp. 045203, 2010
- [14] A. Rossi and D. G. Hasko, *Microwave-assisted transport via localized states in degenerately doped Si single electron transistors*, J. Appl. Phys. 108, 034509, 2010
- [15] M. Erfani, D. G. Hasko, A. Rossi, W. S. Cho, and J. Choi, *Microwave driven arbitrary coupling between trapped charge resonances in a silicon single electron transistor*, unpublished, 2011

Quantum Dynamics and Coherence of Qubits

Vladimir Privman

Department of Physics, Clarkson University, Potsdam, NY 13699, USA

E-mail privman@clarkson.edu; Web <http://www.clarkson.edu/Privman>

Abstract—We review results in theoretical modeling of quantum systems in support of the studies of decoherence and qubit interactions for quantum information processing. The developed modeling tools have been applied to semiconductor materials and nanostructures that show promise for implementation of coherent, controlled quantum dynamics at the level of registers of several quantum bits (qubits), such as spins. Field-theoretical techniques have been utilized to address decoherence and more generally the origin and effects of quantum noise and the loss of entanglement in quantum dynamics of qubits and several-qubit registers. Qubit coupling mechanisms via the indirect exchange interaction have been investigated, and quantum computing designs have been evaluated for scalability. We also describe general and specific research challenges, the solution of which will advance the field of modeling “open quantum systems” to further our understanding of how environmental influences affect quantum coherence and its loss during quantum dynamics.

Keywords—*qubit; decoherence; exchange; entanglement.*

I. INTRODUCTION

We review results in the field of “controlled quantum dynamics,” aimed at investigating general aspects of quantum noise, as well as single- and multi-qubit decoherence, robustness of entanglement, and origins of two-qubit interactions, the latter mediated via the qubits’ coupling with a many-body bath of modes (e.g., acoustic phonons, conduction electrons). Study of “open quantum systems,” with new challenges suggested by the emerging field of quantum information, requires utilization and development of field-theoretical many-body techniques for the description of quantum dynamics. These studies have facilitated evaluation of scalability of existing and emerging quantum computing schemes, for instance, for spin- and quantum-dot based quantum computer designs.

Emergence of entanglement, by induced indirect-exchange Ruderman-Kittel-Kasuya-Yosida (RKKY) type interactions, and its loss due to quantum noise can be quantified by developed calculation techniques for the system’s dynamics, with the environmental (bath) modes traced out, to describe the induced interaction and quantum noise in a unified treatment.

The reported research has been focused on the maintenance of coherence of quantum dynamics controlled by qubit-qubit interactions and quantum noise, both

mediated by coupling to external baths, such as acoustic phonons or conduction electrons coupled to quantum-dot and impurity-atom *spin qubits* in semiconductor-material heterostructures. The latter, RKKY-type mechanism of spin-spin (qubit-qubit) interaction offers an approach to incorporate scalable control of entanglement into solid state quantum computing schemes. Calculations of bath-induced interactions and decoherence have been carried out for systems of relevance to the ongoing measurement and interaction experiments.

In Section II, we generally cite our modeling results. In Section II, we survey the status of research work in the field of evaluation of decoherence. In Section IV, we outline research challenges in the topics involving induced interactions (RKKY-type) and their interplay with quantum noise. Finally, in Section V we address some longer-term issues in the physics of open quantum systems subject to environmental noise.

II. DECOHERENCE AND INDUCED INTERACTIONS

Decoherence (quantum phase noise) [1] and, for more than a single qubit, the associated loss of entanglement, are the main obstacles to scalable quantum computation. Theoretical evaluation of a quantum computing scheme includes identification of system parameter ranges for which the level of quantum noise is within the conditions for fault-tolerant quantum error correction. Coherent quantum control of systems and structures on the nanoscale, but larger than single atoms and molecules, has been explored in experiments that control quantum dynamics beyond the traditional energy-level spectroscopy. Reduction of quantum noise to maintain quantum coherence over the experimental time scales is key to probing processes and concepts that were until recently out of the reach of experimental observations, including such recent discoveries as observation of an electron spin resonance (ESR) signal from a single spin [2,3], or probing RKKY-type indirect exchange interaction that, via conduction electrons, influences the dynamics of two spins of electrons located in separate quantum dots [4].

Here we outline research to advance theoretical evaluation of decoherence, entanglement, and interactions. From the earlier focus on the quantum-Hall-effect systems [5-7], our research has extended to rather general results on decoherence [1,8-10] and, more recently, disentanglement

and RKKY-type interactions for two qubits [11-13], as well as to additive measures of decoherence for multi-qubit registers [1,14]. Model calculations have been carried out for a range of spin- and quantum-dot-based quantum computing schemes in semiconductor nanostructures, e.g., [1,10,15,16]. While the focus has been on semiconductor materials, most of these approaches apply to any qubit-based quantum computing scheme.

III. DECOHERENCE DURING QUANTUM GATE FUNCTIONS

It has been recognized that for times, t , larger than \hbar/kT , which is about 2.5×10^{-14} sec at room temperatures of 300K, Markovian approximation schemes, e.g., [17,18], can be used. For NMR/ESR, these have been utilized primarily for single-qubit calculations of the relaxation and dephasing time scales, T_1 and T_2 , and of the asymptotic large-time properties of the density matrix elements of the qubit, with the environmental (bath) modes traced out.

Quantum information processing necessitates the development of techniques applicable for the “short-time” regime $t < \hbar/kT$, because most quantum-computation schemes are for systems at very low temperatures, for which gate times are shorter than or comparable to \hbar/kT . Then the bath mode correlations with the system of qubits cannot be entirely treated within the no-memory, immediate-rethermalization Markovian approximations. We have developed a new calculational approach designed for this regime, which *does not include* the Markovian assumption, and reported its applications, e.g., [8-10,16].

The level of quantum noise in the idling state, for a single qubit, as well as during the simplest quantum gates, has been well quantified [1,10,19-38]. The calculation involves evaluation of the qubit’s density matrix, followed by calculation of numerical measures of the degree of decoherence. The calculations can be done within both our short-time and the Markovian approximations, and the largest (the worst-case scenario) noise measure values can then be used to test the system as candidate for scalable quantum computer designs.

We have introduced new quantitative measures of decoherence which are approximately *additive* [1,10,14] as long as the noise for each qubit is small (for the short duration of a quantum gate function), and therefore these measures can be used to further extend the results to *several-qubit quantum registers*, in terms of the noise measures of the individual qubits, even when these qubits are *strongly entangled*.

In these calculations, the Hamiltonian of the qubit system and bath of environmental modes, is modeled by

$$H = H_S(t) + H_B + H_{SB}, \quad (1)$$

where

$$H_S(t) = H_i + H_g(t). \quad (2)$$

Here H_i is the Hamiltonian of the idling qubit register, while $H_g(t)$ represents time-dependent gate control. The Hamiltonian of the environment is given by H_B , and H_{SB}

is its interaction with the qubits. The environment is often modeled as a bath of bosonic quantum modes (e.g., phonons).

There have been few available results for evaluation of quantum noise *during general time-dependent* gate functions. The time dependence introduced by non-zero $H_g(t)$, requires time-ordering in the evaluation of the qubit evolution operator, which makes many standard techniques for dynamical calculations inapplicable. We initiated a new approach [39] yielding the first results for a gate-controlled qubit interacting with a boson bath of modes.

Recently reported first experimental successes in coherent control of single electron spins in quantum dots, e.g., [40], pose an interesting theoretical challenge to develop systematic modeling techniques for general-time-dependence gate-controlled qubits, as well as establish additivity criteria to enable evaluation of the level of noise for registers of several such controlled qubits.

IV. INDUCED INTERACTION AND QUANTUM NOISE

Modeling of an open quantum system within the Hamiltonian description, Eqs. (1)-(2), involves significant technical difficulties: While the system Hamiltonian can be just single- or two-spin, the bath-mode Hamiltonian involves many modes, in the simplest case a collection of noninteracting bosonic fields,

$$H_B = \sum_k \omega_k b_k^\dagger b_k. \quad (3)$$

The qubit-bath interaction can involve terms of the form

$$H_{SB} = \Lambda_S \sum_k g_k b_k^\dagger + \Lambda_S^\dagger \sum_k g_k^* b_k + \dots, \quad (4)$$

where Λ_S is a system operator, as well as more complicated expressions in the case of fermionic bath fields (e.g., electrons). There can usually be several interaction terms involved in Eq. (4), and also in Eq. (3), when more than one qubit is studied, and for various bosonic polarizations, for instance for acoustic phonons, or for more than one bath dominating the relaxation of the system.

However, and even more importantly, there are *physical assumptions* that have to be invoked to supplement this description. The open-quantum system dynamics cannot be entirely specified by the Hamiltonian for the system and the selected bath of external modes. We have to also model the effects of the thermalization imposed by the “rest of the universe” on the bath, as well as consider the choice of the initial conditions for the whole system, the latter an issue that represents an important challenge on its own, which will not be addressed here. These topics have a long history in the NMR and ESR literature, primarily for single, idling spins within Markovian approximations [17,18,41-44].

Recent experimental efforts to create and maintain entanglement of two electron spins in gate-formed double quantum dots with interaction mediated by electrons in conducting channels [4,45], have drawn interest to a new set

of problems. The bath modes, while serving as the main source and mediator of the quantum noise causing decoherence, will also cause loss of entanglement of two (and more) spins. However, the same modes, via their interactions with the qubits can also mediate an indirect exchange (RKKY-type) interaction. The latter can create entanglement and, for appropriate initial conditions, drive the approximately coherent quantum dynamics for some time. Ultimately, for long enough times the quantum noise effects will dominate and cause thermalization (unless the qubits are perturbed by quantum-control gate function external potentials).

Let us remark that the original RKKY calculation corresponds to the zero-temperature evaluation of the coupling induced between localized magnetic moments by a “bath” of conduction electrons. The ideas to utilize various solid-state excitations as a medium to couple qubits for quantum information processing have been advanced by several groups [5-7,12,13,46-50]. The main advantage of such coupling is that it should allow for larger distances between qubits and therefore for their easier fabrication and control.

Besides the need to properly incorporate the *physics* of the environmental influences in the open-quantum-system description, which is not a fully understood problem and is usually handled within phenomenological approaches, one should also aim at *tractability* of the resulting equations for the quantities of interest, for instance, the density matrix of the qubits, ρ_S , after the environmental effects were traced out. Typically, a Markovian approximation scheme can lead to a quantum Liouville equation of the type

$$i\hbar\dot{\rho}_S = [H_S, \rho_S] + \text{coherent terms} + \text{noise terms} . \quad (5)$$

The hope is to be able to derive the “coherent” terms, which correspond to Hermitian additions to H_S in the commutator, and the noise terms due to the bath modes.

The added terms in Eq. (5), induced by the system’s interactions with the bath modes, are usually evaluated within the second-order (in the interaction strength) expansion, as well as other approximations [12,13,18,50] aimed at making the results tractable for calculations. For more than one qubit, the qubit-qubit entanglement is created both by the internal qubit-qubit interactions in H_S , and by the induced interactions, which are part of the coherent terms, whereas other coherent terms involve for instance single-qubit operators and represent Lamb shifts.

The noise terms, however, act to unravel the entanglement. Indeed, results have been reported for a system of two qubits, suggesting that the noise-induced decoherence of two entangled noninteracting qubits and their disentanglement are closely related [11,51], with the suppression of entanglement taking place at least as fast as the product of the factors that describe the suppression of each qubit’s coherence. These results were obtained both for a Markovian-type noise model and for the short-time regime, but limited to uncorrelated noise sources for each qubit.

We have reported the first systematic calculations [12,13,50] of the combined effects of the induced interaction and quantum noise due to the phonon or (interacting, correlated) conduction electron bath, with applications for qubit geometries suggested by possible experiments [2-4,45]. While the actual calculations are quite formidable, the expression for the induced interaction is relatively compact, because it only involves components of two spin operators. As an illustration, here is the result for the calculated [50] indirect exchange interaction between two spins at separation \mathbf{d} , mediated by acoustic phonons,

$$H_{\text{int}}(t) = - \sum_{m=x,y,z} \alpha_{n_m}^m \omega_c^{n_m} \sigma_m^{(1)} \sigma_m^{(2)} \frac{2\Gamma(n_m) \text{Re}(1 + i\omega_c |\mathbf{d}|/c_s)^{n_m}}{[1 + (\omega_c |\mathbf{d}|/c_s)^2]^{n_m}} . \quad (6)$$

Here $\sigma_{m=x,y,z}^{(1),(2)}$ are the Pauli matrixes of the qubits, c_s is the speed of sound, and ω_c is the phonon cut-off frequency. For a system of two spins (of outer electrons) of P-donor impurities, placed in bulk Si at a distance \mathbf{d} apart, and subject to a constant uniform magnetic field, H_z , the exchange interaction is primarily due to the longitudinal acoustic phonons [50]. The coupling is super-Ohmic: we can assume that $n_m = 3$ in Eq. (6), for the small-frequency dependence of the standard Caldeira-Leggett spectral function, and that the coupling parameters due to the spin-orbit interaction, satisfy $\alpha_{n_x}^x = \alpha_{n_y}^y \ll \alpha_{n_z}^z$, with $\alpha_3^z \omega_c^2 \approx 8.4 \cdot 10^{-10}$. The cut-off frequency is due to the localization of the wave function, $\omega_c = c_s/a_B \approx 9.3 \times 10^{12} \text{ s}^{-1}$, which in this case is much smaller than the lattice Debye cut-off ($a_B \approx 10^{-9} \text{ m}$ is half of the effective Bohr radius of an electron at the P-impurity).

The expression for the noise effects is much more cumbersome [13,50], and is model-assumption dependent. The interplay of the induced interaction and quantum noise can be used to control the creation of time-dependent entanglement, as illustrated in Figure 1. The obtained results suggest future research into both the buildup of the entanglement and its unraveling, for interacting (and ultimately also controlled via time-dependent external “gate-function” interactions) qubits subject to quantum noise due to various bosonic and fermionic bath modes, in both the short-time and Markovian regimes. Entanglement should be explored as a fragile resource for quantum information processing, and for the relation [11,51] of disentanglement to decoherence.

The concurrence is by now a generally accepted, calculable in closed form measure of quantum-information content of two-qubit entanglement [52]. For the dynamics of two spins interacting with an acoustic-phonon environment, the concurrence as a measure of entanglement can reveal a rather nontrivial behavior; see Figure 1. We point out,

however, that with the full reduced density matrix of the system available, other quantities can also be calculated as needed, e.g., [53].

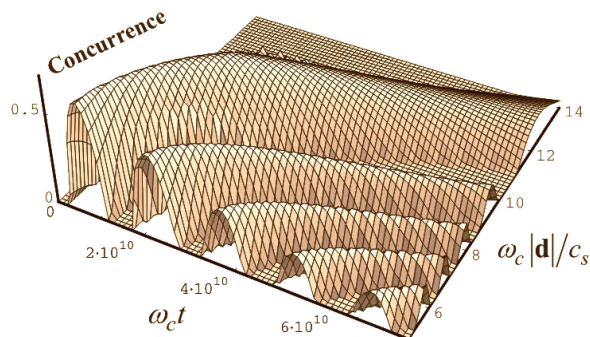


Figure 1. The concurrence as a function of time for various qubit separations, here quantifies the entanglement of two spin-1/2 qubits, due to the interaction and quantum noise induced by a bath of acoustic phonons. The parameters were for P-donor electrons in Si, at $T = 1$ K, in external magnetic field $H_z = 3 \times 10^4$ G. In terms of the single-spin basis $|\pm\rangle \propto |\uparrow\rangle \pm |\downarrow\rangle$; the two spins were initially in $|++\rangle$; the bath was initially thermalized at the temperature T .

V. CHALLENGES

With the actual experimental probes now being carried out at the nanoscale, long-standing open problems have become more pressing, and some new ones have been suggested by experimental developments. For definiteness, we consider time-independent H_S from now on.

Perhaps the most fundamental of these problems is the matter of thermalization vs. bath-induced coherent-dynamics effects in open quantum systems. The “textbook” approach to thermalization [17,42-44] has been to assume that, for large enough times the time evolution of the system plus bath is not just controlled by the combined Hamiltonian, but is supplemented by the instantaneous loss-of-memory (Markovian) approximation, which introduces irreversibility and imposes the bath temperature on the reduced system dynamics in the infinite-time limit, which is then approached as the density matrix elements assume their thermal values:

$$\rho_S(t) \rightarrow e^{-H_S/kT} / \text{Tr}(e^{-H_S/kT}), \quad (7)$$

with the exponential relaxation (diagonal) and decoherence (off-diagonal) rates defining the time scales $T_{1,2}$.

However, it turns out that the traditional phenomenological no-memory approximations, yielding thermalization and the Fermi golden rule for the transition rates, etc., assume in a way too strong a memory loss: They erase the possible bath contributions to the coherent part of the dynamics at shorter times, such as the Lamb shift for a single qubit as well as the induced RKKY interactions for a

bi-partite system. Indeed, while relaxation leading to Eq. (7) is driven by the “on-shell” exchanges with the bath, it is the memory of (correlation, entanglement with) the bath modes that drives the induced interaction via virtual exchanges. Actually, the “on-shell” condition (imposed by the so-called secular approximation, see Section 8.1.3 in [17]) also underestimates additional decoherence at short times: the “pure” or “adiabatic” contribution to the off-diagonal dephasing, that has been estimated by using other approaches [1,8,9,16,33].

Perhaps the simplest way to recognize the ambiguity is to ask if the Hamiltonian in Eq. (7) should have included the bath-induced interaction terms (not shown)? Should the final Boltzmann distribution correspond to the energy levels/basis states of the original “bare” system or the one with the RKKY-interaction/Lamb shifts added, and more generally, a bath-renormalized, “dressed” system?

There is presently no consistent treatment that will address in a satisfactory way all the expected *physics* of the bath-mode effects on the dynamics. The issue is partly technical, because we are after a *tractable*, rather than just a “foundational” answer. It is well accepted that the emergence of irreversibility cannot be treated within tractable and calculationally convenient approaches derived directly from the microscopic dynamics: phenomenology has to be appealed to. However, even allowing for phenomenological solutions, all the known tractable schemes yielding the indirect exchange interaction, treat thermalization in a cavalier way, resulting typically in noise terms corresponding to getting the infinite temperature limit at large times, which thus artificially avoids the issue of which H_S should enter in Eq. (7), whereas the established schemes that yield thermalization at large times, lose some intermediate- and short-time dynamical effects.

We have just discussed the challenges in formulating unified treatments that will cover all or most of the interesting dynamical effects for various time scales, from short to intermediate (for induced interaction effects and pure decoherence) to large (for the onset of thermalization), providing a tractable calculational (usually perturbative, many-body) scheme. This discussion also alludes to several other interesting conceptual challenges in the theory of open quantum systems.

Let us presently comment on the issue of the bath-mode interactions with each other, as well as with impurities, the latter particularly important and experimentally relevant [45,54] for conduction electrons as carriers of the indirect-exchange interaction. Indeed, the traditional treatment of open quantum systems has assumed noninteracting bath modes. When the bath mode interactions had to be accounted for, we have treated the added effects either perturbatively [6], or, for strong interaction, such as Luttinger-liquid electrons in a 1D channel, we took [12] the collective excitations as the new “bath modes.” Generally, however, especially in Markovian schemes, one has to seek approaches that do not involve certain double-counting. Indeed, the assumption that the bath modes are at a fixed

temperature, could be possibly considered as a partial accounting for the effects of the mode-mode and mode-impurity interactions, because these interactions can contribute to thermalization of the bath, on par with other influences external to the bath. This may be particularly relevant for phonons that always have strong anharmonicity for any real material. In a way this problem fits with the previous one: We are dealing with effects that can be, on one hand, modeled by added terms in the total Hamiltonian but on the other hand, may be also mixed up in the process of thermalization that is modeled by actually departing from the Hamiltonian description and replacing it with Liouville equations that include noise effects. Recent experimental advances bring these long-standing challenges to the level of application that requires tractable solutions that can be confronted with experimental data.

There are other interesting topics to be considered, for instance, the question of whether additional sources of quantum noise are important? It has recently been established [55] that potential difference between two leads (reservoirs, or baths, of electrons) can be a source of quantum noise, with the potential difference magnitude playing the role of the temperature parameter. What, then, about a system (qubit) coupled to two thermal baths at different temperatures? Will the resulting heat transfer (energy flow between the bath via the system) generate added quantum noise?

As an example of a more practical issue, let us mention the possible effect of the sample geometry on phonon and conduction electron induced relaxation and interactions. We have already explored [12] the one-dimensional aspect of the electron gas in a channel. Indeed, electrons are easy to confine by gate potentials. The situation for phonons, however, is less clear: can geometrical effects modify, and particularly reduce, their quantum-noise generation capacity, or change the induced interactions? Our preliminary studies [50] seem to indicate strong overall geometry dependence. However, the situation is not entirely clear, especially for the strength of the noise effects, and suggests future explorations because recent experiments with double dot nanostructures in Si membranes [56] indicate that true nanosize confinement (due to the sample dimensions) of otherwise long-wavelength modes (in the transverse sample dimensions) is now possible and will have dramatic effect on the phonon spectrum and, as a result, on those physical phenomena that depend on the phonon interactions with electron spins.

Finally, we point out that several recent experiments, e.g. [57-62], have explored aspects of coherence and control in semiconductor nanostructures for quantum computing. While the progress has been impressive, there is no clear “winner” system. It is likely that the future promising designs will be hybrid, based on the presently explored schemes. It is notable that the ensemble-NMR quantum computing approaches have presently reached partial control and manipulation of 12 qubits [63], which allows consideration of “algorithmic” concepts in multi-qubit system design while the other approaches catch up.

To summarize, we have outlined ongoing theoretical research and a selection of challenging open problems to address, in support of the emerging field of quantum information, ultimately aimed at achieving quantum control of multi-qubit systems.

REFERENCES

- [1] A. Fedorov, L. Fedichkin and V. Privman, *Evaluation of Decoherence for Quantum Control and Computing*, J. Comp. Theor. Nanosci. **1**, 132 (2004).
- [2] M. Xiao, I. Martin, E. Yablonovitch and H. W. Jiang, *Electrical Detection of the Spin Resonance of a Single Electron in a Silicon Field-Effect Transistor*, Nature **430**, 435 (2004).
- [3] I. Martin, D. Mozyrsky and H. W. Jiang, *A Scheme for Electrical Detection of Single-Electron Spin Resonance*, Phys. Rev. Lett. **90**, 018301 (2003).
- [4] N. J. Craig, J. M. Taylor, E. A. Lester, C. M. Marcus, M. P. Hanson and A. C. Gossard, *Tunable Nonlocal Spin Control in a Coupled-Quantum Dot System*, Science **304**, 565 (2004).
- [5] V. Privman, I. D. Vagner and G. Kventsel, *Quantum Computation in Quantum-Hall Systems*, Phys. Lett. A **239**, 141 (1998).
- [6] D. Mozyrsky, V. Privman and I. D. Vagner, *Nuclear-Spin Qubit Dephasing Time in the Integer Quantum Hall Effect Regime*, Phys. Rev. B **63**, 085313 (2001).
- [7] D. Mozyrsky, V. Privman and M. L. Glasser, *Indirect Interaction of Solid-State Qubits via Two-Dimensional Electron Gas*, Phys. Rev. Lett. **86**, 5112 (2001).
- [8] V. Privman, *Initial Decoherence of Open Quantum Systems*, J. Stat. Phys. **110**, 957 (2003).
- [9] V. Privman, *Short-Time Decoherence and Deviation from Pure Quantum States*, Modern Phys. Lett. B **16**, 459 (2002).
- [10] Review: L. Fedichkin and V. Privman, *Quantitative Treatment of Decoherence*, Ch. 8 in: *Electron Spin Resonance and Related Phenomena in Low Dimensional Structures*, Pages 137-162, edited by M. Fanciulli, Topics in Applied Physics **115** (Springer, Berlin, 2009).
- [11] D. Tolkunov, V. Privman and P. K. Aravind, *Decoherence of a Measure of Entanglement*, Phys. Rev. A **71**, 060308 (2005).
- [12] D. Mozyrsky, A. Dementsov and V. Privman, *Quantum Dynamics of Spins Coupled by Electrons in One-Dimensional Channel*, Phys. Rev. B **72**, 233103 (2005).
- [13] D. Solenov, D. Tolkunov and V. Privman, *Coherent Interaction of Spins Induced by Thermal Bosonic Environment*, Phys. Lett. A **359**, 81 (2006).
- [14] L. Fedichkin, A. Fedorov and V. Privman, *Additivity of Decoherence Measures for Multiqubit Quantum Systems*, Phys. Lett. A **328**, 87 (2004).
- [15] S. Saikin, D. Mozyrsky and V. Privman, *Relaxation of Shallow Donor Electron Spin due to Interaction with Nuclear Spin Bath*, Nano Lett. **2**, 651 (2002).
- [16] D. Tolkunov and V. Privman, *Short-Time Decoherence for General System-Environment Interactions*, Phys. Rev. A **69**, 062309 (2004).
- [17] K. Blum, *Density Matrix Theory and Applications* (Plenum, NY, 1996).
- [18] N. G. van Kampen, *Stochastic Processes in Physics and Chemistry* (Elsevier, Amsterdam, 2004), Chapter XVII.
- [19] P. Zanardi, *Dissipative Dynamics in a Quantum Register*, Phys. Rev. A **56**, 4445 (1997).
- [20] Y. Makhlin, G. Schön and A. Shnirman, *Josephson-Junction Qubits*, Fort. Phys. **48**, 1043 (2000).
- [21] A. A. Clerk, S. M. Girvin, A. K. Nguyen and A. D. Stone, *Resonant Cooper-Pair Tunneling: Quantum Noise and Measurement Characteristics*, Phys. Rev. Lett. **89**, 176804 (2002).

- [22] C. J. Wellard and L. C. L. Hollenberg, *Thermal Noise in a Solid State Quantum Computer*, J. Phys. D **35**, 2499 (2002).
- [23] J. M. Martinis, S. Nam, J. Aumentado, K. M. Lang and C. Urbina, *Decoherence of a Superconducting Qubit due to Bias Noise*, Phys. Rev. B **67**, 094510 (2003).
- [24] T. Itakura and Y. Tokura, *Dephasing due to Background Charge Fluctuations*, Phys. Rev. B **67**, 195320 (2003).
- [25] S. A. Gurvitz, L. Fedichkin, D. Mozyrsky and G. P. Berman, *Relaxation and the Zeno Effect in Qubit Measurements*, Phys. Rev. Lett. **91**, 066801 (2003).
- [26] A. J. Berkley, H. Xu, M. A. Gubrud, R. C. Ramos, J. R. Anderson, C. J. Lobb and F. C. Wellstood, *Decoherence in a Josephson-Junction Qubit*, Phys. Rev. B **68**, 060502 (2003).
- [27] A. Shnirman and Y. Makhlin, *Quantum Zeno Effect in Cooper-Pair Transport through a Double-Island Josephson System*, JETP Lett. **78**, 447 (2003).
- [28] T. Itakura and Y. Tokura, *Effect of Multiple Charge Traps on Dephasing Rates of a Josephson Charge Qubit System*, J. Phys. Soc. Japan **72**, 2726 (2003).
- [29] E. M. Chudnovsky, *Universal Decoherence in Solids*, Phys. Rev. Lett. **92**, 120405 (2004).
- [30] G. Ithier, E. Collin, P. Joyez, P. J. Meeson, D. Vion, D. Esteve, F. Chiarello, A. Shnirman, Y. Makhlin, J. Schrieffer and G. Schön, *Decoherence in a Superconducting Quantum Bit Circuit*, Phys. Rev. B **72**, 134519 (2005).
- [31] X. T. Liang, *Short-Time Decoherence of Josephson Charge Qubits in Ohmic and 1/f Noise Environment*, Physica C **432**, 231 (2005).
- [32] C. Calero, E. M. Chudnovsky and D. A. Garanin, *Field Dependence of the Electron Spin Relaxation in Quantum Dots*, Phys. Rev. Lett. **95**, 166603 (2005).
- [33] E. Paladino, M. Sassetti, G. Falci and U. Weiss, *Pure Dephasing due to Damped Bistable Quantum Impurities*, Chem. Phys. **322**, 98 (2006).
- [34] Y. M. Galperin, B. L. Altshuler, J. Bergli and D. V. Shantsev, *Non-Gaussian Low-Frequency Noise as a Source of Qubit Decoherence*, Phys. Rev. Lett. **96**, 097009 (2006).
- [35] M. Mottonen, R. de Sousa, J. Zhang and K. B. Whaley, *High-Fidelity One-Qubit Operations under Random Telegraph Noise*, Phys. Rev. A **73**, 022332 (2006).
- [36] D. Nghiem and R. Joynt, *Exact Solution of Qubit Decoherence Models by a Transfer Matrix Method*, Phys. Rev. A **73**, 032333 (2006).
- [37] J. H. Kim, R. P. Dhungana and K. S. Park, *Decoherence in Josephson Vortex Quantum Bits: Long-Josephson-Junction Approach to a Two-State System*, Phys. Rev. B **73**, 214506 (2006).
- [38] B. Dong, N. J. M. Horing and X. L. Lei, *Qubit Measurement by a Quantum Point Contact: a Quantum Langevin-Equation Approach*, Phys. Rev. B **74**, 033303 (2006).
- [39] D. Solenov and V. Privman, *Evaluation of Decoherence for Quantum Computing Architectures: Qubit System Subject to Time-Dependent Control*, Int. J. Modern Phys. B **20**, 1476 (2006).
- [40] F. H. L. Koppens, C. Buizert, K. J. Tielrooij, I. T. Vink, K. C. Nowack, T. Meunier, L. P. Kouwenhoven and L. M. K. Vandersypen, *Driven Coherent Oscillations of a Single Electron Spin in a Quantum Dot*, Nature **442**, 766 (2006).
- [41] Review: V. Privman, *Onset of Decoherence in Open Quantum Systems*, Proc. SPIE **5115**, 345 (2003).
- [42] W. H. Louisell, *Quantum Statistical Properties of Radiation* (Wiley, 1973).
- [43] A. Abragam, *Principles of Nuclear Magnetism* (Clarendon Press, 1983).
- [44] C. P. Slichter, *Principles of Magnetic Resonance* (Springer, 1991).
- [45] M. R. Sakr, H. W. Jiang, E. Yablonovitch and E. T. Croke, *Fabrication and Characterization of Electrostatic Si/SiGe Quantum Dots with an Integrated Read-out Channel*, Appl. Phys. Lett. **87**, 223104 (2005).
- [46] C. Piermarocchi, P. Chen, L. J. Sham and D. G. Steel, *Optical RKKY Interaction between Charged Semiconductor Quantum Dots*, Phys. Rev. Lett. **89**, 167402 (2002).
- [47] D. Braun, *Creation of Entanglement by Interaction with a Common Heat Bath*, Phys. Rev. Lett. **89**, 277901 (2002).
- [48] D. Porras and J. I. Cirac, *Effective Quantum Spin Systems with Trapped Ions*, Phys. Rev. Lett. **92**, 207901 (2004).
- [49] Y. Rikitake and H. Imamura, *Decoherence of Localized Spins Interacting via RKKY Interaction*, Phys. Rev. B **72**, 033308 (2005).
- [50] D. Solenov, D. Tolkunov and V. Privman, *Exchange Interaction, Entanglement and Quantum Noise Due to a Thermal Bosonic Field*, Phys. Rev. B **75**, 035134 (2007).
- [51] T. Yu and J. H. Eberly, *Finite-Time Disentanglement via Spontaneous Emission*, Phys. Rev. Lett. **93**, 140404 (2004).
- [52] W. K. Wootters, *Entanglement of Formation of an Arbitrary State of Two Qubits*, Phys. Rev. Lett. **80**, 2245 (1998).
- [53] V. Privman, D. Solenov and D. Tolkunov, *Onset of Entanglement and Noise Cross-Correlations in Two-Qubit System Interacting with Common Bosonic Bath*, in: Proc. Conf. ICSICT-2006, Part 2, 1054, edited by T.-A. Tang, G.-P. Ru and Y.-L. Jiang (IEEE Press, Piscataway, NJ, 2006).
- [54] H. W. Jiang, *private communication*.
- [55] D. Mozyrsky and I. Martin, *Quantum-Classical Transition Induced by Electrical Measurement*, Phys. Rev. Lett. **89**, 018301 (2002).
- [56] P. Zhang, E. Tevaarwerk, B.-N. Park, D. E. Savage, G. K. Celler, I. Knezevic, P. G. Evans, M. A. Eriksson and M. G. Lagally, *Electronic Transport in Nanometre-Scale Silicon-on-Insulator Membranes*, Nature **439**, 703 (2006).
- [57] M. H. Mikkelsen, J. Berezovsky, N. G. Stoltz, L. A. Coldren and D. D. Awschalom, *Optically Detected Coherent Spin Dynamics of a Single Electron in a Quantum Dot*, Nature Phys. **3**, 770 (2007).
- [58] K. C. Nowack, F. H. L. Koppens, Y. V. Nazarov and L. M. K. Vandersypen, *Coherent Control of a Single Spin with Electric Fields*, Science **318**, 1430 (2007).
- [59] E. A. Laird, C. Barthel, E. I. Rashba, C. M. Marcus, M. P. Hanson and A. C. Gossard, *Hyperfine-Mediated Gate-Driven Electron Spin Resonance*, Phys. Rev. Lett. **99**, 246601 (2007).
- [60] S. Amasha, K. MacLean, I. P. Radu, D. M. Zumbühl, M. A. Kastner, M. P. Hanson, and A. C. Gossard, *Electrical Control of Spin Relaxation in a Quantum Dot*, Phys. Rev. Lett. **100**, 046803 (2008).
- [61] D. Press, T. D. Ladd, B. Zhang and Y. Yamamoto, *Complete Quantum Control of a Single Quantum Dot Spin Using Ultrafast Optical Pulses*, Nature **456**, 218 (2008).
- [62] D. J. Reilly, J. M. Taylor, J. R. Petta, C. M. Marcus, M. P. Hanson and C. Gossard, *Suppressing Spin Qubit Dephasing by Nuclear State Preparation*, Science **321**, 817 (2008).
- [63] C. Negrevergne, T. S. Mahesh, C. A. Ryan, M. Ditty, F. Cyr-Racine, W. Power, N. Boulant, T. Havel, D. G. Cory and R. Laflamme, *Benchmarking Quantum Control Methods on a 12-Qubit System*, Phys. Rev. Lett. **96**, 170501 (2006).

New Method for Representation of Multi-qubit Systems Using Fractals

Mate Galambos

Department of Telecommunications
 Budapest University of Technology and Economics
 Budapest, Hungary
 e-mail: mate.galambos@mcl.hu

Sandor Imre

Department of Telecommunications
 Budapest University of Technology and Economics
 Budapest, Hungary
 e-mail: imre@hit.bme.hu

Abstract—Visual representation is essential to share ideas, interpret previous achievements or formulate new algorithms quickly and intuitively, however most representations of multi-qubit systems either conceal the properties of individual qubits or fail to visualize entanglement. This study discusses a representation that overcomes these problems through the methodology of fractals. The proposed method visualizes individual qubits as constants of the fractal that corresponds to the whole system. The statistical self similarity allows the total number of qubits to be flexible, making it easy to study subsystems. Generalization of this method through labeled signed binary trees is also presented which makes it possible to create other representations with similar properties.

Keywords - Quantum information; representation; visualization; fractals; binary trees

I. INTRODUCTION

Quantum informatics and communications already promises applications that outperform classical solutions, e.g. Shor's prime factorization [1], the unconditional security of quantum cryptography [2], or practical realization of quantum communication [3]. It is also likely that this discipline will become even more important during the upcoming years. However, quantum mechanics is well-known for its counterintuitive nature that is hard to visualize thus making it problematic to quickly share ideas, interpret previous achievements, or formulate new algorithms quickly and intuitively.

In order to be able to solve these issues, a visual representation could be useful. The Bloch-sphere sufficiently represents one qubit [4] [5], or more qubits that are separable, but entanglement – one of the most important phenomena in quantum informatics – eludes this type of visualization.

Another possible approach is to use objects that have enough degree of freedom to represent the whole system. However this method usually conceals the inner structure, and does not give us an idea of what happens if we measure the state of few qubits instead of the whole system (a method used in many algorithms and protocols). This approach does not handle well those cases where the addition of more qubits is decided or when dividing the system into smaller parts.

There are also methods to generalize the Bloch-sphere through the mathematical structure called Hopf-Fibrations [6], but the arising geometrical structures are vastly complex

and hard to read, thus making the method useless as a visualization technique.

An ideal visualization scheme would preserve the mathematical structure of a multi-qubit system in a way that is easy to interpret by the naked eye using compact and two dimensional images. The ideal solution should also give at least some insight to the states of single qubits, would work for any finite number of qubits, as well as it should work show entanglement. This study aims to give an example of such a scheme based on fractals and a generalization rule to construct other schemes alike.

This paper is organized as follows: Section I introduces visualization of quantum states. Section II presents the new proposed approach using fractals. Section III generalizes this approach through labeled signed binary trees. Finally, Section IV concludes the paper.

II. FRACTAL-BASED REPRESENTATION

For the sake of clarity, the cases of single and multiple qubits should be presented separately.

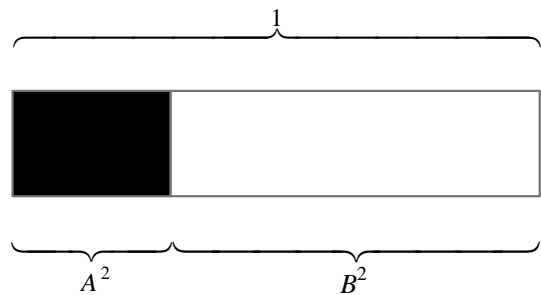


Figure 1. Representation of a single qubit (without phase). The respective lengths A^2 and B^2 of the black and white sides of the bar correspond to the probability of a measurement on the qubit yielding the bit value 0 or 1.

A. Single qubits

Let us write the probability amplitudes in an exponential form:

$$|\varphi\rangle = A \cdot \exp(i \cdot \alpha) \cdot |0\rangle + B \cdot \exp(i \cdot \beta) \cdot |1\rangle, \quad (1)$$

$$A^2 + B^2 = 1. \quad (2)$$

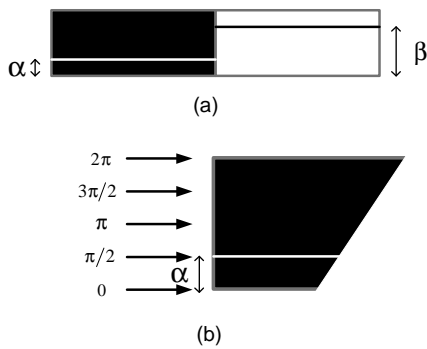


Figure 2. Representing the phase of a single qubit. (a) The vertical position of the lines on each part of the bar represents the phase. (b) An enlarged version of the bar's left side shows the phase. The bottom of the bar corresponds to 0 and the top to 2π .

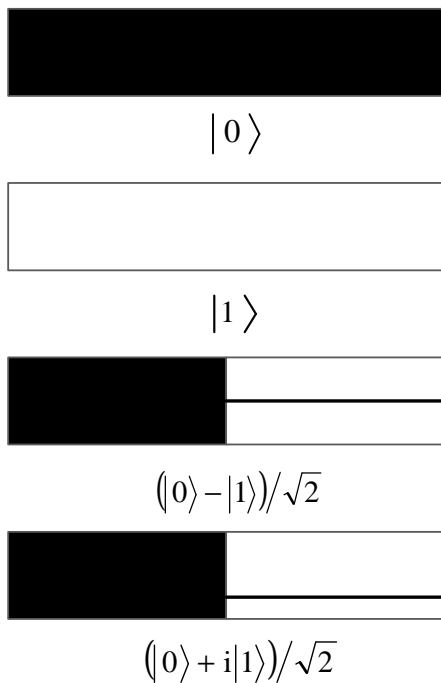


Figure 3. A few simple examples of single qubits.

Let us draw a horizontal bar and then using a vertical gray line divide it into a black and a white side with respective lengths of A^2 and B^2 where the total length of the stripe is considered 1. This should give the probabilities of a measurement on the qubit producing the value 0 or 1. To avoid ambiguity, the black part of the bar corresponding to the measurement yielding 0 should always be placed first, and the white part corresponding to the measurement value 1 should be placed second, thus representing them in ascending order.

A gray frame should also be added to the bar so that the white part can be easily seen in front of a white background.

To visualize the phase let's draw horizontal lines on the black and white parts of the bar, each with the opposite color (black on white and white on black), in a way, that the vertical position of the line represents α and β (the bottom of each stripe should correspond to 0 and the top to 2π).

B. Multiple qubits

To visualize multiple qubits statistically self-similar fractals should be constructed using the bars described in the previous section. It is well known that the complexity of a quantum system grows quickly as function of the number of qubits, but the complexity of a fractal can match this growth: every newly added qubit means a further iteration step in constructing the fractal representing our quantum system.

Therefore, at first, the qubits should be numbered in the order they will be measured at the end of our protocol. Multi qubit systems whose qubits are separable and whose are not should also be distinguished.

For separable qubits the representation of the whole system can be done, by simply copying the scaled down version of the bar corresponding to the subsequent qubit, under each part of the previous bars.

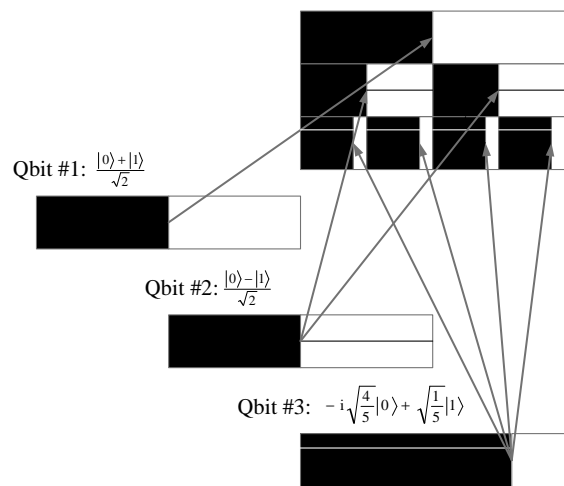


Figure 4. Fractal representation of a multi-qubit system and the separable qubits that serve as its building blocks. Note that although the fractal displays stochastic attributes this is due to the varying building blocks that are not influenced by the construction process (which is deterministic).

In terms of the Lindenmayer system the representation of separable qubits can be formulated as follows:

Let the n^{th} qubit be:

$$|\Phi_n\rangle = A_n \cdot \exp(i \cdot \alpha_n) \cdot |0\rangle + B_n \cdot \exp(i \cdot \beta_n) \cdot |1\rangle. \quad (3)$$

Let us denote the bar representing this qubit by $C_n(w)$ where w stands for the total width of the bar. Let the constants of the fractals be the $C_n(w)$ bars as described above, except for the bottom part of the gray frame on each

(black and white) sides. Let the variables be the bottom parts of the gray frame denoted by D_n^j with respective lengths of L_n^j where the index j runs from 1 to 2^n (odd indexes corresponding to the bottom parts of black and even indexes to the white sides of each bars).

Let the initiator be a straight horizontal gray line D_0^0 , with the length of $L_0^0 = 1$, and the production rule be $(D_n^j \rightarrow C_{n+1}(L_n^j))$ for all j .

Sticking to the convention that the black side is followed by the white on each bar, the widths on the resulting figure from left to right will give us the probabilities of measuring a bit string in ascending order.

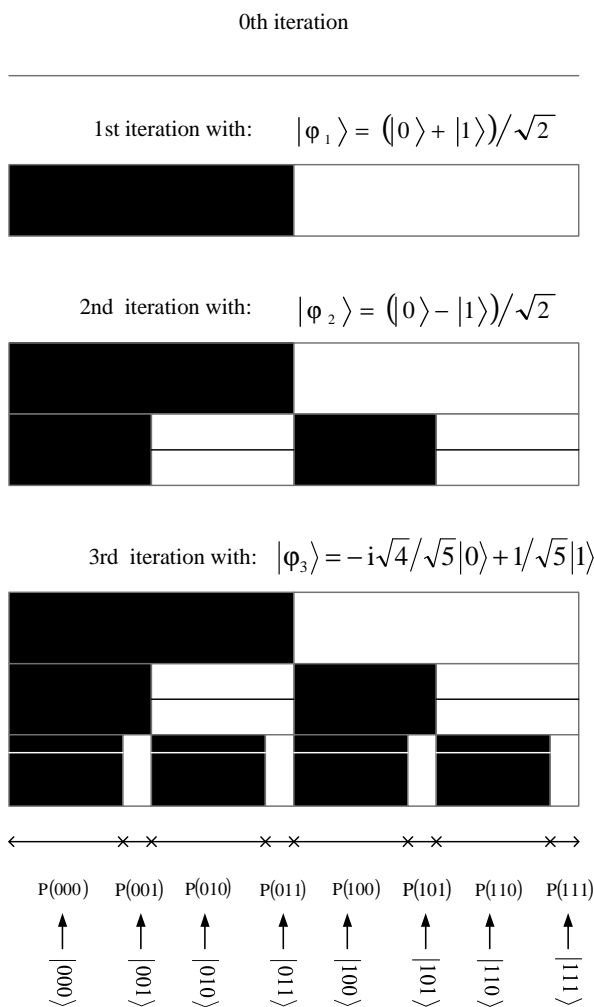


Figure 5. Iterational steps of the fractal representation. The width of the lowermost part of the bars represents the probability of a measurement yielding the value represented by the colors of the parts above it. (Read from top to bottom black means 0, white means 1.) To identify the individual qubits, compare with Figure 4.

However, there is another way of representing the phase. Sometimes, it is more useful to draw figures with all the

phase information in the bars of the last iteration. This kind of representation will be equivalent to the description of the whole system using bracket formalism. If the state of the multi-qubit system is:

$$\begin{aligned}
 |\phi\rangle &= A_{00\dots 0} \cdot \exp(i \cdot \alpha_{00\dots 0}) \cdot |00\dots 0\rangle \\
 &+ A_{00\dots 1} \cdot \exp(i \cdot \alpha_{00\dots 1}) \cdot |00\dots 1\rangle + \dots \\
 &+ A_{11\dots 1} \cdot \exp(i \cdot \alpha_{11\dots 1}) \cdot |11\dots 1\rangle,
 \end{aligned}
 \tag{4}$$

then the representation with this inherited phase can be drawn as follows. Let the black and white parts of the bar read from top to bottom indicate bit values in a certain i^{th} term of the sum (i being a binary number). Let the width of these parts (or to be more precise the width of the undermost part) be A_i^2 , where the total width of all the bars is considered 1. Let the phase in this undermost part be represented by the height of a horizontal line of opposite color as described in part A.

$$\begin{aligned}
 |\phi\rangle &= A_{00\dots 0} \cdot \exp(i \cdot \alpha_{00\dots 0}) \cdot |00\dots 0\rangle \\
 &+ A_{00\dots 1} \cdot \exp(i \cdot \alpha_{00\dots 1}) \cdot |00\dots 1\rangle + \dots \\
 &+ A_{11\dots 1} \cdot \exp(i \cdot \alpha_{11\dots 1}) \cdot |11\dots 1\rangle
 \end{aligned}$$

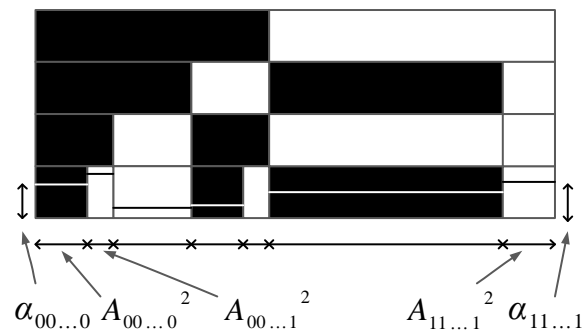


Figure 6. Representation using the collapsed phase. This is equivalent to the bracket description of the whole system. Note that some of the color combinations are missing from the graphs, meaning their width (and detection probability) is zero. One such combination is white, white, white, black (read from top to bottom), meaning the measurement will never yield 1110.

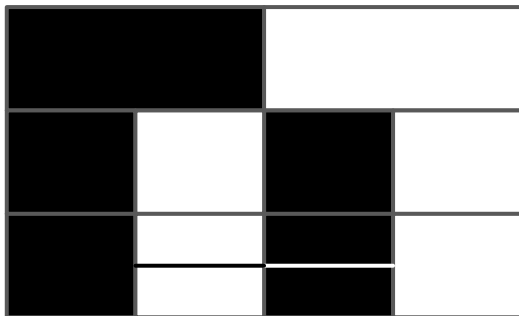
Converting the previous, recursively defined version of the representation to the non-inherited phases can be done by adding all the phases above each other and drawing a horizontal line on the lowermost bar in the height of the sum (where the bar is considered a torus due to 2π periodicity).

This kind of inherited phase can be useful because all the phase information is at the lowermost bars, and not separable states cannot be represented otherwise.

While the inherited phase version is equivalent to the bracket description in a sum form, the non-inherited phase form of separable qubits is equivalent to a tensor product form, and of course many transitional 'mixed' stages are possible between the two.

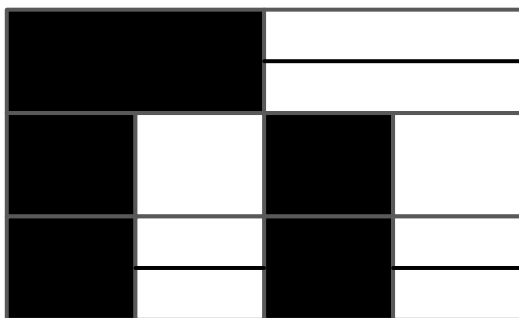
These mixed representations can be constructed with the same iterative process as the non-inherited phase variants, but they use the inherited phase representation as building blocks instead of the bars representing single qubits. (Of course, if a single qubit is separable from the whole system than its inherited phase, non-inherited phase and single bar representation are the same.)

$$|\phi\rangle = \frac{|000\rangle - |011\rangle - |100\rangle + |111\rangle}{2}$$



(a)

$$|\phi\rangle = \frac{|0\rangle - |1\rangle}{\sqrt{2}} \otimes \frac{|00\rangle - |11\rangle}{\sqrt{2}}$$



(b)

Figure 7. Possible representations of the same multi-qubit system. (a) In the inherited phase version it is easy to read the phase of the total qubit triplets, making this useful in case when a phase-sensitive measurement or operation is performed on the whole system. (b) The partially inherited phase representation is useful when the first qubit is treated separately from the other two. Note that the inherited phase representation can only be used in case of separable qubits, thus the last two qubits that are entangled, cannot be represented that way, making this mixed representation a ‘maximally non-inherited’ one.

III. GENERALIZATION THROUGH BINARY TREES

The previously described representation is only one of many possibilities.

To construct another one, first we need to choose a building block that can represent a complex number. It is best to choose the blocks to have one more degree of freedom that can symbolize a binary value. Two blocks are needed to represent a single qubit, although the two can be handled as one object. For example in case of the representation described in Section II, the blocks symbolizing complex numbers are the sides of the bars, the additional degree of freedom is their color, and two of these (with opposite color) are handled as a single bar. Instead of these bars the two complex numbers could be represented using the Bloch-sphere although it is not the best choice since two dimensional representations are easier to interpret, and squared shapes are easier to pack compactly.

To represent multiple qubits a rule is needed that makes it possible to connect two of the building blocks representing complex numbers to each previous block. The resulting structure will be equivalent to a signed, labeled binary tree, where the labels are complex numbers. The signs will correspond to the bit values, although if the blocks representing complex numbers have an additional degree of freedom, it does not have to be visualized through the connection rule.

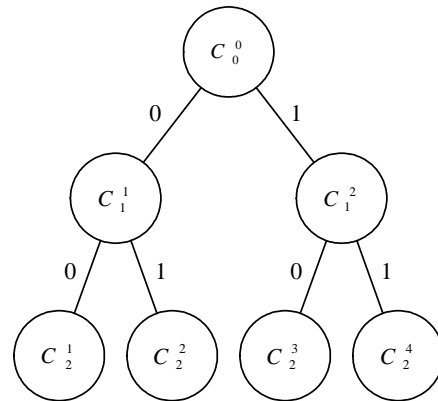


Figure 8. Other representations can be constructed, which are equivalent to a signed labeled binary tree whose labels are complex numbers.

The labels can be calculated either in a fashion when they inherit some of the properties of their ancestors, or in a way when they do not. The later can only be done for separable qubits but can be used to illustrate individual states of single qubits. In this case the n^{th} level of the tree will correspond to the n^{th} qubit, and the label C_n^j will correspond to the probability amplitude of qubit value 0 if j is odd, and 1 if even (where j runs from 1 to 2^n). In the inheriting case the label C_n^j will correspond to the complex number that can be calculated as the product of the probability amplitude described in the non-inheriting case and every other probability amplitude corresponding to the ancestors of that

particular node. This method is useful for representing the system as a whole, and compresses most of the information in the labels of the leaf nodes.

Mixed representations are also possible, as described in Section II. Note that in the first representation the width (and thus the detection probability) is always inherited while the phase can be inherited, not inherited or mixed, making different attributes of the same complex number behave differently.

It is also worth noting, that the complex number associated with the root should have an absolute value of 1. Although the root can represent the global phase, it is not necessary to describe a multi-qubit system, and as such it was not used in the first representation.

IV. CONCLUSION

As discussed, fractals self-similarity and complexity make them ideal candidates for representing multi-qubit systems. In the present paper the properties of an ideal visualization were described, giving an example of such a representation in detail. This representation was generalized through labeled signed binary trees. Even though the two approaches might seem different, these binary trees can be constructed recursively using the methodology of fractals.

ACKNOWLEDGMENT

Special thanks to Laszlo Bacsardi and members of the BME Department of Telecommunication for their helpful comments.

REFERENCES

- [1] P. W. Shor, "Polynomial-Time Algorithms for Prime Factorization and Discrete Logarithms on a Quantum Computer", *SIAM J. Comput.* 26 (5): 1484–1509 (1997)
- [2] C. H. Bennett and G. Brassard, "Quantum cryptography: Public key distribution and coin tossing", *Proc. IEEE International Conference on Comput., Systems and Signal Process.* 1984, pp. 175–179
- [3] L. Bacsardi "Satellite Communication Over Quantum Channel", *Acta Astronautica* 2007: 61(1–6):151–159
- [4] M. Nielsen and I. Chuang, "Quantum Computation and Quantum Information" Cambridge, England: Cambridge University Press, 2000
- [5] S. Imre and B. Ferenc, "Quantum Computing and Communications: An Engineering Approach", Wiley, 2005
- [6] D. Chruscinski, "Geometric Aspects of Quantum Mechanics and Quantum Entanglement", *Journal of Physics: Conference Series* 30 (2006) 9–16

Quantum Structure in Cognition: Fundamentals and Applications

Diederik Aerts, Sandro Sozzo
 Center Leo Apostel for Interdisciplinary Studies
 Vrije Universiteit Brussel
 Krijgskunderstraat 33, B-1160 Brussels, Belgium
 diraerts@vub.ac.be, ssozzo@vub.ac.be

Liane Gabora, Tomas Veloz
 Department of Psychology and Computer Science
 University of British Columbia
 Okanagan Campus, 3333 University Way, Kelowna, Canada
 liane.gabora@ubc.ca, tomas.veloz@ubc.ca

Abstract—Studies in cognitive science show that the ways in which people combine concepts and make decisions cannot be described by classical logic and probability theory. This has serious implications for applied disciplines such as information retrieval, artificial intelligence and robotics. Inspired by a mathematical formalism that generalizes quantum mechanics we have constructed a contextual framework for modeling both concept representation and decision making, together with quantum models that are in strong alignment with experimental data. The results can be interpreted by assuming the existence in human thought of a double-layered structure, a classical logical thought and a quantum conceptual thought, the latter being responsible for the non-classical effects. The presence of a quantum structure in cognition is relevant, for it shows that quantum mechanics provides not only a useful modelling tool for experimental data but also supplies a structural model for human and artificial thought processes. This approach has strong connections with theories formalizing meaning, such as semantic analysis, and has also a deep impact on computer science, information retrieval and artificial intelligence. Specific links with information retrieval are discussed in this paper.

Keywords—quantum mechanics; quantum cognition; decision theory; information retrieval;

I. INTRODUCTION

The aim of this article is to present to the community of quantum technology researchers a newly emerging approach to the modelling of human and artificial thought processes that makes use of the formalism of quantum mechanics. We will introduce and describe the main aspects of this approach which though well developed has not yet been applied to technological problems. There is a community of researchers, physicists, computer scientists and psychologists, focusing on this approach, and the emerging domain of research has been called ‘Quantum Cognition’ [1]. It outlines the application of the formalism of quantum mechanics to situations that traditionally are a subject of investigation in cognitive science, artificial intelligence and semantic theories. More specifically, it aims at modelling entities and/or processes of a cognitive nature, and also puts forward potential solutions to some difficult problems in cognitive science, artificial intelligence, semantic theories and information retrieval. Some interesting technological applications of our perspective to symbolic artificial intelligence and

robotics will be outlined in a forthcoming paper [4]. We focus here on the applications in knowledge representation and with respect to information retrieval.

Let us briefly summarize this paper. In Sec. II we report the problems and paradoxes discovered in decision theory and cognitive science, such as the *Allais* and *Ellsberg paradoxes*, the *disjunction effect* and the *conjunction fallacy*, and the *Pet-Fish problem*. In particular, we stress in this section that these difficulties required a significant change of perspective in our understanding of the role played by classical logic in human thought. In Sec. III we show how the quantum approach is used to model the contextual manner in which concepts interact and combine. Contextuality makes it possible to elaborate quantum models for the above mentioned paradoxes which correctly reproduce the experimental data existing in the cognitive science literature. An explanation of the obtained results can be given by assuming that two differently structured and superposed, *classical logical* and *quantum conceptual*, modes coexist in human thought and their simultaneous presence is responsible of the failures of classical structures to cope with the aforementioned difficulties. Finally, we discuss in Sec. IV the fact that our quantum cognition approach supplies an intuitive basis for the application of the quantum formalism in information retrieval, which is thus more firmly founded.

II. NON-CLASSICAL EFFECTS IN ECONOMICS AND PSYCHOLOGY

Some of the effects in cognition which the quantum cognition community has identified as requiring quantum structures to be modeled were first observed by economists. In two seminal papers Maurice Allais [5] in 1953 and Daniel Ellsberg [6] in 1961 observed that experimental situations exist in economics that are inconsistent with the traditional economic theory of rational choice, namely violations of the so-called *Sure-Thing Principle* [7] and the *expected utility hypothesis* [8], [9]. These deviations, often called paradoxes, were identified as indicating the existence of an *ambiguity aversion*; that is, individuals prefer ‘sure choices’ over ‘choices that contain ambiguity’ and ‘risk taking’. Although it was not (explicitly) identified at the time, they could not be explained by classical logic and probability theory.

However, solutions to them have been proposed within the new field of quantum cognition.

The second identification of effects of a non-classical nature was in psychology, and Amos Tversky and Daniel Kahneman played a crucial role in them [10]. The effects brought to light by them have meanwhile been studied extensively and are referred to as the *conjunction fallacy* [11] and the *disjunction effect* [12]. However, the fundamental contradiction of these effects with classical logic and probability theory, although identified at the time, was not believed to be the core of the problem.

The domain where most manifestly the classical set-theoretical based structures were identified to be failing was in the study of 'how concepts combine'. This was revealed by James Hampton's experiments [13], [14] which measured the deviation from classical set-theoretic membership weights of exemplars with respect to pairs of concepts and their conjunction or disjunction. Hampton's investigation was motivated by the so-called *Guppy effect* in concept conjunction found by Osherson and Smith [15]. These authors considered the concepts *Pet* and *Fish* and their conjunction *Pet-Fish*, and observed that, while an exemplar such as *Guppy* was a very typical example of *Pet-Fish*, it was neither a very typical example of *Pet* nor of *Fish*. Therefore, the typicality of a specific exemplar with respect to the conjunction of concepts can show an unexpected behavior from the point of view of classical set and probability theory. As a result of the work of Osherson and Smith, the problem is often referred to as the *Pet-Fish problem*. It can be shown that neither fuzzy set based theories [16], [17] nor explanation based theories [18], [19] can model this 'typicality effect'. Hampton identified a Guppy-like effect for the membership weights of exemplars with respect to pairs of concepts and their conjunction [13], and equally so for the membership weights of exemplars with respect to pairs of concepts and their disjunction [14], e.g., *Olive* is found to be a not very strong member of *Fruits* and also a not very strong member of *Vegetables*, but it is a very strong member of *Fruits 'or' Vegetables*. The empirical deviations from the expectations of fuzzy set theory are referred to as *overextension* and *underextension*. Several experiments have since been conducted (see, e.g., [20]) but none of the currently existing concepts theories provides a satisfactory description or explanation of these effects. The combination problem is considered so serious that it is sometimes said that not much progress is possible in the field if no light is shed on this problem [19], [20], [21].

Each of the previous problems share a common feature: they have to do with modelling meaning and the structure of human thought, hence a solution to these problems could shed a new light on some disciplines that try to reproduce what happens in human mind, such as artificial intelligence and robotics (see [4]).

III. QUANTUM STRUCTURE IN HUMAN THOUGHT

This section summarizes the results achieved by our research group on quantum cognition. For the sake of clarity, we proceed by steps.

A. Statistical studies of decision processes

Hypothesizing the presence of non-classical logical and probabilistic structures in human thought one of us proposed a quantum model for the modeling of a decision process during an opinion poll [22]. The inspiration for this proposal came primarily from an extensive study carried out on the nature of the quantum probability model [23], [24], and the becoming aware of the exact and detailed difference between classical probability and quantum probability.

This perspective suggested that classical probabilistic structures model only situations that are deterministic in essence, and where the observers 'lack knowledge about'. Situations of this kind may occur also in quantum mechanics, but this theory predicts the existence of situations that are indeterministic in depth, in the sense they do not admit an underlying deterministic process independent of context. For example, in a measurement process the result of the measurement cannot be attributed to the physical entity that is measured, hence the probability of that result in a given state cannot be interpreted as formalizing a subjective lack of knowledge about the entity. It is the interaction of the measured entity with the measurement context that determines the result of the measurement. As a consequence, the measurement context provokes an indeterministic influence on the physical entity, and quantum probability models this indeterminism.

Whenever the above reasoning is applied to decision processes, it can be shown that models of decision making are quantum in essence, because opinions are not always determined 'before the testing of these opinions take place', and can hence in principle easily be influenced by the testing itself [22]. This is evident if one considers an opinion poll, that is, a testing of the dynamics of human decision making with statistics. For certain questions, for example a question such as 'Are you a smoker or not', the situation for classical probability is satisfied. Indeed, people being tested 'are always smokers or not smokers before the test being applied during the opinion poll'. Hence the test for such type of properties only consists of lifting a lack of knowledge. However, if one considers another type of question, e.g., 'Are you against or in favor of the use of nuclear energy', then it seems to be a better hypothesis about the reality of the states of mind of human beings that there are three cases now (i) the person's mind is made up already, in favor; (ii) the persons mind if made up already, against; (these are the two 'classical probability situations, the test only lifts lack of knowledge'); (iii) the persons mind is not made up, and formed 'during and hence partly by the test

itself'. It is this third possibility which introduced a 'non-classical probabilistic effect'. As a consequence, human decision making is intrinsically non-classical, and quantum probability is an obvious choice as an alternative to classical probability, since in quantum probability this extra aspect is 'exactly the one that is allowed to exist'.

B. The Pet-Fish problem within a SCOP formalism

The *SCoP formalism* was developed to cope with the difficulties presented in Sec. II. It is a generalization of the quantum formalism and in which context plays a relevant role in both concept representation and decision processes [25], [26]. This role is very similar to the role played by the measurement context on microscopic entities in quantum mechanics. In the SCOP formalism, a concept is an entity that can be in different states, and such that a given context provokes a change of state of the concept. Let S be a concept. We denote by Σ the set of its states, by \mathcal{M} the set of its contexts and by \mathcal{L} the set of its properties. Moreover, we introduce a special state of the concept S called the *ground state*, denoting it by \hat{p} . The ground state can be considered as the state the concept is in when it is not evoked by any particular context. Furthermore, we introduce for a given concept S a *unit context* 1 which describes the situation where no context occurs. A given context e_1 induces a change of state of the concept S from the the ground state \hat{p} to another state, say p_1 . That \hat{p} and p_1 are different states is manifested by the fact that the frequency measures of different exemplars of the concept, as well as the applicability values of the properties of the context are different for different states.

To build a SCOP model we need not only the three sets Σ, \mathcal{M} and \mathcal{L} , that is, the set of states, the set of contexts and the set of properties, respectively, but also two additional functions μ and ν are required. The function μ is a probability function that describes how state p under the influence of context e changes to state q . Mathematically, μ is a function from the set $\Sigma \times \mathcal{M} \times \Sigma$ to the interval $[0, 1]$, where $\mu(q, e, p)$ is the probability that state p under the influence of context e changes to state q . We write:

$$\mu : \Sigma \times \mathcal{M} \times \Sigma \rightarrow [0, 1]; (q, e, p) \mapsto \mu(q, e, p). \quad (1)$$

The function ν describes the weight, i.e. the renormalization of the applicability of a certain property given a specific state. Mathematically, ν is a function from the set $\Sigma \times \mathcal{L}$ to the interval $[0, 1]$, where $\nu(p, a)$ is the weight of property a for the concept in state p . We write:

$$\nu : \Sigma \times \mathcal{L} \rightarrow [0, 1]; (p, a) \mapsto \nu(p, a). \quad (2)$$

Thus a *SCOP model* is defined by the five elements $(\Sigma, \mathcal{M}, \mathcal{L}, \mu, \nu)$. To build a SCOP model, we collect the contexts thought to be relevant to the model we want to build (more contexts lead to a more refined model). \mathcal{M} is the set of these contexts. Starting from the ground state \hat{p} for the

concept, we collect all the new states of the concept formed by having each context $e \in \mathcal{M}$ work on \hat{p} and consecutively on all the other states. This gives the set Σ . Note that \mathcal{M} and Σ are connected in the sense that to complete the model it is necessary to consider the effect of each context on each state. We collect the set of relevant properties of the concept and this gives \mathcal{L} . The functions μ and ν that define the metric structure of the SCOP system have to be determined by means of well chosen experiments.

It follows from the above representation Psychological studies have revealed that concepts change continuously under the influence of a context, and this change is described using SCOP by a change of the state of the concept. For each exemplar of a concept, the typicality varies with respect to the context that influences it. Analogously, for each property, the applicability varies with respect to the context. This implies the presence of both a *contextual typicality* and an *applicability effect*. The *Pet-Fish problem* is solved in the SCOP formalism because in different combinations the concepts are in different states. In particular, in the combination *Pet-Fish* the concept *Pet* is in a state under the context *The Pet is a Fish*. The state of *Pet* under the context *The Pet is a Fish* has different typicalities, which explains the Guppy effect.

C. A quantum model for concept combinations

On the basis of the SCOP formalism, a mathematical model using the formalism of quantum mechanics, both the quantum probability and Hilbert space models, has been worked out. This allows one to reproduce the experimental results obtained by Hampton on conjunctions and disjunctions of concepts. It is interesting to observe that typically quantum effects, i.e. superposition and interference, appear at once if one considers the following simple quantum model for the disjunction of two concepts [28].

Let us consider two concepts A and B . Both A and B are described quantum mechanically in a Hilbert space \mathcal{H} , so that they are represented by the unit vectors $|A\rangle$ and $|B\rangle$ of \mathcal{H} , respectively. We represent the concept 'A or B' by means of the normalized superposition vector $\frac{1}{\sqrt{2}}(|A\rangle + |B\rangle)$, and also suppose that $|A\rangle$ and $|B\rangle$ are orthogonal, i.e. $\langle A|B\rangle = 0$. An experiment considered in Hampton [13], [14] consists of a test aimed at ascertaining whether a specific item X is 'a member of' or 'not a member of' a concept. We represent this experiment by means of a projection operator M_X on the Hilbert space \mathcal{H} . This experiment is applied to the concept A , to the concept B , and to the concept 'A or B', yielding the probabilities $\mu_X(A)$, $\mu_X(B)$ and $\mu_X(A \text{ or } B)$, respectively. These probabilities represent the degrees to which a subject is likely to choose X to be a member of A , B and 'A or B', respectively. In accordance with the quantum rules, these probabilities are

given by $\mu_X(A) = \langle A|M_X|A\rangle$, $\mu_X(B) = \langle B|M_X|B\rangle$ and

$$\mu_X(A \text{ or } B) = \frac{1}{2}(\langle A| + \langle B|)M_X(|A\rangle + |B\rangle). \quad (3)$$

Applying the linearity of Hilbert space and taking into account that $\langle B|M_X|A\rangle^* = \langle A|M_X|B\rangle$, we have

$$\mu_X(A \text{ or } B) = \frac{\mu_X(A) + \mu_X(B)}{2} + \Re\langle A|M_X|B\rangle \quad (4)$$

where $\Re\langle A|M_X|B\rangle$ is the real part of the complex number $\langle A|M_X|B\rangle$. This is called the *interference term* in quantum mechanics. Its presence produces a deviation from the average value $\frac{1}{2}(\mu_X(A) + \mu_X(B))$, which would be the outcome in the absence of interference. It is the interference term that we found to be responsible of the deviations from classically expected membership weights measured by Hampton.

We note that Eq. (4) is not the most general formula for reproducing all empirical data on the disjunction of concepts. To work out a general model for the disjunction of two concepts, we need to introduce the notion of quantum field theory. More precisely, the Hilbert space \mathcal{H} describing the ‘one-particle way’ must be combined with the tensor product Hilbert space $\mathcal{H} \otimes \mathcal{H}$ describing the ‘two-particle way’ to get the Fock space $(\mathcal{H} \otimes \mathcal{H}) \oplus \mathcal{H}$ to explain the emergence of the new concept ‘ A or B ’. The latter is then represented by the normalized vector

$$\psi(A, B) = me^{i\theta}|A\rangle \otimes |B\rangle + \frac{ne^{i\phi}}{\sqrt{2}}(|A\rangle + |B\rangle), \quad (5)$$

where $m^2 + n^2 = 1$, the experiment is described by the projection operator $M_X \otimes M_X \oplus M_M$, and the probabilities representing the degrees to which a subject is likely to choose the item X to be a member of ‘ A or B ’ is given by

$$\mu_X(A \text{ or } B) = m^2(\mu_X(A) + \mu_X(B) - \mu_X(A)\mu_X(B)) + n^2\left(\frac{\mu_X(A) + \mu_X(B)}{2} + \Re\langle A|M_X|B\rangle\right). \quad (6)$$

We do not discuss here the deep reasons for introducing these quantum field aspects, for the sake of brevity. We limit ourselves to observe that, whenever a subject is asked to decide about the membership of an item X with respect to the concept ‘ A or B ’, the subject will consider two identical items X pondering on the membership of one of them with respect to A ‘and’ the membership of the other with respect to B [28].

The above quantum mechanical formalism has been employed [28] to model all the experimental data obtained in Hampton’s experiments [13], [14].

The formulation above identifies the presence of typically quantum effects in the mechanism of combination of concepts, e.g., contextual influence, superposition, interference, emergence and entanglement [27], [28], [29], [30], [33], [34]. Furthermore, quantum models have also been elaborated to describe the disjunction effect and the Ellsberg paradox, which accord with the experimental data existing

in the literature [28], [30], [35]. It has been shown that it is the overall conceptual landscape, or context, that generates the paradoxical situation encountered in real experiments.

D. Superposed layers in human thought

The analysis above has allowed the authors to suggest the hypothesis that two structured and superposed layers can be identified in human thought: a *classical logical layer*, that can be modeled by using a classical Kolmogorovian probability framework, and a *quantum conceptual layer*, that can instead be modeled by using the (non-Kolmogorovian) probabilistic formalism of quantum mechanics. The thought process in the latter layer is given form under the influence of the totality of the surrounding conceptual landscape, hence context effects are fundamental in this layer [30]. We are still clarifying the relationship between these layers of thought and the two modes of thought – analytic and associative – discussed elsewhere [31], [32], as well as their relationship to convergent versus divergent thought, and the notions of explicit versus implicit cognition.

We conclude this section with two remarks. Firstly, we note that in our approach the explanation of the violation of the expected utility hypothesis and the Sure-Thing Principle is not (only) the presence of an ambiguity aversion. On the contrary, we argue that the above violation is due to the concurrence of superposed conceptual landscapes in human minds, of which some might be linked to ambiguity aversion, but other completely not. We therefore maintain that the violation of the Sure-Thing Principle should not be considered as a fallacy of human thought, as often claimed in the literature but, rather, as the proof that real subjects follow a different way of thinking than the one dictated by classical logic in some specific situations, which is context-dependent. Secondly, we observe that according to our approach ‘there is a definite holistic aspect’ related to the structuring of meaning. However, this holistic aspect is not the one mentioned sometimes with reference to ‘quantum consciousness’ or other very speculative related issues, the presence of holism is of a ‘down to earth’ nature and simply revealing that ‘meaning is related to the whole landscape of conceptual, emotional, . . . , content’.

IV. QUANTUM COGNITION AND INFORMATION RETRIEVAL

Quantum mechanical structures have also been used in the domain of information retrieval [36], [37], [38]. An information retrieval system finds relevant information from a collection of information objects, which may be documents, web pages, images, videos, etc. For example, search engine algorithms exploit the link structure of the web besides the lexical content in web pages. Roughly speaking, they mine human decisions about what pages are good to link to for a particular subject. Novel techniques developed since the eighties have shown that vector space based information

retrieval is potentially more powerful than Boolean logic based information retrieval (in particular, key words matching). Recently, vector space models have been extended to incorporate Hilbert spaces together with the representation and manipulation of word meaning. It has been shown, in particular, that it is the quantum logic structure underlying quantum mechanics that is effective in producing theoretical models for information retrieval. Widdows and Peters [37] proved that the use of quantum logic connective for negation, i.e. orthogonality, is a powerful tool for exploring word meaning and it is more efficient than Boolean ‘not’ of classical logic in document retrieval experiments. Van Rijsbergen [38] introduced a general theory for information retrieval based on quantum logic structures. More precisely, he showed that three keystone models used in information retrieval, a vector space model, a probabilistic model and a logical model, can be described within Hilbert space, where a document can be represented by a vector and relevance by a Hermitian operator.

The above results fit in naturally with the quantum cognition approach outlined in Sec. III, which provides theoretical support for the use of the quantum mechanical formalism in information retrieval and natural language processing in terms of the quantum conceptual layer. It is quite reasonable, indeed, to maintain that a given human or artificial system aiming at extracting information and knowledge from a user should be quantum based, since concepts are combined by human minds in such a way that they entail quantum mechanical structure, more specifically, combined concepts are entangled [28], [39]. But there are other strong reasons for claiming the necessity of using contextual quantum based structures in information retrieval, arising from the research developed in our quantum cognition approach. In fact, the following results have been obtained by using search engines on the world-wide-web.

(i) A Guppy-like effect can be identified by collecting data on concepts and their conjunctions using internet search engines. This effect appears as a consequence of the contextual meaning landscape surrounding the concepts considered and their conjunctions [40].

(ii) Some of Bell’s inequalities can be deduced by considering coincidence experiments and gathering data on concepts and their combinations on the world-wide-web. One can show that these inequalities are violated, which reveals the presence of entanglement [41].

We conclude this paper by suggesting a possible line of research. Knowledge organization systems (KOS) play an increasingly important role in modern society [42], [43]. They employ classical structures to model properties and concepts and hence are subject to the difficulties mentioned in Sec. II. But, one could provide a generalized, or ‘quantized’, version of a KOS using a SCOP quantum based formalism for the properties and concepts. Taking into account the preceding analysis, together with the results obtained by van Rijsbergen

and Widdows, we expect that a SCOP version of KOS will give rise to greater adaptiveness and performance.

ACKNOWLEDGMENTS

This research was supported by Grants G.0405.08 and G.0234.08 of the Flemish Fund for Scientific Research and a grant from the Social Sciences and Humanities Research Council of Canada.

REFERENCES

- [1] We stress that in this paper we are mainly concerned with the Brussels approach to Quantum Cognition. Meanwhile, several researchers have been involved in this domain, and we refer to the Wikipedia page [2] and to the Proceedings of the conferences on Quantum Interaction [3] for an overview.
- [2] See the recent wikipedia page on Quantum Cognition: http://en.wikipedia.org/wiki/Quantum_cognition.
- [3] P. Bruza, W. Lawless, K. van Rijsbergen and D. Sofge, D., *Proceedings of the AAI Spring Symposium on Quantum Interaction, Stanford University, US, March 27–29, 2007*. Washington: AAI Press, 2007; P. Bruza, W. Lawless and K. van Rijsbergen, *Second International Symposium, QI 2008, Oxford, UK, March 26–28, 2009, Proceedings*. Oxford: College Publications, 2008; P. Bruza, D. Sofge, W. Lawless, K. van Rijsbergen and M. Klusch, *Third International Symposium, QI 2009, Saarbrücken, Germany, March 25–27, 2009, Proceedings*, LNCS, Vol. 5494. Berlin: Springer, 2009.
- [4] D. Aerts, M. Czachor, and S. Sozzo, “Quantum interaction approach in cognition, artificial intelligence and robotics,” in *Proceedings of the The Fifth International Conference on Quantum, Nano and Micro Technologies (ICQNM 2011)*, Nice, France, August 21–27, 2011, accepted for publication.
- [5] M. Allais, “Le comportement de l’homme rationnel devant le risque: Critique des postulats et axiomes de l’École Américaine,” *Econometrica*, vol. 21, pp. 503–546, 1953.
- [6] D. Ellsberg, “Risk, ambiguity, and the Savage axioms,” *Quart. J. Econ.*, vol. 75, no. 4, pp. 643–669, 1961.
- [7] L. J. Savage, *The Foundations of Statistics*. New York, NY: Wiley, 1954.
- [8] J. von Neumann and O. Morgenstern, *Theory of Games and Economic Behavior*. Princeton, NJ: Princeton University Press, 1944.
- [9] Ellsberg was studying ‘decision making’ from the White House with respect to the war in Vietnam, having access to all highly classified material with respect to the Vietnam war, when he wrote his seminal article, and it is the same Ellsberg who later released the Pentagon papers containing this classified material, in this way starting the end of the Vietnam war (and risking to go to prison).
- [10] Daniel Khaneman was later to receive the Nobel Price for Economics as a psychologist, and is also considered to be one of the founding fathers of ‘Behavioral Economics’, where some of the effects mentioned in the present article are studied.

- [11] A. Tversky and D. Kahneman, "Extension versus intuitive reasoning: The conjunction fallacy in probability judgment," *Psych. Rev.*, vol. 90, pp. 293–315, 1983.
- [12] A. Tversky and E. Shafir, "The disjunction effect in choice under uncertainty," *Psych. Sci.*, vol. 3, pp. 305–309, 1992.
- [13] J. A. Hampton, "Overextension of conjunctive concepts: Evidence for a unitary model for concept typicality and class inclusion," *J. Exp. Psych.: Lear. Mem. Cog.*, vol. 14, pp. 12–32, 1988.
- [14] J. A. Hampton, "Disjunction of natural concepts," *Memory & Cognition*, vol. 16, pp. 579–591, 1988.
- [15] D. N. Osherson and E. E. Smith, "On the adequacy of prototype theory as a theory of concepts," *Cognition*, vol. 9, pp. 35–58, 1981.
- [16] L. Zadeh, "A note on prototype theory and fuzzy sets," *Cognition*, vol. 12, pp. 291–297, 1982.
- [17] D. N. Osherson and E. E. Smith, "Gradedness and conceptual combination," *Cognition*, vol. 12, pp. 299–318, 1982.
- [18] L. K. Komatsu, "Recent views on conceptual structure," *Psych. Bull.*, vol. 112, pp. 500–526, 1992.
- [19] L. J. Rips, "The current status of research on concept combination," *Mind and Language*, vol. 10, pp. 72–104, 1995.
- [20] J. A. Hampton, "Conceptual combination," in *Knowledge, Concepts, and Categories*, K. Lamberts and D. Shanks, Eds. Hove, UK: Psychology Press, 1997, pp. 133–159.
- [21] H. Kamp and B. Partee, "Prototype theory and compositionality," *Cognition*, vol. 57, pp. 129–191, 1995.
- [22] D. Aerts and S. Aerts, "Applications of quantum statistics in psychological studies of decision processes," *Found. Sci.*, vol. 1, pp. 85–97, 1994.
- [23] D. Aerts, "A Possible explanation for the probabilities of quantum mechanics," *J. Math. Phys.*, vol. 27, pp. 202–210, 1986.
- [24] D. Aerts, "Quantum structures, separated physical entities and probability," *Found. Phys.*, vol. 24, pp. 1227–1259, 1994.
- [25] L. Gabora and D. Aerts, "Contextualizing concepts using a mathematical generalization of the quantum formalism," *J. Exp. Theor. Art. Int.*, vol. 14, pp. 327–358, 2002.
- [26] D. Aerts and L. Gabora, "A theory of concepts and their combinations I & II," *Kybernetes*, vol. 34, pp. 167–191 & 192–221, 2005.
- [27] D. Aerts, "Quantum particles as conceptual entities. A Possible Explanatory Framework for Quantum Theory," *Found. Sci.*, vol. 14, pp. 361–411, 2009.
- [28] D. Aerts, "Quantum structure in cognition," *J. Math. Psych.*, vol. 53, pp. 314–348, 2009.
- [29] D. Aerts, S. Aerts, and L. Gabora, "Experimental evidence for quantum structure in cognition," *Lecture Notes in Artificial Intelligence*, vol. 5494, pp. 59–70, 2009.
- [30] D. Aerts and B. D'Hooghe, "Classical logical versus quantum conceptual thought: Examples in economy, decision theory and concept theory," *Lecture Notes in Artificial Intelligence*, vol. 5494, pp. 128–142, 2009.
- [31] L. Gabora, "Contextual focus: A cognitive explanation for the cultural transition of the Middle/Upper Paleolithic." In (R. Alterman and D. Hirsch, Eds.) *Proceedings of the 25th Annual Meeting of the Cognitive Science Society*, pp. 126–133, 2003.
- [32] L. Gabora, "Revenge of the 'neurds': Characterizing creative thought in terms of the structure and dynamics of human memory". *Creativity Research Journal*, vol. 22(1), pp. 1–13, 2010.
- [33] D. Aerts, "Quantum interference and superposition in cognition: Development of a theory for the disjunction of concepts," in *Worldviews, Science and Us: Bridging Knowledge and Its Implications for Our Perspectives of the World*, D. Aerts, B. D'Hooghe, and N. Note, Eds. Singapore: World Scientific, 2011, to be published.
- [34] D. Aerts, "General quantum modeling of combining concepts: A quantum field model in Fock space," archive reference and link: <http://uk.arxiv.org/abs/0705.1740>.
- [35] D. Aerts, B. D'Hooghe, and E. Haven, "Quantum experimental data in psychology and economics," *Int. J. Theor. Phys.*, vol. 49, pp. 2971–2990 (2010).
- [36] D. Widdows, *Geometry and Meaning*, CSLI Publications, IL: University of Chicago Press, 2006.
- [37] D. Widdows and S. Peters, "Word vectors and quantum logic: Experiments with negation and disjunction," in *Mathematics of Language 8*, Indiana, IN: Bloomington, 2003, pp. 141–154.
- [38] K. van Rijsbergen, *The Geometry of Information Retrieval*, Cambridge, UK: Cambridge University Press, 2004.
- [39] D. Aerts and S. Sozzo, "Quantum structure in cognition: Why and how concepts are entangled," archive reference and link <http://arxiv.org/abs/1104.1322>.
- [40] D. Aerts, M. Czachor, B. D'Hooghe, and S. Sozzo, "The pet-fish problem on the world-wide-web," in *AAAI Fall Symposium on Quantum Informatics for Cognitive, Social, and Semantics Processes*, P. Bruza et al., Eds. Berlin, Heidelberg, Germany: Springer, 2010, pp. 17–21.
- [41] D. Aerts, "Interpreting quantum particles as conceptual entities," *Int. J. Theor. Phys.*, vol. 49, pp. 2950–2970, 2010.
- [42] G. Hodge, *Systems of Knowledge Organization for Digital Libraries. Beyond Traditional Authority Files*, Washington, DC: the Council on Library and Information Resources (2000).
- [43] W. G. Stock, "Concepts and semantic relations in information science," *J. Am. Soc. Inf. Sci. Tech.*, vol. 61, pp. 1951–1969, 2010.

DNA Lattice Nanostructures as Biointerface Materials for Electrochemical Biosensor Studies

Nanobiocomposite Biosensor

Murugan Veerapandian,¹ Chang-Hyun Jang¹, Guie-Sam Lim,² Sung Ha Park,³ Min-Ho Lee⁴ and Kyusik Yun,^{1*}
¹Kyungwon University, ²LG Electronics, ³Sungkyunkwan University, ⁴Korea Electronics Technology Institute,
 Republic of Korea Email: ykyusik@kyungwon.ac.kr

Abstract—We demonstrate the use of well designed artificial DNA lattices as active biointerface material for electrochemical biosensing. Gold-PCB electrodes were modified with metalloid-polymer nanocomposite in presence/absence of DNA nanostructures and then characterized for its electrochemical response toward antigen, bovine serum albumin (BSA) and antibody, anti-bovine serum albumin (anit-BSA) interaction. The surface chemical modifications were achieved by utilization of suitable alkane dithiol and 1-ethyl-3-(3-dimethylaminopropyl) carbodiimide hydrochloride/*N*-Hydroxysuccinimide (EDC/NHS) coupling reaction, respectively. Furthermore, UV-visible spectral and Field Emission-Scanning Electron Microscope (FE-SEM) studies ensured the immobilization and morphological characteristics of the designed nanobiocomposite biosensor.

Keywords-DNA cross tile; Metalloid-polymer; BSA/Anti-BSA; Biosensor; Biointerface

I. INTRODUCTION

DNA is well known as a biomolecular carrier of genetic information, but in recent years the application of DNA-based nanostructures are invaluable for material science and nanotechnology. Unique structural composition and physical-chemical properties makes them possible for diverse architectures [1]. The incorporation of DNA into nano-object design is of great interest to establish high selective and reversible interactions between the components of a nanosystem. Many researchers have highlighted the immobilization and characterization of DNA on surfaces including X-ray photoelectron spectroscopy (XPS) [2, 3], ellipsometry [2], neutron reflectivity [4], surface plasmon resonance (SPR) [5], Raman spectroscopy [6] and scanning tunneling microscopy (STM) [7]. However, relationship between different nanostructures and orientation of surface-tailored DNA, their biological adherence and the behavior of DNA modified electrodes are still remaining as fundamental issues for its exploitation in biosensor studies. By using suitable surface linking/modifying agent optimal concentration of DNA can be easily immobilized on the electrodes. Generally, scanning probe microscopes (STM and AFM) are utilized to achieve imaging of DNA nanostructures [8, 9]. Zhang et al. studied the orientation of DNA on gold electrodes using electrochemical (EC)-STM [8]. Kelly et al. investigated the

different applied potential effect on the orientation of self-assembled DNA helices on gold by EC in-situ atomic force microscope [10].

The target of the present research work is to extend the application of DNA-based nanostructures as biointerface materials. To this regard, we have utilized the artificially designed DNA lattices and modified at the interface of nanocomposite materials and gold-PCB electrodes and performed the biosensing of antigen-antibody interaction. The two different nanocomposite materials incorporated in the current experiments are poly(ethyleneglycol)-silica@silver core (PEG-SiO₂@Ag) and poly(*p*-dioxanone-co-caprolactone)-block-poly (ethylene-oxide)-block-poly(*p*-dioxanone-co-caprolactone) (PPDO-co-PCL-*b*-PEG-*b*-PPDO-co-PCL)/ ABA-poly (ethyleneglycol)-silica@silver core (ABA/ PEG-SiO₂@Ag) [11]. DNA lattices are immobilized on gold-PCB electrodes by ethane dithiol activation (EDT). The electrochemical properties of the above nanocomposite (in absence of DNA lattices) and bionanocomposite (in presence of DNA lattices) structures were evaluated through biofunctionalization (using EDC/NHS coupling reaction) of model protein BSA and anti-BSA. The reaction mechanism and relationship at the bio-nano interface were briefly discussed for its possible application in biosensor studies. Fundamental determination of changes in the oxidation and reduction peak potential from the surface modified nanocomposite particles on before and after treatment with BSA and anti-BSA gives a considerable chance of sensing abilities. Further the morphological and wavelengths of maximum absorbance (λ_{max}) characterization of the immobilized nanostructures were obtained from FE-SEM and UV-visible spectroscopy, respectively. The two hybrid nanocomposite particles used in the current experiment has several distinct features such as polymer/copolymeric shell (PEG/ABA), metalloid core (SiO₂@Ag) and film forming ability for surface and interface studies [11].

II. EXPERIMENTAL

A. Fabrication of nanocomposite particles and DNA lattice structures

poly(ethyleneglycol)-silica@silver core (PEG-SiO₂@Ag) and poly(*p*-dioxanone-co-caprolactone)-block-poly

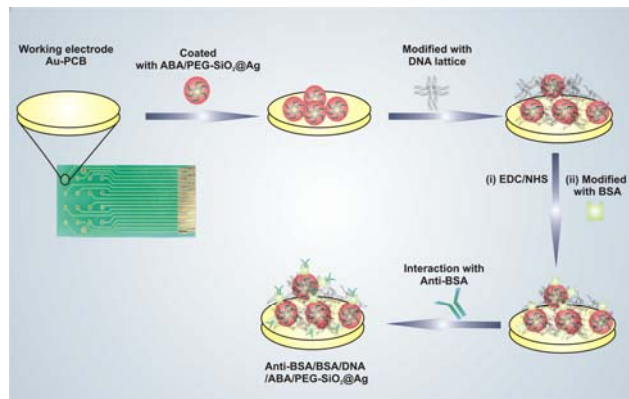
(ethyleneoxide)-block-poly-(*p*-dioxanone-*co*-caprolac -tone) (PPDO-*co*-PCL-*b*-PEG-*b*-PPDO-*co*-PCL)/ABA-poly (ethyl eneglycol)-silica@silver core (ABA/PEG-SiO₂@Ag) were prepared by our previous report [11]. DNA nanostructures of double cross over tiles (DX1 and DX2) [12] were successfully self assembled for DNA lattice growth. These DNA nanostructures are fairly stiff and considerably stable at room temperature [13] sequenced by multiple DNA crossovers. Final concentration of DNA lattice sample utilized in electrode preparation is about 200 nM. The details of DNA base sequence can be found from Table 1. DX1 cross tiles and DX2 cross tiles are composed of individual strands such as DX1#1, DX1#2, DX1#3, DX1#4 and DX2#1, DX2#2, DX2#3, DX2#4, respectively.

B. Electrode pretreatment and immobilization of nanocomposite particles/DNA lattice structures

Platinum and Ag/AgCl electrodes were used as counter and reference electrodes, respectively. Surface of working electrode (gold-PCB) were cleaned by soaking the electrode surface under acetone and ethanol for 5 m separately and rinsed thoroughly with D.I H₂O. Prior to surface functionalization of prepared colloidal PEG-SiO₂@Ag and ABA/PEG-SiO₂@Ag nanocomposite particles the surface of gold-PCB electrode was made hydrophilic by oxygen-plasma coating for 300 s. After plasma cleaning, the electrode surface were drop coated with EDT (1 mM) and kept under room temperature for 12 h. EDT activated electrode surface were then drop coated with 4 μL of above nanocomposite particles, separately. DNA lattice (200 nM) modification on the nanocomposite/gold-PCB surface was prepared by same procedure. Biofunctionalization of BSA and anti-BSA on the surface of these nanocomposite/ (in presence and absence of DNA lattice) gold-PCB electrode were done via EDC/NHS coupling reaction [14]. Cyclic voltammetry scans were recorded under 5 mL PBS (10 mM; pH 7.4) solutions in the potential range of -0.1 to 0.450 V and at the scan rate of 80 mV/s. Each CV scans were repeated for three times. To observe the CV measurements, three-electrode configuration from BioLogic science instrument SP-300 was utilized in the current experiment.

III. RESULTS AND DISCUSSION

The schematic representation of immobilization of nanocomposite particles and its surface modification is explained in Scheme 1. Colloidal solution of nanocomposite particles (ABA/PEG-SiO₂@Ag) is self assembled onto the surface of oxygen plasma treated gold-PCB electrodes. Further a thin film of DNA lattice structures is developed on the nanocomposite particle surface through drop casting method. Evaporation induced self assembly result in the deposition of biointerface membrane. It is demonstrated that



Scheme 1. Fabrication of biocompatible nanobiocomposite biosensor. (unpublished material).

the development of thin structures of polymer film or biomolecules such as DNA or peptides are feasible for number of applications in biosensor studies. For instance, DNA microarrays on polymers such as poly (methyl methacrylate) (PMMA) [15], the synthesis of star shaped poly (ethylene glycol) (PEGs) [16] and immobilization of genetically engineered proteins on gold-MWNT films for biosensor platforms [17]. Further the confinement of sub 100 nm thin films has been reported to have influence in the

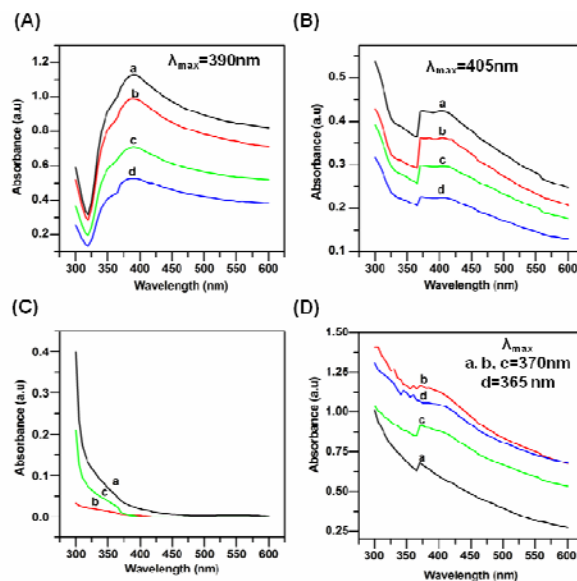


Figure 1. UV-visible spectral studies. (A) PEG-SiO₂@Ag and (B) ABA/PEG-SiO₂@Ag nanocomposite particles of different concentration (100 μL, 80 μL, 60 μL and 40μL (a-d) in D.I water used for analysis). (C) BSA (a), anti-BSA (b) and mixture of BSA/anti-BSA (c). (D) BSA/ABA/PEG-SiO₂@Ag (a), Anti-BSA-BSA/ABA/PEG@SiO₂@Ag (b), BSA/DNA/PEG-SiO₂@Ag (c) and Anti-BSA-BSA/DNA/ABA/PEG-SiO₂@Ag (d). (unpublished material).

diffusion of polymer molecules comprising the film, as well as diffusion of small, lower-molar-mass tracer molecules and other altered properties [18].

Figure 1 (A) and (B) denotes the maximum absorbance spectrum of two nanocomposite particles. As seen from the images the curve peak indicates the presence of SPR from the core silver particles. Further the increased wavelength of maximum absorbance (from (A) 390 to (B) 405 nm) indicates the successful surface modification of ABA triblock copolymer on the PEG/SiO₂@Ag core. This is in-

TABLE I. THE SEQUENCE DETAILS OF ALL STRANDS FROM 5' to 3' (UNPUBLISHED MATERIAL)

| Strand | No. of Base | Sequence(5' to 3') |
|--------|-------------|--|
| DX1#1 | 26 MERS | TGCTA CTACCGCA CCAGAATG CTAGT |
| DX1#2 | 48 MERS | CATTCTGG ACGCCATA AGATAGCA CCTCGACT CATTGGCC TGCGGTAG |
| DX1#3 | 48 MERS | CAGTAGCC TGCTATCT TATGGCGT GGCAAATG AGTCGAGG ACGGATCG |
| DX1#4 | 26 MERS | CATAC CGATCCGT GGCTACTG TCACT |
| DX2#1 | 26 MERS | GTATG GGCAATCC ACAACCGC AGTGA |
| DX2#2 | 48 MERS | GCGGTTGT CCAACTTA CCAGATCC ACAAGCCG ACGTTACA GGATTGCC |
| DX2#3 | 48 MERS | GCTCTACA GGATCTGG TAAGTTGG TGTAACGT CGGCTTGT CCGTTCGC |
| DX2#4 | 26 MERS | TAGCA GCGAACGG TGTAGAGC ACTAG |

consistent with our previous report [10]. On the other hand the BSA, anti-BSA and mixture of both doesn't give a significant absorbance on this specific region (Figure 1(C)). Notably, after surface modification of final nanocomposite particles (in presence/absence of DNA lattice) with BSA and anti-BSA, there is a change observed in the wavelength of maximum absorbance and shape of the peak. For instance in presence of anti-BSA, both the normal BSA-nanocomposite particles and BSA/DNA-nanocomposite particles shows broad peaks. Whereas, in absence of anti-BSA the other two nanocomposite (a: BSA/ABA/PEG-SiO₂@Ag and c: BSA/DNA/ABA/PEG-SiO₂@Ag) particles shows a short but intense peak, which attributes the surface characteristics of the reacted/unreacted nanostructured surface, respectively.

Biocompatibility, biointegration and functionality are the crucial factors for biomedical devices and implants, but also applicable for biosensor in various forms. For instance, immobilization of biomolecules for biosensing studies needs a suitable biocompatible interface material [18]. The key strategy demonstrated here is the use of hybrid nanocomposites (PEG-SiO₂@Ag and ABA/PEG/SiO₂@Ag) as an electrochemical substrate based on their excellent electrical properties and large surface areas for the immobilization of bioreceptors and to fabricate a sensing platform by using an advanced DNA lattice nanostructures as suitable interface material specifically for binding on the

surface of nanocomposite-gold-PCB electrode, which adheres the antigen BSA and significantly interfere with anti-BSA through the antigen-antibody interactions.

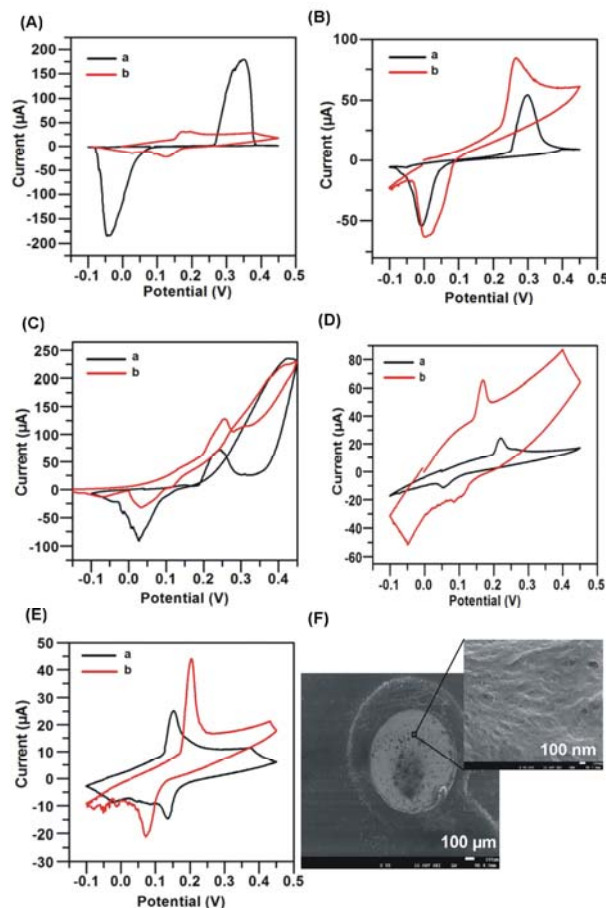


Figure 2. Shows the cyclic voltammograms of nanocomposite particles-Au-PCB electrode at different conditions (Note: (a) PEG-SiO₂@Ag: black trace and (b) ABA/PEG-SiO₂@Ag: red trace) such as bare (A) (a: $E_{pc}=0.34$; $E_{pa}=-0.04$, b: $E_{pc}=0.19$; $E_{pa}=0.12$), BSA modified (B) (a: $E_{pc}=0.30$; $E_{pa}=-0.007$, b: $E_{pc}=0.26$; $E_{pa}=0.0003$), BSA-Anti-BSA modified (C) (a: $E_{pc}=0.24$; $E_{pa}=0.02$; b: $E_{pc}=0.25$; $E_{pa}=0.03$), DNA-BSA modified (D) (a: $E_{pc}=0.22$; $E_{pa}=0.05$, b: $E_{pc}=0.16$; $E_{pa}=0.08$) and DNA-BSA-Anti-BSA modified (E) (a: $E_{pc}=0.15$; $E_{pa}=0.13$, b: $E_{pc}=0.20$; $E_{pa}=0.07$). F: depicts the FE-SEM image of Au-PCB electrode coated with nanocomposite (b) particles and DNA lattice structures. (unpublished material).

Figure 2 shows the cyclic voltammograms and its relevant cathodic peak potential (E_{pc}) and anodic peak potential (E_{pa}). As seen from the images, it is clear that there is a possibility of sensing the significant changes occur between the antigen-antibody interactions that taken place on the hybrid nanocomposite and bio-nanocomposite surfaces immobilized on the gold-PCB electrode. Figure 2 (F) represents the FE-SEM image of gold-PCB electrode surface modified with nanocomposite particles-DNA lattice structures. As observed from the magnified inset image the well aligned DNA lattice structures and nanocomposite particles are

densely packed with large surface areas. Incorporation of DNA lattice nanostructures as interface material acted both as a suitable surface linker/compatible material for integration of biomolecules on the hybrid environment.

IV. CONCLUSION

In conclusion, we have developed a nanobiocomposite biosensor platform for antigen-antibody interaction. A well defined DNA lattice nanostructure shows significantly a biocompatible environment for both nanomaterial and biomolecules (such as model protein BSA) utilized in the study. Furthermore, we demonstrated the cyclic voltammetry response for different surface modified biosensor platform in presence and absence of DNA lattice. A detailed study is in progress to unravel the underlying efficiency for concentration dependant biosensing abilities. Further Bio-AFM based investigations of orientation of these hybrid nanoenvironments are underway. We believe that the concept of integration of DNA lattice nanostructures as interface materials with nanocomposite particles will be sure opens a new insight into other nanobiotechnology. It is expected that a fundamental study performed in the present research will allows us to exploit the present situation of DNA nanotechnology towards a facile construction of new nanomaterial platform for many other biomedical applications.

ACKNOWLEDGMENT

This research was supported by the Kyungwon University Research Fund in 2011, the GRRC program of Gyeonggi province (2010-B02, Development biodevice using DNA tile structure) and Grant No. 10032112 from the Regional Technology Innovation Program of the Ministry of Knowledge Economy to K. S. Yun and by the Research Grant from the National Research Foundation of Korea (NRF2008; 331-2008-1-C00126) to S. H. Park.

REFERENCES

- [1] J.B. Lee, M.J. Campolongo, J.S. Kahn, Y.H. Roh, M.R. Hartman, and D. Luo, "DNA-based nanostructures for molecular sensing," *Nanoscale*, vol.2, pp.188-197, 2010.
- [2] T.M. Herne and M.J. Tarlov, "Characterization of DNA probes immobilized on gold surface," *J. Am. Chem. Soc.* vol. 119, pp. 8916-8920, 1997.
- [3] T. Strother, W. Cai, X.S. Zhao, R.J. Hamers, and L.M. Smith, "Synthesis and characterization of DNA-modified cilicon (111) surface" *J. Am. Chem. Soc.* vol. 122, pp. 1205-1209, 2000.
- [4] R. Levicky, T.M. Herne, M.J. Tarlov, and S.K. Satija, "Using self-assembly to control the structure of DNA monolayers on gold: a neutron reflectivity study" *J. Am. Chem. Soc.* vol. 120, pp. 9787-9792, 1998.
- [5] M.S. Yang, H.C.M. Yau, and H.L. Chan, "Adsorption kinetics and ligand-binding properties of thiolmodified double-stranded DNA on a gold surface" *Langmuir* vol.14, pp.6121-6129, 1998.
- [6] Y.D. Zhao, D.W. Pang, S. Hu, Z.L. Wang, J.K. Cheng, Y.P. Qi, H.P. Dai, B.W. Mao, Z.Q. Tian, J. Luo, and Z.H. Lin, "DNA-modified electrodes Part 3.: spectroscopic characterization of DNA modified gold electrodes" *Anal. Chim. Acta* vol.388, pp. 93-101, 1999.
- [7] Y. Kim, E.C. Long, J.K. Barton, and C.M. Lieber, "Imaging of oligonucleotide-metal complexes by scanning tunneling microscopy" *Langmuir* vol. 8, pp. 496-500, 1992.
- [8] H. Yokota, J. Sunwoo, M. Sarikaya, E. Ger van den, and R. Adbersold, "Spin-stretching of DNA and protein molecules for detection by fluorescence and atomic force microscopy" *Anal. Chem.* vol. 71, pp. 4418-4422, 1999.
- [9] L.Z. Zhi, W.P. Dai, and Y.Z. Rong, "Investigation of DNA orientation on gold by EC-STM" *Bioconjugate Chem.* vol. 13, pp.104-109, 2002.
- [10] S.O. Kelly, J.K. Barton, N.M. Jackson, L.D. McPherson, A.B. Potter, E.M. Spain, M.J. Allen, and M.G. Hill, "Orienting DNA helices on gold using applied electric fields" *Langmuir* vol. 14, pp. 6781-6785, 1998.
- [11] M. Veerapandian and K.S. Yun, "Ultrasonochemically conjugated metalloid/triblock copolymer nanocomposite and subsequent thin solid laminate growth for surface and interface studies," *Langmuir* vol.26(17), pp. 14216-14222, 2010.
- [12] M. Veerapandian, B.G. Kim, R. Amin, J.W. Lee, K.S. Yun, and S.H. Park, "NMR studies of double cross over DNA tiles," in communication.
- [13] X. Li, Xi. Yang, J. Qi, and N.C. Seeman, "Ligation of Triangles Built from Bulged 3-Arm DNA Branched Junctions," *J. Am. Chem. Soc.* vol. 118, pp. 6121-6130, 1996.
- [14] W. Huang, S. Taylor, K. Fu, Y. Lin, D. Zhang, T.W. Hanks, A.M. Rao, and Y.P. Sun, "Attaching proteins to carbon nanotubes via diimide-activated amidation," *Nano Lett.* vol. 2(4), pp. 311-314, 2002.
- [15] F. Fixe, M. Dufva, P. Telleman, and C. B. V. Christensen, "Functionalization of poly(methyl methacrylate) (PMMA) as a substrate for DNA microarrays," *Nucleic Acids Res.* vol. 32(1), pp. e9, 2004.
- [16] K. Wang, W. Huang, Y. Zhou, and D. Yan, "Synthesis and characterization of three-arm star-shaped polyethylene glycols with 1,1,1-trihydroxymethylpropane as cores," *Front. Chem. China.* vol.3(3), pp. 298-303, 2008.
- [17] H.S. Park, T.J. Park, Y.S. Huh, B.G. Choi, S.G. Ko, S.Y. Lee, and W.H. Hong, "Immobilization of genetically engineered fusion proteins on gold-decorated carbon nanotube hybrid films for the fabrication of biosensor platforms," *J. Colloid. Interf. Sci.* vol. 350 pp. 453-458, 2010.
- [18] S. Holger, "Biofunctionalization of polymeric thin films and surface," in *Nanostructured thin films and surfaces*, S.S.R. Kumar Challa. Ed. Weinheim: Wiley-VCH, 2010. pp.55-91.

Improved Linearity CMOS Active Resistor Structure Using Computational Circuits

Cosmin Popa

University Politehnica of Bucharest, Romania

1-3 Iuliu Maniu, Bucharest, Romania

email: cosmin_popa@yahoo.com

Abstract-A new low-power low-voltage active resistor structure with improved performances will be presented. The problem of circuit linearity is solved by implementing an original technique, using a proper current biasing of the differential core, while the existing solutions allow only a partial improvement of the circuit performances. The structures are implemented in $0.35\mu\text{m}$ CMOS technology and are supplied at $\pm 3\text{V}$. The circuits present a very good linearity (in the worst case, total order distortions $< 0.4\%$), correlated with an extended range of the input voltage (at least $\pm 0.5\text{V}$). The tuning range of the active resistors is about hundreds $k\Omega - M\Omega$.

Keywords-Linearity; active resistor circuit; computational circuits; VLSI design.

I. INTRODUCTION

CMOS (Complementary Metal Oxide Semiconductor) active resistors [1][2][3][4] are very important blocks in VLSI analog designs, mainly used for replacing the large value passive resistors, with the great advantage of a much smaller area occupied on silicon. Their utilisation domains include amplitude control in low distortion oscillators, voltage controlled amplifiers and active RC filters. These important applications for programmable floating resistors have motivated a significant research effort for linearising their current-voltage characteristic. The first generation of MOS active resistors [1] [2] used MOS transistors working in the linear region. The main disadvantage is that the realized active resistor is inherently nonlinear and the distortion components were complex functions on MOS technological parameters. A better design of CMOS active resistors is based on MOS transistors working in saturation. Because of the quadratic characteristic of the MOS transistor, some linearization techniques [3][4] were developed in order to minimize the nonlinear terms from the current-voltage characteristic of the active resistor. An important class of these circuits, referring to the active resistors with controllable negative equivalent resistance, covers a specific area of VLSI designs, finding very large domains of applications such as the cancelling of an operational amplifier load or the design of Deboo [5] integrators with improved performances.

The original idea proposed in this paper is to use a linear CMOS differential amplifier for obtaining (with minor changes in the design) two important functions:

- Simulation (in a first-order analysis) of a perfect linear resistor using exclusively MOS active devices, having the advantages of a very good controllability of the equivalent resistance and of an important reduction of the silicon occupied area, especially for large value of the simulated resistance;
- Simulation of a controllable negative resistance circuit with improved linearity;

A. State of the art

The paper contains a section describing the theoretical basis of the design methods, followed by a section presenting some important simulation results and, in the end, a conclusion.

II. THEORETICAL ANALYSIS

A. Improved linearity MOS differential structure

An improved linearity MOS differential structure represents the core of the original active resistor circuit with improved linearity (Figure 1). "SQ" block is a squaring circuit, having the original implementation presented in Figure 3.

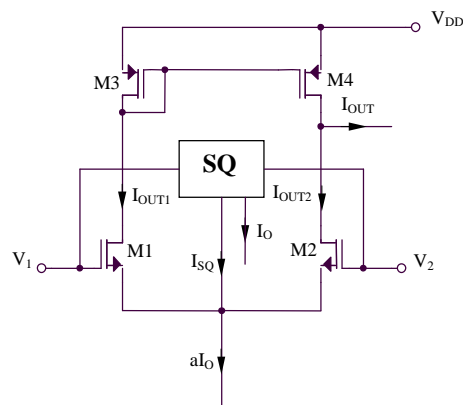


Figure 1. Improved linearity MOS differential structure

The differential output current for this circuit has the following expression:

$$I_{OUT} = (V_1 - V_2) \sqrt{K(aI_O - I_{SQ}) - \frac{K^2}{4}(V_1 - V_2)^2} \quad (1)$$

In order to obtain a linear behavior of the proposed differential structure, the I_{SQ} output current of the squaring circuit "SQ" must be the sum of a constant term and a term proportional with the square of the differential input voltage:

$$I_{SQ} = bI_O - \frac{K}{4}(V_1 - V_2)^2, \quad (2)$$

b being a positive constant, depending on the particular implementation of the squaring circuit. Replacing (2) in (1), it results:

$$I_{OUT} = \sqrt{(a-b)KI_O}(V_1 - V_2) = G_m(V_1 - V_2), \quad (3)$$

$G_m = \sqrt{(a-b)KI_O}$ being the circuit equivalent transconductance.

The proposed method for designing the required voltage squaring circuit is based on a differential amplifier (Figure 3), having a controllable asymmetry between the geometries of its composing transistors. This difference between the aspect ratios of MOS transistors will introduce in the output currents of the differential amplifier a term proportional with the square of the differential input voltage.

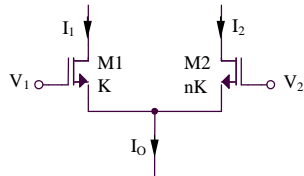


Figure 2. Asymmetrical differential structure

The differential input voltage, V , can be expressed as follows:

$$V = V_{GS1} - V_{GS2} = \sqrt{\frac{2I_1}{K}} - \sqrt{\frac{2(I_O - I_1)}{nK}}, \quad (4)$$

resulting:

$$\frac{K}{2}V^2 = I_1 + \frac{I_O - I_1}{n} - 2\sqrt{\frac{I_1(I_O - I_1)}{n}} \quad (5)$$

The expression of I_1 current can be obtained solving the following second-order equation, derived from (5):

$$I_1^2 \left[\left(\frac{n-1}{n} \right)^2 + \frac{4}{n} \right] + \left(\frac{I_O}{n} - \frac{KV^2}{2} \right)^2 + I_1 \left[2 \frac{n-1}{n} \left(\frac{I_O}{n} - \frac{KV^2}{2} \right) - \frac{4I_O}{n} \right] = 0 \quad (6)$$

So:

$$I_1 = \frac{I_O}{n+1} + \frac{n(n-1)}{2(n+1)^2} KV^2 + \frac{nV}{(n+1)^2} \sqrt{2KI_O(n+1) - K^2 nV^2} \quad (7)$$

and:

$$I_2 = I_O - I_1 = \frac{nI_O}{n+1} - \frac{n(n-1)}{2(n+1)^2} KV^2 - \frac{nV}{(n+1)^2} \sqrt{2KI_O(n+1) - K^2 nV^2} \quad (8)$$

The complete realization of a voltage squaring circuit, based on the previous proposed method, uses a cross-coupling of two differential amplifiers having controllable asymmetries between their geometries, M1-M2 and M3-M4 (Figure 3).

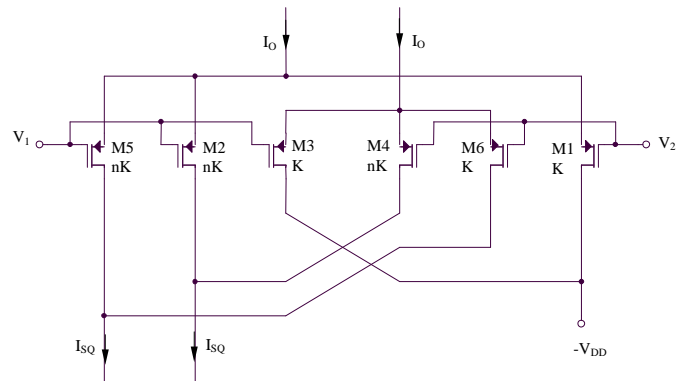


Figure 3. Squaring circuit

Using (7) and (8), it results:

$$\begin{aligned}
 I_{SQ} = I_{D2} + I_{D4} &= \frac{nI_O}{n+1} - \frac{n(n-1)}{2(n+1)^2} KV^2 - \\
 &- \frac{nV}{(n+1)^2} \sqrt{2KI_O(n+1) - K^2 nV^2} + \\
 &+ \frac{nI_O}{n+1} - \frac{n(n-1)}{2(n+1)^2} KV^2 + \\
 &+ \frac{nV}{(n+1)^2} \sqrt{2KI_O(n+1) - K^2 nV^2} = \\
 &= \frac{2nI_O}{n+1} - \frac{n(n-1)}{(n+1)^2} KV^2
 \end{aligned} \quad (9)$$

B. Positive resistance active resistor circuit

The proposed active resistor circuit with positive equivalent resistance is presented in Figure 4.

The current passing between the input pins V_1 and V_2 , $I_{OUT} = I_{OUT1} - I_{OUT2}$ has the following expression:

$$I_{OUT} = (V_1 - V_2) \sqrt{K \frac{aI_O - I_{SQ}}{2} - \frac{K^2}{4} (V_1 - V_2)^2} \quad (10)$$

because each differential amplifier M1-M4 and M2-M3 is biased at a current equal with:

$$I_{OUT1} + I_{OUT2} = \frac{aI_O - I_{SQ}}{2} \quad (11)$$

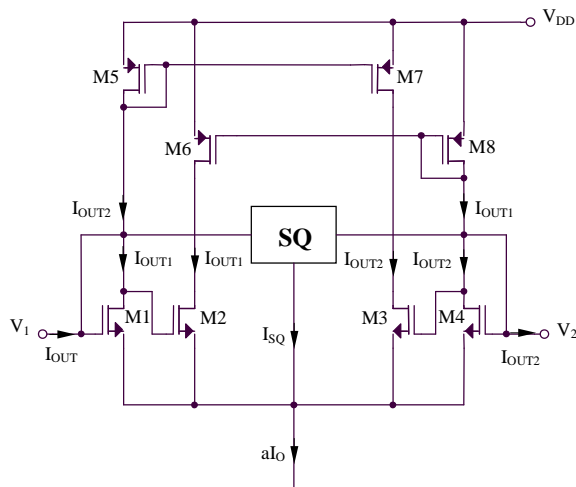


Figure 4. Positive resistance active resistor circuit

Using the expression (9) of I_{SQ} current, it results:

$$I_{OUT} = (V_1 - V_2) \sqrt{\frac{KI_O}{2} \left(a - \frac{2n}{n+1} \right) + \frac{K^2 (V_1 - V_2)^2}{2} \left[\frac{n(n-1)}{(n+1)^2} - \frac{1}{2} \right]} \quad (12)$$

The conditions for obtaining a linear behavior of the circuit can be written as:

$$\frac{n(n-1)}{(n+1)^2} = \frac{1}{2}, \quad (13)$$

resulting:

$$n_{1,2} = 2 \pm \sqrt{5} \quad (14)$$

and:

$$I_{OUT} = (V_1 - V_2) \sqrt{\frac{KI_O}{2} \left(a - 2 \frac{2 \pm \sqrt{5}}{3 \pm \sqrt{5}} \right)} \quad (15)$$

The equivalent resistance of the circuit presented in Figure 5 will be:

$$R_{ECH} = \frac{V_1 - V_2}{I_{OUT}} = \left[\frac{KI_O}{2} \left(a - 2 \frac{2 \pm \sqrt{5}}{3 \pm \sqrt{5}} \right) \right]^{-1/2} \quad (16)$$

C. Negative resistance active resistor circuit

The proposed active resistor circuit with negative equivalent resistance is presented in Figure 5.

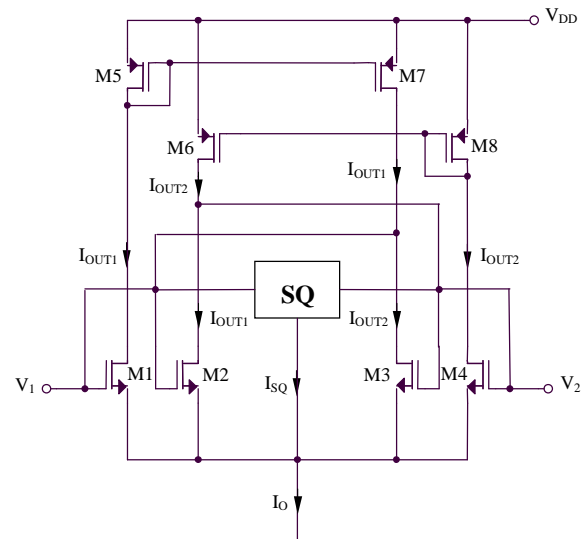


Figure 5. Negative resistance active resistor circuit

The equivalent resistance of the circuit presented in Figure 6 will be:

$$R_{ECH} = -\frac{V_1 - V_2}{I_{OUT}} = -\left[\frac{KI_O}{2} \left(a - 2 \frac{2 \pm \sqrt{5}}{3 \pm \sqrt{5}}\right)\right]^{-1/2}. \quad (17)$$

III. SIMULATED RESULTS

The SPICE [6] simulation $I_{OUT1,2}(V)$ based on $0.35 \mu m$ CMOS technology parameters for the original differential amplifier from Figure 1 (representing the core of the multifunctional structure) is presented in Figure 6, showing a very small linearity error. The supply voltage corresponds to low-power requirements, $V_{DD} = 3 V$.

The simulation shows a very good linearity of the original differential structure.

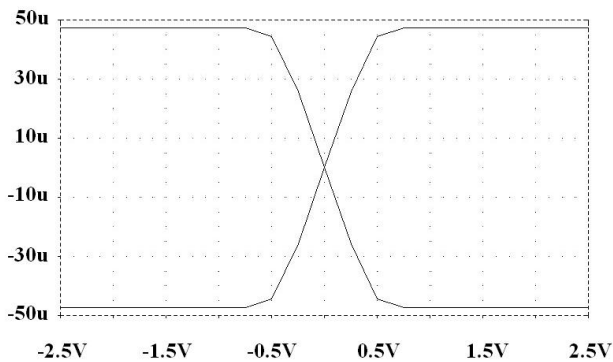


Figure 6. Simulation of the transfer characteristic for the original differential structure

IV. AKNOWLEDGMENTS

This work was supported by POSDRU/89/1.5/S/62557 project.

V. CONCLUSION

A new low-power low-voltage active resistor structure with improved performances has been presented. The linearity is strongly increased by implementing an original technique, using a proper current biasing of the differential core. The structures are implemented in $0.35 \mu m$ CMOS technology and are supplied at $\pm 3V$. The circuits present a very good linearity (in the worst case, $THD < 0.4\%$), correlated with an extended range of the input voltage (at least $\pm 0.5V$). The tuning range of the active resistors is about hundreds $k\Omega$ - $M\Omega$.

REFERENCES

- [1] Z. Wang, "Current-controlled Linear MOS Earthed and Floating Resistors and Application," *IEEE Proceedings on Circuits, Devices and Systems*, 1990, pp. 479-481
- [2] L. Sellami, "Linear Bilateral CMOS Resistor for Neural-type Circuits," *Proceedings of the 40th Midwest Symposium on Circuits and Systems*, vol. 2, 1997, pp. 1330-1333.
- [3] C. Muniz-Montero, R. Gonzalez-Carvajal, A. Diaz-Sanchez, and J.M. Rocha, "Low Frequency, Current Mode Programmable KHN Filters Using Large-Valued Active Resistors", *Circuits and Systems*, 2007. ISCAS 2007. IEEE International Symposium on, 27-30 May 2007, pp. 3868 – 3871
- [4] T. Sanchez-Rodriguez, C. Lujan-Martinez, R. Carvajal, J. Ramirez-Angulo, and A. Lopez-Martin, "CMOS Linear Programmable Transconductor Suitable for Adjustable Gm-C Filters", *Electronics Letters*, Volume 44, Issue 8, April 10 2008, pp. 505 – 506
- [5] A.M. Soliman, M. Ismail, "Novel Passive and Active Compensated Deboo Integrators", *Proceedings of the IEEE*, Vol. 67, Issue 2, 1979, pp. 324-325
- [6] <http://bwrc.eecs.berkeley.edu/classes/icbook/spice/>

Dry Film Resist Microfluidic Channels on Printed Circuit Board and its Application as Fluidic Interconnection for Nanofluidic Chips: Fabrication Challenges

N. B. Palacios-Aguilera, J. Bastemeijer,
J. R. Mollinger, A. Bossche

Electronic Instrumentation Laboratory
Delft University of Technology
Mekelweg 4,

2628CD Delft, the Netherlands
n.b.palaciosaguilera@tudelft.nl,

j.bastemeijer@tudelft.nl, j.r.mollinger@tudelft.nl,
a.bossche@tudelft.nl

V. R. S. S. Mokkalpati

Nanosystems, Health and Environment Department
Austrian Institute of Technology

Donau city strasse 1
1220 Vienna, Austria

v.r.s.s.mokkalpati.fl@ait.ac.at

Abstract—Nowadays, nanofluidic chips are usually fabricated with silicon and/or glass. A simple and reliable integration packaging method that provides fluidic interconnection to the outside world has not been yet fully developed. The use of PCB material as substrate to create dry film resist microfluidic channels is the core technology to provide such an integration method. The feasibility and potential of the proposed packaging method is demonstrated in this work.

Keywords—dry film resist; fluidic interconnection; printed circuit board; nanofluidic channels, integration

I. INTRODUCTION

Microfluidic devices fabricated with dry film resist (DFR) and silicon (Si) and/or glass substrate have been reported [2, 3, 5]. Moreover, nanofluidic devices are usually fabricated with silicon and/or glass [1, 3, 7, 8, 9]; even if nanoimprint technologies are used to fabricate them, a rigid substrate (usually glass) is required [10, 11].

The use of silicon and/or glass to build fluidic systems elevates their cost [6]. Furthermore, the reliable fluidic connection of nanofluidic devices to the outside world still needs to be optimized in order to reduce costs and simplify the fabrication process.

A low-cost fabrication method for microfluidic channels as fluidic interconnection for nanofluidic chips is here presented. Printed circuit board (PCB) material is proposed as the substrate to laminate DFR for the fluidic interconnections.

Following this approach, the fluidic chip can be kept small thus decreasing its cost. Furthermore, the low-cost PCB facilitates the fluidic and electrical connections to the outside world allowing the integration of micro- and nanodevices in a simple and fast way.

In this work, the principle of the packaging integration technology is explained. In Section III, the physical properties of the materials used are presented. In Section IV, the fabrication process is detailed. Then, the challenges associated with the fabrication process are treated; first the challenges associated with the fabrication of DFR fluidic channels on PCB, then, the challenges associated with the

use of different materials as a substrate. Finally, the devices are tested against leakage and the compatibility of the materials is studied by means of a thermal shock test in order to determine delamination.

II. PRINCIPLE

The key material enabling the use of DFR microfluidic channels on PCB for its use as the fluidic interconnection of nanofluidic chips is a nonconductive adhesive (NCA). Figure 1 shows a schematic of the concept.

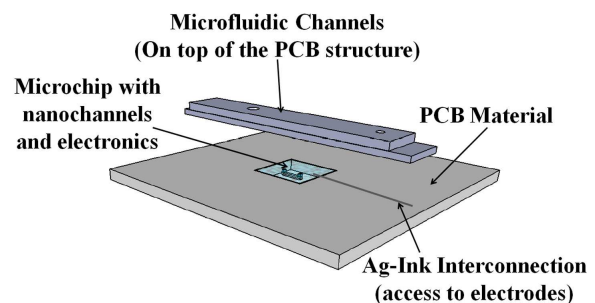


Figure 1. Schematic of the interconnection of nanofluidic chips by means of dry film resist channels on top of PCB material.

The already fabricated nanofluidic chips are inlaid on the PCB material by means of a NCA. The fluidic chip(s) together with the PCB material compose the substrate.

Finally, the lamination of dry film resist on top of the substrate allows fabricating the microfluidic channels that interconnect the nanofluidic chips to the outside world.

Concerning the electric access to the nanofluidic chip(s), ink-jet printed interconnection lines can be applied between the electronic contacts of the fluidic chips and the pads on the PCB. This latter topic however is not treated in this paper.

III. MATERIALS

TMMF dry film resist poses a unique stability when in contact with alkaline solutions and acids [3, 5] and provides high resolution and aspect ratios [2, 5] making it the resist of choice for the fabrication of microfluidic channels.

The DFR used to fabricate the microfluidic channels is TMMF S2030, a permanent photoresist for MEMS from Tokyo Ohka Kogyo Co., Ltd. This negative photoresist is composed 5% of antimony compound and 95% of epoxy resin [2, 3].

Furthermore, the PCB material used as mechanical support for the whole system is Rogers RO4003C, a glass reinforced hydrocarbon laminate with low roughness characteristics.

Table 1 shows the physical characteristics of TMMF S2030 and Rogers RO4003C.

TABLE I. PHYSICAL PROPERTIES OF TMMF S2030 AND ROGERS RO4003C [2, 13]

| Physical Properties of TMMF S2030 and Rogers RO4003C | | |
|--|------------|----------------------|
| Physical Property | TMMF S2030 | Rogers RO4003C |
| Coefficient of thermal expansion (ppm/°C) | 65 | X 11 Y 14 Z 46 |
| Transition glass temperature (°C) | 230 | >280 |
| Moisture absorption (%) | 1.8 | 0.06 |
| Dielectric constant | 3.8 | 3.38±0.005 |
| Transparency (nm) | 400-600 | - |
| Breaking strength (MPa) | 60.3 | - |
| Young modulus (MPa) | 2100 | 26.889 |

The NCA used to glue the fluidic chip to the PCB material is a colorless epoxy-based adhesive with a glass transition temperature (Tg) of 45 °C and a coefficient of thermal expansion (CTE) of 56 ppm/°C when below the glass transition temperature, and 211 ppm/°C when above the glass transition temperature.

IV. FABRICATION PROCESS

The very first step to proceed to the fabrication of the TMMF microfluidic channels on top of PCB material for the fluidic interconnection of nanochips is to form the substrate composed by the PCB and the fluidic chip(s). Figure 2 illustrates this process.

According to Figure 2, to align the PCB material and the nanofluidic chip a double side Kapton tape is rolled in a silicon wafer or glass (a). The PCB and the chip are mounted on the Kapton tape (b). The epoxy-based adhesive is dispensed in the space between the PCB material and the chip (c). The materials are placed in an oven or hot plate at 80 °C for 3 hours to cure the adhesive (d). When the adhesive is totally cured, the materials are left at room temperature for a while to allow them to cool down. The new substrate consisting of the chip inlaid in the PCB material is removed from the Kapton tape (e).

The second stage of the fabrication process consists in laminating the TMMF microfluidic channels on top of the formed substrate. Figure 3 shows the flowchart for this process.

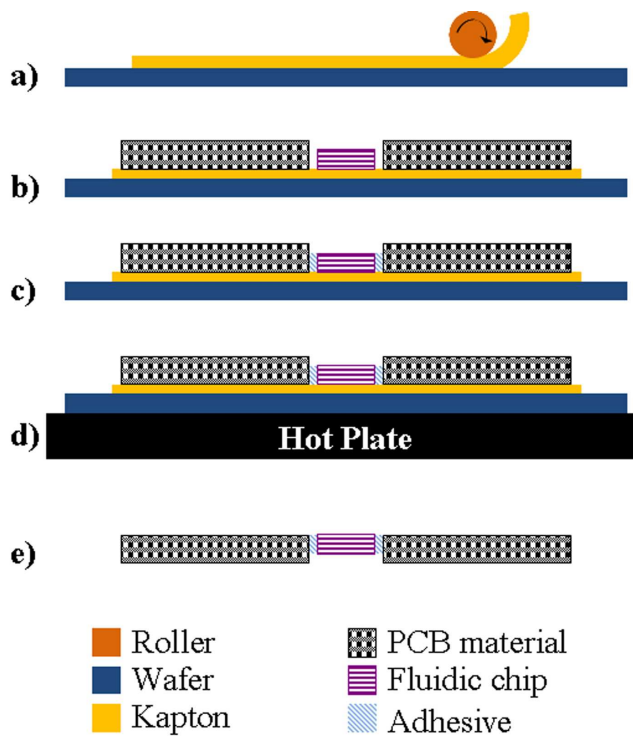


Figure 2. PCB material and nanofluidic chip leveling process flow chart.

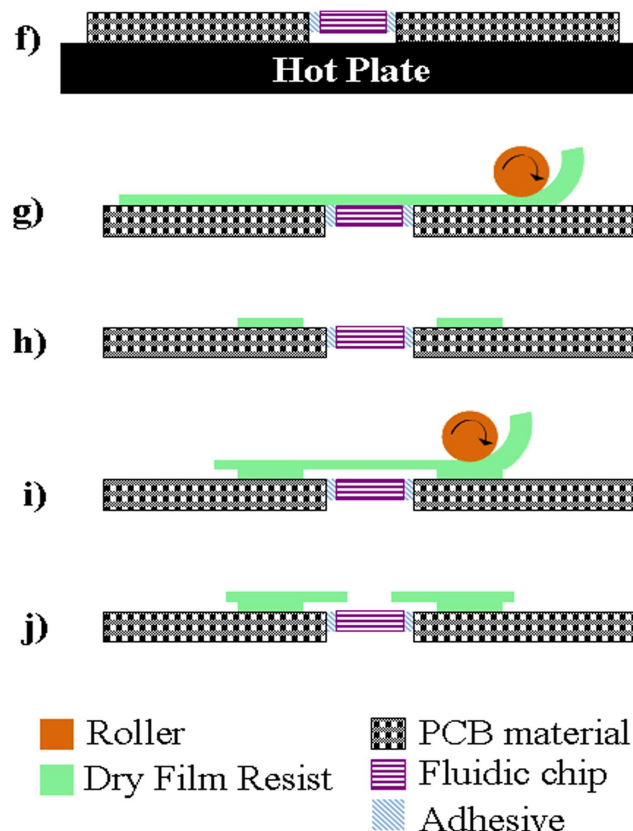


Figure 3. TMMF microfluidic channels lamination on top of the formed substrate.

The substrate is cleaned with ethanol, dried on a hotplate for 2 hours at 120 °C (f). This will avoid that the humidity absorbed by the PCB material affects the DFR lamination process. An oxygen plasma treatment is performed to the substrate in order to improve the adhesion between the TMMF resist and the formed substrate.

The substrate is kept at 45 °C. One of the polyethylene terephthalate (PET) protective layers is removed from the DFR and the TMMF resist is laminated on the substrate (g). The other PET layer is removed after the sample has cooled down. A soft baking step is performed at 90 °C during 5 minutes. The exposure is performed after the sample cools down to room temperature. A post exposure baking step is performed with the same temperature and time as the soft baking step. The TMMF is developed with PGMEA after the sample has cooled down to room temperature (i). A second layer of TMMF is laminated at 45 °C in order to close the microfluidic channels. The second layer is exposed after lamination without removing the remaining PET layer. The sample is cured at room temperature during one day. The PET layer is removed and access holes to the channel are punched with the help of a needle (j). Tests are conducted.

V. CHALLENGES ASSOCIATED WITH THE FABRICATION PROCESS

Here, the challenges encountered are grouped by:

- Challenges associated with the lamination of TMMF on PCB material.
- Challenges associated with the TMMF lamination on top of the fluidic chips.

A. TMMF and Rogers

The challenges associated with the processing of TMMF resist on Rogers materials are: pinholes in the photoresist, trapped bubbles between the resist and the PCB material, cracks in the photoresist, and closed channels.

a) *Pinholes*: TMMF might present pinholes after the soft baking step.

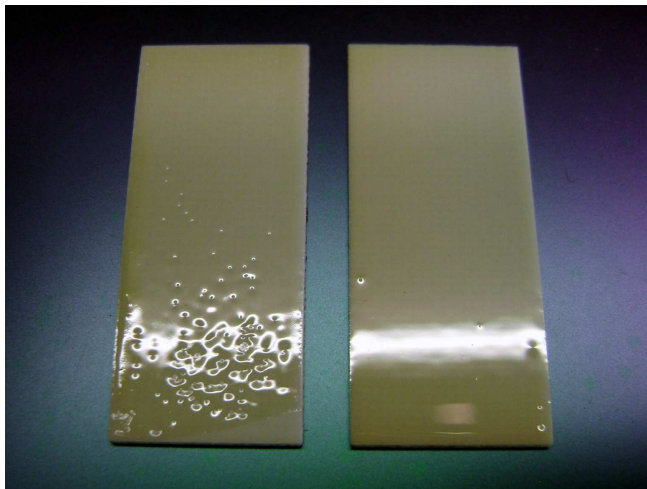


Figure 4. PCB material immersed under water prior to TMMF lamination (left) and PCB material dried at 120 °C prior to TMMF lamination (right). The presence of pinholes on the TMMF resist after soft baking is influenced by the moisture absorbed by the PCB.

Experiments were conducted, and up to some extent, the pinholes can be decreased by using a plasma treatment, nevertheless, the crucial factor determining their presence is the moisture absorbed by the PCB material.

Figure 4 shows two PCB materials where TMMF was laminated and soft baked. In the sample on the left side, the PCB material was immersed in water during 2 hours and its surface was dried with nitrogen prior to TMMF lamination. In the specimen on the right, the PCB material was placed on a hotplate during 2 hours at 120 °C in order to evaporate the absorbed moisture prior to TMMF lamination.

b) *Trapped bubbles and cracks*: Conducted experiments show that if the baking times are either higher or lower than the optimal time and the PCB material contains humidity absorbed from the atmosphere, trapped bubbles and cracks will form in the photoresist structures. The formation of trapped bubbles is directly related to the humidity absorbed by the PCB material and the use of inadequate baking times. The formation of cracks is related to the thermal stresses that result from a forced cooling down of the specimens after the baking steps and improper baking times. Furthermore, the humidity absorbed by the PCB material promotes the formation of cracks.

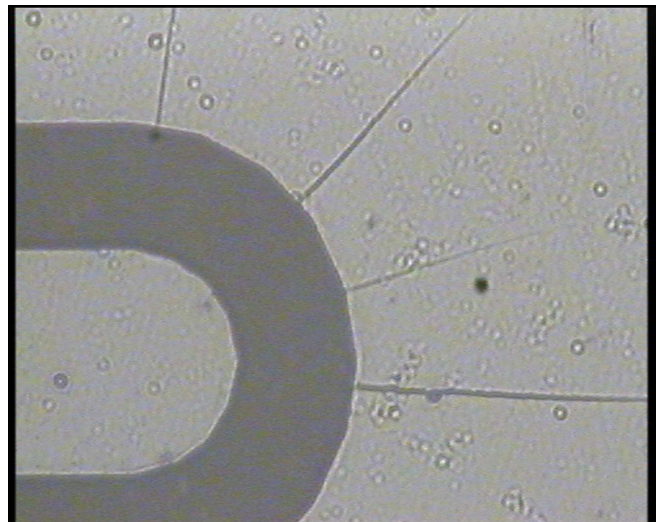


Figure 5. Trapped bubbles between the TMMF resist and the PCB material and cracks due to the humidity absorbed by the PCB material and the improper baking times used for processing of the TMMF.

Figure 5 shows trapped bubbles between the TMMF and the PCB material as well as cracks in the dry film resist structures. The PCB material used for this experiment was not dried prior to TMMF lamination. Moreover, the baking times used in the processing were not optimal.

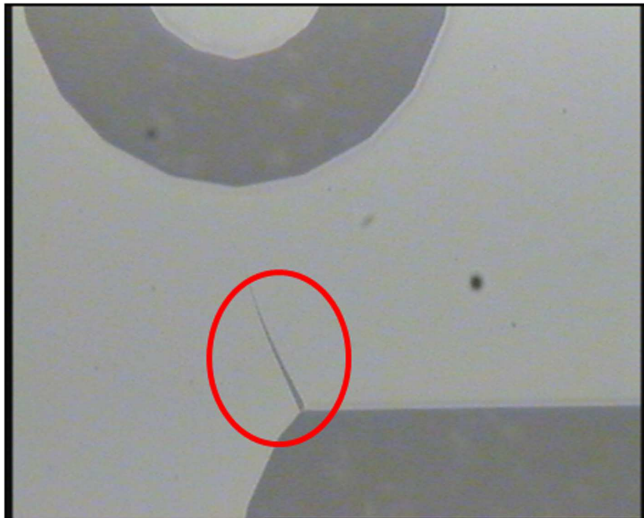


Figure 6. Cracks in the TMMF structures with angles close to 90 °C. The circle in the image points the crack. The cracks are caused by the use of not optimal baking times.

Figure 6 shows a crack in the photoresist structure, but no trapped bubbles. The PCB material used for this experiment was dried prior to TMMF lamination, nevertheless, the baking times were not optimal.

c) *Closed channels:* The exposure time should be controlled accurately when working with Rogers' materials. The effects of an underexposed resist, as Figure 7 shows, are well known. On the other hand, overexposure can result in partially or totally closed fluidic channels.

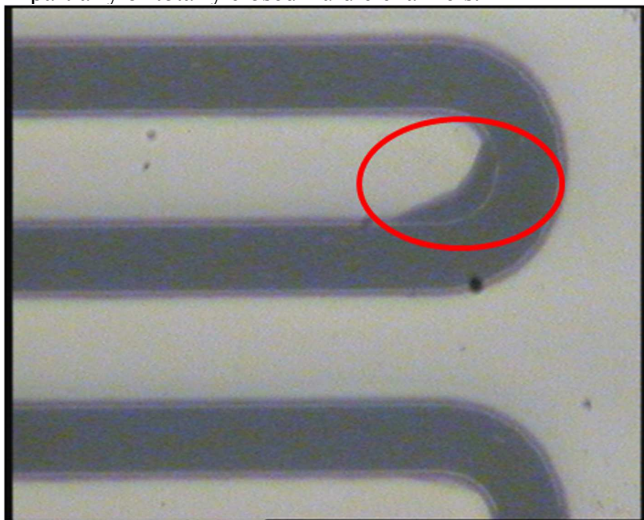


Figure 7. Effects of insufficient exposure time. The circle points an obvious underexposure effect on the TMMF structure.

Scattering and diffraction of ultraviolet (UV) light during exposure is unavoidable when using a nontransparent material. Furthermore, the white color of the PCB material makes reflection of the waves a bigger problem.

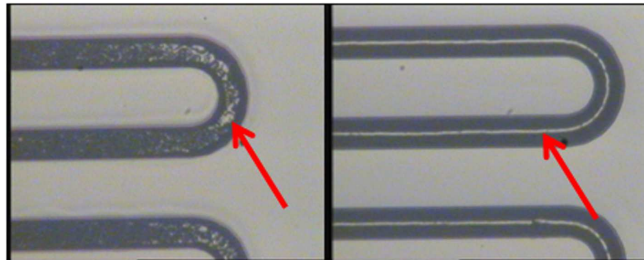


Figure 8. Closed channels on PCB material due to overexposure of the TMMF resist. The arrow in the left image points the effects of an overexposure of 2 seconds. The arrow in the right image points the effects of an overexposure of 6 seconds.

The more a sample is overexposed, the more closed the channels will be. Figure 8 shows a sample overexposed by 2 seconds (left) and a sample overexposed by 6 seconds (right).

B. TMMF and the nanofluidic chips

Nanofluidic chips are usually made of glass and/or silicon. PCB material and Si poses different thermal characteristics. The thermal conductivity of the PCB material is approximately 0.71 W/m²/K [13] and the thermal conductivity of Si is around 140 W/m²/K [12]. Due to the thermal characteristics of the materials, heat transport at the baking steps is not a problem for the PCB material but it is for the Si fluidic chip.

The most common problem associated with the lamination of TMMF on silicon is cracks due to heat transport at the baking steps and the CTE [3]. Figure 9 illustrates this problem.

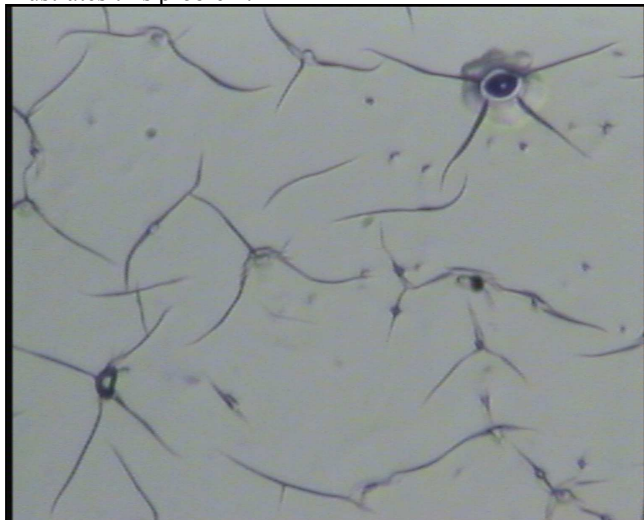


Figure 9. Cracks in the TMMF resist due to the CTEs difference between silicon and the TMMF resist.

When the PCB material and the fluidic chip are of almost the same thickness, the microfluidic chip will conduct heat around 25 times more than the PCB material. Therefore, placing the substrate directly at 90 °C during the baking steps will originate cracks on the TMMF laminated over the fluidic chip. To solve this, the temperature needs to be ramped (2 °C/min) starting at 55 °C during the baking steps,

when the temperature reaches 90 °C the samples are baked 5 minutes. Afterwards the hot plate's temperature is set to 25 °C and the sample is removed from the hot plate when the 25 °C is reached.

Furthermore, if the fluidic chip is considerably thinner than the PCB material, the substrate can be placed directly at 90 °C. In this case, the thermal conductivity of the air between the chip and the hot plate will limit the heat flux to the chip, avoiding the presence of cracks on the TMMF.

VI. EXPERIMENT SETUP

In order to test the feasibility of the proposed interconnection technology, a leakage test was conducted to the devices together with a reliability test.

The leakage test consists of injecting a rodhamine + ethanol + di water solution in the TMMF channels through one of the inlets. A visual inspection follows to detect any leakage. Special attention is given to the interconnection area between the different materials. Figure 10 shows the mentioned interconnection area before closing the TMMF channels.

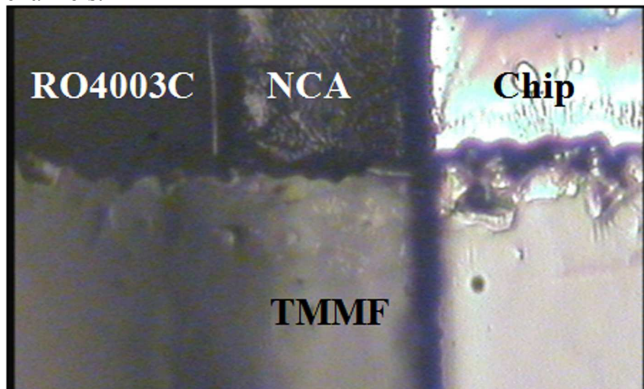


Figure 10. Close up of the interface between the different materials that form the fluidic interconnections to the nanofluidic chips.

The reliability test consists of a thermal shock test based on the MIL-STD-883C. The purpose of this test is to accelerate the appearance of delamination and cracks. The test consists of 15 cycles where each cycle is composed by a high temperature and a low temperature step. The high temperature step is performed at 100 °C (+10 °C, -2 °C) and the low temperature step at 0 °C (+2 °C, -10 °C). Each step is performed for 5 minutes. The liquid used to perform the test is water. After completing the test, a visual inspection is performed at a magnification no greater than 3x [4].

VII. RESULTS

In this section, the results are presented in three subsections. First the results concerning the lamination of TMMF on PCB material are presented. Then the leakage test results are exposed. Finally, the results concerning the compatibility of the different materials and the reliability of the packaging method are presented.

A. TMMF resist channels on PCB material

To obtain good results fabricating microfluidic channels on PCB materials some factors should be kept in mind. The baking times provided by the companies are optimal, nevertheless, different materials conduct the heat in a different rate, and therefore, the material temperatures might deviate from the prescribed temperature, especially when using a hot plate. Furthermore, PCB materials are more reflective than silicon or glass; because of this the exposure time should be tuned accurately, if channels of less than <20 μm are desired, this parameter is critical.

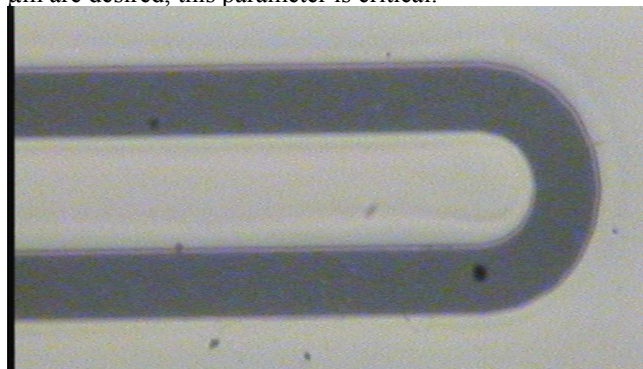


Figure 11. Microfluidic channels on PCB material. The image shows the results of optima processing parameters (exposure and baking times).

Figure 11 shows a TMMF structure on PCB material fabricated with optimal exposure and baking times.

B. Leakage test

Concerning the leakage test, Figure 12 shows a device with the packaging technology presented in this work.

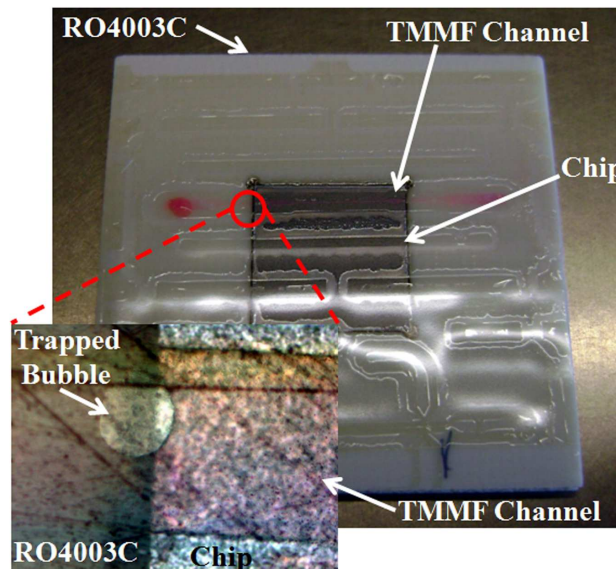


Figure 12. TMMF microfluidic channels on PCB material as fluidic interconnections for nanofluidic chips. The small image in the lower left corner zooms in at the interface of the different materials that compose the device; it shows no leakage of the rodhamine solution.

The pink liquid flowing through the TMMF channel is a solution of rodhamine + ethanol + di water. It is possible to

observe that no leakage occurs. The small image at the lower corner in the left was obtained with a 1X71 Olympus inverted microscope equipped with a los noise self cooling CCD camera (color view II, Olympus); it shows, with 10x magnification, the area where the different materials interconnect. It is possible to observe the liquid solution flowing through the TMMF channel without leakage.

C. Reliability test

Figure 13 shows a device without closed channels after the thermal shock test.

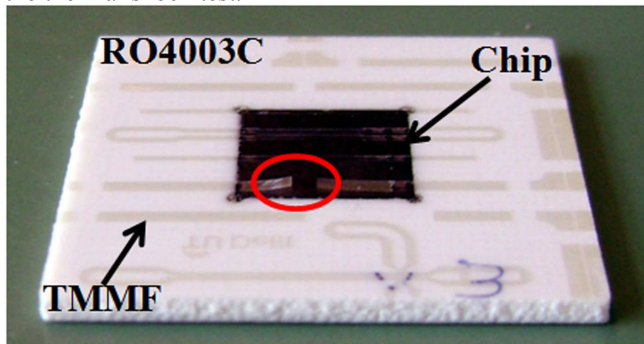


Figure 13. TMMF delamination on top of the Si chip after the thermal shock test. The circle points at the place where the delamination occurs.

The red circle makes emphasis on a failure result from the test. Delamination of TMMF occurs on top of the fluidic chip. From the 3 tested specimens, the failure was observed only in the specimen from Figure 13.

VIII. CONCLUSION AND FURTHER WORK

The use of TMMF resists for the fabrication of microfluidic channels on PCB as fluidic interconnections of nanofluidic chips to the outside world is feasible, providing of simplicity the fabrication process.

The thermal shock reliability test showed that the use of high temperature conditions could bring delamination problems mainly at the interface TMMF–Si chip. This means that the strength of the TMMF microfluidic interconnections decreases and so the probability of leakage increases.

Further work includes the study of the usability of ink-jet printing to create the electrical interconnections between the fluidic chip electrodes and the PCB tracks. The PCB in turn can carry the necessary electronics for control and read-out. This will enable the PCB as the core for the integration of micro- and nanofluidic chips together with the electronics into a complex system.

ACKNOWLEDGMENT

The authors thank the Delft Institute of Microsystems and Nanoelectronics (Dimes) staff for their valuable help.

Furthermore, the authors thank Rogers Corporation for providing low-roughness Rogers' material free of cost and Tokyo Ohka Kogyo Co., Ltd. for providing TMMF S2030 resist to develop this research. This work is supported by the Dutch Technology Foundation STW.

REFERENCES

- [1] N. T. Nguten and S. T. Wereley., "Fundamentals and applications of microfluidics", Artech House Publishers, 2002, pp. 67-129.
- [2] L. Zhang, Thesis: "Bioparticle separation in microfluidic devices for in-line application", Delft University of Technology, Delft, the Netherlands, 2009, pp.112-113.
- [3] V. R. S. S. Mokkalapati, "Micro and nanofluidic devices for single cell and DNA analysis", Delft University of Technology, Delft, the Netherlands, 2011.
- [4] Military standard: test methods and procedures for microelectronics MIL-STD-883C notice 6, August 1987.
- [5] U. Stöhr, P. Vulto, P. Hoppe, G. Urban and H. Reinecke, "High-resolution permanent photoresist laminate for microsystem applications", J. Micro/Nanolith. MEMS MOEMS, vol. 7(3), Jul.-Sep. 2008, doi: 10.1117/1.2964217.
- [6] K. Kalkandjiev et al, "Microfluidics in silicon/polymer technology as a cost-efficient alternative to silicon/glass", Journal of micromechanics and microengineering, Vol. 21, 2011, doi:10.1088/0960-1317/21/2/025008.
- [7] K. Wang et al, "Nanofluidic channels fabrication and manipulation of DNA molecules", IEE Proceedings Nanobiotechnology, Vol. 153, No. 1, Feb. 2006, doi:10.1049/ip-nbt:20050044.
- [8] C. Song and P. Wang, "Fabrication of sub-10 nm planar nanofluidic channels through native oxide etch and anodic wafer bonding", IEEE Transactions on Nanotechnology, Vol 9, No. 2, Mar. 2010, doi:10.1109/TNANO.2009.2038377.
- [9] C. Wu et al, "Design and fabrication of a nanofluidic channel by selective thermal oxidation and etching back of silicon dioxide made on a silicon substrate", Journal of Micromechanics and Microengineering, Vol 17, 2007, doi:10.1088/0960-1317/17/12/001.
- [10] L. J. Guo, X. Cheng and C. Chou, "Fabrication of size-controllable nanofluidic channels by nanoimprinting and its application for DNA stretching", Nanoletters, Vol. 4, No. 1, 2004.
- [11] R. Yang et al, "Fabrication of micro/nano fluidic channels by nanoimprint lithography and bonding using SU-8", Microelectronic Engineering, 2009, doi:10.1016/j.mee.2009.02.002, Article in Press.
- [12] H. R. Shanks et al, "Thermal conductivity of silicon from 300 to 1400 °K", Phys. Rev. (USA), Vol. 130, No. 5, pp. 1743–1748, 1963.
- [13] Rogers Corporation Avanced Circuit Materiaals, "RO4000® laminates – data sheet", Retrieved from <http://rogerscorp.com/acm/products/16/RO4000-Series-High-Frequency-Circuit-Materials-Woven-glass-reinforced-ceramic-filled-thermoset.aspx> on January 20th 2011.

The Radiobiological Effect of the TiO₂ – Cyclodextrin Suspension

Mihaela Corneanu

Genetics Engineering Dept.

Banat's University of Agricultural Sciences and
Veterinary Medicine, 300645-Timișoara, Romania,
micorneanu@yahoo.com

Gabriel C. Corneanu, Aurel Ardelean

Life Sciences Dept.

“Vasile Goldis” Western University
310025-Arad, Romania
gabicorneanu@yahoo.com, ardelean@uvvg.ro

Carmen Lazău, Ioan Grozescu

I.N.C. –D.E.M.C. Timișoara

Timișoara, Romania
carmenlazau@yahoo.com
grozescu@icmct.uvt.ro

Nicoleta G. Hădăruță

Faculty of Food Processing Technology, Banat's
University of Agricultural Sciences and Veterinary
Medicine, 300645-Timișoara, Romania,
nico_hadaruga@yahoo.com

Daniel I. Hădăruță

*Faculty of Industrial Chemistry and Environmental
Engineering*, “Politehnica” University of Timișoara,
300006-Timișoara, Romania,
daniel.hadaruga@chim.upt.ro

Lucian Barbu-Tudoran

Biology Dept.

Babeș-Bolyai University
Cluj-Napoca, România
lucianbarbu@yahoo.com

Abstract — The effect of a TiO₂ nanoparticle suspension (4 mg in 5 ml distilled water) doped or not with gold or iron, complexed or not with α - or β -cyclodextrin, on the mitotic division was studied. The treatment was performed in the M cellular mitotic cycle phase, in the meristematic tissue of *Nigella damascena* radicles, being analyzed the cytogenetic modifications. The cyclodextrin type and the ratio between cyclodextrin and titanium dioxide affect the percentage of normal cells and the chromosome aberration type. The TiO₂ complexed with α -cyclodextrin did not facilitate the reunion of the chromosome broken ends (absence of bridges in anaphase and in telophase). The titanium dioxide doped with iron, complexed with α - or β -cyclodextrin, also reduced the percentage of reunion of the broken ends of the chromosomes. These findings suggest the possibility of using doped or undoped TiO₂, complexed with α -cyclodextrin, in the anticarcinogen therapy.

Keywords - TiO₂-Au, TiO₂-Fe, cyclodextrin, chromosome mutations.

I. INTRODUCTION

Although the bimetallic particles were obtained long ago, their characterization was effected at the end of the 20th century [1]. The conjugation of bimetallic nanoparticles of AuNP type with oligonucleotides facilitates their use in molecular biology experiments and nanobiotechnology [2]. Other types of AuNP biconjugate with peptides, lipids, enzymes, drugs or viruses, were also obtained with application in nanobiotechnology, nanomedicine and/or in gene therapy.

Cyclodextrins are cyclic oligosaccharides. Depending on the glucose moiety number, they are classified in: α -cyclodextrins (with 6 glucose units), β -cyclodextrins (with 7 glucose units), and other greater homologues. The complexes with pharmaceutical products are usually better accepted and tolerated by the organism; they protect the bioactive substances against degradation (oxygen, humidity) and reveal controlled release properties. They are non-toxic and stable at the human digestive enzyme action. They are used in the obtaining of some pharmaceutical products, food additives, in agriculture, a/o [3]. In recent papers, the effect of β -cyclodextrin conjugate with TiO₂ [4] or with different bioactive substances [5], [6] was analyzed, in different experimental conditions.

In the present study nanoparticles of TiO₂-Au and TiO₂-Fe, dispersed in α - or β -cyclodextrin, the ratio between TiO₂ and cyclodextrin being 1:1 or 1:2, were used. The experiments were performed at a radiobiological tester plant (*Nigella damascena* L.), the chromosome aberrations from the meristematic radicle tissue being used as radiobiological indices.

II. MATERIAL AND METHODS

A. Nanoparticle achievement

1) Achievement of undoped and doped TiO₂ nanocrystals.

Undoped and doped titanium dioxide nanocrystals were synthesized by the sol-gel route, using the precursors: titanium isopropoxide, isopropyl alcohol, distilled water, nitric acid, gold (III) chloride trihydrate and ferrous nitrate. 5 ml of titanium isopropoxide (in drops) were mixed with 30

ml of isopropyl alcohol, under continuous stirring. After a few minutes of stirring, distilled water was added, continuously controlling the solution pH with nitric acid in order to avoid the precipitation. In the case of iron-doped and gold-doped TiO₂ ions, after the adjustment of the pH (2.5 for Au, 5.0 for Fe), the previously prepared solutions, namely iron nitrate and gold (III) chloride trihydrate were added under continuous stirring. In both cases, the gel was dried and washed in order to remove the secondary reaction products. The calcination was achieved in the oven, at a temperature of 250°C for undoped TiO₂ and 500°C for Au or Fe doped TiO₂. The achieved nanocrystals based on titanium dioxide were used for complexation with cyclodextrins.

2) *Achievement of complexes based on TiO₂ with α -cyclodextrin or β -cyclodextrin.*

α - and β - cyclodextrins used for the co-crystallization with the previously attained titanium dioxide were of analytical purity (Fluka Chemie AG). In order to perform the complexation/co-crystallization, different solvents were used as suspension medium. In 1 ml distilled water, 0.054 g of α -(α -CD) or 0.067 g of β -cyclodextrin (β -CD) was dissolved, at a temperature of 50°C. 0.075 g of undoped and doped TiO₂ was added to the solution, under continuous and vigorous stirring for 30 minutes at 50°C. For the completion of the complexes crystallization, the solution was cooled and kept for 12 hours at a temperature of 5°C, followed by filtration and drying of the achieved nanocrystals. The obtained materials were characterized by X-ray diffraction (XRD), scanning/transmission electron microscopy (SEM/TEM) and energy dispersive X-ray analysis (EDX).

Biological experiment

The experiment was performed *in vivo*, on the radiogenetic tester species *Nigella damascena* (Fam. *Ranunculaceae*). This species, used for a long time, is for its features: small somatic chromosome number different morphologically (2n=12), synchronized cell mitotic cycle, centromeres situated near the nuclear envelope, and absence of the bioactive substances in seeds [7], [8], [9]. The seeds with radicles of about 10 mm length were treated in the mitotic phase of the cellular cycle (for 2 hours), with a suspension of TiO₂-Au or TiO₂-Fe, complexed or not with α -cyclodextrin, or with β -cyclodextrin (4 mg TiO₂-Me in 5 ml distilled water). After treatment, the radicles were harvested for the cytogenetic investigations.

B. Cytogenetic investigations

The chromosome aberrations were analyzed in the radicular meristematic tissue, on squash preparation type, stain with a Carr solution. The normal and aberrant phases of the mitotic cycle were analyzed, as well as the metabolic and structural modifications of the chromosomes and of the mitotic spindle. Although in the literature there are numerous papers about the environmental factors' effect at the chromosome level, regarding the nanoparticles' effect at the chromosome level the information is poor. The investigation performed at the Chinese hamster ovary, with TiO₂ particles, in the presence or absence of the UV light, evidenced that these not enhance the chromosomal

aberrations' frequency [10]. Similar results were obtained by other authors, in the genotoxicity tests performed in Chinese hamster ovary, as well as in experiments on aquatic organisms (*Daphnia magna*, *Onchorhynchus mykiss* and green algae *Pseudokirchneriella subcapitata*), acutely exposed to the ultrafine TiO₂ particle-types [11], or in experiments in fish (*Nothobranchius rachovi*), at which the mitotic index was analyzed in different organs and variants [12], [13].

III. RESULTS AND DISCUSSIONS

A. Characterization of the nanoparticles

The XRD patterns (Fig. 1) analyses present the crystallization as anatase form of the undoped/Au or Fe doped TiO₂, even if the calcination temperatures for the TiO₂ doping surpass the value of 250°C. The presence of the dopant in the crystalline network of the titanium dioxide prevents the transition of phases from anatase to rutile. From the diffraction spectra it is noticed that the dopants did not present separate peaks, which means that they are distributed uniformly in the crystalline network. From the surface morphology (SEM) it can be observed that the TiO₂-Au and TiO₂-Fe nanospheres' dimensions range between 10 and 20 nm (Fig. 2, a and b). EDX microprobe provided a semiquantitative elemental analysis of the surface indicating the Ti, O, Au and Fe presence (Fig. 2, c and d).

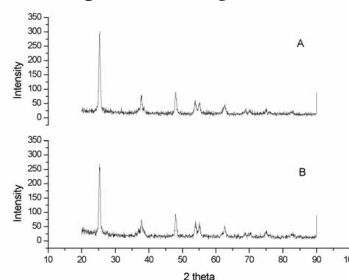


Figure 1. X-ray pattern of TiO₂ doped: (A) – with Au ions; (B) – with Fe ions.

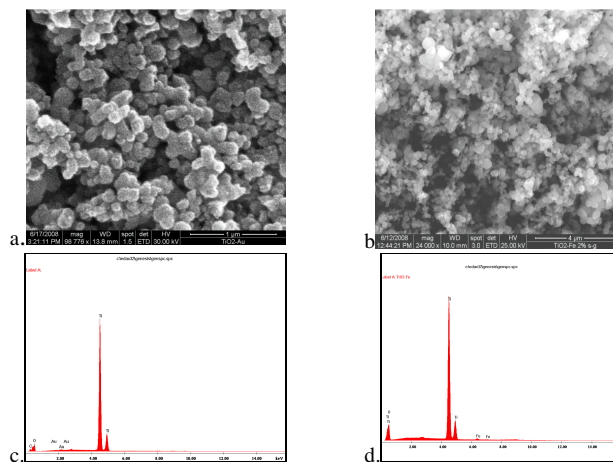


Figure 2. SEM micrographs of : a. TiO₂-Au, b. TiO₂-Fe, EDX spectra of: c. TiO₂-Au, d. TiO₂-Fe

From the SEM analyses of TiO₂ complexes with α - or β -cyclodextrin (Figs. 3-5), the needle-like, parallelepiped shape of the crystals (or co-crystals) for the undoped TiO₂/ α -CD and β -CD complexes can be seen. The crystals have much smaller dimensions compared to those of the raw materials (pure α - or β -CD), the length being in the range of 10-100 nanometers, and the width of only a few tens of nanometers. In the case of complexes TiO₂-Au/ α -CD, the crystals present similar morphologies and dimensions to the undoped TiO₂, but these are more agglomerated. In the case of TiO₂-Au/ β -CD complexes, the crystal morphology is different; the crystals are more uniform, of smaller dimensions, agglomerated, of rhomboidal (generally polyhedral) form. The approximate dimensions of the crystals are between tens and hundreds of nanometers.

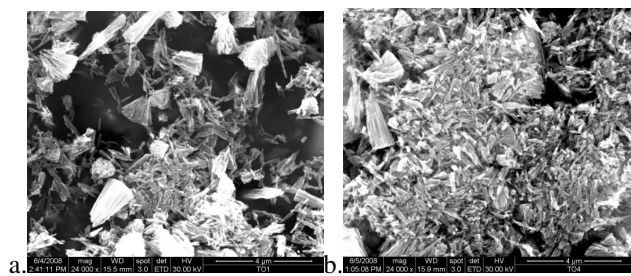


Figure 3. SEM image for undoped TiO₂-CD: a. TiO₂/ α -CD b. TiO₂- β -CD

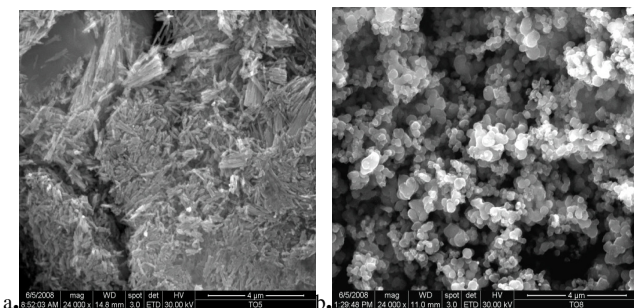


Figure 4. SEM image for TiO₂-Au-CD: a. TiO₂-Au/ α -CD b. TiO₂-Au/ β -CD

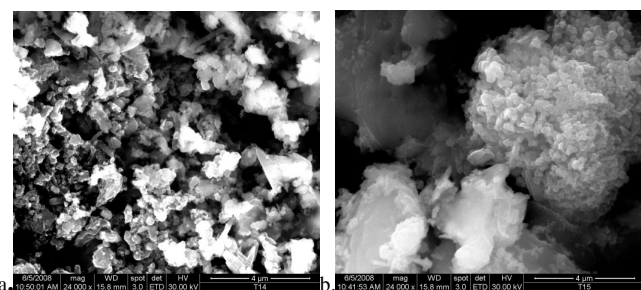


Figure 5. SEM image for TiO₂-Fe-CD: a. TiO₂-Fe/ α -CD b. TiO₂-Fe/ β -CD

B. Percentage of the normal and aberrant mitotic phases

The percentage of the normal cells, in all experimental variants, recorded inferior values in comparison with untreated Control. In the experimental variants, the percent

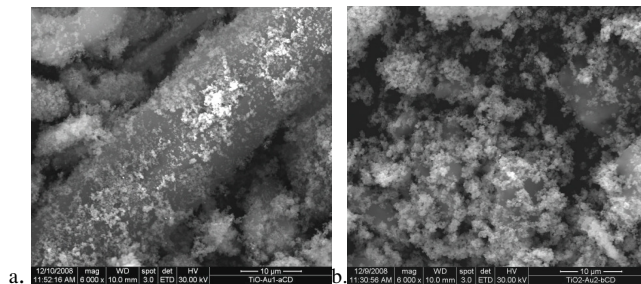


Figure 6. SEM image with TiO₂-Au nanoparticles on the: a. α -CD crystals surface b. β -CD crystals surface.

The EDX analyses of the obtained complexes with undoped/doped TiO₂ have indicated a higher concentration of Ti in the complexes, especially in the case of α -CD complexation, which can be explained by the fact that pure α -CD and its complexes are more soluble in the water system than β -CD or the corresponding complexes.

The TiO₂-Au or TiO₂-Fe nanoparticles are disposed on the surface of the α -CD or β -CD (Fig. 6). For the radical treatment, the complex TiO₂-Me / cyclodextrin was suspended in distilled water, having as a result an aqueous solution of TiO₂-Au or TiO₂-Fe nanoparticles in α -CD or β -CD (Figs. 7, 8), without crystalline structure, easily absorbed by the cells.

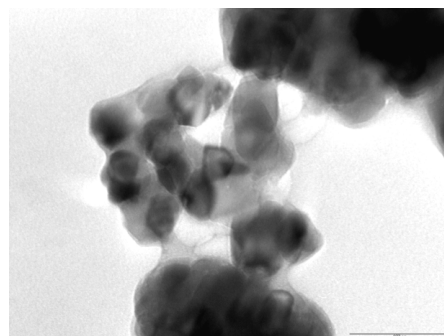


Figure 7. TEM image with a TiO₂-Au suspension in α -CD solution

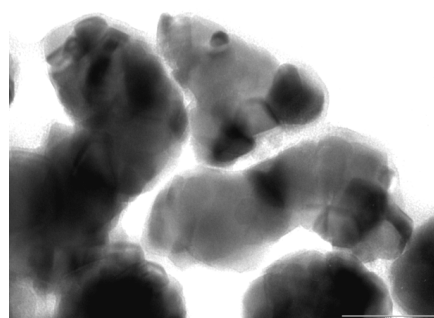


Figure 8. TEM image with a TiO₂-Au suspension in β -CD solution

of normal cells was dependent especially on the nanoparticle types (Table I). Thus, in the treatments with unconjugated TiO₂, the percentage of normal cell recorded values of about 96% (except for the variant with β -cyclodextrin in ratio 1:2),

92-94% in variants with Au-TiO₂ and around 95% in the variants with Fe-TiO₂.

The normal cell percentage in the presence of TiO₂ nanoparticles, without metals or cyclodextrin, recorded values similar to those recorded by the TiO₂ nanoparticles complexed with cyclodextrin α or β .

Because the cyclodextrin is a hydrosoluble substance and in an aqueous solution these crystals are dissolved, the shape of the cyclodextrin crystals does not influence their absorption in the plant meristem and implicitly the percentage of aberrant or normal cells in different mitotic phases, as well as the structural modifications of the chromosomes and of the mitotic spindle.

TABLE I. THE NORMAL CELL PERCENTAGE IN DIFFERENT PHASES OF THE MITOTIC CYCLE

| Experimental Variant | Normal cells in mitosis (%) | Normal cell percentage in mitosis phases | | | | |
|------------------------------------|-----------------------------|--|--------------|-----------|----------|-----------|
| | | Prophase | Prometaphase | Metaphase | Anaphase | Telophase |
| Control | 99.40 | 99.80 | 100.00 | 97.90 | 96.70 | 99.40 |
| TiO ₂ | 96.80 | 97.44 | 100.00 | 96.23 | 95.72 | 94.38 |
| TiO ₂ - α 1:2 | 96.61 | 91.49 | 100.00 | 100.00 | 96.67 | 97.22 |
| TiO ₂ - α 1:1 | 96.00 | 100.00 | 100.00 | 97.87 | 92.13 | 91.14 |
| TiO ₂ - β 1:2 | 98.88 | 99.07 | 100.00 | 100.00 | 97.54 | 97.77 |
| TiO ₂ - β 1:1 | 96.29 | 98.55 | 100.00 | 96.77 | 94.84 | 94.67 |
| TiO ₂ -Au- α 1:2 | 94.28 | 98.66 | 100.00 | 94.34 | 90.22 | 95.36 |
| TiO ₂ -Au- α 1:1 | 94.06 | 98.72 | 100.00 | 93.24 | 88.73 | 93.51 |
| TiO ₂ -Au- β 1:2 | 94.28 | 93.88 | 100.00 | 91.43 | 84.95 | 97.20 |
| TiO ₂ -Au- β 1:1 | 92.60 | 100.00 | 100.00 | 92.69 | 90.74 | 92.62 |
| TiO ₂ -Fe- α 1:2 | 95.69 | 96.90 | 100.00 | 94.74 | 93.46 | 98.16 |
| TiO ₂ -Fe- α 1:1 | 95.55 | 100.00 | 100.00 | 93.10 | 86.05 | 98.04 |
| TiO ₂ -Fe- β 1:2 | 95.56 | 96.30 | 100.00 | 91.11 | 98.11 | 96.67 |
| TiO ₂ -Fe- β 1:1 | 95.25 | 100.00 | 100.00 | 92.31 | 92.31 | 92.59 |

C. Structural modifications of the chromosomes

As a consequence of the free radicals action, the chromosomes are broken, which leads to structural chromosome aberrations. In different phases of the mitosis, or under influence of some substances, the broken ends of the chromosomes can be reunited or not. In the absence of the reunion processes, acentric fragments, minutes, a/o result (Figs. 9, 10, 12), and after the reunion of two broken chromosomes, mainly bridges (Fig. 11), or arch result.

The BR index (anaphasic fragment frequency/anaphasic bridge frequency), points out the possibility of a substance or another factor to reunite of the broken ends of the chromosomes. A low BR index, suggests a substance with role in reunion of the broken ends of the chromosomes, having a radioprotective role [14]. A high BR index suggests that a substance not favor the reunion of the broken

chromosome ends, the affected cells being eliminate from tissue (Table II).

The cyclodextrin type and ratio between TiO₂:cyclodextrin influenced the reunion or not of the broken ends of the chromosomes, and implicitly the aberration type (Table II). The absence of bridges in anaphase and telophase at variants with TiO₂- α -cyclodextrin, suggests that the α -cyclodextrin does not facilitate the chromosomal reunion processes of the chromosome broken ends. Thus, in variant TiO₂- α -cyclodextrin (ratio 1:2), 66.66% acentric fragments are present in anaphase and 11.11% in telophase, while the chromosomal bridges are absent. This feature can be used for the progressive elimination from organism of the cells with a high multiplication ratio (carcinogen cells). At a ratio of 1:1 between the two components, the percentage of acentric fragments is lower (15.73, and 8.86%), the reunion process of the broken ends being also absent.

TABLE II. THE STRUCTURAL AND METABOLIC MODIFICATIONS OF THE CHROMOSOMES

| Experimental variant | Prophase (%) | | Metaphase (%) | | | Anaphase | | | Telophase | |
|------------------------------------|--------------|------|---------------|----------------------|---------------------------|---------------------|-------------------|----------|---------------------|-------------------|
| | PCC | DCC | DCC | Spindle inactivation | Kinetochores Inactivation | Fragments/100 cells | Bridges/100 cells | BR index | Fragments/100 cells | Bridges/100 cells |
| Control | 0.09 | 0.00 | 0.05 | 0.00 | 0.00 | 0.00 | 0.00 | 0.00 | 0.00 | 0.00 |
| TiO ₂ | 0.12 | 0.80 | 0.00 | 0.00 | 0.00 | 4.88 | 0.00 | 4.88 | 2.64 | 0.00 |
| TiO ₂ - α 1:2 | 0.00 | 2.33 | 0.00 | 0.00 | 0.00 | 66.66 | 0.00 | 66.66 | 11.11 | 0.00 |
| TiO ₂ - α 1:1 | 0.00 | 0.00 | 0.00 | 0.00 | 0.00 | 15.73 | 0.00 | 15.73 | 8.86 | 0.00 |
| TiO ₂ - β 1:2 | 0.00 | 0.00 | 0.35 | 0.00 | 0.00 | 4.10 | 0.00 | 4.10 | 4.44 | 0.00 |
| TiO ₂ - β 1:1 | 0.72 | 0.72 | 0.00 | 0.00 | 0.00 | 8.39 | 0.65 | 12.91 | 10.06 | 0.59 |
| TiO ₂ -Au- α 1:2 | 0.00 | 0.00 | 1.79 | 0.00 | 0.00 | 4.28 | 0.35 | 12.23 | 1.34 | 2.46 |
| TiO ₂ -Au- α 1:1 | 0.00 | 0.00 | 0.00 | 0.00 | 0.00 | 4.73 | 0.11 | 43.00 | 3.56 | 0.04 |
| TiO ₂ -Au- β 1:2 | 4.08 | 0.00 | 0.00 | 0.57 | 0.57 | 5.38 | 1.08 | 4.98 | 2.80 | 2.80 |
| TiO ₂ -Au- β 1:1 | 0.00 | 0.00 | 0.00 | 0.46 | 0.46 | 13.89 | 5.56 | 2.49 | 15.93 | 3.28 |
| TiO ₂ -Fe- α 1:2 | 3.10 | 0.00 | 2.11 | 0.35 | 1.05 | 13.08 | 0.93 | 14.07 | 2.75 | 2.75 |
| TiO ₂ -Fe- α 1:1 | 0.00 | 0.00 | 2.30 | 1.15 | 1.15 | 37.21 | 0.00 | 37.21 | 5.88 | 0.00 |
| TiO ₂ -Fe- β 1:2 | 1.85 | 1.85 | 4.44 | 3.33 | 1.11 | 1.92 | 0.00 | 1.92 | 1.67 | 0.00 |
| TiO ₂ -Fe- β 1:1 | 0.00 | 0.00 | 0.00 | 1.92 | 0.24 | 11.54 | 7.69 | 1.49 | 17.28 | 4.94 |

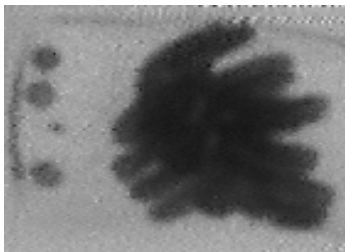


Figure 9. Acentric fragments in metaphase (TiO₂-Fe/α-CD, 1:1)

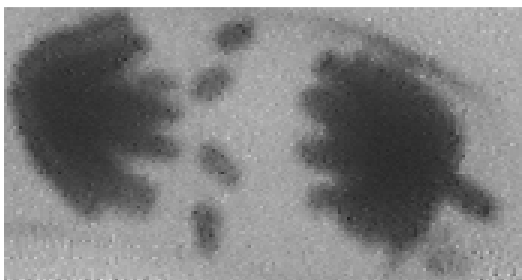


Figure 10. Acentric fragments in telophase (TiO₂-Fe/α-CD, 1:1)



Figure 11. Bridge in anaphase (TiO₂-Fe/β-CD, 1:1)

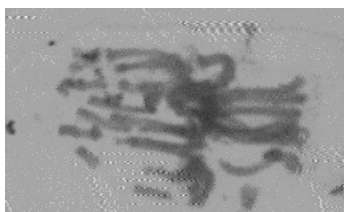


Figure 12. Kinetochore inactivation and chromosome break (TiO₂-Au/β-CD, 1:1)

The β-cyclodextrin presence induces a very low percent of reunion of the broken ends, only at a ratio of 1:1.

Complexed with cyclodextrin, the Fe-TiO₂ manifested the inhibition of the reunion process of the chromosomes' broken ends (the absence of the bridges or their presence in a lower percentage), the efficacy being dependent on the cyclodextrin type and the ratio TiO₂ : cyclodextrin.

The nanoparticles conjugated with gold or iron, independent of the cyclodextrin type presence and of the ratio TiO₂ : cyclodextrin, induced in a small percentage (0.57%-1.92%) the inactivation of the mitotic spindle, as well as the kinetochore inactivation (0.46-1.15%; Fig. 12).

The most stable phase from the cellular cycle was prometaphase, and the most sensitive one was anaphase, independent on the experimental variant (Table I). Although in the literature there are numerous papers about the

environmental factors' effect at the chromosome level, regarding the nanoparticles' effect at the chromosome level the information is poor. The investigation performed at the Chinese hamster ovary, with TiO₂ particles, in the presence or absence of the UV light, evidenced that these not enhance the chromosomal aberrations' frequency [10]. Similar results were obtained by other authors, in the genotoxicity tests performed in Chinese hamster ovary, as well as in experiments on aquatic organisms (*Daphnia magna*, *Onchorhynchus mykiss* and green algae *Pseudokirchneriella subcapitata*), acutely exposed to the ultrafine TiO₂ particle-types [11], or in experiments performed in fish (*Nothobranchius rachovi*), at which the mitotic index (the metaphase number in 100 microscopic fields) was analyzed in different organs and experimental variants [12], [13]. The recorded values were dependent on the organ, being bigger in animals treated with TiO₂, in comparison with untreated Control. Other authors [15] analyzed the percentage of chromosomal aberrations induced by three commercial TiO₂ types in isolated human lymphocyte cultures. The percentage of chromosomal aberrations depended on the treatment type, the features of the used product, a/o. The anatase crystallization form induced a significant increase of the total chromosomal number, but without establishing a dose – response relation. The main types of recorded chromosomal aberrations were not presented.

D. Metabolic modifications of the chromosomes

The metabolic modifications of the chromosomes affected especially the condensation degree of the chromatin fibre and the synchronisation of this process, and others (Table II). Their presence reveals the action of a stress or an experimental factor which makes the interphase cells enter into mitosis abruptly.

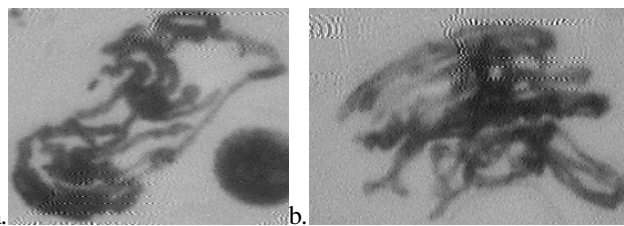
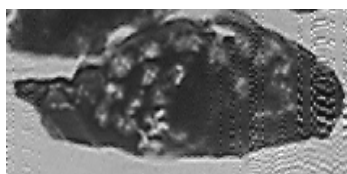


Figure 13. a. PCC in prophase (TiO₂-Fe/β-CD, 1:2); b. DCC in metaphase (TiO₂-β-CD, 1:1)

The main metabolic modifications are premature chromosome condensation (PCC; Fig. 13a.), or delay in chromosome condensation (DCC; Figs. 13b, 14), as well as gaps (the uncoloured regions on the chromosome length), differences in condensation degree of the chromatin fibers in eu- and heterochromatin regions of the chromosomes, resulting a banding aspect of the chromosomes (met especially in metaphase), the parallel disposition of the chromatin fibers in prophase, a/o. PCC and DCC were met in a low percentage (0.72-4.08%), especially in variants treated with β-cyclodextrin, independent of the presence or absence of the chelated metal (gold or iron).

Figure 14. DCC in metaphase (TiO₂-β-CD, 1:1)Figure 15. Lyses areas in interphase nucleus (TiO₂-Au/β-CD, 1:1)

The presence of some lysed areas in nucleus in different percentage in almost all treated variants (Fig. 15) underline the presence of an exobiotic factor in the cell.

IV. CONCLUSIONS

The undoped and doped TiO₂ nanocrystals used in this experiment presented the *anatase* form crystallization, the TiO₂-Au and TiO₂-Fe nanospheres presented dimensions ranging between 10-20 nm.

The TiO₂-Me nanoparticles, complexed or not with α- or β-cyclodextrin, presented a different morphology, dependent on the doped metal and cyclodextrin type. The TiO₂-Me nanocrystals are present at the surface of cyclodextrin crystals.

In an aqueous solution, cyclodextrin crystals are dissolved and TiO₂-Me are suspended in a cyclodextrin solution, being thus absorbed in the meristem cells.

Doped or undoped TiO₂ nanocrystals, complexed with α- or β-cyclodextrin, induced both metabolic and structural modifications at the chromosome and mitotic spindle level, depending on the chelated metal, the cyclodextrin type and the ratio TiO₂: cyclodextrin (1:2 or 1:1).

As the cyclodextrin is a hydrosoluble substance, the different form of crystals of the complexed TiO₂-Me-cyclodextrin, did not influence the percentage of aberrant or normal cells in different mitotic phases, as well as the structural or metabolic modifications of the chromosomes and of the nuclear spindle.

The cyclodextrin type and ratio between TiO₂: cyclodextrin influenced both the reunion process of the chromosome broken ends, and the chromosome aberration type.

The α-cyclodextrin induced a high acentric fragment percentage in anaphase and telophase, and did not facilitate the reunion processes of the chromosome broken ends (the absence of bridges from cells). For this reason the variant TiO₂-α-cyclodextrin (ratio 1:2), can be used for the progressive elimination, from organism, of the cells with a high mitotic multiplication rate (carcinogen cells).

The TiO₂ conjugated or not with a metal (gold or iron), complexed or not with a cyclodextrin, induced, in a low percentage, the metabolic modification of the chromosomes, their compaction degree in prophase and metaphase being affected (**PCC** and **DCC**), as well as the inactivation of the kinetochore or mitotic spindle.

ACKNOWLEDGEMENTS

These researches were sponsored by the IMUNO-NANOMAT grant 70/2007, CNMP-Bucharest (Romania).

REFERENCES

- [1] G. Schmid, A. Lehnert, J.-O. Mahm, and J.-O. Bowin, "Ligand-stabilized bimetallic colloids identified by HIRTEM and ETk," *Angew. Chem. Int. Ed. Engl.*, 30, pp. 843-876, 1991.
- [2] A. Csáki, R. Möller, and W. Fritzsche, "Gold nanoparticles as novel label for DNA diagnostics," *Expert Rev. Mol. Diagn.*, 2(2), pp. 187-193, 2002.
- [3] A. Biwer, G. Antranikian, and E. Heinzle, "Enzymatic production of cyclodextrins," *Appl. Microbiol. Biotechnol.*, 59 (6): 609-617, 2002.
- [4] P. Lu, F. Wu, and N. Deng, "Enhancement of TiO₂ photocatalytic redox ability by β-cyclodextrin in suspended solutions," *Applied Catalysis B: Environmental*, 53, pp. 87-93, 2004;
- [5] S. Swaroop, B. Mishra, and K.I. Priyadarsini, "β-cyclodextrin inclusion complex of curcumin," *BARC Newsletter*, 285, pp. 208-212 2007;
- [6] X. Zhang, F. Wu, and N. Deng, "Degradation of paracetamol in self assembly β-cyclodextrin/TiO₂ suspension under visible irradiation," *Catalyst Comm*, 11, pp. 422-425, 2010.
- [7] J. Moutschen, "Some implications of radio-induced structural changes of chromosomes in *Nigella damascena* L.," *Nucleus*, 11, pp. 174-185, 1968.
- [8] J. Gilot-Delhalle, "Contribution à l'étude cytotoxonomique du genre *Nigella* L.," *Caryologia*, 23, pp. 211-223, 1970.
- [9] G.C. Corneanu, "The radiogenetic comparative study of some species from the *Nigella* L. genus," *Doctoral Thesis*, Cluj-Napoca, 1974, 200 pages.
- [10] E. Theogaraj, S. Riley, L. Hughes, M. Maier, and D. Kirkland, "An investigation of the photo-clastogenic potential of ultrafine titanium dioxide particles," *Mutat. Res.*, 634 (1-2), pp. 205-219, 2007.
- [11] D.B. Warheit, R.A. Hoke, C. Finlay, M.E. Donner, K.L. Reed, and C.M. Sayes, "Development of a base set of toxicity tests using ultrafine TiO₂ particles as a component of nanoparticle risk management", *Toxicology Letters*, 171 (3), pp. 99-110, 2007.
- [12] T. Demidova and E. Krysanov, "Mitotic index in *Nothobranchius rachovi* tissues in the presence of metal oxide nanoparticles," 2nd NanoImpactNet Conference, pp. 58, 2010.
- [13] E. Krysanov and T. Demidova, "Influence of presence TiO₂ nanoparticles in aquatic environment on mitotic index in thymus of *Nothobranchius rachovi*," 2nd NanoImpactNet Conference, pp. 56, 2010.
- [14] A. Lazanyi, "The effect of sulphoguanidine and p-nitrobenzoic acid on the chromosome breakage – reunion process by γ-, X-, and β-irradiation in *Vicia faba*". *Int. J. Rad. Biol.*, 10 (4), pp. 329-342, 1965.
- [15] H. Norppa, J. Catalán, H. Järventaus, M. Vippola, and K. Savolainen, "Induction of chromosomal aberrations by carbon nanotubes and titanium dioxide nanoparticles in human lymphocytes *in vitro*," 2nd NanoImpactNet Conference, pp. 91, 2010

Indirect Eavesdropping in Quantum Networks

Stefan Rass

Universität Klagenfurt, Department of Applied Informatics
 Universitätsstrasse 65-67
 9020 Klagenfurt, Austria
 stefan.rass@uni-klu.ac.at

Sandra König

Universität Klagenfurt
 Universitätsstrasse 65-67
 9020 Klagenfurt, Austria
 sakoenig@edu.uni-klu.ac.at

Abstract—Quantum networks are communication networks in which adjacent nodes enjoy perfectly secure channels thanks to quantum key distribution (QKD). Drawing end-to-end security from QKD-supported point-to-point security can be done by virtue of multipath transmission. This concept buys security at the cost of strongly connected networks and perfect routing. Particularly the latter is hard to ensure, since congestions or (passive) eavesdropping may cause QKD key-buffers to run empty, thus enforcing local re-routing of packets. Hence, the adversary may use eavesdropping not to extract information, but to *redirect* the information flow towards a relay-node that he controls. Such attacks can readily invalidate the stringent requirements of multipath transmission protocols and thus defeat any formal arguments for perfect secrecy. Moreover, this form of "indirect eavesdropping" seems to be unconsidered in the literature so far. We investigate whether or not unconditional security in a quantum network with non-reliable routing is possible. Using Markov-chains, we derive various sufficient criteria for retaining perfect secrecy under imperfect packet relay. In particular, we explicitly do not assume trusted relay or quantum repeaters available.

Keywords—Quantum Cryptography, Markov-Chain, Secure Routing, Information-Theoretic Security

I. INTRODUCTION

Quantum key distribution (QKD) [1] is renowned for providing unconditional security over direct channels with no intermediate nodes. Securing an entire network by means of QKD calls for additional measures, as up to now, the technology is still limited to point-to-point security. Creating end-to-end security has been subject of independent research, culminating in multipath transmission regimes. The latter can provide unconditional end-to-end security from perfectly protected links, which is exactly what QKD can do. However, most results in this area hinge on two major ingredients: sufficient graph connectivity and the sender having the routing under full control. Since the requirements for multipath transmission are stringent and therefore easily invalidated, a passively eavesdropping adversary may cause QKD key-buffers to run empty and thus enforce re-routing of packets over a set of nodes under his control. Since QKD can only protect links but not nodes, he can use eavesdropping on a link to redirect and extract information from another node. We call this *indirect eavesdropping*. Even without the adversary becoming active, local congestions

may as well cause deviations from the intended routing, and consequently destroy the protection of the secret message. Our contribution in this paper is investigating the extent to which quantum networks are resilient to such incidents.

Organization of the paper: We consider networks employing QKD for point-to-point- and multipath routing for end-to-end security, referred to as *quantum networks*. For convenience of the reader, we briefly review the use of QKD with multipath transmission in Section III. In Section IV, we introduce a Markov-chain model for the path that a data packet takes from the sender to the receiver, with a particular focus to multipath transmission. Conditions under which a random routing regime can yield perfect secrecy are derived in Section V, with an example supporting the practicability of our results in Section VI. Final remarks are given in Section VII.

II. RELATED WORK

Most closely related to our work are the results in [2], who provide a stochastic routing algorithm along with probabilistic measures of secrecy in a randomly compromised network. We improve on this by taking an existing routing regime and giving conditions under which it can provide perfect secrecy under random compromise. Motivated by the physical distance limitations of practical QKD implementations (cf. [3], [4], [5] to name a few) in spite of the theoretical possibility of unlimited distance QKD transmission [6], multipath transmission over disjoint channels remains a theoretical necessity for perfect end-to-end security [7]. In particular, [8], [9], [10], [11] and references therein form the basis for our work, where our goal is investigating a hidden assumption within these results: what happens if the routing is random rather than fully controllable? Implementations of multipath transmission within the TCP protocol are currently under standardization, and many other protocols like stream control transmission protocol (SCTP [12]) as well facilitate concurrent transmission. Similarly as for a recently proposed extension of SSL by QKD [13], [14], one could imagine QKD being integrated in such protocols. Load-balancing, local congestions and most importantly (adversarial) eavesdropping can all cause re-routing of packets and therefore make otherwise disjoint

routes intersecting. Our work is an explicit account for security under such random distortions. To the best of our knowledge, such indirect eavesdropping attacks have not yet been considered elsewhere in the literature.

III. QKD-BASED MULTIPATH TRANSMISSION

Our adversary model will be a computationally unbounded passive threshold adversary Eve. That is, given a network $G = (V, E)$, with a sender s and receiver r (both in V), the adversary can compromise up to $k \leq |V \setminus \{s, r\}|$ nodes in G (thanks to QKD, an activity on any of the links would be detected anyway). Moreover, Eve knows all relevant protocol specification and the network topology, but sticks to the protocol in a merely passive attempt to extract secret content flowing over the network.

For a string $M \in \{0, 1\}^*$, let $|M|$ be its length (in bits), and let H be the Shannon-entropy. We will use the following security model (similarly to the model given in [7]):

Definition III.1. Let $\varepsilon > 0$, and let Π be a message transmission protocol. Suppose that for conveyance of a message $M \in \{0, 1\}^*$, the packets $C_1, \dots, C_n \in \{0, 1\}^*$ are transmitted over the network (constituting the protocol's transcript). The adversary's view on the transmission of M is $\text{adv}(M) \subseteq \{C_1, \dots, C_n\}$. We call a protocol ε -secure, if $H(M|\text{adv}(M)) \in \{0, H(M)\}$ and $\Pr[H(M|\text{adv}(M)) = 0] \leq \varepsilon$, i.e., the adversary can disclose M with a chance of at most ε . We call the protocol Π efficient, if the size of the transcript, i.e., $\sum_{i=1}^n |C_i|$, is polynomial in the size of the message M , the size of underlying network (in terms of nodes), and $\log \frac{1}{\varepsilon}$. A protocol that is ε -secure for any $\varepsilon > 0$ is said to enjoy perfect secrecy.

It is easy to see that if a protocol is ε -secure with $\varepsilon < 2^{-|M|}$, then simply guessing the message is more likely than breaking the protocol itself.

Multipath transmission pursues a simple idea: having t paths from s to r that are node-disjoint, the sender can transmit a message m by first putting it through a (t', t) -secret sharing (Shamir's for instance), giving the shares s_1, \dots, s_t and sending each share over its own (distinct) path to r . The adversary is successful if and only if he catches at least t' shares. Obviously, the scheme is unconditionally secure if $t' > k$ (where k is the adversary's threshold), but in addition, we require full knowledge of the topology, and assured delivery over the chosen disjoint paths. The general interplay between network connectivity and unconditional security has been studied extensively, and our goal in the next section is finding out whether or not unconditional security can be retained if the paths are not fully under the sender's control (i.e., what happens if the adversary indirectly fiddles with the routing).

IV. A MARKOV-CHAIN ROUTING MODEL

Assume a quantum network modeled as a graph $G = (V, E)$ with $|V|$ nodes and $\text{nb}(v)$ denoting the set of v 's

neighbors. Formally, we put $\text{nb}(v) := \{u \in V | (v, u) \in E\}$. For each $v \in V$, it is trivial to (empirically) estimate the probability distribution supported on $\text{nb}(v)$, indicating the chances for a packet to leave towards the j -th neighbor. If the transition from u to v is denoted as $u \rightarrow v$, then this (local) distribution comprises the probabilities $\Pr[u \rightarrow v_i]$ where $v_i \in \text{nb}(u)$. The whole process can be considered as a Markov chain, with the transition matrix P describing the hops along which a data packet travels. In other words, the "chain" is the list of intermediate nodes that a packet comes across, with the *state* of the chain being the node that currently hosts the message before forwarding it. As outlined in Section III, it is reasonable to assume a multipath transmission regime in the absence of infinitely long quantum channels. Hence, we will look at an ensemble of t independently traveling packets with corresponding trajectories (traces) starting off the nodes v_1, v_2, \dots, v_t . Without loss of generality, and to ease notation in the sequel, call the starting nodes $1, 2, \dots, t$, with the sender's node being number "0", having the neighborhood $\text{nb}(0) = \{1, 2, \dots, t\}$. The receiver's node has number r . So, $|V| = r + 1$ and $V = \{0, 1, 2, \dots, r\}$.

To simplify technicalities, let us assume a *synchronous* forwarding regime, i.e., the nodes simultaneously forward their packets at fixed times. Despite this assumption appearing restrictive, it does in no way affect the validity of the obtained results, as will become evident soon. In particular, the derived formulas equally perfectly apply to a setting in which nodes independently forward their data.

Let the distribution $\pi_i(n, v) : \mathbb{N} \times V \rightarrow [0, 1]$ describe the chance that the i -th trajectory ($i = 1, 2, \dots, t$) is within node v at time $n \in \mathbb{N}$. The whole distribution is denoted as $\pi_i(n)$, and the whole ensemble of t trajectories is denoted as $\pi(n) = (\pi_1(n), \dots, \pi_t(n))$. The particular state of the i -th trajectory at time n is written as $X_i(n)$. Consider an arbitrary but fixed trajectory i in the following. It is well known from the theory of Markov chains that the state of the i -th chain is governed by $\pi_i(n) = P^n \cdot p_i(0)$, where P is the transition matrix. Our chain has only a *single absorbing state*, which is the receiver's state r (the receiver will surely not pass on his message any further). Furthermore, it can be assumed irreducible, because if it were not, then there would be at least two nodes u, v in the network whose chance of getting a packet from u to v is zero, so they could never communicate.

We write H_{jA} for the time (measured in *hops*) that it takes a trajectory to get from j to a set of $A \subseteq V$ target nodes,

$$H_{jA} = \min \{n \geq 0 : X_i(n) \in A | X(0) = j\}.$$

The probability h_{jA} of the chain ever reaching A from j is therefore $h_{jA} = \Pr[H_{jA} < \infty]$, and the family $(h_{jA}; j \in V)$ is the smallest non-negative solution of the equation system

$$h_{jA} = \sum_{i \in V} p_{ji} h_{iA}, \quad (1)$$

where $h_{jA} = 1$ for all $j \in A$ and p_{ji} is the probability of passing from node j onwards to node i (see [15, p.123] for details). Writing down this system for, say $n = 5$ equations with $A = \{1, 3\}$, we get (after some minor algebra),

$$\begin{aligned} -p_{21} - p_{23} &= (p_{22} - 1)h_{2A} + p_{24}h_{4A} \\ -p_{41} - p_{43} &= p_{42}h_{2A} + (p_{44} - 1)h_{4A}, \end{aligned}$$

where we additionally substituted $h_{rA} = 0$, as r is the only absorbing state of our chains. Let us write (in a slight abuse of notation) $P_{-R,-C}$ to denote the matrix P with all rows in R and all columns in C deleted. Similarly, we use the notation $P_{R,C}$ to denote the matrix P only with the rows in R and columns in C retained. To ease notation, let us put $Q := P_{-r,-r}$, i.e., Q is P without the r -th row and column. If I is the identity matrix, and $\mathbf{1}$ is the vector of all 1's, then the above equation system takes the compact form

$$-Q_{-A,A} \cdot \mathbf{1} = (Q_{-A,-A} - I)h_A, \quad (2)$$

where h_A is the family $(h_{1A}, h_{2A}, \dots, h_{rA})$, excluding $h_{rA} = 0$ and $h_{jA} = 1$ for all $j \in A$. In order to have the values h_j for $j \neq r$ and $j \notin A$ well-defined, we ought to show that $(Q_{-A,-A} - I)$ is invertible. This is our first

Lemma IV.1. *Let P be a stochastic matrix of an irreducible Markov-chain with the state space V and exactly one absorbing state $r \in V$. Select any set of states $A \subset V$ with $r \in A$, and let $Q = P_{-A,-A}$ be the submatrix of P that describes transitions between states outside of A . Then $Q - I$ is invertible.*

Proof: Partition the state set V into $V_1 = A$ and $V_2 = V \setminus A$, then $r \in V_1$ and Q describes transitions within V_2 . For each $v \in V_2$, write $\pi_{V_2}(n, v)$ for the chance of the chain being in state v after n steps. From the theory of Markov-chains, we know that the vector $\pi_{V_2}(n) = (\pi_{V_2}(n, v))_{v \in V_2}$ is given by $\pi_{V_2}(n) = Q^n \pi_{V_2}(0)$. As the chain is irreducible, we will eventually reach r from any state in V_2 , and since r is absorbing, this means that $Q^n \rightarrow 0$ as $n \rightarrow \infty$. Now, put $(Q - I)x = 0$. Then $Qx = x$ and on iterating $Q^n x = x$. As $n \rightarrow \infty$, $Q^n x = x \rightarrow 0$, so $Q - I$ is invertible. ■

Lemma IV.1 helps constructing a formula giving us the chance that exactly l trajectories pass through a given area $A \subseteq V$ that is under the adversary's control. We can solve the system (2) for any given set A and see whether it is passed with certainty. Similarly as for the binomial distribution, we can ask for the probability of a subset of l trajectories hitting A within finite time, with the remaining ones never reaching A . The probability we are after is the sum over all subsets of size l . Formally, we have

Proposition IV.2. *Let a graph $G = (V, E)$ be given, and assume a random walk of t trajectories starting at nodes $1, 2, \dots, t$. For a given $A \subseteq V$, the chance of l trajectories*

passing through A is given by

$$p(A, l) = \sum_{\substack{M \subseteq [1:t] \\ |M|=l}} \left[\prod_{i \in M} h_{iA} \prod_{i \in ([1:t] \setminus M)} (1 - h_{iA}) \right],$$

where the vector $h_k = (h_{iA})_{i \in V}$ is calculated as described above (i.e., put $h_{rA} = 0$, $h_{jA} = 1$ for all $j \in A$, and calculate the remaining probabilities by solving (2)). Here, $[1:t]$ is a shorthand notation for the set $\{1, 2, \dots, t\}$.

V. PERFECT SECRECY UNDER RANDOM ROUTING

According to Proposition IV.2, the adversary will not learn anything unless he conquers some set A that is passed by sufficiently many, say l , trajectories. Consequently, his best strategy is attacking the set with maximum likelihood of seeing sufficiently many trajectories. It follows that the most vulnerable subset of nodes in the network is

$$A^* = \operatorname{argmax}_{A \subseteq V} \Pr[l \text{ trajectories traverse } A] = \operatorname{argmax}_{A \subseteq V} p(A, l). \quad (3)$$

The following result is an immediate consequence of the above discussion:

Theorem V.1. *A network with a routing regime described by a transition matrix P can provide perfect secrecy if and only if for some integer $l \geq 1$, we have $p(A, l) < 1$ for all $A \subseteq V$ that the adversary can compromise.*

Despite this maximum likelihood optimization problem being sound, it is yet infeasible to evaluate as the number of subsets to test is exponential (in the adversary's threshold). We shall therefore set out to find sufficient criteria that are easier to test.

For a 1-passive adversary, we have the following criterion:

Theorem V.2. *Let $t = |nb(s)| \geq 1$ count the sender s 's neighbors. If, for each $v \in V$, we have $\sum_{i=1}^t h_{iv} < t$, then the network provides perfect secrecy against a 1-passive adversary.*

Proof: Put the secret message through a (t, t) -secret sharing and let each share take its own individual path through the network (i.e., do a random walk according to the transition matrix P). With the random indicator variable

$$\mathbb{I}_{i,j} := \begin{cases} 1, & \text{if } h_{ij} > 0 \\ 0, & \text{otherwise,} \end{cases}$$

the number of trajectories passing through a node $v \in V$ is given by $N_v := \sum_{i=1}^t \mathbb{I}_{i,v}$, and its expected value is $E(N_v) = E(\sum_{i=1}^t \mathbb{I}_{i,v}) = \sum_{i=1}^t h_{iv}$. The assertion now directly follows from Markov's inequality, since

$$\Pr[N_v \geq t] \leq \frac{E(N_v)}{t} < \frac{t}{t} = 1,$$

which holds for all $v \in V$. The network thus provides perfect secrecy by Theorem V.1. ■

Theorem V.3. Let $G = (V, E)$ be a graph, and let the sender and receiver be $s, r \in V$. Let the adversary be k -passive, i.e., up to k nodes in G can be compromised. For perfect secrecy, it is necessary that $|\text{nb}(s)| > k$. In that case, with $V^* := V \setminus \{s, r\}$, if

$$\forall i \in \text{nb}(s) : h_{ij} \leq \frac{1}{ek} \quad \forall j \in V^* \setminus \{i\},$$

then the network provides perfect secrecy.

Proof: Without loss of generality, assume s 's neighbors to be the nodes $\{1, 2, \dots, t\}$, and put the secret message m through a (t, t) -secret-sharing scheme, transmitting the i -th share over the i -th neighbor of s (the remaining path of each is individual and determined by the network's transition matrix P). Observe that the adversary will not learn anything unless he gathers all t shares.

If $t \leq k$, then the adversary can "cut off" s from the rest of the network, thus reading all information conveyed by s , and perfect secrecy is impossible by Theorem V.1.

Assume $t > k$ henceforth, so there exists at least one honest neighbor of s in every attack scenario. Let $A \subseteq V$ with $A = \{j_1, \dots, j_k\}$ be a set of compromised nodes. The (mutually dependent) events $T_l^{j_i}$ for $i = 1, 2, \dots, k$ occur when the trajectory starting off the node l reaches node j_i . For each (starting node) $l = 1, 2, \dots, t$, we have

$$\Pr[T_l^{j_i}] = h_{lj_i} \leq \max\{h_{lv} | v \in V \setminus \{l, s, r\}\} \leq \frac{1}{ek}, \quad (4)$$

where the last inequality follows from our hypothesis. Since $\Pr[T_l^{j_i}] \leq \frac{1}{ek}$, then Lovász local lemma (symmetric version) implies

$$\Pr\left[\bigcap_{\nu=1}^k \overline{T_l^{j_\nu}}\right] > 0. \quad (5)$$

In other words, the l -th trajectory has a positive chance of evading the set $\{j_1, \dots, j_k\}$. Since inequality (4) holds independently of the particular j_i 's, (5) is true for all these sets. If condition (4) holds for all $l = 1, 2, \dots, t$, then in every attack scenario there is at least one trajectory with a positive chance of not passing through the compromised area in the graph. So, for every $A \subset V$ with $|A| \leq k$, it holds that $p(A, t) < 1$ and the network can provide perfect security. ■

Efficiency

Regarding the bandwidth demand, we require the overall network traffic (bit complexity) and round complexity to be polynomial in $\log \frac{1}{\varepsilon}$ for any chosen $\varepsilon > 0$. Assume the network satisfies the condition for perfect secrecy in Theorem V.1.

Fix some $\varepsilon > 0$. We will prove the following transmission regime to enjoy efficient bit- and round-complexity, i.e., polynomial efforts in $\log \frac{1}{\varepsilon}$. Let the secret message transmitted from s to r be m :

- 1) put m through a (n, n) -secret sharing, giving the shares s_1, \dots, s_n (the number n will be determined below).
- 2) for $i = 1, 2, \dots, n$ do the following: put the i -th share s_i through a (t, t) -secret sharing, where $t = |\text{nb}(s)|$, and transmit the j -th share of s_i over the j -th neighbor of s .

Obviously, the attacker will not learn anything unless he gets all the information flowing over the network (due to the (n, n) - and (t, t) -sharings). Our task is proving n to be polynomial in $\log \frac{1}{\varepsilon}$ and the size of the network. For the proof, define an indicator variable for each round $i = 1, 2, \dots, n$ via

$$\mathbb{I}_i = \begin{cases} 1, & \text{if the share } s_i \text{ was disclosed;} \\ 0, & \text{otherwise,} \end{cases}$$

so that \mathbb{I}_i measures the adversary's success (in a binary scale) in the i -th round. By our hypothesis, Theorem V.1 implies $\Pr[\mathbb{I}_i = 1] < 1$ for all rounds i and all sets of nodes that the adversary could have conquered (recall that the adversary is k -passive). Put $\rho := \max_{i=1,2,\dots,n} \Pr[\mathbb{I}_i = 1]$, then $\rho < 1$. Since $0 \leq \mathbb{I}_i \leq 1$ for all i , the first moment $E(\mathbb{I}_i)$ exists and \mathbb{I}_i 's deviation from its mean is bounded by $-1 \leq \mathbb{I}_i - E(\mathbb{I}_i) \leq 1$ for all i . Define $S := \sum_{i=1}^n \mathbb{I}_i$, then since $E(\mathbb{I}_i) \leq \rho$, we get $E(S) = \sum_{i=1}^n E(\mathbb{I}_i) \leq n\rho$. Moreover, $S - E(S) \geq S - n\rho \geq \tau$ for some τ to be fixed later. Application of a variant of Hoeffding's inequality (with relaxed independence constraints; see [16]) gives

$$\Pr[S - n\rho \geq \tau] \leq \Pr[S - E(S) \geq \tau] \leq \exp\left(-\frac{\tau^2}{2n}\right)$$

Since $\frac{1}{n}S \geq \min_i \mathbb{I}_i$, we can choose τ to satisfy $\frac{\tau}{n} \leq \min_i \mathbb{I}_i - \rho \leq \frac{1}{n}S - \rho$. So we can continue the chain of inequalities on the left-side as

$$\Pr\left[\min_i \mathbb{I}_i - \rho \geq \frac{\tau}{n}\right] \leq \Pr[S - n\rho \geq \tau] \leq \exp\left(-\frac{\tau^2}{2n}\right),$$

and by taking $\delta := \frac{\tau}{n}$ we conclude that

$$p := \Pr\left[\min_i \mathbb{I}_i \geq \rho + \delta\right] \leq \exp\left(-\frac{n\delta^2}{2}\right)$$

for all $\delta \geq 0$. By construction, the adversary is successful if and only if $\mathbb{I}_i = 1$ for all rounds $i = 1, 2, \dots, n$, or equivalently, $\min_i \mathbb{I}_i = 1$. Choosing $\delta := 1 - \rho > 0$, the number n of rounds until $\Pr[\min_i \mathbb{I}_i \geq \rho + \delta = 1] < \varepsilon$ is achieved comes to $n \in \mathcal{O}\left(\log \frac{1}{\varepsilon}\right)$. The bit-complexity is $n \cdot t \cdot |m|$, where $|m|$ is the length of the message, and as such in $\mathcal{O}\left(|m| \cdot |\text{nb}(s)| \cdot \log \frac{1}{\varepsilon}\right)$, i.e., polynomial in the network size and $\log \frac{1}{\varepsilon}$. Summarizing the discussion, we have proved

Theorem V.4. If a given network provides perfect secrecy according to Theorems V.1, V.2 or V.3, then there is an efficient protocol achieving this.

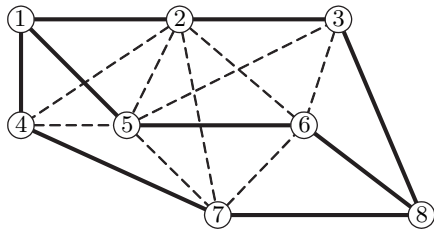


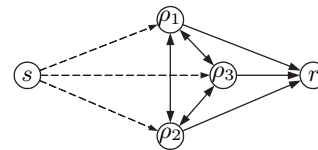
Figure 1. Example multipath transmission from 1 to 8

VI. APPLICATION TO QUANTUM NETWORKS

It is important to emphasize that Theorems V.1, V.2 and V.3 *should not* directly be applied to the communication network at hand. Instead, we are interested in estimating the harm that any deviation from a prescribed routing strategy causes. Going back to multipath transmission, our goal is using the results from the previous section to classify a given network as (in)secure under the assumption of random detours that a packet takes upon local congestions or empty local quantum-key-buffers.

We illustrate the application of Theorem V.3 using a simple example, which we hope demonstrates the general line of reasoning. Take the network shown in Figure 1, with each link secured by means of QKD. Alice (node 1) performs a multipath communication over three disjoint channels $\rho_1 = (1 \rightarrow 2 \rightarrow 3 \rightarrow 8)$, $\rho_2 = (1 \rightarrow 5 \rightarrow 6 \rightarrow 8)$, $\rho_3 = (1 \rightarrow 4 \rightarrow 7 \rightarrow 8)$ (shown bold) to Bob's node 8. Assume that each node does the packet forwarding reliably, up to some chance of α for the packet to deflect from the prescribed route. Thus, assuming stochastic independence for the sake of simplicity, with probability $1 - \alpha^{\text{length}(\rho_i)-2}$, the packet will travel over ρ_i as desired. Notice that any path is accessible from any other, and that an adversary will surely not waste resources by attacking anywhere else than on the chosen paths. Hence, we can create an abstract model for such a multipath transmission by restricting the focus on whether the packets travel as desired (likelihood determined by the reliability of routing, i.e., the probability of the packet not deviating from its prescribed route), or whether they take detours (should happen with a small chance only) that could yield to intersecting paths and disclosure of the secret message.

For the analysis of a general network $G = (V, E)$ under a multipath transmission scenario, we therefore consider the auxiliary graph $G' = (V', E')$: let ρ_1, \dots, ρ_t be paths in G , then each of these becomes a node in G' , which is connected to the sender and receiver, so put $V' := \{\rho_1, \dots, \rho_t\} \cup \{s, r\}$. Attacking elsewhere than on the paths ρ_1, \dots, ρ_t is less paying for the adversary than compromising the paths themselves, so we may safely disregard any nodes in the network that are not on a chosen path. Also, assume that a packet can jump from any path to any other, so the nodes ρ_1, \dots, ρ_t form a clique. Finally, each path ρ_i is connected


 Figure 2. Auxiliary graph G' describing state transitions

to the receiver r in a one-way manner, as the receiver is absorbing and will not pass anything further. Similarly, the sender is (one-way-)connected to all his chosen paths, though these transitions are of no further interest, since an accidental jump from a path back to the sender can trivially be corrected by the sender putting the packet back on its correct path. The set of edges therefore comes to $E' = \{\rho_1, \dots, \rho_t\}^2 \cup \{(\rho_i, r), (s, \rho_i) | i = 1, 2, \dots, t\}$. The resulting transition graph for the example is depicted in Figure 2, with arrows indicating possible state transitions.

The topology of the auxiliary graph G' , excluding the transitions from s to each ρ_i (for obvious reasons) defines the Markov-chain on which we can invoke the results from Section V. For the analysis, it remains to specify the following likelihoods:

- $\Pr[\rho_i \rightarrow r]$: with the parameter α as above, this is $\Pr[\rho_i \rightarrow r] = 1 - \alpha^{\text{length}(\rho_i)-2}$. Notice that several events of node failure are not necessarily independent, and correlations among these must be considered in a more accurate (perhaps more realistic) model.
- $\Pr[\rho_i \rightarrow \rho_j]$: this quantity depends on the particular chances of jumping from a node on ρ_i to any node on ρ_j , and must be worked out individually for the network at hand. For the sake of simplicity and illustration, we assume an equal likelihood of jumping on any other path once ρ_i is left. For the example, we take $\Pr[\rho_i \rightarrow \rho_j] = \frac{1}{t-1}(1 - \Pr[\rho_i \rightarrow r])$.

Since the jumps from the sender to each of his chosen paths are uninteresting, we do not need to model the corresponding transition probabilities, nor must these appear in the transition matrix of the Markov-chain. These links are merely included to have G' consistent with our criteria, and are therefore shown dashed.

With $\alpha = 0.01$, we end up finding the transition matrix:

$$P = \begin{matrix} & \rho_1 & \rho_2 & \rho_3 & r \\ \begin{matrix} \rho_1 \\ \rho_2 \\ \rho_3 \\ r \end{matrix} & \begin{pmatrix} 0 & 0.01 & 0.01 & 0.98 \\ 0.01 & 0 & 0.01 & 0.98 \\ 0.01 & 0.01 & 0 & 0.98 \\ 0 & 0 & 0 & 1 \end{pmatrix} \end{matrix}$$

Now, we can use Theorem V.3 on this matrix to see that the network is indeed secure against a 2-passive adversary: with $V^* = \{1, 2, 3\}$ and by solving (2) for $A = \{1\}, \{2\}, \{3\}$, we find $h_{ij} = \frac{1}{99} < \frac{1}{2e} \approx 0.184$, for each $i, j \in V^*, j \neq i$. It follows that the network remains secure even under

much less reliable routing. Indeed, we can tolerate up to $\alpha \approx 0.155$, i.e., a more than 15% chance of the packets becoming re-routed via indirect eavesdropping or congestion control. Finally, Theorem V.4 tells that resilience against such incidents can be retained efficiently.

VII. CONCLUSION

We have obtained simple criteria for protection against passive adversaries. Carrying over our results for active (Byzantine) adversaries, one needs a slightly different transmission technique. In fact, (k, n) -secret sharing is resilient against an active adversary compromising up to $\lfloor (n-k)/2 \rfloor$ shares [17]. Future work will include refining and adapting our criteria for Byzantine adversaries, as well as investigating transmission efficiency (notice that the proof of Theorem V.4 no longer holds for active adversaries. Still, QKD enhanced multipath routing can indeed bring perfect secrecy to future networks, even without much change to the existing routing regimes apart from using QKD. More detailed examples are subject to ongoing research in the context of a project where this framework is going to be tested empirically. We will report on this in future papers.

Our results are only indirectly dependent on the quantum nature of the network, as the attack targets the multipath transmission regime only by *exploiting* general QKD properties. These are, moreover, independent of the particular QKD-implementation, and equally well apply to discrete or continuous quantum information encodings. In general, any successful denial-of-service attack, regardless of whether on a conventional or quantum line, can be used for indirect eavesdropping in the described form, as soon as secure multipath transmission is used.

This work is an explicit account for an adversary who turns the QKD eavesdropping detection against the network. If end-to-end security is set up by means of multipath transmission, then "disconnecting" (by eavesdropping) otherwise adjacent nodes may enforce local re-routing of packets and in turn direct the information flow right into the adversary's hands. We presented various sufficient criteria for this kind of "indirect eavesdropping attacks" to be repealable. In general, our criteria can be used to decide whether or not a network retains perfect secrecy under randomly compromised nodes and routes.

REFERENCES

- [1] C. Bennett and G. Brassard, "Public key distribution and coin tossing," in *IEEE Int. Conf. on Computers, Systems, and Signal Processing*. IEEE Press, 1984, pp. 175–179.
- [2] H. Wen, Z. Han, Y. Zhao, G. Guo, and P. Hong, "Multiple stochastic paths scheme on partially-trusted relay quantum key distribution network," *Science in China Series F: Information Sciences*, vol. 52, no. 1, pp. 18–22, 2009.
- [3] T. Schmitt-Manderbach, "Long distance free-space quantum key distribution," Ph.D. dissertation, Ludwig-Maximilians-University Munich, Faculty of Physics, 2007.
- [4] E. Diamanti, H. Takesue, C. Langrock, M. M. Fejer, and Y. Yamamoto, "Field trial of differential-phase-shift quantum key distribution using polarization independent frequency up-conversion detectors," *Opt. Express*, vol. 15, pp. 15 920–15 927, 2007.
- [5] H. Xu, L. Ma, A. Mink, B. Hershman, and X. Tang, "1310-nm quantum key distribution system with up-conversion pump wavelength at 1550 nm," *Optics Express*, vol. 15, pp. 7247–7260, Jun. 2007.
- [6] H.-K. Lo and H. F. Chau, "Unconditional security of quantum key distribution over arbitrarily long distances," *Science*, vol. 283, pp. 2050–2056, 1999, arXiv:quant-ph/9803006.
- [7] M. Franklin and R. Wright, "Secure communication in minimal connectivity models," *J. of Cryptology*, vol. 13, no. 1, pp. 9–30, 2000.
- [8] M. Franklin and M. Yung, "Secure hypergraphs: privacy from partial broadcast," in *Proc. of the 27th annual ACM Symp. on Theory of computing*, ser. STOC '95. New York, NY, USA: ACM, 1995, pp. 36–44.
- [9] Y. Wang and Y. Desmedt, "Perfectly secure message transmission revisited," *IEEE Trans. on Inf. Theory*, vol. 54, no. 6, pp. 2582–2595, 2008.
- [10] M. Fitzi, M. K. Franklin, J. Garay, and S. H. Vardhan, "Towards optimal and efficient perfectly secure message transmission," in *Proc. of 4th Theory of Cryptography Conf. (TCC)*, ser. LNCS 4392. Springer, 2007, pp. 311–322.
- [11] M. Ashwin Kumar, P. R. Goundan, K. Srinathan, and C. Pandu Rangan, "On perfectly secure communication over arbitrary networks," in *PODC '02: Proc. of the 21st annual Symp. on Principles of distributed computing*. New York, NY, USA: ACM, 2002, pp. 193–202, last access: 05/17/2011.
- [12] R. Stewart, "RFC4960: Stream Control Transmission Protocol," <http://tools.ietf.org/html/rfc4960>, September 2007, last access: 05/17/2011.
- [13] M. Pivk, C. Kollmitzer, and S. Rass, "SSL/TLS with quantum cryptography," in *Proc. of the 3rd Int. Conf. on Quantum, Nano and Micro Technologies*. IEEE Computer Society, February 2009, pp. 96–101.
- [14] A. Mink, S. Frankel, and R. Perlner, "Quantum key distribution (qkd) and commodity security protocols: Introduction and integration," *Int. J. of Network Security & Its Applications (IJNSA)*, vol. 1, no. 2, pp. 101–112, July 2009.
- [15] D. Stirzaker, *Stochastic Processes & Models*. Oxford University Press, 2005.
- [16] W. D. Smith, "Tail bound for sums of bounded random variables," URL: <http://www.math.temple.edu/~wds/homepage/works.html>, April 2005, last access: 05/17/2011.
- [17] R. McEliece and D. Sarwate, "On sharing secrets and Reed-Solomon codes," *Communications of the ACM*, vol. 24, no. 9, pp. 583–584, 1981.

Geometry Induced Microparticle Separation in Passive Contraction Expansion Straight Channels

Mustafa Yilmaz, Meral Cengiz, Huseyin Kizil
 Dept. of Metallurgical and Materials Eng.
 Istanbul Technical University
 Istanbul, 34469 Turkey
 e-mail: kizilh@itu.edu.tr

Arzu Ozbey, Levent Trabzon
 Dept. of Mechanical Eng.
 Istanbul Technical University
 Istanbul, 34437 Turkey

Abstract—Particle separation in passive micro fluidic channels has been investigated in straight channels with contracting and expanding geometry is studied. The angles in the entrance of contracting part of the channel are varied and the influence of the forces on the particle focusing is studied at various fluid flow rates. Single focusing position could be achieved for a certain flow rate and an angle of inclination at the entrance of a contracting part in the direction of flow.

Keywords- microparticle; separation; wall effect; focusing.

I. INTRODUCTION

Microparticle separation techniques have attracted extensive attention for their importance in clinical diagnostics, treatment, and various biomedical applications. Most common separation techniques involve centrifugation and membrane based filtration on macro scale systems. Microfluidics based particle separation systems have advantages over these techniques due to small amounts of sample and reagent, less time consumption, lower cost and high throughput. In general, separation techniques could be categorized as passive and active with respect to any available applied external forces. Active separation systems require external forces such as ultrasound, magnetic field, and dielectric field for controlling the behavior of the particles suspended in fluid [1–2]. Passive separation techniques do not require external forces; the separation relies entirely on the hydrodynamic effects, which are mainly caused by channel geometry. However, most of the passive separation systems suffer from low throughput and filtration efficiency due to low channel Re numbers [1–2].

The first experiment about inertial forces was accomplished by Segre and Silberberg [3] in which particles migrate to a radial equilibrium position at the pipe radius of 0.62 from the axis of the pipe, which is known as “Tubular Pinch Effect”. Working with a wide range of Re numbers, Matas et al. [4] experimentally confirmed the tubular pinch effect and found that the equilibrium positions shift towards the wall with increasing Re. Kim et al. [5] observed that particles focused to a narrow band along the perimeter, which is about $0.2 D_h$ (hydraulic diameter) in low Re number

($Re < 20$). On the other hand, Di Carlo et al. [6] investigated the inertial focusing in a straight microchannel and proved that uniformly distributed particles in rectangular channels migrate across the streamlines of four symmetric equilibrium positions at the centers of the sides and move closer to the walls as particle Re number increases. Lateral migration of particles mainly depends on the ratio of the particle diameter to the channel hydraulic diameter (a_p/D_h). Inertial effects are significantly large and particle focusing occurs in short distances in $a_p/D_h > 0.07$ criterion. They also point out that the focusing positions that occur in the straight channels can be determined by the fold symmetry of the channel’s cross section. In a rectangular channel the flow will have two focusing positions [7]. Di Carlo et al. [8] also studied the equilibrium positions of cells with comparing the expanding channel types. It was determined that the equilibrium positions moved closer to the channel centerline in rapid expanding channel while they were closer to the channel wall in the gradual expanding channel. Recently, Asgar et al. [9] discovered that the inertial focusing positions of particles in a straight microchannel also depend on the channel aspect ratio. They found that particles converge to an equilibrium in two focused streams along the longer sidewalls for both $H/W > 1$ and $W/H > 1$ (H: Height, W: Width) at the same channel Re number. Shear gradient induced lift force is linked to the flow velocity profile at the location of the particle. Due to its larger weight and size, the particle moves a little more slowly than the fluid and relative velocity is larger on the wall side, a pressure difference acts on the particle to push it towards to the wall. The second lift force where induced lift force is linked to the vicinity of the solid surface is called as wall effect. The relative velocity closed to the wall side of the particle is reduced by the presence of the wall, and the pressure on the wall side is larger than that on the centerline side. A lift force is exerted on the particle towards the channel center.

In this study, straight microfluidic channels with contracting and expanding geometry are studied. The angles in the entrance of contracting part of the channel are varied and the influence of the forces on the particle focusing is measured at various fluid flow rates.

II. MICROCHANNEL DESIGN

The angle of the entrance to contraction part was varied while other parameters were kept constant. Schematic view of the designed channel geometry is shown in Fig. 1, and dimensions are given in Table 1.

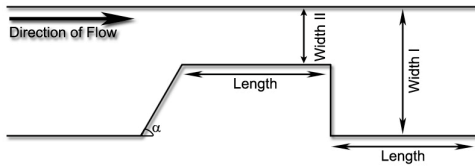


Figure 1. Schematic view of designed channel geometry

III. METHODS

A. Fabrication

SU – 8 3050 (MicroChem Corp.) was spun on the 4 inch Si wafer at 500 rpm for 10 s with 100 rpm/s acceleration and then 3000 rpm for 30 s with 300 rpm/s acceleration. A soft bake process was done at 95 °C for 15 min. After lithography, SU-8 coated wafer was post baked at 65 °C for 1 min. following at 95 °C for 5 min, and developed. Then it was placed in a petri dish for PDMS casting. Vacuum oven was used for degassing the PDMS and kept at the curing temperature of 150 °C for 2 hours. After curing, PDMS was peeled off the mold and placed in oxygen plasma furnace with a glass substrate side by side for the surface treatment to improve the adhesion between PDMS and glass, then both pieces were bonded together for the final construction of the microfluidic device.

TABLE 1. Design parameters of the channel geometry

| | |
|----------|-------------|
| Width I | 100 μm |
| Width II | 40 μm |
| Length | 200 μm |
| α | 30,45,60,90 |

B. Characterization

A mixture of 0.04 ml solution containing 1% of 9.9μm diameter green fluorescent particles and 70 mL DI water was prepared. Flow rates were determined with respect to the particle Re numbers (Re_p). It has been shown that particle inertial lift forces are dominant when $Re_p > 1$, causing the particles to migrate laterally inside the channels [10]. Flow rates and particle Re numbers used in this study are given in Table 2.

For obtaining a stable image from green fluorescent particles, exposure rate and color were adjusted with respect to red, green and blue. Exposure rates were varied between the values of 80 μs to 160 μs in which microchannel borders are not visible so that the particle images could easily be viewed. For obtaining an image over time, accumulation settings were set at 40 frames, meaning each image taken contains accumulated 40 frames.

TABLE 2. Flow rates and particle Reynolds numbers in expanding/contracting part of channel

| Flow rate (μl/min) | Re_p (expansion part) | Re_p (contraction part) |
|--------------------|-------------------------|---------------------------|
| 105 | 0,38 | 1,49 |
| 120 | 0,44 | 1,70 |
| 140 | 0,51 | 1,99 |
| 160 | 0,58 | 2,27 |
| 180 | 0,65 | 2,55 |

IV. RESULTS AND DISCUSSION

A. Focusing Positions

Using the line profile option of the DP72 microscope camera software, the positions of the accumulated particle flows images were obtained. The line profile system depends on the RGB color value of the points along the chosen line. From the RGB values focusing width and position were determined. The obtained images showing the focusing positions of the micro channels are given in Fig. 2. It can be seen from the figure highly concentrated single focusing can be obtained at certain flow rates for angled designs (30° - 45° - 60°) at the upper side of the channel for certain flow rates while this could not be possible for 90° degree design.

B. Intensity Analysis

The brightness of the color image can be obtained with using the line profile option of the microscope. By using color intensity values it can be determined whether a certain flow rate can produce a single focus or a dual focus positions. While the intensity values give the value of the brightness of the focusing, that value needs to be adjusted with respect to the width of the focus in order to normalize the intensity value. Single focusing could be categorized as high intensity over low width values. In other words, in order to define a single focusing position for a certain flow rate, its intensity/width value must be much higher than that of its second focusing position value. Furthermore, for the single focusing position determination at different flow rates intensity/width value is divided by the flow rate values to normalize the color intensity with respect to flow rate. The obtained results are shown in Fig. 3. Left side of each graph corresponds to expansion region of the channel while the right side corresponds to contraction part of the channel. From the graphs, for a certain Re_p value whether a focusing position is single or double is seen. Mark x shows the single focusing positions. For 45 and 60 degree designs have single focusing for two different flow rates in the contraction part of the channel while 30 degree design has only one and 90 degree design has none.

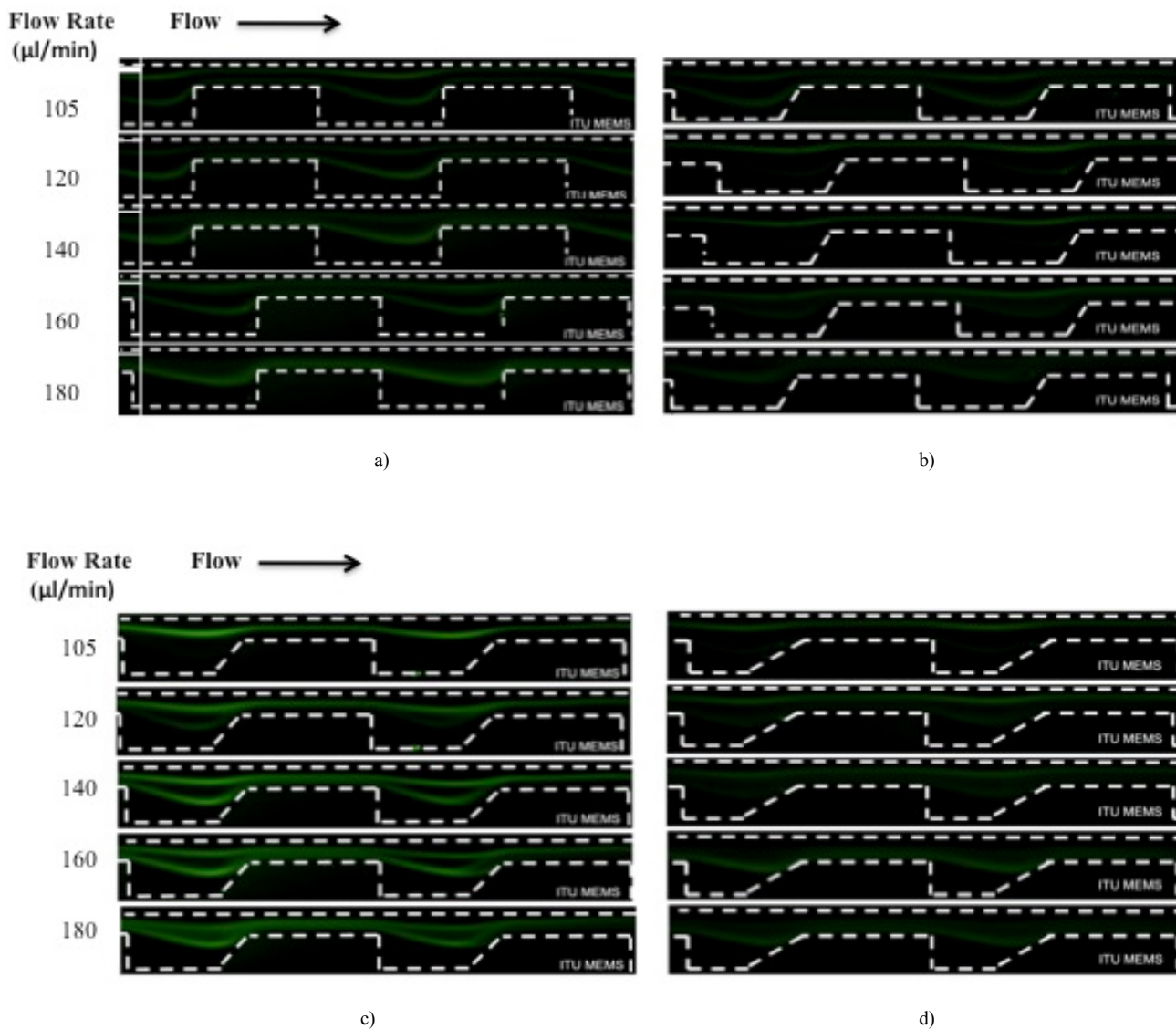


Figure 2. Particle flow with different angle of entrance at contraction part a) 90° b) 60° c) 45° d) 30°

V. CONCLUSIONS

Single focusing position could be achieved for a certain flow rate and an angle of inclination at the entrance of a contracting part in the direction of flow. This result can be explained with the vortex forces prior to the contraction part and the wall effect at the proposed angle. Fig. 4 illustrates these forces affecting the particle in the channel. From this figure, the x component of the vortex force will be decreasing with decreasing angle. This force is in the direction of the flow causing an increase in the flow rate. But that effect will not have significant effect at low angle values causing no change in the flow rate. In 60°, 45° and 30° channel designs there exists a wall induced inertial lift force which affects prior to the

contracting part. This lift force is perpendicular to the angled wall so that its x and y components are not same for different angle values. It has lower x component in lower angled designs. The x component of this wall induced inertial lift force has a decelerating effect for the fluid and particle flow and the y component of this wall induced inertial lift force is the main driving force for obtaining the single focusing position. The x component of the wall induced lift force of 60° design is higher than that of 45° or 30° design, at which the fluid flow will be affected more and its flow rate will be lower than those designs. As a result, a single focus was obtained in even expansion part of the channel at certain flow rates for 60° design.

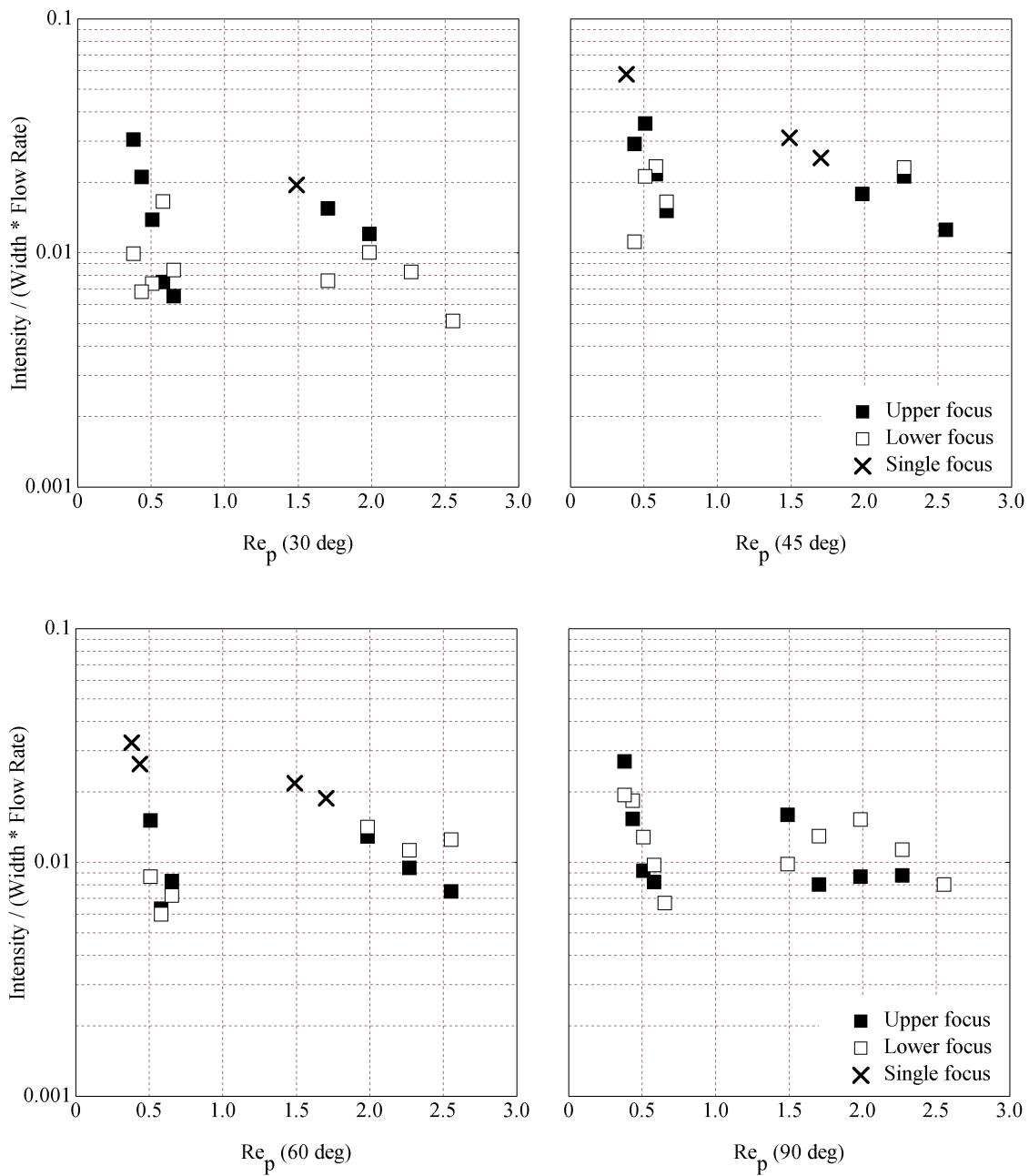


Figure 3. Normalized intensity vs. Particle Reynolds number for channels with different angle of entrance at contraction part

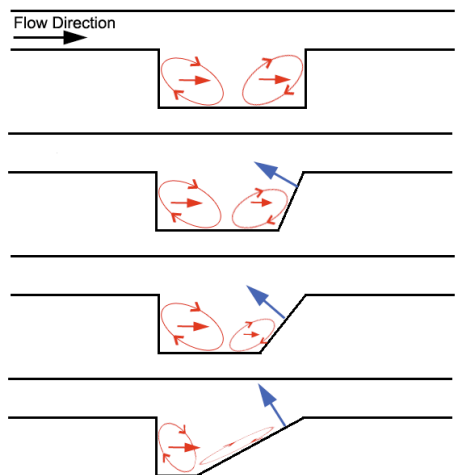


Figure 4. Geometry effects on the focusing mechanism

ACKNOWLEDGMENT

This paper presents part of the work carried out under The Scientific and Technological Research Council of Turkey, TUBITAK. Their support is gratefully acknowledged.

REFERENCES

[1] T. Kulrattanarak , R.G.M van der Sman, C.G. Schroën, and R.M. Boom “Classification and evaluation of microfluidic devices for continuous suspension fractionation” *Advances in Colloid and Interface Science* 142, 2008, pp. 53–66.

[2] N. Pamme “Continuous flow separations in microfluidic devices” *Lab Chip*, 2007, pp. 1644–1659.

[3] G. Segre and A. Silberberg, “Radial particle displacements in Poiseuille flow of suspensions,” *Nature (London)* 189, 1961, pp. 209-210.

[4] P. Matas, J. Morris, and E. Guazzelli, “Inertial migration of rigid spherical particles in Poiseuille flow,” *J. Fluid Mech.* 515, 2004, pp. 171-195.

[5] Y. Kim and J. Yoo, “The lateral migration of neutrally-buoyant spheres transported through square microchannels,” *J. Micromech. Microeng.* 18, 2008, 065015. doi:10.1088/0960-1317/18/6/065015.

[6] D. DiCarlo, D. Irimia, R.G. Tompkins, and M. Toner “Continuous inertial focusing, ordering, and separation of particles in microchannels” *Proc. Natl. Acad. Sci. U.S.A.*, 104, 2007, pp. 18892-18897.

[7] D.R. Gosselt and D. DiCarlo “ Particle focusing mechanisms in curving confined flows” *Analytical Chemistry*, 81, 2009, pp. 8459 – 8465.

[8] A.J. Mach and D. DiCarlo “Continuous scalable blood filtration device using inertial microfluidics” *Biotechnology and Bioengineering*, 2010, pp. 302-311.

[9] S.I. Rubinow and J.B. Keller, “The transverse force on a spinning sphere moving in a viscous fluid”, *Journal of Fluid Mechanics*, vol. 11, 1961, pp. 447 – 459.

[10] J.S. Park and H.I. Jung, “Multiorifice flow fractionation: Continuous size – based separation of microspheres using a series of contraction/expansion microchannels”, *Analytical Chemistry*, 81, 2009, pp. 8280 – 8288.

Microfluidic Gate

Utilization of Self-Assembling, Free-Flowing Superstructures of Superparamagnetic Beads for Enhanced Mixing and Colloidal Separation

Bernhard Eickenberg, Frank Wittbracht, Andreas
Hütten

Department of Physics, Thin Films and Physics of
Nanostructures
University of Bielefeld
Bielefeld, Germany
e-mail: beickenb@physik.uni-bielefeld.de

Alexander Weddemann

Department of Electrical Engineering and Computer
Science
Massachusetts Institute of Technology
Cambridge, USA

Abstract— Due to dipolar interactions, superparamagnetic beads self-assemble into one- and two-dimensional superstructures under the influence of a homogeneous magnetic field. When the magnetic field is adiabatically rotated in-plane, the superstructures follow the rotation. We developed a microfluidic device in which the rotation of these agglomerates is used to simultaneously enhance mixing and allow for colloidal separation. The device shows high separation efficiencies. When taking the mass separation rate into account, the optimal working regime of the device lies around 120 $\mu\text{m/s}$, where it yields 80% of the total amount of beads.

Keywords- *microfluidics; superparamagnetic beads; dipolar coupling; reconfigurable matter; rotating magnetic fields.*

I. INTRODUCTION

Due to promising applications in biomedical analysis, superparamagnetic beads have been thoroughly studied during the last decades [1-3]. Their surface functionalization allows the specific binding of biomolecules like DNA or proteins [4,5] whereas the permanent magnetic moment of the particles makes it possible to manipulate their movement in microfluidic channels through external magnetic fields [6-8] or detect them with magnetoresistive sensors [9-11]. This makes them applicable as carriers or markers for biomedical diagnostics in lab-on-a-chip systems.

Another promising application is the utilization of the beads as reconfigurable matter [12]: Under the influence of a homogeneous magnetic field, the magnetic moment vectors align parallel to the external field. This alignment leads to an increase in the effective magnetization and thus results in a higher magnetic stray field. Since the stray field is inhomogeneous, adjacent particles attract each other and form one- (chains) or two-dimensional (clusters) superstructures [13-15]. Once the magnetic field is removed, the superstructures disassemble on a time scale of several seconds.

Just like the particles, superstructures can be manipulated with external magnetic fields as their orientation follows the direction of the field. Therefore, adiabatic rotation of the field leads to rotation of the agglomerates [16] which can be utilized to enhance mixing in microfluidic devices, as demonstrated by Lee et al. [17] and Sawetzki et al. [18]. They used microfluidic chambers and optical tweezers to confine magnetic assemblies in microfluidic compartments and utilize them as active micromixers.

In this work, the formation and rotation of superstructures composed of superparamagnetic beads is employed to design a combined microfluidic system which enables enhanced fluid mixing and colloidal separation. Figure 1 shows the overview of the separation mechanism of the device: Superparamagnetic beads form one- and two-dimensional rotating superstructures under the influence of an external homogeneous magnetic field. At the separation junction (two diverging channels separated by a barrier) the rotation of the agglomerates leads to a transversal movement due to interactions of the superstructures with the barrier. The direction of this movement depends on the orientation of the rotation (clockwise or counter-clockwise). Thus, the flow of agglomerates can be limited to either one of the two diverging channels, depending on the parameters of the external field. If no magnetic field is applied, the individual particles are distributed statistically over both channels.

At the T-junction (depicted in Figure 2), the rotation of the superstructures leads to a perturbation of the boundary layer between the two parallel, laminar flows. A convective fluid flux from the upper layer into the lower layer and *vice versa* is created and leads to enhanced mixing. Without the rotation, thermal diffusion would be the only driving force for mixing. Unlike the other magnetic mixing devices mentioned above, this device utilizes free-flowing components that can be assembled in real-time.

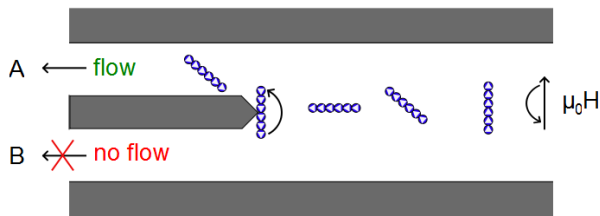


Figure 1. Operation principle of the microfluidic gate: The rotation of the superstructures leads to a transversal movement of the agglomerates at the separation junction. The direction of the movement depends on the orientation of the rotation of the magnetic field. Thus, the particle flow can be restricted to one channel.

In this paper, we describe the experimental realization of the proposed microfluidic device. In the results section, both the performance of the colloidal separation and the mixing enhancement are evaluated.

II. EXPERIMENTAL

The microfluidic structure was created by soft-lithography techniques [19]. Figure 2 shows a microscopy image of the SU8-3025 casting mold. The actual channel system was made from PDMS that was sealed with a silica wafer by plasma oxidation of the surfaces.

The structure consists of two inlet reservoirs I_1 and I_2 that are connected to a T-junction *via* channels of $77 \mu\text{m}$ width. A bead reservoir B is used to introduce beads into the system. The main channel connecting the T-intersection with the outlet reservoir O has a width of $79 \mu\text{m}$ and is split into two channels of $28 \mu\text{m}$ width by a $23 \mu\text{m}$ wide barrier. Liquid flow is induced by hydrostatic pressure.

Dynabeads MyOne™ beads with a mean diameter of $1.05 \mu\text{m}$ at a standard deviation of 1.9% were chosen for the experiments [20]. The bead surface is covered with carboxylic acid ligands. The mass saturation magnetization of the MyOne™ beads is $23.5 \text{ Am}^2/\text{kg}$. For the experiments, a stock solution of 10 mg/mL was diluted with deionized water to a final concentration of $120 \mu\text{g/mL}$. Reservoir B was then filled with this solution, whereas I_2 was filled with a 65 mM solution of flavin adenine dinucleotide (FAD) to allow for optical evaluation of the mixing behavior. The ratio of the flow from I_1 and I_2 to O, respectively, was adjusted *via* the water level in I_1 .

A modified RCT basic (IKA) magnetic stirrer with a maximum in-plane field strength of 690 Oe was placed beneath the microfluidic chip to provide the rotating magnetic field. The field strength leads to a degree of saturation of 73% in the MyOne™ beads. A rotation frequency of 50 rpm was chosen for the whole experiment.

For evaluation, the amount of chains (transversal width of one or two beads) and clusters (transversal width of three or more beads) passing through channel A and B was counted separately. Superstructures fracturing at the barrier were counted as flowing through both channels. The ratio of

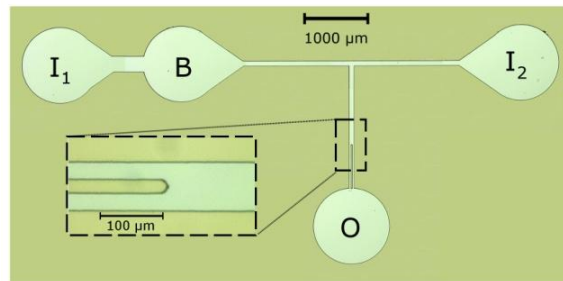


Figure 2. Microscopy image of the SU8-3025 casting mold with the inlet reservoirs I_1 and I_2 , the outlet reservoir O and the bead reservoir B. The small image shows a magnification of the separation junction.

beads flowing through channel A and B was obtained through the ratio of the area of the superstructures. Flow velocities were evaluated by tracking of superstructures in the channel.

III. RESULTS AND DISCUSSION

The influence of the rotating bead superstructures on the boundary layer between the water and the FAD solution can be seen in the optical microscopy images displayed in Figure 3. The interface between the two flows is highlighted in red. Due to hydrodynamic interactions with the surrounding fluid, the rotating agglomerates create a transversal convective flow that enhances the mixing of the two parallel streams. This way, they are acting as free-flowing magnetic microstirrers that can be easily assembled and disassembled on demand in real-time.

At the separation junction, the interaction of the bead agglomerates with the barrier leads to a colloidal separation as described in Figure 1. Depending on the chosen direction

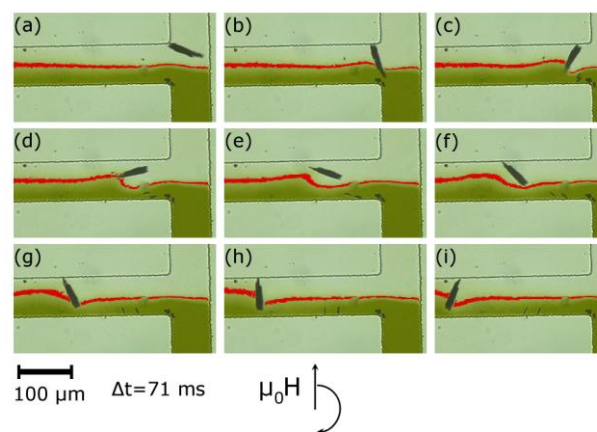


Figure 3. Microscopy images of the fluid interface at the T-junction. The rotation of the superstructures causes a convective flux orthogonal to the flow direction, thus enhancing mixing. The interface between the two liquids is highlighted in red. For better perceptibility, the contrast of the yellow FAD was increased.

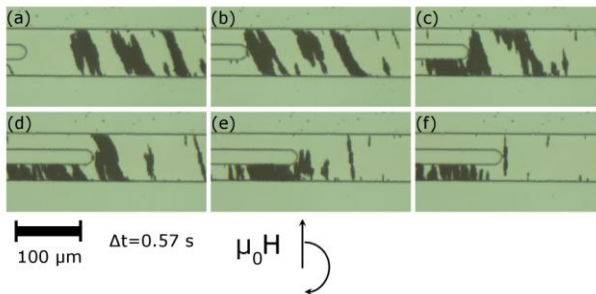


Figure 5. Optical microscopy images showing the separation of cluster agglomerates. Even at high local bead densities, the separation is efficient and no clogging of the channels is observed.

of the magnetic field rotation, the particle flow can be restricted to the upper or lower channel. As can be seen from the optical microscopy images in Figure 4, even high bead densities can be successfully guided. Figure 5 shows a series of optical microscopy images of the separation process. Through the effect of the clockwise rotation, the one-(5-a) and two-(5-b) dimensional bead agglomerates are guided into the lower channel. Only at higher flow velocities above 100 μm/s, breakage of chains (5-c) or even clusters (5-d) occurs at the separation barrier due to high

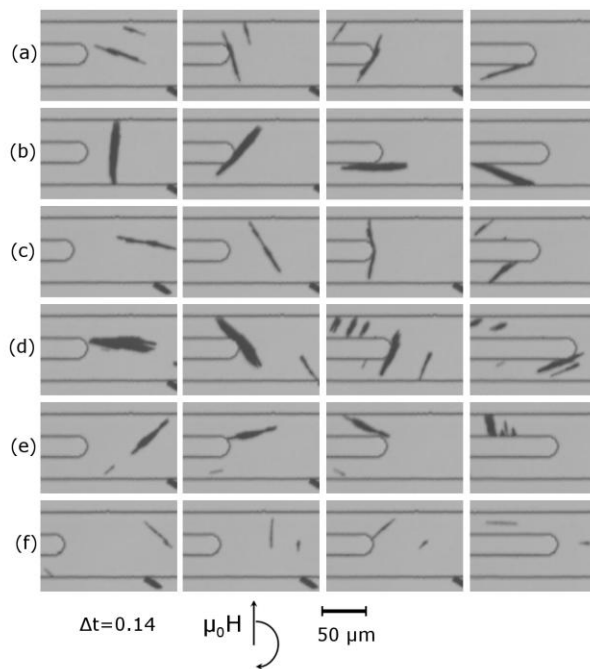


Figure 4. Even at flow velocities of 274 μm/s, chains (a) and clusters (b) can be guided into the lower channel by clockwise rotation of the magnetic field. At these flow velocities, however, chains (c) and clusters (d) may fracture at the separation barrier due to shear induced stresses. Additionally, due to the high velocity, some superstructures pass the separation junction without interacting with the barrier (e). At all flow velocities, occasional fragments (f) with lateral dimensions smaller than the channel diameter pass the junction without being guided.

shear induced stresses, thus reducing the separation efficiency. Additionally, fragments with lateral dimensions smaller than the width of the diverging channels cannot be guided successfully, since they often passed the separation junction without interacting with the barrier (5-f). However, they do not significantly lower the separation efficiency as the amount of beads per fragment is insignificantly low. In contrast to breakage of clusters, the presence of fragments is visible at all flow velocities. Adjustment of the bead concentration and the parameters for the chain formation process might reduce the amount of fragments, though.

The evaluation of the separation efficiency was performed for clockwise rotation. Figure 6 shows the fraction of chains, clusters and total amount of beads that was successfully guided into the lower channel B. At low mean flow velocities (42 and 63 μm/s) more than 90% of the superstructures are successfully separated. The low percentage of particles flowing through channel A can be attributed to the fragments mentioned above which do not interact with the separation barrier. When the flow velocity is increased to 120 μm/s, the overall separation yield slightly decreases to 89% due to the increased probability of chain breakage: Only 71% of the chains are guided into the lower channel, whereas most of the clusters (84%) remain stable and resist the fragmentation by shear induced stress. At high flow velocities of 274 μm/s, cluster breakage becomes more common and reduces the ratio of guided clusters to 61%. At these high velocities, several clusters pass the separation junction without performing a 180° rotation, so that they reach channel A without interacting with the barrier (5-e), thus decreasing the separation yield. This effect could be counteracted by increasing the rotation frequency of the magnetic field, though a higher rotation speed might increase the probability of cluster breakage. Still, 63% of the total amount of beads are successfully guided into the lower channel, showing that a significant separation can still be achieved at these velocities.

To analyze the efficiency of the design, we define the separation efficiency ϵ as follows:

$$\epsilon = (x - 0.5)/0.5 \quad (1)$$

with x as the fraction of separated beads. Thus, ϵ takes into account that without the application of an external field, 50% of the beads would be guided into each of the two diverging channels. Figure 6 shows the values of ϵ depending on the flow velocity. For velocities of up to 120 μm/s, high efficiencies between 0.92 and 0.77 are obtained. Only at higher flow velocities of 274 μm/s the efficiency drops to 0.26. However, higher flow velocities mean that a larger volume and therefore a higher amount of beads is transported and guided per time. We therefore introduce the mass separation rate ξ as

$$\xi = \Gamma \cdot c_{\text{Bead}} \cdot \epsilon \quad (2)$$

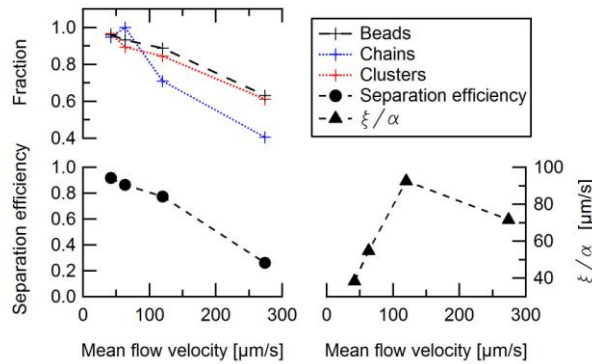


Figure 6. Evaluation of the separation performance. (a) The fraction of the total amount of beads and of chain/cluster superstructures guided into channel B. (b) Development of the separation efficiency ε with the mean flow velocity. (c) Development of the quantity ξ/α with the mean flow velocity. The optimal working regime for the device lies around 120 $\mu\text{m/s}$.

with c_{bead} as the bead concentration and Γ as the volume flow rate which is given by

$$\Gamma = |\mathbf{u}| \cdot A \quad (3)$$

with $|\mathbf{u}|$ as the flow rate and A as a geometry parameter. Since c_{bead} and A do not depend on the flow velocity but only on experimental conditions which were not changed during the presented experiments, we introduce the experimental parameter α :

$$\alpha = c_{\text{bead}} \cdot A \quad (4)$$

Figure 6 shows the progression of the quantity ξ/α , which takes all flow velocity dependent effects into account, with the flow velocity. The plot shows an increase of the device efficiency from 38 $\mu\text{m/s}$ to 93 $\mu\text{m/s}$ when increasing the flow velocity from 42 $\mu\text{m/s}$ to 120 $\mu\text{m/s}$. A further increase of the velocity decreases the efficiency to a value of 72 $\mu\text{m/s}$. Thus we can deduce that the optimal working regime for the device lies around 120 $\mu\text{m/s}$ for an operation frequency of 50 rpm.

IV. CONCLUSION

The proposed microfluidic design offers simultaneous enhancement of fluid mixing and highly efficient colloidal separation through the use of self-assembling, free-flowing superstructures that can be built and disassembled on a time scale of several seconds. The structure can be realized by application of an external homogeneous time-dependant field without the need for micro-structured components. The optimal working regime for the device lies around a flow velocity of 120 $\mu\text{m/s}$ for rotation frequencies of 50 rpm.

In future work, the presented design will be used to separate biomolecules from a biological sample matrix and localize them on the bead surface, allowing for detection without background interference by the matrix components.

ACKNOWLEDGMENT

The authors thank the FOR 945 for financial support in the framework of project 3. Alexander Weddemann gratefully acknowledges the Alexander-von-Humboldt-Foundation for financial support.

REFERENCES

- [1] N. Pamme, "Magnetism and microfluidics", *Lab Chip*, vol. 6(1), 2006, pp. 24-38.
- [2] E. Verpoorte, "Beads and chips: new recipes for analysis", *Lab Chip*, vol. 3(4), 2003, pp. 60N-68N.
- [3] M. A. M. Gijs, "Magnetic bead handling on-chip: new opportunities for analytical applications", *Microfluid. Nanofluid.*, vol. 1(1), 2004, pp. 22-40.
- [4] Z. H. Fan, S. Mangru, R. Granzow, P. Heaney, W. Ho, Q. Dong, and R. Kumar, "Dynamic DNA hybridization on a chip using paramagnetic beads", *Anal. Chem.*, vol. 71, 1999, pp. 4851-4859.
- [5] F. G. Pérez and M. Mascini, "Immunomagnetic separation with mediated flow injection analysis amperometric detection of viable *Escherichia coli* O157", *Anal. Chem.*, vol. 70, 1998, pp. 2380-2386.
- [6] L. E. Johansson, K. Gunnarsson, S. Bijelovic, K. Eriksson, A. Surpi, E. Göthelid, P. Svedlindh, and S. Oscarsson, "A magnetic microchip for controlled transport of attomole levels of proteins", *Lab Chip*, vol. 10, 2010, pp. 654-661.
- [7] T. Deng, G. M. Whitesides, M. Radhakrishnan, G. Zabow, and M. Prentiss, "Manipulation of magnetic microbeads in suspension using micromagnetic systems fabricated with soft lithography", *Appl. Phys. Lett.*, vol. 78 (12), 2001, pp. 1775-1777.
- [8] M. Panhorst, P. B. Kamp, G. Reiss, and H. Brückel, "Sensitive bondforce measurements of ligand-receptor pairs with magnetic beads", *Biosens. Bioelectron.*, vol. 20(8), 2005, pp. 1685-1689.
- [9] D. L. Graham, H. A. Ferreira, and P. P. Freitas, "Magnetoresistive-based biosensors and biochips", *Trends in Biotechnology*, vol. 22(9), 2004, pp. 455-462.
- [10] V. C. Martins, J. Germano, F. A. Cardoso, J. Loureiro, S. Cardoso, L. Sousa, M. Piedade, L. P. Fonseca, and P. P. Freitas, "Challenges and trends in the development of a magnetoresistive biochip portable platform", *J. Magn. Magn. Mater.*, vol. 322, 2010, pp. 1655-1663.
- [11] C. Albon, A. Weddemann, A. Auge, K. Rott, and A. Hütten, "Tunneling magnetoresistance sensors for high resolution particle detection", *Appl. Phys. Lett.*, vol. 95(2), 2009, 023101.
- [12] P. S. Doyle, J. Bibette, A. Bancaud, and J.-L. Viovy, "Self-assembled magnetic matrices for DNA separation chips", *Science*, vol. 295(22), 2002, p. 2237.
- [13] S. Melle, O. G. Calderon, M. A. Rubio, and G. G. Fuller, "Microstructure evolution in magnetorheological suspensions governed by Mason number", *Phys. Rev. E*, vol. 68, 2003, 041503.
- [14] A. Weddemann, F. Wittbracht, B. Eickenberg, and A. Hütten, "Magnetic field induced assembly of highly ordered two-dimensional particle arrays", *Langmuir*, vol. 26, 2010, pp. 19225-19229.
- [15] A. Weddemann, F. Wittbracht, A. Auge, and A. Hütten, "Particle flow control by induced dipolar interaction of superparamagnetic microbeads", *Microfluid. Nanofluid.*, vol. 10(2), 2011, pp. 459-463.
- [16] A. K. Vuppu, A. A. Garcia, and M. A. Hayes, "Video microscopy of dynamically aggregated paramagnetic particle chains in an applied rotating magnetic field", *Langmuir*, vol. 19, 2003, pp. 8646-8653.
- [17] S. H. Lee, D. van Noort, J. Y. Lee, B.-T. Zhang, and T. H. Park, "Effective mixing in a microfluidic chip using magnetic particles", *Lab Chip*, vol. 9, 2009, pp. 479-482.
- [18] T. Sawetzki, S. Rahmouni, C. Bechinger, and D. W. M. Marr, "In situ assembly of linked geometrically coupled microdevices", *PNAS*, vol. 105, 2008, pp. 20141-20145.
- [19] J. Friend and L. Yeo, "Fabrication of microfluidic devices using polydimethylsiloxane", *Biomicrofluidics*, vol. 4, 2010, 026502.

- [20] G. Fønnum, C. Johansson, A. Molteberg, S. Mørup, and E. Aksnes, "Characterisation of Dynabeads ® by magnetization measurements and mossbauer spectroscopy", *J. Magn. Magn. Mat.*, vol. 293, 2005, pp. 41-47.

Rotating magnetic field assisted formation of highly ordered two-dimensional magnetic bead arrays

Frank Wittbracht, Bernhard Eickenberg, Andreas
Hütten
Department of Physics, Thin Films and Physics of
Nanostructures
Bielefeld University
Bielefeld, Germany
fwittbra@physik.uni-bielefeld.de

Alexander Weddemann
Department of Electrical Engineering and Computer
Science, Research Laboratory of Electronics/Laboratory
for Electromagnetic and Electronic Systems
Massachusetts Institute of Technology
Cambridge, United States

Abstract—The authors present a method for the formation of highly ordered two-dimensional arrays of magnetic beads based on dipolar particle interactions in rotating magnetic fields. Growth mechanisms of the arrays inside the carrier liquid are presented. After evaporation of the carrier liquid, the resulting bead monolayers on silicon substrates are analyzed with respect to size and defect structure.

Keywords- magnetic bead arrays; formation of bead monolayers; rotating magnetic fields

I. INTRODUCTION

Magnetic beads and nanoparticles are promising candidates for various lab-on-a-chip applications [1-3]. Their magnetic moments allow for the manipulation by external magnetic gradient fields [4, 5]. Detection of magnetic beads or nanoparticles may be achieved by the use of magnetoresistive sensors due to their magnetic stray field [6]. When combined with appropriate functional groups on the surfaces, the individual magnetic bead or particle may act as markers for biological or chemical analytes. For these applications, low particle concentrations have to be applied in order to prevent particle coupling based on dipolar interactions.

If superparamagnetic beads are suspended in a liquid and immersed in a homogeneous external magnetic field, a torque acts on their magnetic moment vector favoring parallel alignment with the external field orientation. Since the external magnetic field is homogeneous, no magnetic force is acting on the particle ensemble. However, in the case of high particle concentrations, the inhomogeneous magnetic stray field of neighboring particles leads to an attractive force, which entails the formation of one-dimensional agglomerates [7]. These one-dimensional assemblies may be used as, e.g. static components in on-chip sandwich immunoassays [8] or as dynamic components in micropumps driven by magnetic gradient fields [9]. Magnetic assemblies may also be influenced by rotating magnetic fields allowing for stable rotations depending on the applied field frequency [10]. Higher rotation frequencies of the external magnetic field lead to higher shear stresses along the bead chains due to the hydrodynamic interaction with the carrier liquid. At higher shear stresses the probability for chain collapse is

enhanced [11]. Therefore, two dimensional assemblies of magnetic beads may be formed. This work will focus on the growth of such two-dimensional bead arrays and analyzes the size of resulting monolayers after evaporation of the carrier liquid.

In this contribution we describe the experimental techniques to generate magnetic bead assemblies based on dipolar particle interactions in rotating magnetic fields. Furthermore, the resulting monolayers are analyzed with respect to symmetry, growth modes and sizes of the resulting monolayers in dependence of the particle concentration.

II. EXPERIMENTAL

Superparamagnetic microbeads Dynabeads M-270 SA [12] were used in the experiments. These microbeads have a radius of 1.4 μm with a standard deviation below 2% and are coated with a streptavidin functionalization. The iron content of these beads is 14%. In order to avoid salt crystallization after liquid evaporation, the buffer of the stock solution was exchanged with deionized water by subsequent centrifugation and resuspension. Two different suspensions at 0.2 and 1.0 mg/ml were prepared. The rotating magnetic field was created by a magnetic stirrer RCT classic (IKA, Germany) at a maximum field strength of 330 Oe. At this field strength a linear response of the magnetization in dependence of the external magnetic field is expected according to the magnetic characterization of the beads [13]. Assemblies were performed on a silicon wafer, which was cleaned with acetone and ethanol prior to spotting the solutions. Optical microscopy images were collected with a Keyence VHX-600 during formation of the agglomerates and after liquid evaporation. Rotation frequencies of 400, 800 and 1200 rounds per minute (rpm) are applied.

The microscopy data is evaluated with respect to agglomerate sizes based on the analysis of pixels at a defined color value within a certain area. The expected error of this counting method is about 2.43% when compared to manual counting of magnetic beads. Furthermore, the defect concentrations are obtained by manual counting of one-

dimensional and two-dimensional defects within the bead arrays.

III. RESULTS AND DISCUSSION

After spotting the microbead solutions, the rotational magnetic field entails the formation of two-dimensional agglomerates due to stray field interaction. In Fig. 1 a typical resulting cluster is shown. The in-plane rotating magnetic field strongly favors the growth of two-dimensional agglomerates over three-dimensional assemblies. From Fig. 1(a) we can identify a hexagonal symmetry for the agglomerates which is also reproduced in the fast Fourier transform (FFT) image of Fig. 1(b) as presented in Fig. 1(b). The Voronoi tessellation of Fig. 1(a) is shown in Fig. 1(c), where Voronoi cells with 4, 5, 6 and 7 neighbors are dyed in yellow, red, white and green, respectively. The Voronoi tessellation also shows the high degree of hexagonal ordering inside the clusters, but additionally reproduces the frustration along the edge of the cluster and the two vacancies in the middle of the cluster shown in Fig. 1(a). The formation of clusters can be described as a two step process. In the first step collapsing chains form agglomeration seeds, comparable to nucleation in nanoparticle synthesis [14]. In the second step, these nuclei grow at the cost of chains and single particles. Chain addition to previously formed clusters corresponds to a slow growth mode which entails the formation of highly ordered arrays with low defect concentration. Besides, also merging of clusters can be observed, which is exemplarily shown in a series of microscopy images in Fig. 2. Neighboring clusters merge due to attractive magnetic forces. The rotating magnetic field entails reordering processes along the cluster-cluster interface in order to obtain a stable magnetic configuration. However, due to the larger areas of broken symmetry along the boundaries, the merging of clusters may lead to a higher concentration in the bead arrays when compared to the growth based on chain addition. During evaporation of the carrier liquid superstructures are transferred to the substrate.

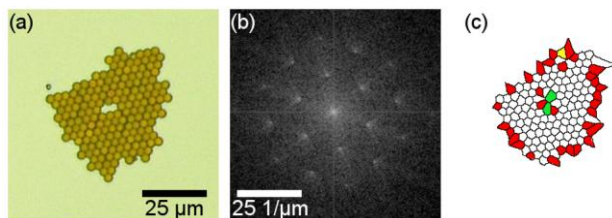


Figure 1. Optical microscopy image of a highly ordered two-dimensional assembly under the influence of a magnetic field rotating at 400 rpm (a). FFT of (a) showing the hexagonal symmetry of the assemblies and the high degree of ordering (b). Voronoi tessellation of (a) where cells with 4-, 5-, 6- and 7-fold symmetry are dyed in yellow, red, white and green, respectively.

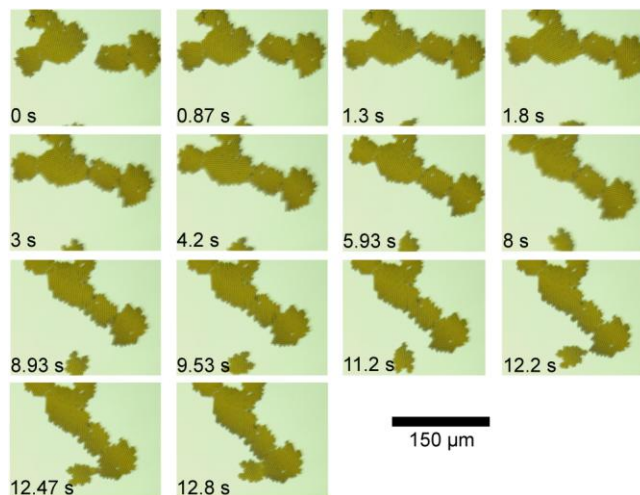


Figure 2. Series of optical microscopy images showing the merging of previously formed clusters under the influence of a rotating magnetic field at a frequency of 400 rpm.

The resulting structures are exemplarily shown in Fig. 3 for the case of three subsequent spotting procedures of a 1 mg/ml bead solution. If no magnetic field is applied (Fig. 3(a)), a randomly dispersed pattern of superstructures and single particles is obtained, which shows no visible ordering. The FFT of the image also reproduces this finding: no sharp peaks can be observed in the FFT pattern (Inset of Fig. 3(a)). In contrast, the sample which was prepared under the influence of a rotating magnetic field with a frequency of 400 rpm clearly shows hexagonal ordering (Fig. 3(b)) in the microscopy image and the corresponding FFT pattern (Inset of Fig. 3(b)). Fig. 3(b) shows one cluster with low particle coverage in the second layer. An analysis of the second layer growth shows that the second layer coverage of clusters assembled under the influence of a rotating magnetic field is below 5%. The quantitative evaluation of the cluster sizes for different experimental parameters is depicted in Fig. 4(a). The inset of Fig. 4(a) shows the agglomerate sizes without the influence of the magnetic field. For both of the investigated concentrations, an increase in the cluster size by applying a rotating magnetic field when compared to the reference sample (inset) is obtained. The iterative supply of bead solution in order to enhance the effective bead concentration on the substrate may lead to a shift of the cluster sizes to higher particle numbers. This particular aspect of the cluster growth mechanism resembles the behavior of nanoparticles in the growth regime of Ostwald ripening [15]. The assembly of few larger particle arrays is favored over the formation of many small clusters. According to our experiments, the rotation frequency of the magnetic field does not influence the size of the resulting agglomerates. However, the defect concentrations show a dependence on

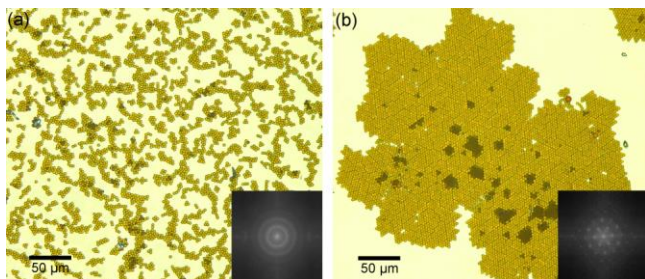


Figure 3. Optical microscopy images of the resulting particle layers after liquid evaporation. If no rotating magnetic field is applied, the beads show a randomly dispersed pattern (a), which is also reproduced in the corresponding FFT of the image (inset). Under the influence of a rotating magnetic field, particles assemble in two-dimensional arrays (b) with a high degree of hexagonal ordering, which is also visible in the FFT pattern (inset).

the field frequency as shown in Fig. 4(c). In Fig. 4(b) an example for a one-dimensional defect structure within the bead arrays is shown. The concentration of one-dimensional and two-dimensional defects increases with increasing rotation frequency of the external magnetic field. This behavior may be attributed to a difference in the time scales of magnetic and geometric reorganization processes. While remagnetization occurs on a nanosecond timescale [16], the geometrical reordering of particles cannot follow the fast magnetodynamics inhibiting the geometric reordering.

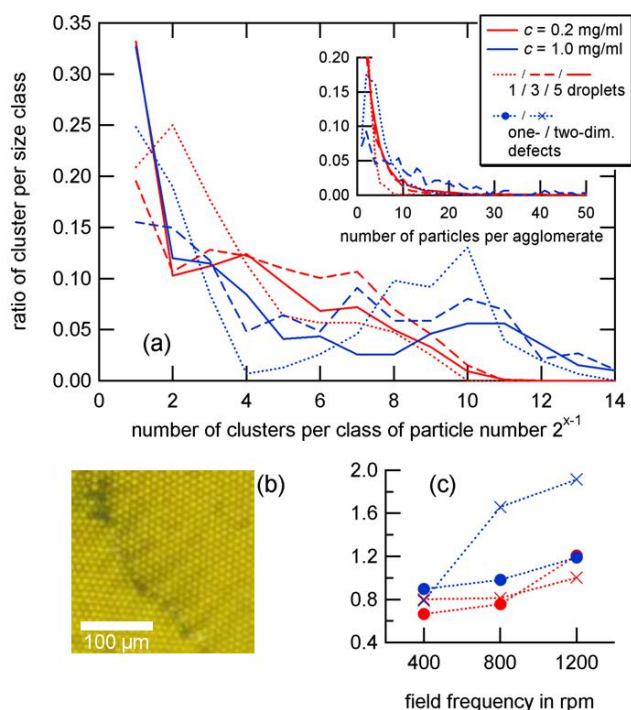


Figure 4. Evaluation of cluster growth for concentrations of 0.2 mg/ml and 1 mg/ml and 1, 3 and 5 iterative replenishments (a). The inset shows the results without applying a magnetic field. A one-dimensional defect structure of a particle clusters prepared under the influence of a rotating magnetic field (b). The defect concentration of one- and two-dimensional defect structures increases with increasing the rotation frequency (c).

CONCLUSIONS AND OUTLOOK

We have shown that highly ordered two-dimensional arrays consisting of superparamagnetic beads can be prepared by applying a rotating magnetic field. The properties, such as one- and two-dimensional defect concentrations, can be controlled by the field frequency. The magnetic field entails a high degree of hexagonal ordering and leads to the formation of larger clusters when compared to the reference samples that were prepared without a magnetic field.

The ability to assemble these highly ordered objects on demand by switching on a magnetic field may lead to the design of novel microfluidic devices based on the reconfigurability of the particle arrays. Especially the possibility to assemble bead arrays with specific surface functionalization in certain regions of lab-on-a-chip devices may be of major interest in future works.

ACKNOWLEDGMENT

The authors thank the FOR 945 for financial support in the framework of the project 3. Alexander Weddemann gratefully acknowledges the financial support of the Alexander von Humboldt foundation.

REFERENCES

- [1] N. Pamme, "Magnetism and Microfluidics," *Lab Chip*, vol. 6, pp. 24-38, 2006
- [2] M.A.M. Gijs, "Magnetic bead handling on chip: new opportunities for analytical applications," *Microfluid. Nanofluid.*, vol. 1, pp. 22-40, 2004
- [3] A. Hütten, D. Sudfeld, I. Ennen, G. Reiss, K. Wojczykowski, and P. Jutzi, "Ferromagnetic FeCo nanoparticles for biotechnology," *J. Magn. Magn. Mat.*, vol. 293, pp. 93-101, 2005
- [4] M. Panhorst, P.B. Kamp, G. Reiss, and H. Brückl, "Sensitive bond-force measurements of ligand-receptor pairs with magnetic beads," *Biosens. Bioelectron.*, vol. 20(8), pp. 1685-1689, 2005
- [5] U. Lehmann, C. Vandevyver, V.K. Patashar, and M.A.M. Gijs, "DNA-Reinigung in Tröpfchen auf einem magnetischen "La-on-a-Chip," *Angew. Chem.*, vol. 118, pp. 3132-3137, 2006
- [6] C. Albon, A. Weddemann, A. Auge, K. Rott, and A. Hütten, "Tunneling magnetoresistance sensors for high resolution particle detection," *Appl. Phys. Lett.*, vol. 95(2), pp. 023101-023104, 2009
- [7] J.H.E. Promislow, A.P. Gast, and M. Fermigier, "Aggregation kinetics of paramagnetic colloidal particles," *J. Chem. Phys.*, vol. 102(13), pp. 5492-5498, 1995
- [8] F. Lacharme, C. Vandevyver, and M.A.M. Gijs, "Full on-chip nanoliter immunoassay by geometrical magnetic trapping of nanoparticle chains," *Anal. Chem.*, vol. 80(8), pp. 2905-2910, 2008
- [9] R.J.S. Derks, A.J.H. Frijns, M.W.J. Prins, and A. Dietzel, "Multibody interactions of actuated magnetic particles used as fluid drivers in microchannels," *Microfluid. Nanofluid.*, vol. 9, pp. 357-364, 2010

- [10] I. Petousis, E. Homburg, R. Derks, and A. Dietzel, "Transient behaviour of magnetic micro-bead chains rotating in a fluid by external fields," *Lab Chip*, vol. 7, p. 1746-1751, 2007
- [11] F. Wittbracht, B. Eickenberg, A. Weddemann, and A. Hütten, "Towards a programmable microfluidic valve: Formation dynamics of two-dimensional magnetic bead arrays in transient magnetic fields", *J. Appl. Phys.*, vol. 109, pp. 114503-1-114503-5, 2011
- [12] M-270 SA datasheet: www.invitrogen.com (last access date: 06.07.2011)
- [13] G. Fonnum, C. Johansson, A. Molteberg, S. Mørup, and E. Aksnes, "Characterisation of Dynabeads[®] by magnetization measurements and Mössbauer spectroscopy," *Journal of Magn. Magn. Mat.*, vol. 293, pp. 41-47, 2005
- [14] V.K. LaMer and R.H. Dinegar, "Theory, Production and Mechanism of Formation of Monodispersed Hydrosols," *J. Am. Chem. Soc.*, vol. 72, pp. 4847-4854, 1950
- [15] W. Ostwald, *Lehrbuch der allgemeinen Chemie*, vol. 2, part 1, **1896**, Leipzig, Germany
- [16] A. Weddemann, A. Auge, D. Kappe, F. Wittbracht, and A. Hütten, "Dynamic simulations of the dipolar driven demagnetization process of magnetic multi-core nanoparticles," *J. Magn. Magn. Mat.*, vol. 322(6), pp. 643-646, 2010

Microfluidics Blood Separations through Optical Sorting and Deterministic Lateral Displacement

Alexander Zhbanov

Graduate Program of Medical System Engineering
Gwangju Institute of Science and Technology (GIST)
Gwangju, Republic of Korea
e-mail: azhbanov@gist.ac.kr

Sung Yang

Graduate Program of Medical System Engineering
School of Information and Mechatronics
Department of Nanobio Materials and Electronics
Gwangju Institute of Science and Technology (GIST)
Gwangju, Republic of Korea
e-mail: syang@gist.ac.kr

Abstract—This paper presents an analysis and parametrical modeling of blood plasma separation devices with optical sorting and deterministic lateral displacement mechanisms. The new device for optical sorting is offered. The modeling with the novel device shows that this device can separate red blood cells of different sizes from whole blood. Special numerical technique with periodical boundary conditions was applied for simulation of deterministic lateral displacement. Comparison of optical sorting and deterministic lateral displacement is performed. Unexplored optical and mechanical properties of blood components and indispensability of additional researches are also discussed.

Keywords—blood separation; optical sorting; deterministic lateral displacement

I. INTRODUCTION

Separation of the cellular component of human blood is of essential interest for medicine and research. In general outline human blood consists of plasma, erythrocytes or red blood cells (RBCs), reticulocytes, platelets, and leukocytes or white blood cells (WBCs). About 55% of whole blood is blood plasma. The proportion of blood volume that is occupied by erythrocytes is normally about 48% for men and 38% for women. This proportion is a hematocrit. Normally leukocytes take up approximately 1% of blood volume in a healthy adult human. The number of WBCs in the blood is a very sensitive indicator of diseases. Thus it is especially important to remove all RBCs for further analysis of WBCs. There are diverse classes of WBCs. A major separation of leukocytes includes five types, neutrophils, lymphocytes, monocytes, eosinophils, and basophils [1].

Usually, human blood is separated by large volume centrifugation [2]. With modern lab equipment such as lab-on-a-chip-type devices this approach is not so effective. This has led to an interest in adopting new microscopic separation techniques. Two of these promising methods are optical sorting [3][4] and deterministic lateral displacement [5] methods.

In the present paper, we first consider the new design for optical sorting and then we compare it to the deterministic lateral displacement. Also we discuss unexplored optical and mechanical properties of blood components.

II. OPTICAL AND MECHANICAL PROPERTIES OF BLOOD

The analysis of the reviews devoted to optical sorting and deterministic lateral displacement shows that only separation of colloidal particles of spherical shape in special mixture is well investigated [6-12]. Fractionation of real human blood requires essential efforts and more complicated devices [13].

Major problem here is that we have multi-component mixture of composite particles in non-Newtonian liquid.

Not all of the physical properties of these particles and liquid are well known.

A. Refractive Index and Absorption Coefficient

Mostly examined are the refractive index of whole blood, blood plasma, and RBCs. We collected some of measured refractive indexes and description of measuring methods in Table I.

If λ is the wavelength in nm then according to [26] the spectral dependence of refractive index of blood plasma is:

$$n_p = 1.3254 + 8405.3/\lambda^2 - 3.9572 \cdot 10^8/\lambda^4 - 2.3617 \cdot 10^{13}/\lambda^6. \quad (1)$$

We managed to find in the literature only one mention of platelet [22] and WBC [25] refractive index.

Absorption and scattering coefficients of whole blood at different oxygenation and different wavelength of incident light is widely published [16][27-29]. These coefficients for blood components are studied not completely. Absorption coefficient is very important for estimation of heating of plasma and particles during optical sorting.

B. Mechanical Properties of Blood

In a first approximation the blood plasma can be considered as a Newtonian liquid, but whole blood is a non-Newtonian.

At a normal physiological hematocrit of 45%, the viscosity of blood is $\eta = 4 \cdot 10^{-2}$ poise, which is roughly 4 times that of water. Plasma alone (zero hematocrit) has a viscosity of $\eta = 1.1 \cdot 10^{-2}$ to $1.6 \cdot 10^{-2}$ poise, depending upon the concentration of plasma proteins [30]. Variation of viscosity with shear rate at different haematocrits is well studied [31].

The movement of a particle in the viscous medium is characterized by Reynolds number $Re = \rho v R / \eta$, where, ρ is the fluid density, v is the particle velocity, R is a characteristic dimension (for example, radius of spherical particle), and η is the fluid viscosity. In our case for very low Reynolds numbers ($Re \ll 1$) the drag force on a sphere is described by Stokes' law:

$$F_D = -6\pi\eta v R, \quad (2)$$

For a 10 μm diameter spherical particle at a speed of 20.0 $\mu\text{m/s}$ the drag force is changed from 2.1 to 3.0 pN depending on plasma viscosity.

TABLE I. SIZE AND REFRACTIVE INDEX OF BLOOD COMPONENTS AND METHODS OF MEASURING

| Samples | Size (μm) | Refractive index | Wave-length (nm) | Method | Ref. |
|-----------------------|------------------------|------------------|------------------|--------------------------------|------|
| Lymphocytes (rats) | | 1.3545 - 1.3580 | | Abbé refractometer | [14] |
| Cytoplasm (rats) | | 1.3583 - 1.3584 | | | |
| RBC | 5.5 | 1.40 | 842 | Scattering | [15] |
| Whole blood | | 1.38 | 488 633 | | [16] |
| RBC | 6.3 | 1.41 | 632.8 | Scanning flow cytometer | [17] |
| RBC | 7.5 | 1.4 | 440 1000 | Scattering | [18] |
| Plasma | | 1.335 | | | |
| RBC | | 1.405 | 820 | Optical coherence tomography | [19] |
| RBC | 4.82-5.6 | 1.385 - 1.405 | 632.8 | Scattering | [20] |
| Haemoglobin cytoplasm | | 1.3871 1.3800 | 532 632.8 | Total internal reflection | [21] |
| Blood plasma | | 1.3515 - 1.3479 | 532 632.8 | | |
| Lecithin | | 1.4852 1.4838 | 532 632.8 | | |
| Platelet | 2-4 | 1.3999 | 660 | Scanning Flow Cytometer | [22] |
| RBC | ≈ 8 | 1.3999 | | Tomographic phase microscopy | [23] |
| RBC | 7.7 | 1.418 | 663 | Digital holographic microscopy | [24] |
| RBC | | 1.399 | 1064 | | [25] |
| WBC | | 1.360 | | | |

Elastic properties of blood cells are very important in collision between particles or between particles and mechanical hindrance. To the best of our knowledge, mainly works have been devoted to the coefficient of elasticity of RBCs. For example, in [32], the homogeneous Young's modulus for spherical red blood cells was measured as $E =$

11.0 ± 0.5 Pa. In all probability the elastic properties of over blood cells are still unknown.

III. OPTICAL SORTING

According to investigations of continuous flow separation [4, 33-38] optical fractionation may offer unparalleled selectivity for particle size and refractive index. WBCs have larger size than RBCs and smaller refractive index. Hence WBCs are undergone to greater drag force and smaller optical force than RBCs. It allows us to propose a device of optical sorting which separates only RBCs from whole blood.

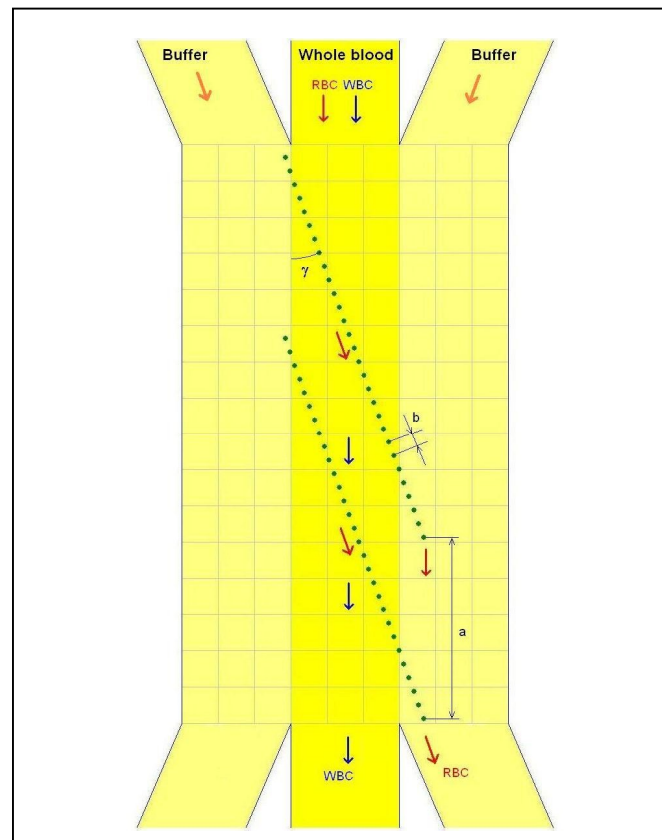


Figure 1. Schematic drawing of possible device for optical separation.

A two buffer streams of plasma and a central stream of whole blood move at equal speed (Fig. 1.). The optical traps are shown in Fig. 1 by green dots. RBCs are deviating by light (red arrows); WBCs are practically not at same conditions (blue arrows).

For our simulation, we assume that RBCs and WBCs are spherical balls. The radii of RBCs are $R_{RBC} = 2.5, 3.0, 3.5,$ and $4.0 \mu\text{m}$. The refractive index of plasma is $n_p = 1.335$, refractive indexes of RBCs and WBCs are $n_{RBC} = 1.40$ and $n_{WBC} = 1.36$ respectively. The distance between light spots is $b = 4$ and $5 \mu\text{m}$. The angle of trap layout is $\gamma = 15^\circ$ and 20° . The laser power per trap is $P = 5.0, 6.5$ and 8.3 mW/trap . The speed of plasma is $20 \mu\text{m/s}$ for all presented calculations. Trajectories of RBCs (red lines) and WBCs (blue lines) for

distance $b = 4 \mu\text{m}$ and angle $\gamma = 20^\circ$ are shown in Fig. 2. Trajectories of RBCs are deviated on angle γ while WBCs practically freely pass through tweezers array.

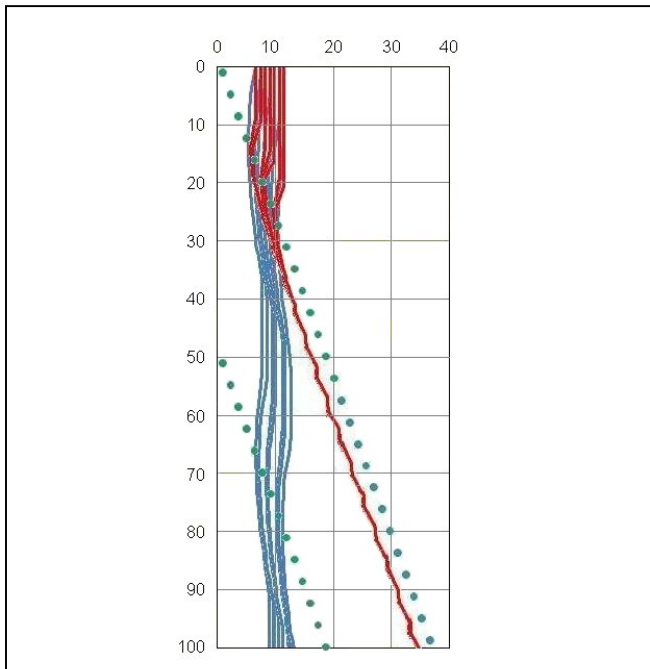


Figure 2. Calculated trajectories of RBCs (red lines) and WBCs (blue lines).

TABLE II. VELOCITY OF RBC AT SMALL DISTANCE BETWEEN LIGHT POSTS

| R, nm | Distance between light posts, $b = 4 \mu\text{m}$ | | | | | |
|-------|---|---------------------|---------------------|---------------------|---------------------|---------------------|
| | P = 5 mW/trap | | P = 6.5 mW/trap | | P = 8 mW/trap | |
| | $\gamma = 15^\circ$ | $\gamma = 20^\circ$ | $\gamma = 15^\circ$ | $\gamma = 20^\circ$ | $\gamma = 15^\circ$ | $\gamma = 20^\circ$ |
| 2.5 | 18.67 | 17.56 | 18.32 | 17.49 | 17.93 | 17.18 |
| 3.0 | 18.33 | 17.94 | 17.34 | 17.09 | 15.86 | 15.69 |
| 3.5 | 18.23 | 17.81 | 16.87 | 16.46 | 14.70 | 14.28 |
| 4.0 | 17.97 | 17.71 | 16.53 | 16.15 | 14.32 | 14.01 |

TABLE III. VELOCITY OF RBC AT LARGE DISTANCE BETWEEN LIGHT POSTS

| R, nm | Distance between light posts, $b = 5 \mu\text{m}$ | | | | | |
|-------|---|---------------------|---------------------|---------------------|---------------------|---------------------|
| | P = 5 mW/trap | | P = 6.5 mW/trap | | P = 8 mW/trap | |
| | $\gamma = 15^\circ$ | $\gamma = 20^\circ$ | $\gamma = 15^\circ$ | $\gamma = 20^\circ$ | $\gamma = 15^\circ$ | $\gamma = 20^\circ$ |
| 2.5 | 16.96 | 16.64 | 13.69 | 14.20 | Stop | Stop |
| 3.0 | 18.48 | 17.41 | 18.05 | 16.96 | 17.95 | 16.82 |
| 3.5 | 18.77 | 18.13 | 18.31 | 17.70 | 17.64 | 17.20 |
| 4.0 | 18.56 | 18.06 | 17.94 | 17.51 | 16.52 | 16.64 |

To calculate the optical force we followed [4, 33], the drag force was evaluated by (2).

Some results of our simulations for average velocity of RBCs are summarized in Table II and III. At some set of parameters it is possible to keep RBC at the trap. At the same time WBCs practically do not change speed.

IV. DETERMINISTIC LATERAL DISPLACEMENT

Deterministic lateral displacement has been applied to the size separation of particles and DNA molecules by pumping through an array of obstacles [5, 13, 39-41]. The array consisted of rows of micrometer-scale posts with a consistent gap between the posts in each row. Each row of obstacles is shifted horizontally with respect to the previous row (Fig. 3).

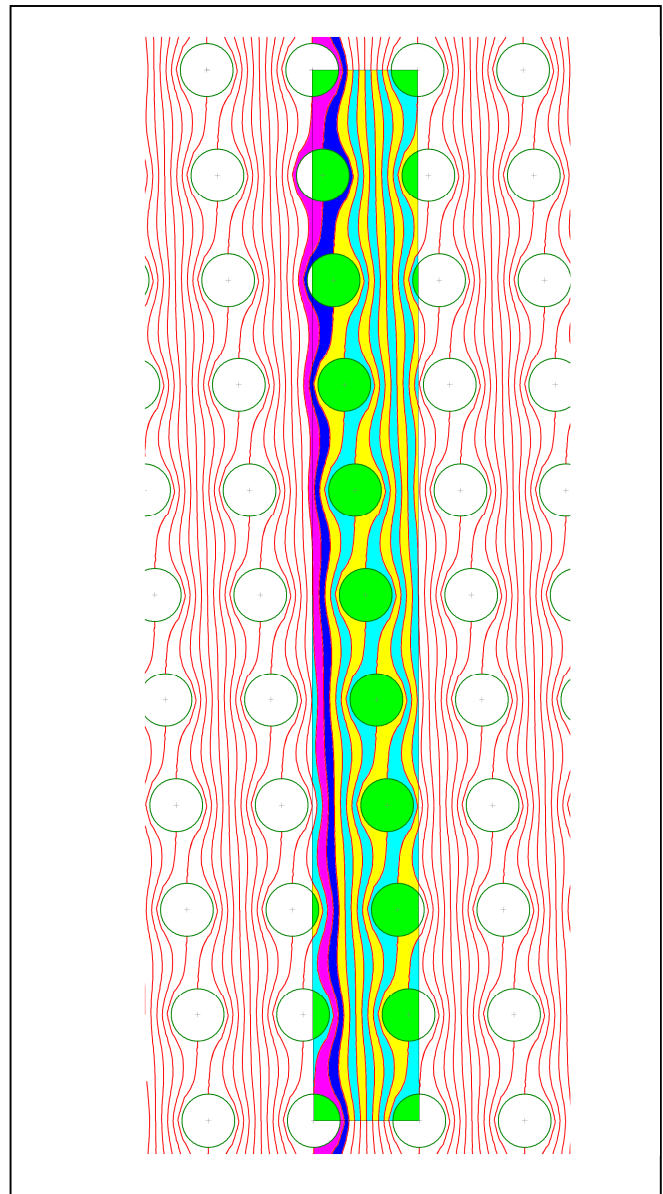


Figure 3. Streamlines in low Reynolds number flow through a periodic array of micrometer-scale obstacles.

The green circles represent the array of obstacles; the red lines are the streamlines in Fig. 3. The shift of each next row equals to tenth of the horizontal distance between obstacles in our illustration. The total fluid flux through each gap between two obstacles is divided into 10 flow streams in Fig. 3. After 10 horizontal rows the picture is repeated. Rectangular periodical part of obstacle array is colored in Fig. 3.

According to deterministic lateral displacement conception, small particles shall move in zigzag mode (blue and pink paths in Fig. 3) along a streamline from top to bottom. Large particles should jump from one post to another and deviate to the right from horizontal direction.

Apparently the flow in infinite periodic array of obstacles is presented by the primitive cell shown in Fig. 4. Obstacles are painted in green color; the cell is marked by pink color. We applied the finite element method and used special numerical technique to take into account periodical boundary conditions for simulation of deterministic lateral displacement in primitive cell. This reception allows to reduce number of nodes essentially.

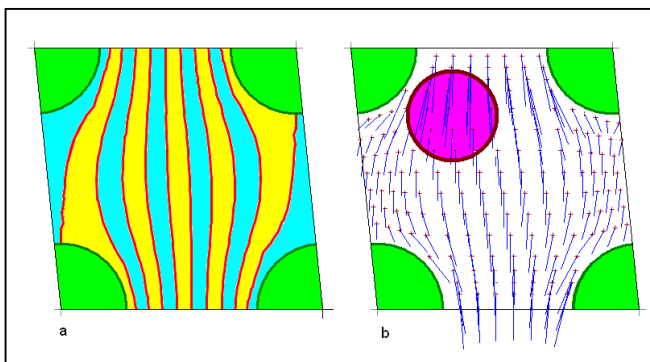


Figure 4. Streamlines (a) and velocity distribution (b) for primitive cell of obstacle array.

For simulation which shown in Figs. 3 and 4 the diameter of cylindrical obstacles was 10 μm , Distance between centers of cylinder in horizontal direction and period of obstacle rows in vertical direction were 20 μm .

The large problem is a trajectory analysis of individual blood cell:

- Application of the Stokes' law (2) for evaluation of the drag force is incorrect;
- The size of a particle is comparable with distance between posts as shown in Fig. 4b. Such particle has to perturb the fluid flow;
- Parameters of collision between a blood cell and obstacles are unknown. Conditions of sticking of a cell to an obstacle are unknown too;
- Density of blood cells is quite high therefore RBCs undergo impacts at passing through an array.

Let's note also that boundary conditions between plasma and obstacles as well as between plasma and blood cells are insufficiently studied.

V. CONCLUSION

The review of measured optical and mechanical properties of blood is presented. It is noted, that physical properties of many blood components are studied not fully. Thus it is essential to investigate refractive indexes and absorption coefficients of reticulocytes, platelets, and white blood cells (neutrophils, lymphocytes, monocytes, eosinophils, and basophils). Also elastic properties of all blood cells except RBCs are practically unknown.

We offered a new device for optical sorting of blood cells. The modeling with the novel device shows that this device can separate RBCs of different sizes from whole blood. For simulation of deterministic lateral displacement we developed special finite-element technique which allows to take into account periodical boundary conditions for primitive cell and to reduce number of nodes.

We can conclude that optical separation possesses certain advantages in comparison with deterministic lateral displacement:

- Smaller distance of separation;
- Tunable distance between light spots and tunable power per trap;
- Absence of mechanical interaction and hence absence of mechanical damage of cells.

Additionally we note that the gaps between mechanical posts in deterministic lateral displacement method can be littered by the stuck cells.

At the same time optical separation has the certain drawbacks:

- Heating of plasma and blood cells;
- Optical traps can hold small blood particles and obstruct to extraction of RBC;
- Speed of the RBC guided by optical traps is smaller than speed of a free RBC thus it is possible a collision between RBCs.

The large benefit of the deterministic lateral displacement is that the method is very simple and devices are very cheap. Although the optical sorting still are on a development stage the deterministic lateral displacement are already close to clinical tests.

ACKNOWLEDGMENT

This research was partially funded by grants from the National Research Foundation of Korea (NRF, Project No. 2010-0012897), the Ministry of Education, Science and Technology (MEST, WCU Program, Project No. R31-2008-000-10026-0), and the institute of Medical System Engineering (iMSE) in the GIST, Republic of Korea.

REFERENCES

- [1] M. Toner and D. Irimia, "Blood-on-a-Chip," *Annu. Rev. Biomed. Eng.*, vol. 7, Aug. 2005, pp. 77-103, doi:10.1146/annurev.bioeng.7.011205.135108.
- [2] J. P. Hester, R. M. Kellogg, A. P. Mulzet, V. R. Kruger, K. B. McCredie, and E. J. Freireich, "Principles of blood separation and component extraction in a disposable continuous-flow single-stage channel," *Blood*, vol. 54, July 1979, pp. 254-268.

- [3] M. P. MacDonald, G. C. Spalding, and K. Dholakia, "Microfluidic sorting in an optical lattice," *Nature*, vol. 426, Nov. 2003, pp. 421-424, doi:10.1038/nature02144.
- [4] K. Xiao and D. G. Grier, "Multidimensional Optical Fractionation of Colloidal Particles with Holographic Verification." *Phys. Rev. Lett.*, vol. 104, Jan. 2010, pp. 028302 (4 pages), doi:10.1103/PhysRevLett.104.028302.
- [5] L. R. Huang, E. C. Cox, R. H. Austin, and J. C. Sturm, "Continuous Particle Separation through Deterministic Lateral Displacement." *Science*, vol. 304, May 2004, pp. 987-990, doi:10.1126/science.1094567.
- [6] H. Andersson and A. van den Berg, "Microfluidic devices for cellomics: a review," *Sens. Actuators B*, vol. 92, July 2003, pp. 315-325, doi:10.1016/S0925-4005(03)00266-1.
- [7] N. Pamme, "Continuous flow separations in microfluidic devices," *Lab Chip*, vol. 7, December 2007, pp. 1644-1659, doi:10.1039/B715936F.
- [8] K. Dholakia, W. M. Lee, L. Paterson, M. P. MacDonald, R. McDonald, I. Andreev, P. Mthunzi, C. T. A. Brown, R. F. Marchington, and A. C. Riches, "Optical separation of cells on potential energy landscapes: enhancement with dielectric tagging," *IEEE J. Sel. Top. Quant.*, vol. 13, Nov.-Dec. 2007, pp. 1646-1654, doi:10.1109/JSTQE.2007.911314.
- [9] K. Dholakia, M. P. MacDonald, P. Zemánek, and T. Čižmár, "Cellular and Colloidal Separation Using Optical Forces." *Methods Cell Biol.*, vol. 82, 2007, pp. 467-485, doi:10.1016/S0091-679X(06)82017-0.
- [10] A. Jonáš and P. Zemánek, "Light at work: The use of optical forces for particle manipulation, sorting, and analysis." *Electrophoresis*, vol. 29, Dec. 2008, pp. 4813-4851, doi:10.1002/elps.200800484.
- [11] A. Lenshof, Th. Laurell, "Continuous separation of cells and particles in microfluidic systems," *Chem. Soc. Rev.*, vol. 39, March 2010, pp. 1203-1217, doi:10.1039/b915999c.
- [12] A. A. S. Bhagat, H. Bow, H. W. Hou, S. J. Tan, J. Han, and C. T. Lim, "Microfluidics for cell separation," *Med. Biol. Eng. Comput.*, vol. 48, Oct. 2010, pp. 999-1014, doi:10.1007/s11517-010-0611-4.
- [13] J. A. Davis, D. W. Inglis, K. J. Morton, D. A. Lawrence, L. R. Huang, S. Y. Chou, J. C. Sturm, and R. H. Austin, "Deterministic hydrodynamics: Taking blood apart." *PNAS*, vol. 103, Oct. 2006, pp. 14779-14784, doi:10.1073/pnas.0605967103.
- [14] K. W. Keohane and W. K. Metcalf, "The cytoplasmic refractive index of lymphocytes, its significance and its changes during active immunization," *Exp. Physiol.*, vol. 44, March 1959, pp. 343-350.
- [15] D. H. Tycko, M. H. Metz, E. A. Epstein, and A. Grinbaum, "Flow-cytometric light scattering measurement of red blood cell volume and hemoglobin concentration," *Appl. Optics*, vol. 24, May 1985, pp. 1355-1365, doi:10.1364/AO.24.001355.
- [16] D. K. Sardar and L. B. Levy, "Optical properties of whole blood," *Lasers Med. Sci.*, vol. 13, June 1998, pp. 106-111, doi:10.1007/s101030050062.
- [17] A. N. Shvalov, J. T. Soini, A. V. Chernyshev, P. A. Tarasov, E. Soini, and V. P. Maltsev, "Light-scattering properties of individual erythrocytes," *Appl. Optics*, vol. 38, Jan. 1999, pp. 230-235, doi:10.1364/AO.38.000230.
- [18] J. Mroczka, D. Wysoczanski, "Optical parameters and scattering properties of red blood cells," *Optica Applicata*, vol. 32, no. 4, 2002, pp. 691-700.
- [19] X. Xu, R. K. Wang, J. B. Elder, and V. V. Tuchin, "Effect of dextran-induced changes in refractive index and aggregation on optical properties of whole blood," *Phys. Med. Biol.*, vol. 48, May 2003, pp. 1205-1221, doi:10.1088/0031-9155/48/9/309.
- [20] N. Ghosh, P. Buddhiwant, A. Uppal, S. K. Majumder, H. S. Patel, and P. K. Gupta, "Simultaneous determination of size and refractive index of red blood cells by light scattering measurements," *Appl. Phys. Lett.*, vol. 88, Feb. 2006, pp. 084101 (3 pages), doi:10.1063/1.2176854.
- [21] Y. L. Jin, J. Y. Chen, L. Xu, and P. N. Wang, "Refractive index measurement for biomaterial samples by total internal reflection," *Phys. Med. Biol.*, vol. 51, October 2006, pp. N371-N379, doi:10.1088/0031-9155/51/20/N02.
- [22] I. V. Kolesnikova, S. V. Potapov, M. A. Yurkin, A. G. Hoekstra, V. P. Maltsev, and K. A. Semyanov, "Determination of volume, shape and refractive index of individual blood platelets," *J. Quant. Spectrosc. Radiat. Transf.*, vol. 102, Nov. 2006, pp. 37-45, doi:10.1016/j.jqsrt.2006.02.050.
- [23] Y. K. Park, M. Diez-Silva, G. Popescu, G. Lykotrafitis, W. Choi, M. S. Feld, and S. Suresh, "Refractive index maps and membrane dynamics of human red blood cells parasitized by *Plasmodium falciparum*," *PNAS*, vol. 105, Sep. 2008, pp. 13730-13735, doi:10.1073/pnas.0807334105.
- [24] B. Rappaz, P. Marquet, E. Cuche, Y. Emery, C. Depeursinge, and P. J. Magistretti, "Measurement of the integral refractive index and dynamic cell morphometry of living cells with digital holographic microscopy," *Optics Express*, vol. 13, Nov. 2005, pp. 9361-9373, doi:10.1364/OPEX.13.009361.
- [25] A. Bankapur, E. Zachariah, S. Chidangil, M. Valiathan, and D. Mathur, "Raman tweezers spectroscopy of live, single red and white blood cells," *PLoS ONE*, vol. 5, April 2010, pp. e10427 (11 pages), doi:10.1371/journal.pone.0010427.
- [26] V. V. Tuchin, D. M. Zhestkov, A. N. Bashkatov, and E. A. Genina, "Theoretical study of immersion optical clearing of blood in vessels at local hemolysis," *Opt. Express*, vol. 12, June 2004, pp. 2966-2971, doi:10.1364/OPEX.12.002966.
- [27] F. J. Janssen, "A study of the absorption and scattering factors of light in whole blood." *Med. Biol. Eng. Comput.*, vol. 10, March 1972, pp. 231-240, doi:10.1007/BF02474113.
- [28] D. J. Faber, M. C. G. Aalders, E. G. Mik, B. A. Hooper, M. J. C. van Gemert, and T. G. van Leeuwen, "Oxygen Saturation-Dependent Absorption and Scattering of Blood," *Phys. Rev. Lett.*, vol. 93, July 2004, pp. 028102 (4 pages), doi:10.1103/PhysRevLett.93.028102.
- [29] A. N. Bashkatov, E. A. Genina, V. I. Kochubey, and V. V. Tuchin, "Optical properties of human skin, subcutaneous and mucous tissues in the wavelength range from 400 to 2000nm," *J. Phys. D: Appl. Phys.*, vol. 38, Aug. 2005, pp. 2543-2555, doi:10.1088/0022-3727/38/15/004.
- [30] D. Elad and S. Einav, "Physical and flow properties of blood," in: *Standard handbook of biomedical engineering and design*, chapter 3, M. Kutz, Ed. New York: McGraw-Hill, 2003, pp. 3.1-3.25.
- [31] J. P. Woodcock, "Physical properties of blood and their influence on blood-flow measurement," *Rep. Prog. Phys.*, vol. 39, Jan. 1976, pp. 65-127, doi:10.1088/0034-4885/39/1/002.
- [32] J. Guck, R. Ananthakrishnan, C. C. Cunningham, and J. Käs, "Stretching biological cells with light." *J. Phys.: Condens. Matter*, vol. 14, May 2002, pp. 4843-4856, doi:10.1088/0953-8984/14/19/311.
- [33] P. T. Korda, M. B. Taylor, and D. G. Grier, "Kinetically locked-in colloidal transport in an array of optical tweezers," *Phys. Rev. Lett.*, vol. 89, Sep. 2002, pp. 128301 (4 pages), doi:10.1103/PhysRevLett.89.128301.
- [34] K. Ladavac, K. Kasza, and D. G. Grier, "Sorting mesoscopic objects with periodic potential landscapes: Optical fractionation." *Phys. Rev. E*, vol. 70, July 2004, pp. 010901(R) (4 pages), doi:10.1103/PhysRevE.70.010901.
- [35] S.-K. Hoi, C. Udalgama, C.-H. Sow, F. Watt, and A. A. Bettiol, "Microfluidic sorting system based on optical force

- switching,” *Appl. Phys. B*, vol. 97, Dec. 2009, pp. 859-865, doi:10.1007/s00340-009-3687-5.
- [36] S.-K. Hoi, V. H. Kim, N. M. Huy, C.-H. Sow, Y.-S. Ow, and A. A. Bettiol, “Passive optical separation and enrichment of cells by size difference,” *Biomicrofluidics*, vol. 4, Dec. 2010, pp. 044111 (9 pages), doi:10.1063/1.3523057.
- [37] K. Xiao, and D. G. Grier, “Sorting colloidal particles into multiple channels with optical forces: Prismatic optical fractionation,” *Phys. Rev. E*, vol. 82, Nov. 2010, pp. 051407 (9 pages), doi:10.1103/PhysRevE.82.051407.
- [38] K. H. Lee, S. B. Kim, K. S. Lee, and H. J. Sung “Enhancement by optical force of separation in pinched flow fractionation,” *Lab Chip*, vol 11, Jan. 2011, pp. 354-357. doi:10.1039/c0lc00225a.
- [39] D. W. Inglis, J. A. Davis, R. H. Austin, and J. C. Sturm, “Critical particle size for fractionation by deterministic lateral displacement,” *Lab Chip*, vol. 6, May 2006, pp. 655-658, doi:10.1039/b515371a.
- [40] D. W. Inglis, “Efficient microfluidic particle separation arrays,” *Appl. Phys. Lett.*, vol. 94, Jan. 2009, Vol. pp. 013510 (3 pages), doi:10.1063/1.3068750.
- [41] S. Chang and Y.-H. Cho, “A continuous size-dependent particle separator using a negative dielectrophoretic virtual pillar array,” *Lab Chip*, vol. 8, Nov. 2008, pp. 1930-1936, doi:10.1039/b806614k.

PVC Inorganic Hybrids Based on Kaolinite/Urea Intercalates

Kalendova Alena¹, Zykova Jitka², Matejka Vlastimil³, Machovsky Michal⁴, Malac Jiri¹

¹Centre of Polymer Systems, Department of Polymer Engineering, Faculty of Technology, Tomas Bata University in Zlin, nam. T.G.Masaryka 5555, 760 01 Zlin, Czech Republic, kalendova@ft.utb.cz

²Department of polymer Engineering, Faculty of Technology, Tomas Bata University in Zlin, nam. T.G.Masaryka 275, 762 72 Zlin, Czech Republic

³Department of Nanotechnology Centre, VSB-Technical University of Ostrava, 17. listopadu 15/2172, 70833 Ostrava-Poruba, Czech Republic, vlastimil.matejka@vsb.cz

⁴Polymer Centre, Faculty of Technology, Tomas Bata University in Zlin, nam. T.G.Masaryka 275, 762 72 Zlin, Czech Republic

Abstract—Polymer/clay hybrids materials receive much attention due to their interesting mechanical and thermal properties. Composites of poly(vinyl chloride) have been prepared by melt intercalation method using commercial type of pure kaolinite (SAK47), urea intercalated kaolinite (SAK47/urea), and intercalated/exfoliated kaolinite after washing of urea from kaolinite-urea (del. SAK47). In the next step the untreated and treated kaolinite was modified by Bis(2-ethylhexyl)phthalate, DEHP, (SAK47/DEHP, SAK47/urea/DEHP and del. SAK47/DEHP). For the PVC/kaolinite composites the suspension type of PVC with K value 60 was used. Untreated and treated kaolinite samples as well as PVC composites were examined by X-ray diffraction (XRD) and microscopy (SEM). The interactions between kaolinite and modifier were discussed by FTIR-ATR. Tested mechanical properties were improved almost for all PVC mixtures. The highest values of tensile strength and E-modulus were observed for PVC+del.SAK47/DEHP.

Keywords- PVC; composite; kaolinite; urea; DEHP

I. INTRODUCTION

In worldwide commercial importance, polyvinyl chloride (PVC) is the third most widely produced plastic, after polyethylene and polypropylene [1]. It was first recognized and characterized in 1835 by Henri Victor Regnault and it became commercially significant in Germany prior to World War II [2]. PVC can be modified by large amounts of modifying agents like plasticizers, fillers (calcium carbonate, kaolinite, and calcined kaolinite), and so on. This material can offer many good properties, such as low flammability, high chemical resistance, barrier properties low cost, and formulating versatility. On the other hand, the properties such as its poor impact toughness and low heat-softening temperature limit its application [3]. Next PVC mixtures disadvantage is migration and toxicity of some additives used in PVC, which may have a negative impact on the environment and human health. For all that, PVC production is expected to exceed 40 million tons by 2016 [4].

Kaolinite is a common phyllosilicate mineral, with a general chemical formulation $\text{Al}_2\text{Si}_2\text{O}_5(\text{OH})_4$. This clay has 1:1 dioctahedral structure which is composed of tetrahedral sheets SiO_4 and octahedral sheets $(\text{Al}_2(\text{OH})_4)$. The layers linked together by hydrogen bonds between surface

hydroxyl groups on the octahedral side and the basal oxygen atoms on the tetrahedral side [5]. Because of hydrophobic properties of kaolinite and hydrophilic character of polymer the modification of kaolinite is necessary. The separation of kaolinite results in particle size reducing and an increase of the specific surface area. The good kaolinite modification result in better intercalation between filler and polymer matrix. In addition the properties of composite materials could be improved. Kaolinite has many industrial applications; it is used in paper, paint, rubber, plastics and ceramics industries. Its largest applicability as filler in PVC is on production electrical cables or film anti-blocking, tiles and so one [6-9].

This paper follows up our research of PVC inorganic hybrids based on kaolinite/urea. In this part it is compared the kaolinite/urea based PVC composition with kaolinite/urea/DEHP mixtures. All presented mixtures were prepared by melt intercalation. The morphology and mechanical properties composites based on pure kaolinite, urea intercalated kaolinite, intercalated/exfoliated kaolinite after washing of urea from kaolinite-urea, and kaolinite additionally modified with DEHP were examined and compared. Furthermore, infrared spectroscopy was used in order to get insight into interactions between minerals and modifier at a molecular level.

II. EXPERIMENTAL

A. Materials

Suspension type of polyvinyl chloride (Neralit 601) with K-value 60 (Spolana a. s., Czech Republic) was used as the polymer matrix.

Three types of filler were studied: commercial kaolinite, urea intercalated kaolinite, and intercalated/exfoliated kaolinite after washing of urea. Firstly, Kaolinite SAK47 (LB Minerals) was investigated without any additional treatment in received state. Beside kaolinite as a main component of SAK47, it contains quartz and mica as admixtures as was revealed using X-ray diffraction method. According to data available from producer of SAK47 82 % of particles are smaller than 10 μm [10].

Next urea was used for the intercalation of SAK47. The sample preparation was performed according to procedure described by Valaskova 'et. al.' [11] and Zykova 'et. al.'

[12]. 500 g of SAK47 (LB Minerals) was homogenized for 5 min with 330 g of urea (Lachner, p.a. grade) in vibrating mill. Intercalation of urea into kaolinite interlayer was achieved by 48 hours long heating of the homogenized mixture at 95 °C in laboratory oven [11,12].

Further delamination of kaolinite was achieved using 5 hour long low-temperature ultrasound washing of urea with distilled water. This process is explained in detail in publications [11,12]. For 100 g of intercalate 3 l of distilled water was used. After washing liquid portion was removed by sedimentation, obtained solid portion was dried at 60 °C. By this way was obtained del. SAK47 (intercalated/exfoliated kaolinite after washing of urea).

Finally all three types of filler (SAK47, SAK47/urea, and del. SAK47) were treated by Bis(2-ethylhexyl)phthalate (DEHP). DEHP is an organic compound with the formula $C_6H_4(C_8H_{17}COO)_2$ and it is the most important phthalate, Untreated and treated kaolinite was modified by DEHP (DEZA a.s., Czech Republic) in laboratory mixer at 80 °C for 1 hour and then dried on the oven at 100 °C for 24 hours. After treatment the powder was obtained.

B. PVC Composite Processing

PVC/kaolinite composite samples were prepared, in accordance with Zykova ‘et. al.’ [12], via the melt intercalation method on the two-roll mill Collin W100T for 20 minutes, using speed 10 rpm and the temperature of the front and behind rolls was 181 and 177 °C. The exact composition of the polymer/clay composites can be seen in Table 1.

TABLE I. PVC/KAOLINITE MIXTURES COMPOSITION

| Polymer | Filler | wt. (%) | Sample name |
|---------|-----------------|---------|----------------------|
| sPVC | | | Unfilled PVC |
| sPVC | SAK47 | 5 | PVC+SAK47 |
| sPVC | SAK47+DEHP | 5 | PVC+SAK47/DEHP |
| sPVC | SAK47/Urea | 5 | PVC+SAK47/urea |
| sPVC | SAK47/Urea/DEHP | 5 | PVC+SAK47/urea/DEHP |
| sPVC | Del. SAK47 | 5 | PVC+ del. SAK47 |
| sPVC | Del. SAK47/DEHP | 5 | PVC+ del. SAK47/DEHP |

C. Methods

X-ray diffraction was (XRD) obtained using PANalytical X’Pert PRO diffracto-meter equipped with CuK_{α} radiation ($\lambda = 0.154 \text{ nm}$) at room temperature. The scans were taken in a 2θ range from 4 to 30 °, with 0.02 ° step size and the counting time of one scan 5 s.

Fourier transform infrared spectrometer (FTIR) Avatar 320 (Nicolet CZ, s.r.o) was employed to get insight into interactions between mineral and urea modifier at a

molecular level. ATR method was used with number of scan 64.

The scanning electron microscopy (SEM) photographs of the samples were taken to assess the morphology kaolin/PVC composites by a VEGA\LMU. Before examination, samples were coated by thin layer of Ag/Pd.

Mechanical properties were measured by Alpha Technologies Tensometer 2000 and a speed of testing was 500 mm/min. The dogbone specimens (type V in accordance with standard CSN EN ISO 527-2) were used for the measurement.

III. RESULTS AND DISCUSSION

X-ray powder diffraction method was used to observe urea and urea/DEHP intercalation process. Significant segments of XRD patterns described process of intercalation as well as delamination are pictured in Figure 1. Decrease in intensity of d_{001} basal diffraction of kaolinite with maxima at $d=0.717 \text{ nm}$ is evident after the intercalation with urea. The new peak with maxima at $d=1.072 \text{ nm}$ is connected with formation of kaolinite-urea complex [11] and is connected with increase in interlayer distance due to the insertion of urea molecules. After the washing this diffraction disappears (see pattern del. SAK47) in Figure 1. After DEHP addition to SAK47 the maximum $d= 0,717 \text{ nm}$ intensity is decreased, but it is still very strong. In the case of SAK47/urea/DEHP the original maximum of kaolinite at $d=0.7171 \text{ nm}$ was almost disappeared and the maximum at $d=1.072 \text{ nm}$ is lower comparing SAK47/urea intercalate. This fact could be connected with lower organization of layers. For del. SAK47/DEHP is the basal diffraction d_{001} on the same position as for del. SAK47. The peak intensity reveals that the intercalation and delamination of kaolinite was not complete in this case.

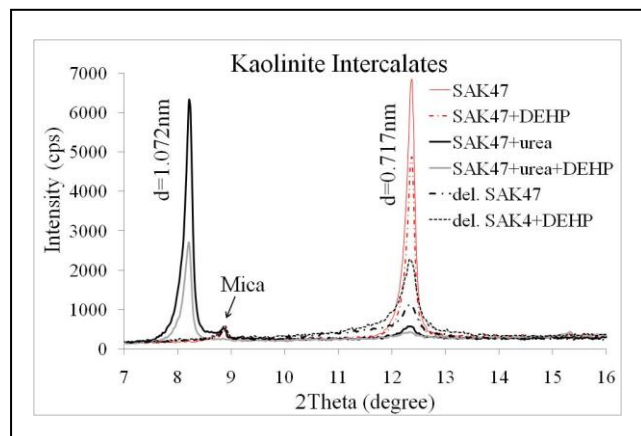


Figure 1. XRD of used fillers: unmodified SAK47, intercalated SAK47/urea, del. SAK47, SAK47/DEHP, SAK47/urea/DEHP and del. SAK47/DEHP.

Next Figures 2-4 demonstrate the XRD patterns of unfilled PVC and PVC/kaolinite samples. In Figure 2 is observed that in the PVC+SAK47 composite the

characteristic peak of kaolinite (d_{001}) is still visible. It indicated that filler still keeps its original crystal structure.

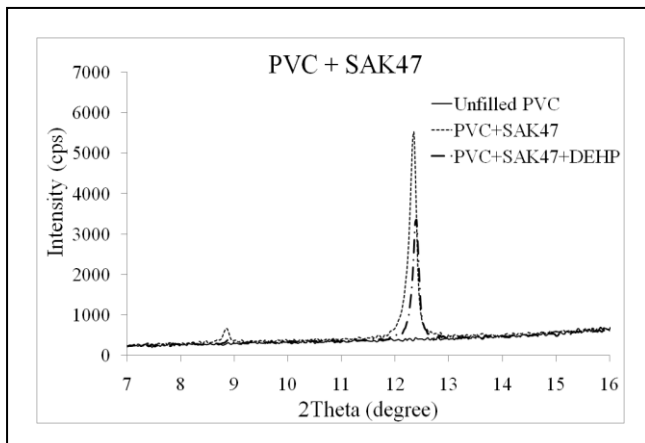


Figure 2. XRD patterns: Pure PVC, PVC/SAK47 and PVC/SAK47/DEHP.

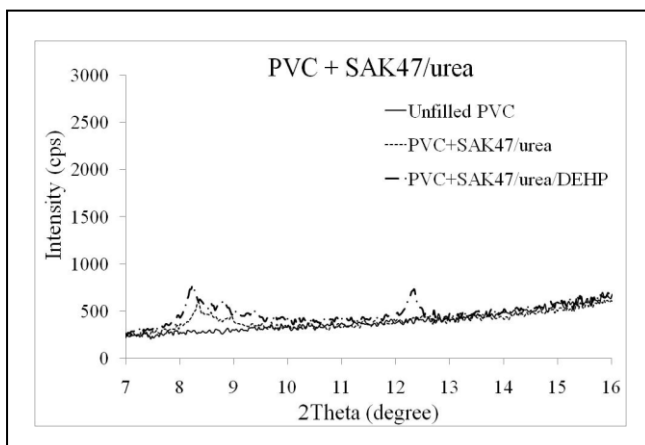


Figure 3. XRD patterns: Pure PVC, PVC/SAK47/urea and PVC/SAK47/urea/DEHP.

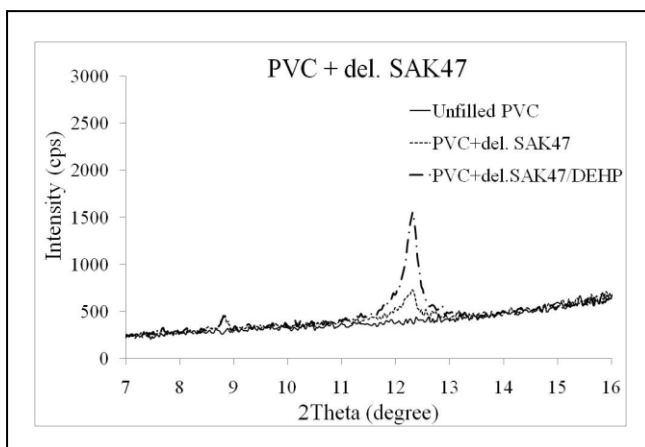


Figure 4. XRD patterns: Pure PVC, PVC/del.SAK47 and PVC/del.SAK47/DEHP.

For the PVC+SAK47/DEHP kaolinite maximum intensity was fall down around 40 %. This fact could indicate the

improved kaolinite dispersion in polymer matrix. The $d=0,717$ nm is almost disappeared in case of PVC+SAK47/urea and PVC+SAK47/urea/DEHP composite (Figure 3). It was observed broad low intensity peak at $d=1.072$ nm, which is connected with increase of interlayer distance. Next in the pattern of PVC+del.SAK47 (Figure 4) the kaolinite diffraction peak at $0,717$ nm also almost disappears. On the other hand when the DEHP was employed to the process of del.SAK47 modification the intensity of this maximum was increased. The intensity of (d_{001}) is around 70 % lower comparing PVC+SAK47 mixture. From XRD results that modified kaolinites are probably more dispersed into the polymer matrix than untreated SAK47.

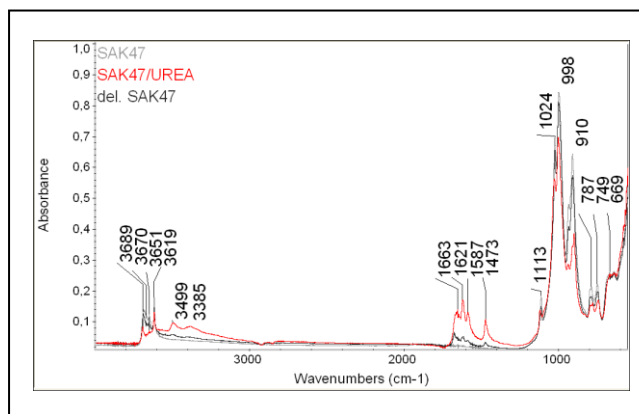


Figure 5. FTIR-ATR spectra of natural kaolinite SAK47 and modified kaolinite SAK47/urea, del. SAK47.

The FTIR-ATR method was used to study the changes in the kaolinite structure after intercalation. The spectra of unmodified and modified kaolinite are presented in Figure 5 and 6. There are three kinds of hydroxyl groups in unmodified kaolinite SAK47: inner-surface hydroxyl group at 3689 and 3670 cm^{-1} , inner hydroxyl 3619cm^{-1} , and absorbed water hydroxyl with vibration 3651 cm^{-1} in Figure 5 [3,13]. Next vibrations 1113 , 1026 and 910 cm^{-1} characterize the Si-O stretching vibrations. O-Al-OH stretching vibrations are connected with vibrations 787 , 749 and 669 cm^{-1} . The general features of kaolin intercalated with urea (SAK47/urea) are practically the same as for SAK47 (Figure 5). Nonetheless, there are some differences in the NH stretching region of SAK47/urea spectrum. Two new bands appear at 3499 and 3385 cm^{-1} . These bands could refer to a small amount of hydrogen bonding of urea to the kaolinite surface through its NH group. Further, in the region $1400-1700$ cm^{-1} the changes in spectra of SAK47/urea was noticed. New vibrations at 1663 , 1621 , 1587 and 1473 cm^{-1} were observed comparing unmodified SAK47. This may suggest that modification by urea results in some intercalation of the SAK47. After washing with distilled water the intensity of observed vibration connected with urea are dropped, but they are still visible. This fact could indicate that the bonded part of intercalation agent stay in the clay structure after washing.

FTIR spectra SAK47/urea modification by DEHP are showed in the Figure 6. New vibration was observed in the region above 3000 cm⁻¹. Next new maximum is at 1781 and 1417 cm⁻¹. It is supposed that they could be connected with the DEHP and urea interactions.

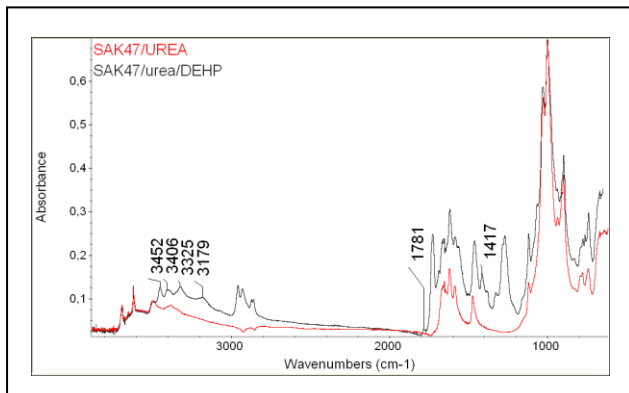


Figure 6. FTIR-ATR spectra of SAK47/urea and SAK47/urea/DEHP.

SEM was used for the morphological study of the unmodified and modified kaolinite within the PVC matrix. The structure PVC composites based on untreated and treated SAK47 modified by urea was previously described in paper [12]. It was observed that the PVC filled by 5 wt. % of untreated kaolinite (SAK47) shows inhomogeneity which suggests the poor interfacial adhesion between polymer and filler, see Figure 7. On the other hand, PVC filled by 5 wt. % of SAK47 modified by urea indicated better dispersion with low amount of aggregates. In composition PVC/del.SAK47 kaolinite layers seem to be delaminated into individual layers or stacks of several layers of kaolin in PVC. In the case of DOP the homogeneity was further improved. These results are in good agreement with XRD and mechanical properties.

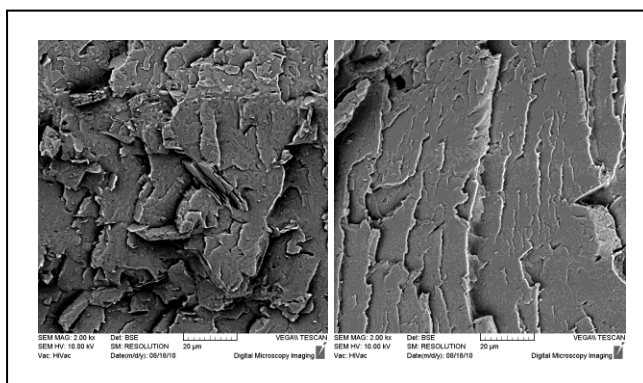


Figure 7. SEM: PVC/SAK47 and PVC/SAK47/urea.

Mechanical properties tested PVC composites are summarised in Table 2. It can be seen that the tensile strength all presented PVC composite samples is higher as compared to unfilled PVC. The lowest value of tensile strength from tested PVC composites has the mixture PVC+SAK47/urea. The highest value was observed for

PVC+del.SAK47/DEHP with change around 13 % comparing pure PVC. In addition, all composite samples also show E-modulus increase as compared to unfilled PVC. The Sample PVC+del.SAK47/DEHP offers the highest value with an improvement 28 %. The lowest E-modulus from tested composites was obtained for PVC+SAK47 (untreated kaolinite). Generally it could be said that highest values of E-modulus gives the compositions with additional treatment with DEHP. It could indicated that these mixtures offers better dispersion in polymer matrix.

TABLE II. MECHANICAL PROPERTIES OF PVC/KAOLINITE MIXTURES

| Samples | Tensile Strength (MPa) | S ^a (Mpa) | E-modulus (MPa) | S ^a (MPa) |
|----------------------|------------------------|----------------------|-----------------|----------------------|
| Unfilled PVC | 46.0 | 2.9 | 1630 | 85 |
| PVC+SAK47 | 49.5 | 1.82 | 1630 | 156 |
| PVC+SAK47/DEHP | 49,7 | 0,80 | 1756 | 77,0 |
| PVC+SAK47/urea | 48.6 | 1.51 | 1995 | 169 |
| PVC+SAK47/urea /DEHP | 50,4 | 1,83 | 2006 | 165 |
| PVC+ del. SAK47 | 51.7 | 0.24 | 1689 | 161 |
| PVC+ del. SAK47/DEHP | 52,2 | 0,41 | 2082 | 145 |

^a standard deviation

IV. CONCLUSION

The effect of the untreated, treated kaolinite by urea and DEHP on the morphology and mechanical properties was investigated.

Firstly, XRD and FTIR study confirms that kaolinite modification results in intercalation of the SAK47. FTIR-ATR spectra indicated hydrogen bonding of urea to the kaolinite surface through its NH group. Furthermore the rest of urea was observed in spectra after distilled water washing. This fact could indicate that the bonded part of intercalation agent stay in the clay structure after washing. FTIR spectra kaolinite/urea modified by DEHP show new vibration in the region above 3000 cm⁻¹, 1781 and 1417 cm⁻¹. It is supposed that they could be connected with the DEHP and urea interactions.

The XRD patterns show that the urea and DEHP have the influence on the PVC composite morphology. The largest changes in XRD patterns were observed by compositions based on urea and urea/DEHP.

Tested mechanical properties, tensile strength and E-modulus, were improved almost for all PVC mixtures. The highest values of tensile strength and E-modulus were observed for PVC+del.SAK47/DEHP with change around 13 % and 28 % comparing pure PVC. This improvement could be connected with delamination of kaolinite layers, which results in the increase of the specific surface area.

ACKNOWLEDGMENT

This article (specify by the fact) was written with support of Operational Program Research and Development for Innovations co-funded by the European Regional Development Fund (ERDF) and national budget of Czech

Republic, within the framework of project Centre of Polymer Systems (reg. number: CZ.1.05/2.1.00/03.0111). Next the Financial support of the Ministry of Education of the Czech Republic, project MSM 7088352101 and MSM 6198910016 is gratefully acknowledged. Finally this project was supported by the internal grant of TBU in Zlín No. IGA/23/FT/11/D funded from the resources of specific university research.

REFERENCES

- [1] Veris Consulting and ACC, "ACC Resin Statistics Annual Summary",
<http://www.americanchemistry.com/s_acc/sec_policyissues.asp?CID=996&DID=6872> 07.06.2011.
- [2] L. I. Nass, Encyclopedia of PVC (Vol. 1). Marcel Dekker, New York, 1976, ISBN 0-8247-6165-0.
- [3] Y. Turhan, M. Dogan, and M. Alkan, "Poly(vinyl chloride)/Kaolinite Nanocomposites: Characterization and Thermal and Optical Properties", *Ind. Eng. Chem. Res.*, 2010, Vol. 49, pp. 1503–1513.
- [4] M. Ebner, "Ceresana Research Releases New Comprehensive PVC Market Study", *Newsire Today* (2008-11-18), <<http://www.newswiretoday.com/news/42864/>> 07.06.2011.
- [5] J. Matusik, E. Stodolak, K. Bahranowski, "Synthesis of Polylactide/Clay Composites using Structurally Different Kaolinites and Kaolinite Nanotubes". *Applied Clay Science*, 2011, Vol. 51, pp. 102–109.
- [6] T. A. Elbokl and C. H. Detellier, "Intercalation of cyclic imides in kaolinite", *Journal of Colloid and Interface Science*, 2008, Vol. 323, pp. 338-348.
- [7] Y. Turhan, M. Dogan, and M. Alkan, "Poly(vinyl chloride)/Kaolinite Nanocomposites: Characterization and Thermal and Optical Properties", *Ind. Eng. Chem. Res.*, 2010, Vol. 49, pp. 1503-1513.
- [8] L. Domka, A. Malicka, N. Stachowiak, "Production and Structural Investigation of Polyethylene Composites with Modified Kaolin", *Acta Physica Polonoca A*, 2008, Vol. 114, No. 2, pp. 413-421.
- [9] S. J. der Gaast, M. Zbik, J. T. Klopogge, and G. N. Paroz, "Birdwood kaolinite: a highly ordered kaolinite that is difficult to intercalate/an XRD, SEM and Raman Spectroscopic Study", *Applied Clay Science*, 2002, Vol. 20, pp. 177-187.
- [10] LB MINERALS, s.r.o.
<<http://www.lb-minerals.cz/en/products/2-kaolinites/13-blended-kaolinites/76-sak-47>> 07.06.2011.
- [11] M. Valášková, M. Rieder, V. Matějka, P. Čapková, and A. Sliva, "Exfoliation/Delamination of Kaolinite by Low-Temperature Washing of Kaolinite–Urea Intercalates", *Applied Clay Science*, 2007, Vol. 35, pp. 108–118.
- [12] J. Zykova, A. Kalendova, V. Matejka, P. Zadraba, and J. Malac, "Influence of kaolinite modification on the PVC composites properties", 3rd WSEAS International Conference ADVANCES in SENSORS, SIGNALS and MATERIALS: Material Science, WSEAS Press 2010, University of Algarve, Faro, Portugal, pp. 30–34. ISBN: 978-960-474-248-6. ISSN: 1792-6238, 1792-6211.
- [13] R. L. Ledoux and J. L. J. White, "Infrared studies of hydrogen bonding interaction between kaolinite surfaces and intercalated potassium acetate, hydrazine, formamide, and urea. *J. Colloid Interface Sci.*, 1996, Vol. 21 (2), pp. 127–152.